Synthesis, Spectroscopy and Simulation of Doped Nanocrystals

Cover photographs taken by the author at Shaab Hamdalla, Tobia Arba and Ras Abu Soma in Safaga (Egypt), 2002.

SYNTHESIS, SPECTROSCOPY AND SIMULATION
OF DOPED NANOCRYSTALS

SYNTHESE, SPECTROSCOPIE EN SIMULATIE
VAN GEDOTEERDE NANOKRISTALLEN

(met een samenvatting in het Nederlands)

PROEFSCHRIFT

ter verkrijging van de graad van doctor aan de Universiteit Utrecht op gezag van de Rector Magnificus, prof. dr. W. H. Gispen, ingevolge het besluit van het College voor Promoties in het openbaar te verdedigen op maandag 10 februari 2003 des middags te 2.30 uur

door

JAN FREDERIK SUYVER

geboren op 14 juli 1975, te Den Haag

Promotores: Prof. dr. J. J. Kelly
                     Prof. dr. A. Meijerink

                     Debye Instituut
                     Universiteit Utrecht

Power to the one who doesn't want it!

Contents

Chapter 1

Introduction

What is so special about nanocrystals? Who was the first to study nanocrystals? Why should one want to study them? What is the motivation for using transition metal doped systems? What kind of devices would benefit from having nanocrystals as the active component? These are a few of the more important questions that need answering before the remainder of this thesis should be read. In this first chapter a general overview of the field of doped semiconductor nanocrystals is presented and the questions posed above will be answered.

1.1   Small, smaller and smallest

The perception of the everyday world around us is generally biassed. Most people never give a thought to the size dependence of the fundamental properties of a material[1] and, if they do, then they tend to think that they are size independent. Take for example gold. What would happen if a sample of gold is cut into smaller pieces? Most people would argue that this would just yield several smaller pieces of gold, distinguishable only by size. However, it turns out that the answer to this question is actually determined by the final size of the pieces! If the pieces are "large" (a more quantitative description is presented in the next section) then the answer is indeed just smaller pieces of gold that look and behave exactly like the original gold sample. But, if the pieces are "small", then something amazing happens: the smaller pieces of gold have properties fundamentally different from those of the original sample!

   This effect is already known for a long time. It was none other than the great Faraday who, in 1856, first started to study the size dependence of the physical properties of a material. He also used gold, but proceeded in the other direction: he started with very small pieces of gold (nanocrystalline gold) in solution and, by pressing them together, made bigger pieces of gold. His amazement at what he observed is clear from the March 11, 1856 entry in his diary [2]:

> . . . and then put on the gold above the convex surface of a rock crystal plano convex lens and pressed it by hand steadily, rocking it a little. This pressure converted the violet or dark tint of the place [of contact] to a beautiful green − far more beautiful than any I have seen in a gold leaf beaten − the effect was perfect.

Faraday was one of the greatest scientists of the 19$^{\text{th}}$ century. So, it is not all that surprising that his diary continues with, what we now know to be, a rather accurate explanation of this phenomenon:

> Has the pressure converted the layer of atoms into a continuous layer by expansion and welding, and is that all the difference? I rather think it is. . . . So it appears that these different layers are all gold, and owe their different appearances not to composition but to physical differences.

---

[1]These properties include the hardness of a material, its melting point, the color, electrical resistivity and many others that can be found in the usual tables and books [1].

Faraday discovered that the color (or to be more precise: the electronic structure) of a metal can become size dependent below a certain critical size. What this critical size was, and why it was different for the different metals that he investigated, was something that Faraday did not understand, and could not have understood. Many years later, the first experiments were published that proved that this size dependence of material properties also applied to semiconductors [3]. It was found that both the absorption and the emission of CdS shifted to shorter wavelengths for smaller crystal sizes. Again, a qualitative explanation was sought in terms of the reduced size of the CdS crystal.

So, it had been experimentally proven that the fundamental properties of a material can become strongly dependent on the size of the material below a certain threshold size. But still no adequate explanation of these effects was published. It would take understanding of the structure of metals, the discovery of the electron and the advent of quantum mechanics before, in the second half of the 20$^{\text{th}}$ century, a quantitative explanation was found. In the next section, a brief overview of some interesting observations on (semiconductor) nanocrystals is presented in the language of modern physics: quantum mechanics.

1.2 Quantum mechanics in reduced dimensionality

In this section several of the effects that arise when a (semiconductor) material is reduced in size are discussed in some more detail. First, a particle in an infinite square well is considered to show the relevant trend in the simplest configuration possible. Then, a few important concepts of semiconductor solid state theory and of transition metal dopant ions are outlined for the infinite crystal case. Next, the influence of the finite size of the crystal on the band structure is presented, along with the most important approximations involved in calculating the size dependence of the bandgap of a semiconductor material. In the next section several applications for which nanocrystals may play a key-role are discussed. Finally, this chapter ends with a brief overview of the research presented in the remainder of this thesis.

1.2.1 Introduction

In 1926, the birth of one of the most influential equations in physics, the time independent Schrödinger equation,

$$\left[-\frac{\hbar^2}{2m}\partial_{\mathbf{x}}^2 + U(\mathbf{x}) \right] \psi(\mathbf{x}) \;=\; E\,\psi(\mathbf{x}) \;, \tag{1.1}$$

heralded the era of quantum mechanics[2]. Physical phenomena would no longer be described in terms of particles at specific locations in space, but rather using the wave function $\psi(\mathbf{x})$ whose absolute value squared gives the probability of finding a particle at the position $\mathbf{x}$. Due to the fact that the wave function has a non-zero spatial extension, interesting effects appear. The simplest example of these effects (and of great conceptual importance to the field of semiconductor nanocrystals) is found for a particle of mass m in an infinite square potential well of width W in one dimension,

$$ U(x) \;=\; \left\{ \begin{array}{ll} 0 & \text{if } |x| \leq W/2 \\ \infty & \text{if } |x| > W/2 \end{array} \right. . \tag{1.2}$$

When this potential is inserted into equation (1.1), the wave functions $\psi_n(\mathbf{x})$ and the energies E_n can be calculated analytically. This is a simple problem and the derivation can be found in many textbooks on elementary quantum mechanics [4]. The size dependence is now immediately seen from the allowed energy levels of the particle in the well,

$$ E_n \;=\; \frac{\hbar^2 \pi^2 n^2}{2mW^2} \quad (n = 1, 2, 3, \ldots) . \tag{1.3}$$

The energy of these levels is inversely proportional to the square of the well-size. When W becomes large the energy level spacing $(E_{n+1} - E_n)$ tends to zero and the size dependence is removed.

Naturally, the potential in equation (1.2) is not realistic. The potential barrier between a real material and its surroundings will be always finite (typically a few electron volts), which complicates the solutions. However, the general trend, increasing energy for decreasing width of the potential well, will still be found for a real material. After a brief discussion of a few selected topics from semiconductor physics and the incorporation of (transition metal) dopant ions, section 1.2.4 will provide a short discussion of the size dependence of a real finite-sized semiconductor material.

1.2.2   Semiconductor crystals of infinite size

In an infinite and perfect semiconductor, there is a strict periodicity of the atoms in the lattice. This implies that there is a periodical interaction between the (free) electrons and the potential generated by the lattice atoms, which results in a band

---

[2]In in remainder of this thesis, ∂_x will denote partial differentiation with respect to x. In other words, $\partial_x \equiv \frac{\partial}{\partial x}$. Furthermore, all vectors will be written boldfaced: $\mathbf{x}$.
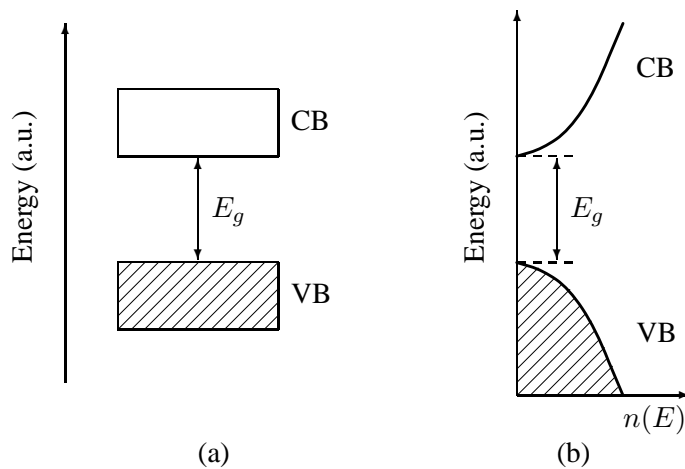
Figure 1.1: *(a) The band structure of an infinite and perfect semiconductor with a bandgap E_g at 0 K. (b) The same picture, but now showing the density of states for both bands. Here 'VB' denotes the valence band and 'CB' denotes the conduction band. The electronic states in the valence band are all occupied, as indicated by the dashed area. Note that the vertical scales are different for the two pictures.*

structure [5]. The presence of a band structure implies that certain energies are allowed for electrons and holes[3] in the semiconductor, while others are not. The most simple example of a band structure is shown in figure 1.1(a), where energy is denoted vertically and the horizontal axis has no real physical significance. However, sometimes this axis is chosen to represent position in the crystal or list different processes that can occur.

This picture is strictly speaking only valid for a material with zero defects and at 0 K. In this case, the lower band, the valence band (VB), consists of electronic states that are all occupied[4]. The higher band, the conduction band (CB), is com-

---

[3]A hole can be thought of as the absence of an electron at a position in the crystal where, normally speaking, there should be an electron. As a result, the net charge of a hole is equal to that of an electron but opposite in sign. A hole is found in the valence band, while the free electrons are present in the conduction band.

[4]Due to the Pauli-principle only one electron is allowed per state. Because the states fill up from the bottom, as this is the lowest energy in the system, the valence band (of a semiconductor) will consist of electronic states that are all occupied at 0 K.

prised of unoccupied states. The width (in energy) of the region where no electrons or holes are allowed is denoted by E_g, the bandgap energy. For a typical semiconductor this energy is in the range of 0.5 eV to 4 eV.

Another way to depict such a band structure is to plot the energy versus the density of states, $n(E)$, as is shown in figure 1.1(b). This describes the number of states per unit volume (i.e. the density) that are accessible for a charge carrier with a given energy E. The density of states for an electron in the conduction band of a three dimensional semiconductor increases with energy, [5]

$$n(E) \; \propto \; \sqrt{E - E_c} \quad (\text{if } \; E \geq E_c) \,, \tag{1.4}$$

where E_c denotes the energy of the conduction band edge. A similar relation can be written for the hole in the valence band. Note that the condition $E \geq E_c$ is required, because no states exist in the bandgap. Equation (1.4) is only valid near the edge of the band, as the width of the bands is finite (typically $1-2$ eV, not shown in figure 1.1(b)) and therefore the density of states must decrease for a certain energy.

The actual value of the density of states depends on the material properties such as the crystal structure, the bandgap and the effective masses of the electron and the hole. Note that the graphical representations that are shown in figure 1.1, are only a very crude model of a real band structure. A more correct picture would involve calculating the energy of allowed electron and hole states at many different **k** points, where **k** denotes the wavevector ($\hbar$**k** is the momentum of the electrons or holes). This is quite difficult and very time consuming. Details of such a procedure can be found in the literature [6].

When a semiconductor crystal is illuminated with photons of sufficiently high energy then the light can be absorbed by the material. The absorption of light by the semiconductor usually[5] results in the promotion of an electron from the valence band to the conduction band. Another way to describe this process, is to say that the absorption of light by the semiconductor results in the excitation of the semiconductor and the formation of an electron (in the conduction band) - hole (in the valence band) pair. Such an electron-hole pair is usually denoted by the term 'Mott-Wannier exciton'[6] or simply 'exciton'.

---

[5]Some materials also exhibit sub-bandgap absorption. This is ignored here for simplicity.

[6]There are in fact several distinctively different types of excitons [7]. Three types occur frequently. First of all, the Mott-Wannier exciton, which is a spatially extended electron-hole pair, such as those found in a semiconductor. Secondly, the Frenkel exciton, which is located almost exclusively on a single lattice site, such as the excited state of a luminescent dopant. Finally, the self-trapped

One can associate a wave function with the electron and hole in the semiconductor. These wave functions are solutions of equation (1.1). This means that both the electron and the hole have a certain spatial extension. Therefore, also the bound state of the electron and hole (i.e. the exciton) will have a spatial extension. To simplify the theoretical description of an exciton, one treats the exciton as if it were a single particle moving with a center of mass motion and ignores the fact that the exciton is actually a composite particle. Because of the center of mass motion, a reduced mass is assigned to the exciton: $\mu \equiv [(m_e^\star)^{-1} + (m_h^\star)^{-1}]^{-1}$. This reduced mass is defined by the effective masses of the electron and hole, denoted as $m_e^\star$ and $m_h^\star$, respectively. These effective masses are related to the degree of interaction of the electron and hole with the semiconductor lattice. Rather than treating an electron with mass m_e in the periodic potential of the host lattice, one assumes that the electron is free, but with an effective mass $m_e^\star$ which accounts for the interaction with the periodic potential. Naturally, the hole is treated similarly. This treatment is known as the *effective mass approximation*. Because the exciton behaves as a single particle, it is useful to find a measure of the size of this quasi-particle. For this reason, the exciton Bohr radius is introduced. This radius can be written as [8]

$$a_{\mathrm{B}} \;=\; \varepsilon_{\mathrm{r}} m_0 \mu^{-1} a_0 \;=\; \frac{4\pi\varepsilon_0\varepsilon_{\mathrm{r}}\hbar^2}{m_0 e^2}\left(\frac{m_e^\star + m_h^\star}{m_e^\star m_h^\star}\right)\;, \tag{1.5}$$

where m_0 is the free electron mass, a_0 denotes the Bohr radius of hydrogen and ε_{r} is the dielectric constant of the semiconductor.

For a typical semiconductor the exciton Bohr radius is usually in the range of $10 - 100$ Å. This means that for a ~ 5 nm semiconductor particle, strange effects can start to occur. The exciton 'wants' to be significantly larger than the crystal! In this case it is no longer possible to use the normal (infinite semiconductor) approach which was reviewed in this section to account for the physical and chemical properties of the semiconductor. Understanding the properties of such small crystals will only be possible if the finite character of the material is taken into account. This will be discussed in section 1.2.4.

exciton, which is localized in the lattice through interaction with the lattice distortion caused by the exciton itself and can be found in an ionic solid. An example of the first two types of excitons can be found in the luminescence mechanism of nanocrystalline ZnS:Mn^{2+}, as discussed in chapter 2.

1.2.3   Incorporation of dopant ions

When small amounts of dopant ions[7] are incorporated into a semiconductor or an insulator, many interesting applications are possible. A distinction between two types of dopant incorporation must be made, 'interstitial' and 'substitutional'. An interstitial is an ion that is not located on any of the lattice positions of the host lattice. A well-known example of an interstitial is hydrogen or sodium in a II-VI compound [8]. These interstitial ions hardly ever emit (visible) light. One example of the effect of an interstitial is the (undesired) quenching of the luminescence of ZnS:Cu,Al by interstitial Cu [9]. Even though interstitial dopants can be very useful for some applications (for example in the hydrogen uptake by metallic palladium), they will not be discussed in this thesis. The substitutional dopant is more common, especially in luminescent materials. In fact, the dopants discussed in this thesis are always substitutional as they are located on a host lattice site and do not belong to the host lattice material. A typical example, of great commercial value, is trivalent europium in yttrium oxysulfide, $Y_2O_2S:Eu^{3+}$, where the Eu^{3+} is present on some of the Y^{3+} lattice positions. This material is responsible for the red emission in a three-color television screen and is a very important phosphor[8]. Throughout this thesis the material $X{:}Y$ will denote a host lattice of X with substitutional dopants Y.

The dopants that will be discussed in this thesis are divalent manganese, Mn^{2+}, and divalent copper, Cu^{2+}. Both are transition-metal ions, or ionized d-metals. These ions show interesting luminescence properties due to their strong sensitivity to the crystal field of the host lattice. A typical example of the influence of the crystal field on the energy levels of a transition metal ion is seen in the Tanabe-Sugano diagram shown in figure 1.2 [10]. In this diagram the energy of the different electronic states (within the d^n configuration) of the dopant ion is shown as a function of the crystal field induced by the surrounding ligands. Figure 1.2 shows the Tanabe-Sugano diagram of a d^5 ion, such as Mn^{2+}, on a site in the crystal with octahedral symmetry. Similar diagrams are available for the other transition metal ions (such as Cu^{2+}) as well as for other site symmetries.

As can be seen from the figure, there is a large shift in the energy levels as a function of the crystal field. For example, for the $^4T_1 \rightarrow {}^6A_1$ transition in Mn^{2+},

---

[7]A dopant ion is usually an ion chemically different from that of the host lattice which is found at any position in the crystal. It can also be an ion which also occurs in the host lattice, but is found at an aberrant position in the crystal.

[8]Any material which luminesces, regardless of the precise excitation or emission mechanism, can be called a 'phosphor'.
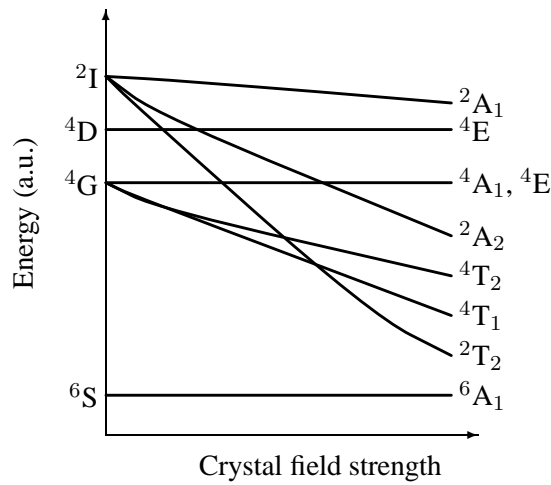
Figure 1.2: *Schematic representation of a Tanabe-Sugano diagram for a d^5 ion such as Mn^{2+} in a site with octahedral symmetry. Note that not all energy levels are plotted and that the lowest lying level, in this case the $^6A_1$ level, is defined to be at zero energy.*

it is directly clear from figure 1.2 that a site with a weaker crystal field will result in Mn^{2+} emission at higher energy. The crystal field in ZnS is stronger than in ZnSe due to the fact that selenium has a larger radius than sulfur. As a result, the Mn^{2+} emission in ZnS is expected to be at longer wavelength than this emission in ZnSe. This agrees with the data presented in the rest of this thesis (the emission wavelength for Mn^{2+} in ZnS is 600 nm, while the emission wavelength for Mn^{2+} in ZnSe is 570 nm).

1.2.4 Semiconductor crystals of finite size

As pointed out in section 1.2.2, when a semiconductor becomes sufficiently small, the (bulk) exciton Bohr radius can become comparable to, or even bigger than the crystal dimensions. However, because of the potential step present at the surface of the crystal, the exciton wave function cannot extend beyond the edge of the crystal without a severe energetic 'penalty'. As a result, the total exciton wave function will have to be squeezed to fit into the crystal. This results in an increase in the kinetic energy of the exciton, usually called the *confinement energy*. When this happens there will be a change in the band structure of the semiconductor. This
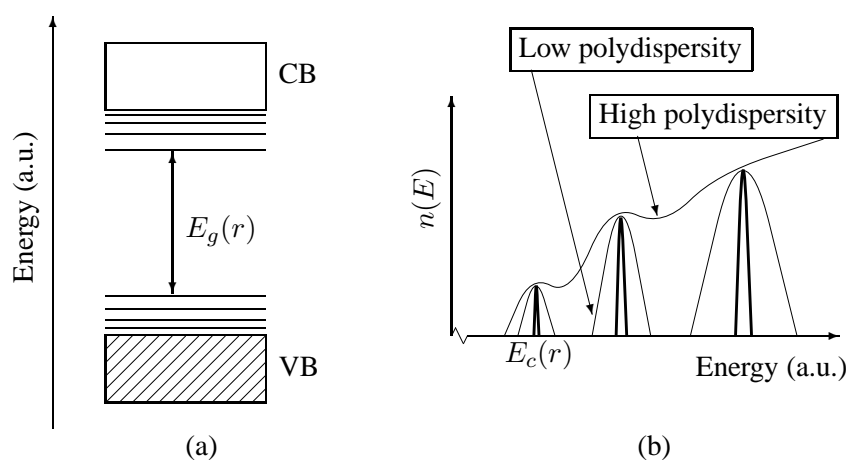
Figure 1.3: *(a) The band structure for a nanocrystal with a crystal size r and a size dependent bandgap $E_g(r)$. Again, 'VB' denotes the valence band and 'CB' denotes the conduction band. (b) The density of states for an electron in the conduction band of a nanocrystal. Here, $E_c(r)$ denotes the size dependent energy of the conduction band edge. The thick lines indicate the result without any size-variation. Also indicated in this picture, by the thin lines, is the effect of a low ($\sim$2 %) and a high polydispersity ($\sim$20 %) of the crystal size on the density of states.*

change is quite significant and consists of two separate effects, both of which are schematically shown in figure 1.3. These effects are often referred to as *quantum size effects*.

The first effect occurs because of the relatively small number of atoms in a nanocrystal (typically $\sim 10^2 - 10^5$). As a result, only a finite number of molecular orbitals can contribute to the formation of the band structure. Therefore the continuity of the bands will be lost for energies where the density of states is low. Equation (1.4) shows that the density of states is lowest at the edges of the bands, and therefore discrete energy levels will start to appear at the band edges when the crystal size is reduced. Because of the quantization of the energy levels near the top of the valence band and the bottom of the conduction band, sharp transitions at discrete energies will emerge, as shown in figure 1.3(a). The density of states at

the band edges consists of a series of (nearly) delta-functions,

$$n(E) \; = \; \sum_i \delta_{E-E_i} \; , \qquad (1.6)$$

where i indicates the (discrete) energy levels of the semiconductor at energy E_i and δ denotes the Kronecker delta symbol ($\delta_j = 1$ if $j = 0$ and $\delta_j = 0$ for all other values of j). As was the case for equation (1.4), one has to write down separate versions of equation (1.6) for the electrons in the conduction band and for the holes in the valence band.

The effect of the discrete density of states is schematically depicted in figure 1.3(b), which shows results for an electron in the conduction band. Note that the valence band is not shown and that the axes are interchanged with respect to those of figure 1.1(b). For a real material the density of states will never consist of a sum over true delta functions. Due to the Dirac uncertainty ($\Delta E \cdot \Delta \tau \geq \hbar/2$), the finite lifetime of the excited state will result in a broadening of the delta functions to narrow (Lorentzian) bands, as is shown in this figure. Also shown in figure 1.3(b) is the influence of a particle size distribution (i.e. the polydispersity), which quickly obscures most of the discrete features in the density of states of an ensemble of nanocrystals. Equation (1.6) applies mainly near the band edges, in the energy range where the number of molecular orbitals is very low. This effect, and as a result the applicability of equation (1.6), becomes more pronounced as the size is reduced further, until the one-atom limit is reached.

The second quantum size effect was already mentioned: the confinement energy. Because of the increasing confinement energy for decreasing crystal size, the valence band will move downward and the conduction band will move upward. The net effect is that the bandgap increases. This results in a blue-shift of the (band-band) excitation energy of the semiconductor, which is also observed for the CdS nanocrystal example that was discussed in section 1.1. An analytical expression of the effect of the crystal size on the bandgap energy is presented in the form of the widely used Brus equation [11],

$$E_g(r) \; = \; E_g(r \to \infty) + \frac{\hbar^2 \pi^2}{2r^2} \left(\frac{1}{m_e^\star} + \frac{1}{m_h^\star} \right) - \frac{1.786 e^2}{4\pi \varepsilon_0 \varepsilon_r r} + \mathcal{O}(r^{-3}) \; . \quad (1.7)$$

The first term on the right hand side represents the (infinite crystal) bandgap of the semiconductor. The second term is inversely proportional to the crystal radius squared, as was found in equation (1.3). This can indeed be thought of as the infinite square-well contribution to the bandgap. The third term, linear in $1/r$,

takes into account Coulomb-interaction effects on the electrons and holes. The numerical factor in this term originates from calculations of wave function overlap integrals and its value may vary slightly from material to material. Finally, $\mathcal{O}(r^{-3})$ indicates that corrections to equation (1.7) will involve $1/r$ cubed and can usually be ignored.

The Brus equation will be used throughout this thesis. Therefore, it is important to realize the approximations that have been made in order to derive equation (1.7), as well as when they are expected to fail. The most important approximations are, in no particular order:

- *Effective mass approximation.* It is assumed that the electrons and holes in the lattice behave as free electrons and holes, but with a different mass. The magnitude of the effective mass is defined through the inverse of the second derivative of E with respect to $\mathbf{k}$. This approximation breaks down when a significant number of the electronic wave functions inside the nanocrystal have wave function overlap with the edge of the crystal (where the potential landscape is no longer periodic). As a result, equation (1.7) is expected to fail for very small nanocrystals. At these sizes, typically less than $\sim$100 lattice positions in the crystal, one also reaches the *cluster and magic number* limit. In this size limit not all crystals remain stable. For example, nanocrystalline silicon is only stable as clusters of Si_{12}, Si_{33}, Si_{39} and Si_{45} if there are less than 60 silicon atoms in the nanocrystal [12]. For these crystals the band structure can be very distorted. When this size range is reached, only quantum-chemical calculations can determine the band structure and equation (1.7) becomes meaningless.

- *Spherical nanocrystals.* By assuming that the nanocrystal is spherical, decoupling of the Schrödinger equation into a radial part (depending on r) and a spherical harmonic part (depending on the angles θ and ϕ) is possible. This significantly reduces the difficulty of calculating the energy states because the wave functions involved are now products of the two separate wave functions: $\psi_{Elm}(\mathbf{r}) = R_{Elm}(r) \times Y_{lm}(\theta, \phi)$. This approximation is often quite good since most chemically synthesized nanocrystals have aspect ratios (defined as the ratio between the longest and shortest axes) smaller than 1.1. High aspect ratio nanocrystals can also be synthesized [13] and for such nanocrystals this approximation indeed breaks down.

- *Infinite potential barrier.* The true potential-step at the surface of a nanocrystal is not infinite. A typical value for this barrier is in the order of 1 to

3 eV (due to the work function of the semiconductor). This value is quite large compared to typical electron and hole energies. As a result, only a small fraction of the electron and hole wave functions will 'leak' out of the nanocrystal. This can result in a tunnel conductivity from the nanocrystal to its surroundings (i.e. other nanocrystals or a conducting substrate) and an overestimation of the semiconductor bandgap based on equation (1.7). The exact nature, form and magnitude of the surface potential will only become important in very small nanocrystals or for nanocrystals with an exceptionally low work function. This infinite potential barrier approximation also implies that $E_g(r)$ is insensitive to an externally applied potential and to the surroundings of the nanocrystal. The effect of the surroundings will indeed probably be very small, but the effect of an externally applied potential can be quite significant. Therefore, this approximation is expected to fail when the externally applied potential becomes too large.

Even though this list is incomplete, it is clear that there is a considerable number of approximations involved with equation (1.7). Fortunately, for the nanocrystals discussed in this thesis these approximations are valid to a degree sufficient to make equation (1.7) very useful. Therefore, the Brus equation is used throughout this thesis.

1.3 Applications of nanocrystals

In this section potential applications of nanocrystalline composite systems that have been suggested in recent literature are briefly mentioned. As this field of research is still relatively young and many new ideas are published every month, any overview of applications cannot be complete. Several of these suggestions will never leave the drawing board, while others are close to realization in a commercial device.

A promising idea for the use of nanocrystals outside of the field of lighting applications, is in non-volatile computer memories [14]. These memories are based on the fact that the injection of an electron into a nanocrystal significantly alters the threshold voltage for electron injection. These memories will not lose information when the power is switched off. However, addressing such a very large array of nanocrystals will be very challenging. Other applications using chemically synthesized nanocrystals or nanocrystal-composite materials include biological labelling, where the nanocrystals are chemically linked to a protein allowing for the transport of the nanocrystal into a living cell [15]; nanocrystal lasers, where the emission
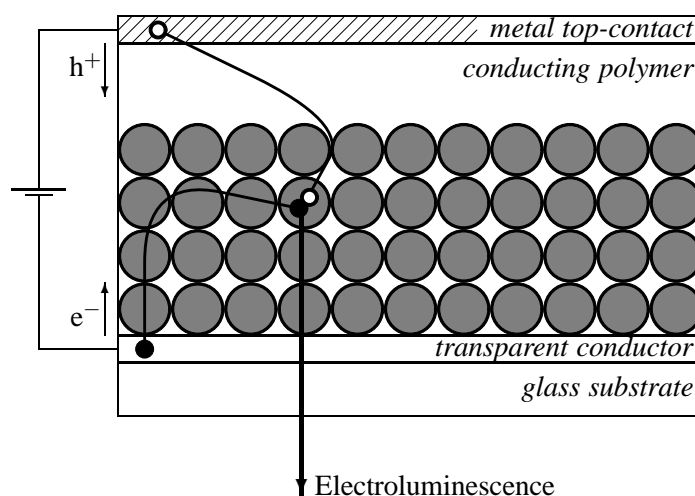
Figure 1.4: *Schematic representation of an electroluminescent device based using (doped) nanocrystals as the optically active component. It is assumed that the nanocrystals conduct electrons and the polymer conducts holes.*

color of the device can be altered by changing the nanocrystal size [16]; printing of thin-film transistors, where the effect of the nanocrystals can be seen most clearly in the significant increase in the field effect mobility [17]; and possibly photonic materials using a nanoparticulate matrix, where the self-organization of the nanocrystals has a clear advantage over the preparation of such a material using lithography [18]. One possible application, nanocrystals in an electroluminescent device, is of interest for this thesis and will therefore be discussed in some more detail.

1.3.1 Electroluminescent nanocrystals

Figure 1.4 shows a schematic setup required for the fabrication of an electroluminescent device based on (doped) nanocrystals. The bottom contact is a glass substrate covered with a transparent conductor (such as indium tin oxide). For the case shown in figure 1.4, the transparent conductor injects the electrons into the *n*-type nanocrystal layer[9]. The nanocrystals are deposited on the transparent

---

[9]Here it is assumed that the bottom contact is the electron injector, whereas the top contact is the hole injector. However, for a device this is not necessary and may actually be reversed, such as is the case for polymer light-emitting diodes.

conductor. This can be done using processing techniques such as dip-coating or spin-coating. The nanocrystal layer will form a disordered and highly porous layer (in contrast to the rather naive impression shown in figure 1.4).

After the nanocrystal layer is formed, a conducting polymer layer is deposited on top of the nanocrystals. Because of the high porosity of the nanocrystal layer, the polymer can soak into the nanoparticulate matrix, towards the conducting substrate. The use of a suitably thick nanocrystal layer and appropriate deposition conditions will prevent the polymer from actually reaching the substrate and causing a short circuit. As the nanocrystals are *n*-type, the polymer should be a *p*-type conductor.

Finally, the top contact is deposited. The top contact, a thin metal film, has two functions. First of all, it injects the holes into the conducting polymer. Secondly, this metal film reflects light, thus increasing the luminosity of the device. The metal layer should be able to inject the holes efficiently into the polymer. Such metals may oxidize and therefore the whole device will have to be shielded from the ambient air. This can be done using a protective coating as is standard for solid-state light-emitting diodes (not shown in figure 1.4). This coating will probably be required regardless of the metal layer, as typical *p*-type conducting polymers are sensitive to oxygen and/or water.

When a bias voltage is applied, electrons will be injected into the nanocrystals, where they are mobile. The electrons move from nanocrystal to nanocrystal via normal conductivity (if the nanocrystal layer is sintered, then "necks" will be formed between adjacent nanocrystals, resulting in conductivity) or through tunnelling, which can be efficient as long as the nanocrystals are not too far apart. The holes are conducted through the polymer, and at a certain point they are injected into a nanocrystal. As the holes are not mobile inside the nanocrystal layer, the injected hole will remain localized inside a specific nanocrystal. This then explains the use of a nanoparticulate matrix: because of the exceptionally large surface area of the nanocrystals, electron-hole pair recombination can occur everywhere inside the active layer. Using a bulk active layer (impermeable for the holes) would only result in recombination at the surface, where the holes can penetrate, and therefore a much lower luminosity.

When the hole recombines with an electron, electroluminescence can occur. For an undoped semiconductor, the electroluminescence emission energy can be the bandgap energy or it can be subbandgap if the emission originates from electron-hole recombination at a defect site in the host lattice. If a luminescent dopant is incorporated into the nanocrystals, then the electroluminescence can occur via the

dopant and the emission color will be determined by the dopant energy levels. Both possibilities will be discussed in this thesis.

1.4 Outline of the thesis

This thesis consists of a total of eight chapters. This first chapter is aimed at providing a general overview of some of the more important concepts that are needed for reading the thesis. It is by no means a complete overview, and many books are available that provide a comprehensive introduction to this field [19, 20].

Chapters two, three and four discuss research on nanocrystalline ZnS doped with Mn^{2+}. The second chapter begins by showing the influence of the synthesis conditions of chemically prepared nanocrystalline ZnS:Mn^{2+} on the photoluminescence characteristics and the crystal size obtained. This study culminates in a detailed description of the luminescence mechanism of the two luminescence bands observed. The emission energy and bandwidth are found to vary with the sample temperature. Chapter three discusses the origin of this effect in more detail. In explaining this temperature dependence of the luminescence, proof is given of the size independence of the electron-phonon interaction. The fourth chapter lists some of the photoelectrochemical properties of layers of nanocrystalline ZnS:Mn^{2+} deposited onto the transparent conductor indium tin oxide. Most interestingly, both an anodic and a cathodic photocurrent are observed, confirming the nanoparticulate nature of the electrode. The origin of the photocurrent and the stability of the electrodes are discussed. The attempts to measure electroluminescence from nanocrystalline ZnS:Mn^{2+} were unfortunately unsuccessful.

Chapters five, six and seven constitute the second part of this thesis. These chapters deal with doped nanocrystalline ZnSe. Because the chemicals involved in these syntheses are highly sensitive to oxygen and water, all these syntheses have been performed in the protective environment of a glovebox (dry nitrogen or dry argon). The first two of these three chapters deal with the procedure required to synthesize nanocrystals with different dopants and their (temperature dependent) photoluminescence properties, average particle sizes and luminescence mechanisms. Chapter seven presents electrochemistry of electrodes of bulk *n*-type ZnSe as well as electrochemical measurements on layers of ZnSe:Cu nanocrystals. Most importantly, indirect as well as direct evidence of electroluminescence of these nanocrystals is presented.

Chapter eight, the final chapter in this thesis, is markedly different from the rest of this thesis. This chapter does not involve experiments in the classical sense,

rather simulations are presented. These simulations were needed in order to calculate the probability for dopant pair-state formation in a nanocrystal. As it turns out, this probability is size dependent due to the large surface to volume ratio in a nanocrystal. The chapter then continues with a technical part discussing how these results can be approximated and predicted without simulations. The chapter ends with a general sketch for an algorithm to calculate these pair-state probabilities when preferential pair-formation is included.

References

[1] D. R. Lide, *Handbook of Chemistry and Physics, 74th edition*, CRC press: Boca Raton (1994).

[2] *Faraday's diary, Vol. VII*, The Royal Institution of Great Brittain, Edited by T. Martin, Bell and Sons: London, page 63 (1936).

[3] G. Jaeckel, *Z. Tech. Phys.* **6**, 301 (1926).

[4] B. H. Bransden and C. J. Joachain, *Introduction to Quantum Mechanics*, Longman Scientific & Technical: Essex (1989).

[5] N. W. Ashcroft and N. D. Mermin, *Solid State Physics*, Saunders College Publishing: Fort Worth (1976).

[6] J. M. Ziman, *Theory of Solids*, Cambridge University Press: Cambridge (1972).

[7] B. Henderson and G. F. Imbusch, *Optical Spectroscopy of Inorganic Solids*, Clarendon Press: Oxford, page 27 (1989).

[8] C. F. Klingshirn, *Semiconductor Optics*, Springer: Berlin (1995).

[9] Y. Y. Chen, J. G. Duh, B. S. Chiou and C. G. Peng, *Thin Solid Films* **392**, 50 (2001).

[10] Y. Tanabe and S. Sugano, *J. Phys. Soc. Japan* **9**, 753 (1954).

[11] L. Brus, *J. Phys. Chem.* **90**, 2555 (1986).

[12] J. Pan and M. V. Ramakrishna, *Phys. Rev. B* **50**, 15431 (1994).

[13] L. Manna, E. C. Sher and A. P. Alivisatos, *J. Am. Chem. Soc.* **122**, 12700 (2000).

[14] S. Tiwari, F. Rana, H. Hanafi, A. Hartstein and E. F. Crabbé, *Appl. Phys. Lett.* **68**, 1377 (1996).

[15] M. Bruchez Jr., M. Moronne, P. Gin, S. Weiss and A. P. Alivisatos, *Science* **281**, 2013 (198).

[16] V. I. Klimov, A. A. Mikhailovsky, S. Xu, A. Malko, J. A. Holligsworth, C. A. Leatherdale, H. J. Eisler and M. G. Bawendi, *Science* **290**, 314 (2000).

[17] B. A. Ridley, B. Nivi and J. M. Jacobson, *Science* **286**, 746 (1999).

[18] K. P. Velikov, C. G. Christova, R. P. A. Dullens, and A. van Blaaderen, *Science* **296**, 106 (2002).

[19] S. V. Gaponenko, *Optical Properties of Semiconductor Nanocrystals*, Cambridge University Press: Cambridge (1998).

[20] L. Bányai and S. W. Koch, *Semiconductor Quantum Dots*, World Scientific: Singapore (1993).

Chapter 2

Synthesis and photoluminescence of nanocrystalline ZnS:Mn^{2+}

The influence of the synthesis conditions on the properties of nanocrystalline ZnS doped with Mn^{2+} is discussed. Different Mn^{2+} precursors and different ratios of the precursor concentrations $[S^{2-}]/[Zn^{2+}]$ were used. The type of Mn^{2+} precursor does not influence the luminescence properties for the synthesis method described. On going from an excess of $[Zn^{2+}]$ precursor to an excess of $[S^{2-}]$ precursor, the particle diameter suddenly increases from 3.7 nm to 5.1 nm, which is accompanied by a change in the luminescence properties. Photoluminescence measurements also showed the absence of the ZnS defect emission at around 450 nm when an excess $[S^{2-}]$ is used during the synthesis. This effect is explained by a low sulfur vacancy concentration in nanocrystals prepared in the presence of excess $[S^{2-}]$. The ZnS luminescence is quenched at room temperature. This quenching is attributed to the thermally activated (activation energy of 62 meV) detrapping of a bound hole from a sulfur vacancy. An overview of the processes leading to the luminescence of the ZnS:Mn^{2+} nanocrystals is presented.

2.1   Introduction

Over the last few years, a considerable interest in the novel optical and electrical properties of doped semiconductor nanocrystals has emerged [1–5]. These structures are interesting from a physical and chemical point of view mainly because several of their properties are very different from those of bulk materials [3]. In particular, the significant size-dependent change in the bandgap has attracted much attention. This so-called quantum-size effect allows one to tune the emission and excitation wavelengths of a nanocrystal by varying the crystal radius r. A quite good first order approximation to calculate the energy of the bandgap is given by the Brus equation [1], as shown in equation (1.7). In the case of zincblende ZnS (the stable crystallographic configuration at temperatures below 1000 °C), the bulk values of all the relevant material parameters are known: E_g = 3.5 eV, $m_{\mathrm{e}}^{\star}$ = $0.28m_0$, $m_{\mathrm{h}}^{\star} = 0.49m_0$ and $\varepsilon_{\mathrm{r}} = 8.9$ [6]. For nanocrystalline ZnS this results in the following relation between the the bandgap $E_g(r)$, in electron volts, and the particle radius r, in nanometers,

$$E_g(r) \; = \; 3.5 - \frac{0.29}{r} + \frac{2.11}{r^2} \; . \tag{2.1}$$

Solving equation (2.1) for r, one obtains the following relation between the particle radius r, in nanometers, and the experimentally observed bandgap E_g, in electron volts,

$$r(E_g) \; = \; \frac{0.29 \; - \; 2.91 \, \sqrt{E_g \; - \; 3.49}}{2 \, (3.50 \; - \; E_g)} \; . \tag{2.2}$$

It is important to stress once more that equation (2.2) is only a first-order approximation. Deviations from a perfect spherical nanocrystal, as well as the finite value of the potential-step at the surface of the nanocrystal (through the workfunction of ZnS) have not been taken into account. These points have been discussed in more detail in section 1.2.4, together with their expected influence on the validity of equation (2.2). In the literature many theoretical papers consider the influence of these effects; examples of methods used are atomistic simulations [7], special variations of the Hartree-Fock approximation [8], tight-binding models that also include the luminescent dopant [9] and exact analytical calculations [10]. However, these papers usually do not produce a closed-form solution of $E_g(r)$; besides, the deviations from equation (2.2) will be quite small in the size-range under investigation in this thesis. Furthermore, to test the prediction of these advanced theories, exceptionally monodisperse ensembles of nanocrystals are needed, or experiments should be performed on a single nanocrystal. Both

these methods are difficult and beyond the scope of this thesis. Therefore, equations (1.7) and (2.2) will be used without modification.

Manganese-doped materials represent a class of phosphors which have already found their way into many applications. The $^4T_1 \rightarrow {}^6A_1$ transition within the $3d^5$ configuration of the divalent manganese ion (Mn^{2+}) has been studied extensively and its orange-yellow luminescence in ZnS is well documented [11]. This luminescence has also been observed in nanocrystalline ZnS:Mn^{2+} [12, 13] and applications have already been suggested [14–16]. Different types of Mn^{2+} centers are present in nanocrystalline ZnS:Mn^{2+} but the orange luminescence originates exclusively from Mn^{2+} ions on Zn^{2+} sites, where the Mn^{2+} is tetrahedrally coordinated by S^{2-} [17, 18].

Previous workers have always used equal concentrations of Zn^{2+} and S^{2-} precursors in the synthesis of these ZnS:Mn^{2+} nanocrystals. This chapter will focus on the effect of the synthesis conditions on several properties of these nanocrystals. Two different Mn^{2+} precursors were used and the influence of the ratio of $[Zn^{2+}]$ to $[S^{2-}]$ was investigated. The experimental comparison will include measurements of the diameter, reflectivity, temperature-dependent photoluminescence emission and excitation as well as luminescence lifetimes. From these results, new insight into the ZnS related luminescence and a qualitative description of the luminescence mechanism is obtained.

2.2   Experimental

The inorganic wet-chemical synthesis used to prepare ZnS:Mn^{2+} nanocrystals is similar to that described in the literature [19]. All steps of the synthesis were performed at room temperature and under ambient conditions. The final volume of solution that resulted from the synthesis was kept constant at 100 ml. To ensure that the nanocrystals would not grow into bulk crystals when they agglomerate, a capping polymer was used. For each synthesis x ml of a 0.85 M solution of $Na_2S \cdot 9H_2O$ was used. First, 10.2 g of $Na(PO_3)_n$ was dissolved in (80 - x) ml ultrapure water ($\rho \sim 16$ MΩ cm). While the solution was stirred, 10 ml of a 1 M solution of $Zn(CH_3COO)_2 \cdot 2H_2O$ was added. Next, the Mn^{2+} precursor was added: 10 ml of either a 0.1 M solution of $MnCl_2 \cdot 4H_2O$ or a 0.1 M solution of $Mn(CH_3COO)_2 \cdot 4H_2O$. Finally, x ml of the sulphide solution was added to the mixture. Immediately after the sulfide addition, an opaque white suspension was formed. After centrifuging and washing the particles twice with ultrapure water and once with ethanol (96 % pure, 4 % water), the particles were left to dry in

a vacuum desiccator for at least 15 hours. This resulted in a fine powder with a white or yellowish color, depending on the amount of S^{2-} used in the synthesis (an excess of S^{2-} gives a yellowish product).

To determine the average particle diameter, X-ray powder diffractograms were measured with a Philips PW 1729 X-ray generator using Cu K$_\alpha$ radiation at a wavelength of 1.542 Å. The X-ray diffraction pattern showed broad peaks at positions that are in good agreement with the zincblende modification of ZnS, as will be shown in section 2.3.1. The broadening of the lines in the X-ray diffractograms is attributed to the nanocrystalline nature of the samples and was used to calculate the diameter d of the nanocrystals by means of the Debye-Scherrer equation [20],

$$d = \frac{0.89\lambda}{B\cos\theta} \; . \tag{2.3}$$

Here λ denotes the wavelength of the X-rays, B is the full width at half maximum of the diffraction peak (in radians) and θ represents the maximum scatter angle. It is known that the Debye-Scherrer equation gives reasonably accurate values for the particle diameter, comparable to values obtained via high-resolution transmission electron microscopy measurements [19].

Reflectivity of the samples was measured using a Perkin-Elmer Lambda 16 UV/VIS spectrometer. Emission and excitation spectra were recorded with a SPEX Fluorolog spectrofluorometer, model F2002, equipped with two monochromators (double-grating, 0.22 m, SPEX 1680) and a 450 W xenon lamp as the excitation source. All photoluminescence emission and excitation spectra were corrected for the spectral response of the emission and excitation monochromators and of the photomultiplier tube. The excitation spectra were also corrected for the spectral distribution of the excitation source. Temperature-dependent emission spectra were recorded using a liquid helium flow-cryostat equipped with a sample heater to stabilize the temperature between 4 K and room temperature. The chemical composition of the samples was determined using a Perkin-Elmer Optima-3000 inductively-coupled plasma spectrometer.

2.3   Results and discussion

Since the goal of this chapter is to study the influence of the synthesis on the properties of these nanocrystals, all data in this chapter will show the precursor ratio [S^{2-}] to [Zn^{2+}] instead of the actual amounts of S^{2-} and Zn^{2+} present in the samples. However, these concentrations have also been measured using inductively-coupled
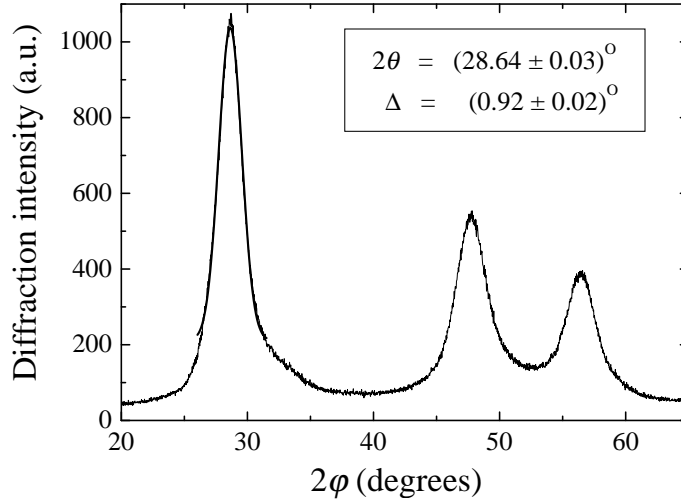
Figure 2.1: *X-ray diffractogram of a ZnS:Mn²⁺ sample. The line through the data in the interval from 2φ = 25° to 2φ = 32° is a fit using a Gaussian distribution of the diffraction signal, as shown in equation (2.4).*

plasma spectroscopy. From these measurements it was concluded that an excess of either S^{2-} or Zn^{2+} precursor during the synthesis indeed resulted in an excess of S^{2-} and Zn^{2+} present in the samples. For example, when a precursor ratio of $[S^{2-}]$ / $[Zn^{2+}]$ = 2.3 was used, the actual ratio of S^{2-} to Zn^{2+} present in the samples was found to be 1.3, while a precursor ratio of 0.5 resulted in a ratio of 0.9. Furthermore, it was found that typically about 10 % of the manganese used in the synthesis is incorporated into the nanocrystal.

2.3.1 Nanocrystal size dependence

Figure 2.1 shows a typical X-ray powder diffractogram of nanocrystalline ZnS doped with Mn^{2+}. Three broad peaks are found. A Gaussian distribution of the X-ray diffraction signal,

$$\mathcal{G}(\varphi) \; = \; \frac{1}{\Delta\sqrt{\pi/2}} \, \exp\left[-\frac{1}{2}\left(\frac{\varphi-\theta}{\Delta}\right)^{2} \right] , \qquad (2.4)$$

gives a good fit of the data, as can be seen from the drawn line in the interval from $2\varphi = 25°$ to $2\varphi = 32°$. From the fit, the peaks are found to be centered at $2\theta = 28.64°$, $2\theta = 47.79°$ and $2\theta = 56.40°$. The literature values for the diffraction maxima in the zincblende modification of ZnS have d-values of 3.12_x, 1.91_5 and 1.63_3 respectively [21] and correspond to the $\{111\}$, $\{220\}$ and $\{311\}$ lattice planes. Using Bragg's law,

$$2d \sin\theta \; = \lambda \quad (n = 1) \; , \tag{2.5}$$

with λ in Ångstroms, the expected X-ray powder diffraction maxima are calculated to be centered at $2\theta = 28.58°$, $2\theta = 47.54°$ and $2\theta = 56.38°$ with relative intensities of 100 %, 50 % and 30 % respectively. The assumption $n = 1$ in equation (2.5) is justified because for $n \geq 2$ the X-ray diffraction signal intensity will be much lower than for $n = 1$. Note that the agreement between the experimental data shown in figure 2.1 and the positions and relative intensities of the diffraction peaks expected for zincblende ZnS is good.

Due to the nanocrystalline nature of the sample, the peaks are broadened considerably. Equation (2.4) gives a a good fit of the peak at $2\theta = 28.64°$, as is shown by the line through the data in figure 2.1. The results for the fitting parameters are included in the figure. It is important to realize that it is *not correct* to use $B = 2\Delta \cdot 2\pi/360$ (remember that B should be in radians) to find the crystal size from equation (2.3), as can be seen from the angles for which the intensity in equation (2.4) dropped to $\frac{1}{2}$ of the maximum intensity,

$$\varphi \; = \; \theta \pm \Delta\sqrt{2\ln 2} \; . \tag{2.6}$$

As a result, the correct full width at half maximum to be used in equation (2.3) is

$$B[\text{radians}] \; = \; 2\frac{2\pi\Delta\sqrt{2\ln 2}}{360} \; = \; \frac{\pi\Delta}{45}\sqrt{\frac{\ln 2}{2}} \; , \tag{2.7}$$

for fitting a Gaussian profile to the diffraction data. When this subtle, but important point is taken care of, an average particle diameter of 3.76 nm is found from the fit in figure 2.1. The second ($2\theta = 47.79°$) and third ($2\theta = 56.40°$) peaks have also been used to determine the particle diameter and values of 3.44 nm and 3.60 nm have been found, respectively. As was indeed expected, these results are quite similar, indicating an average particle diameter of $\langle d_x \rangle = (3.6 \pm 0.2)$ nm. This proves that the size of the nanocrystals can be accurately determined using any of the diffraction peaks. This point will become important in chapter 5.
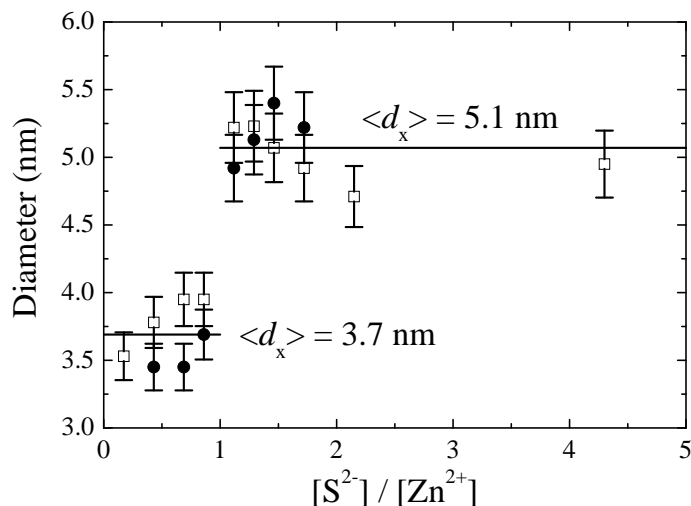
Figure 2.2: *Size of the nanocrystals as derived from the X-ray diffraction data and the Debye-Scherrer equation. Samples were made using either MnCl$_2$ ($\square$) or Mn(CH$_3$COO)$_2$ ($\bullet$) as the Mn^{2+} precursor.*

The diffractogram shown in figure 2.1 was measured using a long integration time. As a result, the signal to noise ratio of this measurement is very good. However, because of time considerations, the rest of the samples presented in this chapter were not measured with such long integration times. Because of this, and because the fitting was not done using an electronic file but by hand using a printout, the error in the calculation of d will be significantly larger than that based on figure 2.1. Unfortunately, no precise determination of the actual error was possible. Therefore, the error in the value of the radius of the nanocrystals has to be estimated. A reasonable assumption would be in the order of a few percent of the calculated diameter. To be on the safe side, the error is assumed to be 10 % of the diameter calculated using equation (2.3).

Figure 2.2 shows the diameter of the nanocrystals determined from the X-ray diffraction measurements. An identical trend is visible both for the nanocrystals made using MnCl$_2$ and Mn(CH$_3$COO)$_2$ precursors. When an excess of S^{2-} instead of a stoichiometric concentration is used in the synthesis, the average nanocrystal
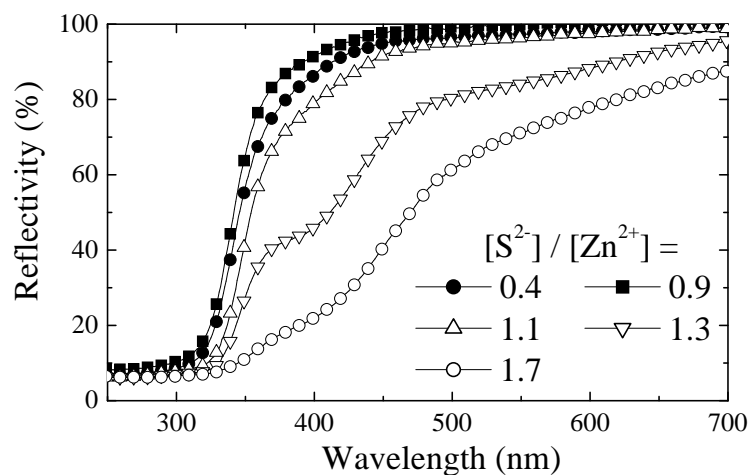
Figure 2.3: *Reflectivity measurements of the ZnS:Mn $^{2+}$ nanocrystals. Samples were made using either MnCl$_2$ (closed symbols) or Mn(CH$_3$COO)$_2$ (open symbols) as the Mn^{2+} precursor. The $[S^{2-}]$ / $[Zn^{2+}]$ precursor ratios used for the different samples are indicated.*

diameter is significantly larger than when an excess of Zn^{2+} is used. From the data presented in figure 2.2, it is seen that an excess of S^{2-} results in nanocrystals with a diameter of (5.1 ± 0.3) nm, while an excess of Zn^{2+} results in nanocrystals with a diameter of (3.7 ± 0.2) nm. This implies that excess of $[S^{2-}]$ during the synthesis results in an increase of the particle diameter of $\Delta\langle d_x \rangle = (1.4 \pm 0.4)$ nm according to X-ray powder diffraction measurements. It is important to note that in this analysis the polydispersity was not taken into account. The polydispersity was found to be not larger than 15% based on transmission electron microscope measurements and no dependence on the $[Zn^{2+}]$ / $[S^{2-}]$ ratio was observed [22].

Figure 2.3 shows the reflectivity measurements of several of the samples. The data presented in this figure corroborate the conclusion made on the basis of figure 2.2: there is a shift in the onset of absorption to lower energy on going from an excess of $[Zn^{2+}]$ to an excess of $[S^{2-}]$. This shift in the onset of absorption is due to the change in the nanocrystal bandgap. The particle size was calculated from the absorption spectrum, using equation (2.2). The bandgap energy is defined as

the energy for which the reflectivity has dropped to 50% of the difference between the reflectivity in the plateau before the ZnS absorption onset and the reflectivity at 280 nm. An increase in the average particle size based on all the reflectivity measurements (note that not all data are shown in figure 2.3) of $\Delta \langle d_{\mathrm{r}} \rangle = (0.9 \pm 0.2)$ nm was found. This agrees with the $\Delta \langle d_{\mathrm{x}} \rangle$ that was calculated from the X-ray diffraction measurements.

The second feature that is clearly visible in figure 2.3 is the decrease in reflectivity when an excess of $[S^{2-}]$ is used. This trend is also visible to the naked eye: the samples acquire a yellowish color. This color is attributed to elementary sulfur, probably on the surface of the nanocrystals. A small fraction of MnS may also be formed (dark brown and non-luminescent). No evidence for the formation of colloidal sulfur is found from the X-ray diffractograms. The strong absorption in the visible part of the spectrum for samples synthesized with an excess of S^{2-} makes it difficult to observe clearly the shift in bandgap as a function of the $[S^{2-}]$ / $[Zn^{2+}]$ ratio. Fortunately, the excitation spectra, shown below in figure 2.5, do provide clear evidence for this effect.

2.3.2 Influence of the synthesis on the photoluminescence

Figure 2.4 shows the emission spectra for samples made using $MnCl_2$. Relative intensities can be compared. The spectra show two broad peaks. The first, at ~ 420 nm, is also observed for undoped ZnS and is attributed to defect related emission of the ZnS. This emission was reported in the literature to be a ZnS related luminescence with a sub-microsecond lifetime [23]. The well-known ZnS related luminescence of zinc vacancies (at ~ 480 nm) is not observed in these nanocrystals, indicating that this emission is completely quenched. This emission is usually very weak or completely absent for $ZnS:Mn^{2+}$ nanocrystals. The nature of the ZnS related luminescence will be discussed below. The peak at ~ 590 nm corresponds to the $^4T_1 \rightarrow {}^6A_1$ transition of the Mn^{2+} ion [24]. The spectra of the samples made from $Mn(CH_3COO)_2$ are comparable and show very similar results.

It is clear that increasing the S^{2-} concentration beyond the stoichiometric ratio leads to a decrease of about two orders of magnitude in the ZnS related luminescence while there is no significant effect on the Mn^{2+} luminescence. It is interesting to note that a similar trend was observed for large (~ 1 μm) $ZnS:Mn^{2+}$ colloidal systems [24]. However, for these large particles the effect on the ZnS related luminescence was not as pronounced, which is probably due to the much smaller surface to volume ratio of these colloids. The change in emission spectrum of the nanocrystals did not change the overall quantum efficiency significantly. This is
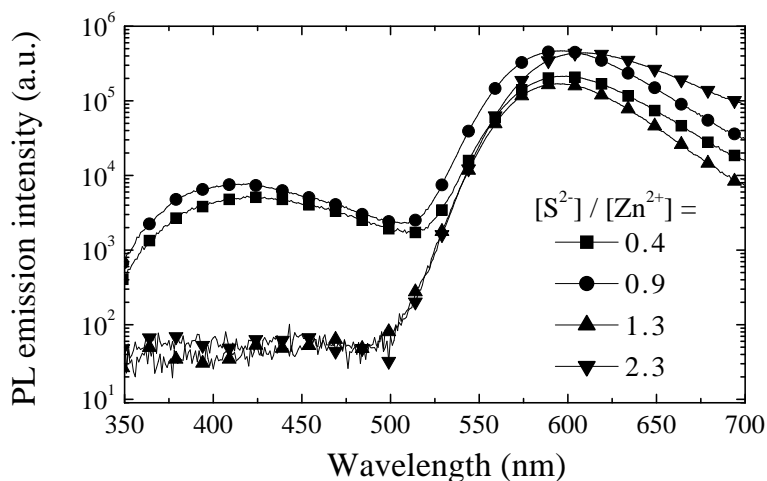
Figure 2.4: *Emission spectra for the samples made with MnCl$_2$ as the Mn^{2+} precursor and different $[S^{2-}]$ / $[Zn^{2+}]$ ratios. All spectra were recorded at room temperature for 300 nm excitation. Note the logarithmic intensity scale. Relative intensities can be compared.*

due to the fact that the dominant (Mn^{2+} related) luminescence is not (strongly) affected.

Photoluminescence excitation measurements were also performed by exciting the doped nanocrystals in the wavelength region 300 nm to 520 nm while monitoring the Mn^{2+} emission (measured at 590 nm) or the ZnS emission (measured at 420 nm). Figure 2.5 shows the excitation spectrum of the Mn^{2+} photoluminescence for several $[S^{2-}]$ / $[Zn^{2+}]$ precursor ratios. In this figure, ϕ denotes the photon flux per constant wavelength interval. A maximum in the Mn^{2+} emission intensities was observed at an excitation wavelength of roughly 330 nm (particle-size dependent), which indicates that the Mn^{2+} excitation takes place via energy transfer from the ZnS host lattice. In these excitation spectra, a clear (86 meV) blue shift is observed on going from a synthesis with excess $[S^{2-}]$ (ratios 1.1, 1.3, 1.7 and 2.3) to a $[S^{2-}]$ deficient synthesis (ratios 0.4 and 0.9). This discrete shift at a $[S^{2-}]$ / $[Zn^{2+}]$ ratio of about 1 is in good agreement with the increase in particle diameter as observed in both X-ray diffraction and reflectivity measurements (see figures 2.2 and 2.3).
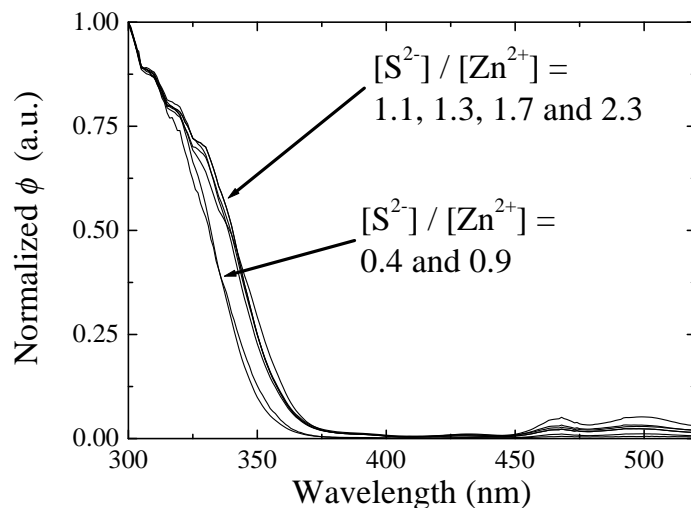
Figure 2.5: *Excitation spectra of the Mn^{2+} emission (measured at 590 nm) at room temperature for the samples made with different [S^{2-}] to [Zn^{2+}] precursor ratios. The Mn^{2+} precursor was MnCl$_2$ and all excitation spectra were normalized at 300 nm.*

The change in energy found in figure 2.5 can be used together with equation (2.2) to calculate the change in particle size. The value found, $\Delta\langle d_e\rangle = (0.9 \pm 0.2)$ nm agrees well with the values reported for $\Delta\langle d_x\rangle$ and $\Delta\langle d_r\rangle$, presented earlier in this chapter. In the excitation spectrum additional excitation bands can be observed at $\sim$465 nm and at $\sim$500 nm. These bands are assigned to direct excitation of the Mn^{2+} ion, the $^6A_1 \rightarrow {}^4T_2$ and the $^6A_1 \rightarrow {}^4T_1$ transition, respectively. As these transitions are spin forbidden, their intensity will be considerably lower than the allowed excitation of the ZnS host lattice (at 330 nm).

The observed changes in particle diameter and luminescence properties can result from two different effects. It must be noted that a 0.85 M solution of Na$_2$S in water is very alkaline (pH = 13.5). Therefore, the observed changes could be due to either the large change in pH during the synthesis, or to the higher S^{2-} concentration. To verify that the observed changes are not due to the pH, the synthesis was performed by changing the pH of the solution before the S^{2-} precursor was added by means of a 1 M solution of NaOH. During these syntheses, the ratio of
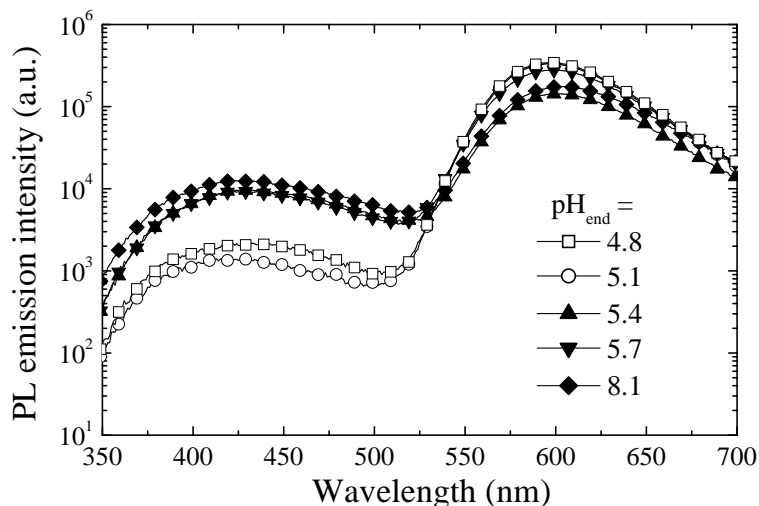
Figure 2.6: *Emission spectra for the ZnS:Mn^{2+} samples made at different pH. All spectra were recorded at room temperature for 300 nm excitation. Note the logarithmic intensity scale. Relative intensities can be compared.*

[Zn^{2+}] to [S^{2-}] precursor was kept at the stoichiometric value.

Figure 2.6 shows photoluminescence emission spectra for ZnS:Mn^{2+} nanocrystals prepared at several pH values, where 5.4 is the natural pH of the solution for the synthesis method used. Acidic conditions are also shown for comparison. It is clear that even for addition of 50 ml of a 1 M solution of NaOH (pH$_{end}$ = 8.1) before addition of the S^{2-} precursor, no change in the ZnS related luminescence was observed. No trend in particle size was found as a result of pH variation. The quenching of the ZnS related photoluminescence when the synthesis is performed in an acidic environment could be due to surface dissolution of the ZnS nanocrystals. This dissolution can introduce quenching sites at the surface of the nanocrystal. Since one of the charge carriers involved in the ZnS related luminescence is delocalized, the presence of surface quenching sites can result in a decrease of the photoluminescence quantum efficiency.

Since the pH of the Na$_2$S solution cannot explain the trends observed in figures 2.2, 2.3 and 2.4, it must be concluded that these are due to the additional [S^{2-}]
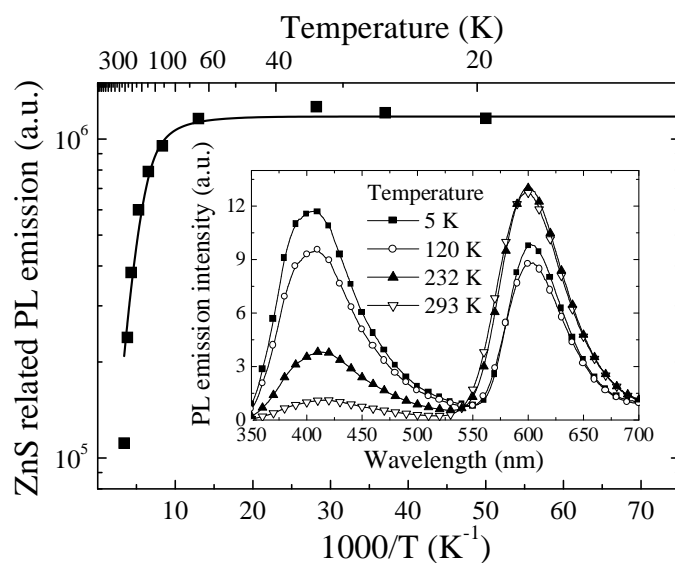
Figure 2.7: *Temperature dependent photoluminescence emission measurements for a $[Zn^{2+}] = [S^{2-}]$ sample. Excitation was at 300 nm. The drawn line is a fit using equation (2.8). Inset: Temperature dependence of the ZnS:Mn^{2+} photoluminescence emission spectrum*

present during the synthesis. For ZnO nanocrystals it is known that the ZnO related luminescence is due to oxygen vacancies ($V_O^{\bullet}$ according to the Kröger-Vink notation for identifying defects [25]) in the crystal and that the introduction of extra oxygen vacancies (for example by using excess Zn during the synthesis) strongly enhances the green luminescence [26]. It seems reasonable to assume a similar process for ZnS: the $V_S^{\bullet}$ centers are involved in the ZnS defect emission. In the presence of excess S^{2-}, the concentration of $V_S^{\bullet}$ centers will be lower. This does not influence the total quantum efficiency significantly because the Mn^{2+} related photoluminescence is the dominant feature in the emission spectrum.

2.3.3 Temperature dependence of the photoluminescence

Temperature-dependent photoluminescence measurements for a sample made from a solution with equal concentrations of Zn^{2+} and S^{2-} are shown in the inset of figure 2.7. From this it is clear that for lower temperatures, the ZnS related pho-

toluminescence increases in intensity while the Mn^{2+} related photoluminescence decreases. Figure 2.7 shows the temperature quenching of the ZnS related luminescence intensity. A fit of the data with an Arrhenius function (drawn line in figure 2.7),

$$I(T) = \frac{I_0}{1 + A \exp\left(-\frac{\Delta E}{k_{\mathrm{B}} T}\right)} \ , \tag{2.8}$$

gives an activation energy of $\Delta E = (62 \pm 8)$ meV. This temperature dependence of the luminescence intensity indicates that there is a thermally activated energy transfer process with a 62 meV activation energy. To explain the process behind this temperature dependence it is important to understand the excitation mechanism of both the self-activated (defect) emission and the Mn^{2+} emission. This mechanism will be discussed in detail in the next section.

On careful inspection of the inset of figure 2.7 it can also be seen that the width of the two emission peaks as well as their spectral positions are dependent on temperature. The analysis of the peak-energy and the spectral width of the emission bands as a function of temperature is quite complex and lengthy. The interested reader can find the details of this analysis in chapter 3.

2.3.4   Luminescence mechanism

In the literature various mechanisms have been proposed to explain the luminescence of $ZnS:Mn^{2+}$. In the recent literature on nanocrystalline $ZnS:Mn^{2+}$ it is often suggested that first an electron is captured by Mn^{2+}. However, in the literature on the luminescence of bulk $ZnS:Mn^{2+}$ careful high-resolution measurements have been reported which indicate that the Mn^{2+} center is attractive for holes [27, 28]. In view of the known oxidation states of manganese (2+, 3+, 4+ and 7+ are well-known, whereas 1+ is not stable) it seems indeed more likely that Mn^{2+} is hole attractive. Based on the measurements several possible excitation mechanisms for the Mn^{2+} were suggested (see figure 8 in Ref. [27]). In one mechanism the Mn^{2+} ion first traps a hole and the subsequent recombination with an electron results in Mn^{2+} in the excited state. Alternatively, an exciton may be bound to Mn^{2+} and recombination of the bound exciton promotes the Mn^{2+} to the excited state. Both mechanisms may be active in bulk and nanocrystalline $ZnS:Mn^{2+}$.

Figure 2.8 shows schematically the energy transfer processes that occur in nanocrystalline $ZnS:Mn^{2+}$ after UV excitation. The excitation of the $ZnS:Mn^{2+}$ nanocrystals starts with the creation of a Mott-Wannier exciton by the incident photon ($h\nu_{\mathrm{ex}} \geq E_g$). The electron is immediately transferred to a shallow trap
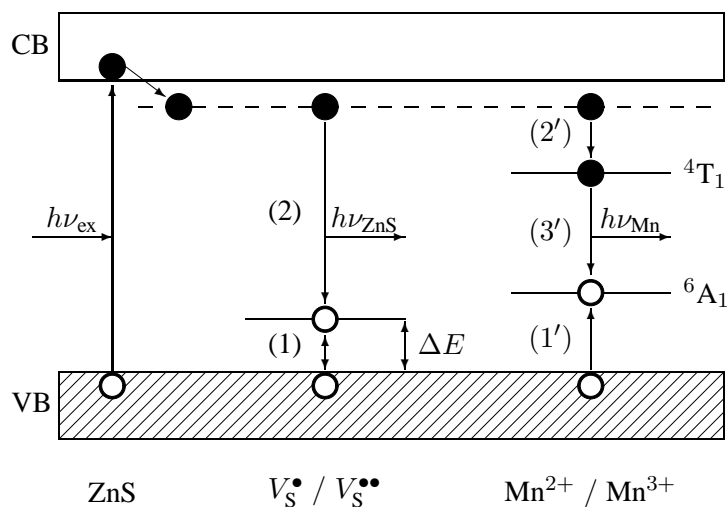
Figure 2.8: *Schematic representation of the energy-transfer processes that lead to the ZnS and Mn^{2+} related photoluminescence emissions. All processes are described in detail in the text. The energy levels are not plotted to scale.*

(denoted by the dashed line). Because the electron effective mass is quite small, this shallow trap-state is delocalized over the entire nanocrystal. The hole (with a significantly larger effective mass) remains initially in the valence band of the ZnS nanocrystal and will be trapped on a longer time scale.

Recombination of the electron-hole pairs can occur via different routes, resulting in non-radiative relaxation, Mn^{2+} emission or defect related emission. Non-radiative relaxation will occur at certain defect states or surface states (not shown in figure 2.8). For efficiently luminescing materials this process is undesirable. In the model for the defect-related emission presented above, first the hole is trapped at a sulphur vacancy, denoted by $V_S^{\bullet}$, resulting in a $V_S^{\bullet\bullet}$ state. Subsequent recombination with an electron in a shallow trap gives rise to the violet emission:

$$
\begin{aligned}
&(1) \quad V_S^{\bullet} + h_{VB}^{+} \quad \overset{\Delta E}{\longleftrightarrow} \quad V_S^{\bullet\bullet}, \\
&(2) \quad V_S^{\bullet\bullet} + e^{-} \quad \longrightarrow \quad V_S^{\bullet} + h\nu_{ZnS}.
\end{aligned}
$$
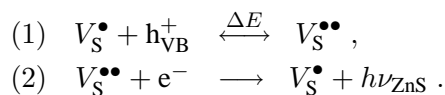
These processes, denoted by (1) and (2) are schematically shown in figure 2.8. The quenching of the defect-related emission can be understood if the first step is

reversible with a back transfer energy of $\Delta E = 62$ meV.

The emission from Mn^{2+} can be excited either directly by recombination of a bound exciton at Mn^{2+} or via trapping of a hole by Mn^{2+} [27, 28]. Subsequent recombination with an electron in a shallow trap results in Mn^{2+} in an excited state, $\left(\text{Mn}^{2+}\right)^*$, which gives rise to the well-known orange Mn^{2+} emission:

$$
\begin{aligned}
(1') \quad & \text{Mn}^{2+} + \text{h}_{\text{VB}}^+ & \longrightarrow \quad & \text{Mn}^{3+} , \\
(2') \quad & \text{Mn}^{3+} + \text{e}^- & \longrightarrow \quad & \left(\text{Mn}^{2+}\right)^* , \\
(3') \quad & \left(\text{Mn}^{2+}\right)^* & \longrightarrow \quad & \text{Mn}^{2+} + h\nu_{\text{Mn}} .
\end{aligned}
$$
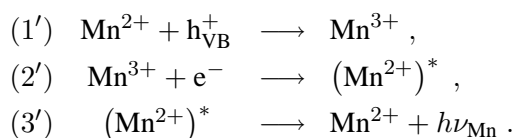
These processes, denoted by $(1')$, $(2')$ and $(3')$ are also schematically shown in figure 2.8. The transfer of the delocalized electron to the manganese will probably not immediately result in Mn^{2+} in the ^{4}T$_1$ excited state. Most likely, the Mn^{2+} will be in a higher excited state, from which it will relax nonradiatively to the metastable ^{4}T$_1$ state.

The thermally-activated quenching of the defect emission and the accompanying increase in the Mn^{2+} emission can now be understood: at elevated temperatures the holes are detrapped from the $V_{\text{S}}^{\bullet\bullet}$ levels and some of the holes that are released may now be retrapped by Mn^{2+}. After a subsequent recombination with an electron, Mn^{2+} in excited state is formed resulting in Mn^{2+} emission. This can explain the increase of the Mn^{2+} related emission intensity in the temperature regime where the violet defect-related emission quenches.

2.4 Conclusions

In conclusion, this chapter shows that by using an excess of sulphide for the synthesis of nanocrystalline ZnS:Mn^{2+}, the particle diameter is increased by about 1 nm, while the defect-related luminescence from ZnS is no longer observed. The Mn^{2+} luminescence is not affected. These results and the temperature dependence of the defect and Mn^{2+} emission are explained by a model in which sulphur vacancies are involved in the defect luminescence.

References

[1] L. Brus, *J. Phys. Chem.* **90**, 2555 (1986).

[2] Y. Wang and N. Herron, *J. Phys. Chem.* **95**, 525 (1991).

[3] A. P. Alivisatos, *J. Phys. Chem.* **100**, 13226 (1996).

[4] D. J. Norris, N. Yao, F. T. Charnock and T. A. Kennedy, *Nano Lett.* **1**, 3 (2001).

[5] R. S. Kane, R. E. Cohen and R. Silbey, *Chem. Mater.* **11**, 90 (1999).

[6] D. R. Lide, *Handbook of Chemistry and Physics, 74th edition*, CRC Press: Boca Raton (1994).

[7] I. D. Morokhov, V. I. Petinov, L. I. Trusov and V. F. Petrunin, *Sov. Phys. Usp.* **24**, 295 (1981).

[8] C. Yannouleas and U. Landman, *Phys. Rev. Lett.* **82**, 5325 (1999).

[9] V. Albe, C. Jouanin and D. Bertho, *Phys. Rev. B* **57**, 8778 (1998).

[10] T. Uozumi, Y. Kayanuma, K. Yamanaka, K. Edamatsu and T. Itoh, *Phys. Rev. B*, **59**, 9826 (1999).

[11] S. Shionoya and W. M. Yen, *Phosphor Handbook*, CRC Press: Boca Raton, page 170 (1998).

[12] R. N. Bhargava, D. Gallagher, X. Hong and A. Nurmikko, *Phys. Rev. Lett.* **72**, 416 (1994).

[13] K. Sooklal, B. S. Cullum, S. M. Angel and C. J. Murphy, *J. Phys. Chem.* **100**, 4551 (1996).

[14] C. N. Xu, T. Watanabe, M. Akiyama and X. G. Zheng, *Appl. Phys. Lett.* **74**, 1236 (1999).

[15] R. Bhargava, *J. Lumin.* **70**, 85 (1996).

[16] J. F. Suyver, R. Bakker, A. Meijerink and J. J. Kelly, *Phys. Stat. Sol. (b)*, **224**, 307 (2001). See also chapter 4.

[17] P. H. Borse, D. Srinivas, R. F. Shinde, S. K. Date, W. Vogel and S. K. Kulkarni, *Phys. Rev. B* **60**, 8659 (1999).

[18] Y. L. Soo, A. H. Ming, S. W. Huang, Y. H. Kao, R. N. Bhargava and D. Gallagher, *Phys. Rev. B* **50**, 7602 (1994).

[19] I. Yu, T. Isobe and M. Senna, *J. Phys. Chem. Solids* **57**, 373 (1996).

[20] B. D. Cullity, *Elements of X-ray Diffraction*, Addison-Wesley: Massachusetts, page 102 (1978).

[21] R. Jerkins, W. F. McClune, T. M. Maguire, M. A. Holomany, M. E. Mrose, B. Post, S. Weissmann, H. F. McMurdie and L. Zwell, *Powder Diffraction File*, JCPDS International center for diffraction data (1985).

[22] Dr. A. A. Bol (Philips research, Eindhoven), *Private communication.*

[23] S. Oda and H. Kukimoto, *J. Lumin.* **18/19**, 829 (1979).

[24] W. G. Becker and A. J. Bard *J. Phys. Chem.* **87**, 4888 (1983).

[25] F. A. Krøger, *The chemistry of imperfect crystals*, North-Holland Publishing Company: Amsterdam (1973).

[26] A. van Dijken, E. A. Meulenkamp, D. Vanmaekelbergh and A. Meijerink, *J. Phys. Chem. B* **104**, 1715 (2000).

[27] T. Hoshina and H. Kawai, *Jap. J. Appl. Phys.* **19**, 267 (1980).

[28] P. Jaszczyn-Kopec, B. Canny and G. Syfosse, *J. Lumin.* **28**, 319 (1983).

Chapter 3

Temperature-induced line broadening, line narrowing and line shift in the luminescence of nanocrystalline ZnS:Mn^{2+}

Emission spectra of nanocrystalline ZnS:Mn^{2+} have been recorded as a function of temperature between 4 K and 300 K. For the two emission bands observed (a defect related emission band around 420 nm and a Mn^{2+} related emission band around 590 nm) the temperature dependence of the width and the position of the emission bands has been analyzed. The shift and the broadening of the Mn^{2+} emission can be satisfactorily explained by theoretical models and parameters for electron-phonon coupling that are similar to those for bulk ZnS. For the defect related emission the shift to lower energies follows the decrease in bandgap of bulk ZnS with increasing temperature. The width of the defect related emission decreases as the temperature is raised. This anomalous behavior is explained by inhomogeneous broadening at low temperatures.

3.1 Introduction

The photoluminescence emission spectra of a luminescent material usually show a characteristic temperature dependence: as the temperature is increased the emission energy shifts (either to higher or to lower energies), the emission band or line broadens and at some temperature the emission is quenched [1, 2]. Theories to explain these phenomena are based on the temperature dependence of the electron-phonon interaction in both the ground state and the excited state of the luminescence center [3]. Typically, these theories distinguish between two separate coupling regimes, determined by the value of the Huang-Rhys factor[1]. The weak-coupling regime, for which sharp zero-phonon lines are observed, has roughly a Huang-Rhys factor $S < 1$ [4]. The strong coupling regime on the other hand has a large Huang-Rhys factor, $S > 5$, and is characterized by broad vibronic bands in the photoluminescence spectrum (both for the excitation and the emission spectra) [5, 6]. The mechanism for the line broadening (and therefore the temperature dependence of the line width) is different for the weak and strong coupling regimes [3]. The models developed to describe the line broadening in both the weak and the strong coupling regimes have been shown to be in good agreement with the experimentally observed temperature-induced broadening of the emission band [4, 5].

The theoretical work on the shift of the emission line has focussed mainly on the weak-coupling regime and the models available can adequately describe the temperature-induced shift of the strong zero-phonon line. For the strong coupling case it has been shown that the same model may be applied since the position of the maximum of the broad vibronic band follows the shift of the zero-phonon line [6]. Experimental work to develop and test the theoretical models has concentrated mainly on well-defined model systems, for example single crystals doped with lanthanide ions (weak coupling) [4], transition metal ions (intermediate coupling) [7] or s^2 ions (strong coupling) [8].

In this chapter, the temperature dependence of the energy and the width of the two emission bands observed for nanocrystalline $ZnS:Mn^{2+}$ are reported and discussed. In the previous chapter, work on the luminescence of nanocrystalline $ZnS:Mn^{2+}$ has shown that both a violet defect related host lattice emission and an orange Mn^{2+} emission can be observed. The defect related emission was assigned

---

[1]The Huang-Rhys parameter, denoted by S, is a dimensionless constant that describes the number of the vibrational level corresponding to the maximum in the absorption or emission spectrum. The value of S is proportional to the square of the displacement between the excited state and the ground state parabolas in the configurational coordinate diagram.

to recombination of an electron in a shallow trap or the conduction band with a hole trapped in a sulphur vacancy ($V_S^\bullet$ according to the Kröger-Vink notation for labelling defects [9]) while the Mn^{2+} emission is due to the localized $^4T_1 \rightarrow {}^6A_1$ transition within the $3d^5$ configuration of Mn^{2+}.

The aim of the work in this chapter is twofold: firstly, it is interesting to investigate if the quantum confinement effects (which are known to influence the excitonic excited state of a nanocrystalline semiconductor such as ZnS [10, 11]) also influence the electron-phonon coupling for luminescent centers in these nanocrystals. To study this in detail, the temperature dependence of the luminescence bandwidth and emission energy of both the Mn^{2+} related emission and the defect emission have been measured as a function of temperature. The observed temperature dependence is analyzed using the theoretical models developed for bulk crystalline materials. Secondly, it is observed that for nanocrystalline $ZnS:Mn^{2+}$ the band corresponding to the defect related emission becomes narrower as the temperature is increased. An explanation for this peculiar effect is presented.

3.2 Experimental

The inorganic synthesis method used to prepare $ZnS:Mn^{2+}$ nanocrystals is similar to that described in the literature [12]. All steps of the synthesis were performed at room temperature and under ambient conditions. To ensure that the nanocrystals would not grow into bulk crystals when they agglomerate, a capping polymer was used. To this end, 10.2 g of $Na(PO_3)_n$ was dissolved in 80 ml of ultrapure water ($\rho \sim 16$ MΩ cm). While the solution was stirred, 10 ml of a 1 M solution of $Zn(CH_3COO)_2 \cdot 2H_2O$ was added. Next, the Mn^{2+} precursor was added: 10 ml of a 0.1 M solution of $MnCl_2 \cdot 4H_2O$. Finally, 10 ml of a 1 M solution of $Na_2S \cdot 9H_2O$ was added to the mixture. Immediately after the sulfide solution was added, an opaque white suspension was formed, consisting of (agglomerates of) individual nanocrystals surrounded by the $Na(PO_3)_n$ polymer. The particles were centrifuged and washed twice with distilled water and once with ethanol, and were left to dry in a vacuum desiccator for at least 15 hours. This resulted in a fine powder with a white color.

To determine the average particle diameter, X-ray powder diffractograms were measured with a Philips PW 1729 X-ray generator using Cu K_α radiation at a wavelength of 1.542 Å. The X-ray diffraction pattern showed broad peaks at positions that are in good agreement with the zincblende modification of ZnS. The broadening of the diffraction peaks is attributed to the nanocrystalline nature of the sam-

ples and was used to calculate the diameter of the nanocrystals using the Debye-Scherrer equation [13]. Emission spectra were recorded with a SPEX Fluorolog spectrofluorometer, model F2002, equipped with two monochromators (double-grating, 0.22 m, SPEX 1680) and a 450 W xenon lamp as the excitation source. All photoluminescence spectra were corrected for the spectral response of the emission monochromator and the photomultiplier tube. Temperature-dependent emission spectra were recorded using a liquid helium flow-cryostat equipped with a sample heater to stabilize the temperature between 4 K and room temperature.

3.3   Results and discussion

Prior to the luminescence measurements, the nanocrystalline $ZnS:Mn^{2+}$ samples were analyzed using powder X-ray diffraction to determine the average particle size. From the width of the diffraction peaks the crystal size was calculated using the Debye-Scherrer equation [13]. An average particle diameter of 3.7 nm was found, in agreement with previous results for ZnS nanocrystals synthesized using the same procedure as was demonstrated in chapter 2 [14]. The polydispersity was not analyzed, but based on the results from Ref. [15] it can be estimated to be around 15 %.

Figure 3.1 shows the photoluminescence emission spectra of a powder of 3.7 nm $ZnS:Mn^{2+}$ nanocrystals under 300 nm excitation measured at different temperatures. Two distinct broad emission bands are observed in this spectral range. The spectra are scaled to 1 for the maximum of both emission bands separately and therefore a part of the spectrum (between the two peaks) is discarded. In this way the shift of the position of the emission bands and the change in bandwidth as a function of temperature could be determined accurately. The absolute and relative intensities of the emission bands also change as a function of temperature. This has been reported and discussed in detail in the previous chapter [14]. The lower energy band has its maximum around 2 eV ($\sim$590 nm) and is assigned to the $^4T_1 \rightarrow {}^6A_1$ transition within the $3d^5$ configuration of the Mn^{2+} ion [16]. This orange/yellow emission from Mn^{2+} has been observed in many materials and finds application for example in electroluminescent devices [17]. The higher energy emission band has a maximum around 3 eV ($\sim$420 nm). This violet emission is a well-known defect related emission which is also observed in undoped bulk ZnS [18]. The emission is assigned to recombination at sulphur vacancies in the material as was demonstrated in the previous chapter [14]. A longer wavelength blue emission, probably related to Zn vacancies and observed for undoped ZnS bulk and nanocrystals, is
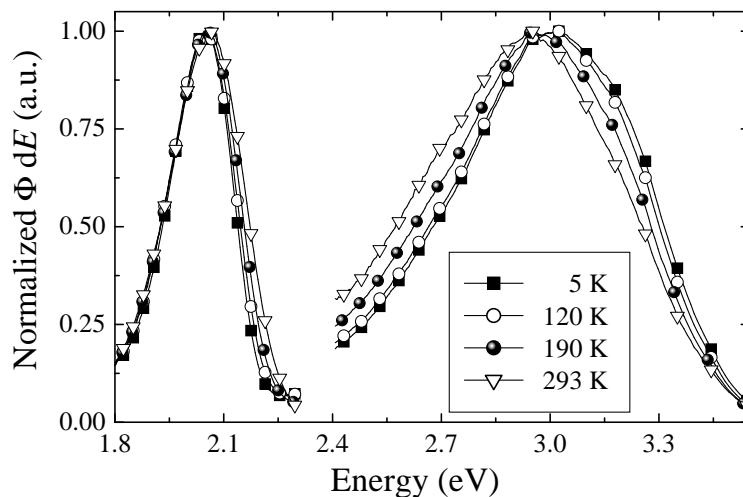
Figure 3.1: *Photoluminescence emission measurements (normalized photon flux per constant energy interval as a function of energy) of a sample of 3.7 nm ZnS:Mn^{2+} nanocrystals for the four different temperatures indicated in the figure. Excitation was at 300 nm. Each spectrum is normalized with respect to the maximum of its emission peak.*

not observed here. This emission is usually very weak or completely absent for ZnS:Mn^{2+} nanocrystals.

The emission spectra shown in figure 3.1 are plotted as a relative emitted photon flux for a constant energy interval ($\Phi \, dE$) versus energy. In the strong-coupling limit the emission bands are expected to be Gaussians in this representation [19]. Figure 3.2(a) shows a typical emission spectrum of the Mn^{2+} related emission (drawn line), as well as the best fit of the emission spectrum with a Gaussian profile (dotted line),

$$I_{\text{PL}}(E) \ \propto \ \exp\left[-\frac{1}{2}\left(\frac{E - E_0}{\Delta}\right)^2\right] . \tag{3.1}$$

Here E_0 denotes the energy of the maximum emission intensity and Δ is a measure for the width of the emission band (see chapter 2 for a discussion relating Δ to the full width at half maximum of the emission band).
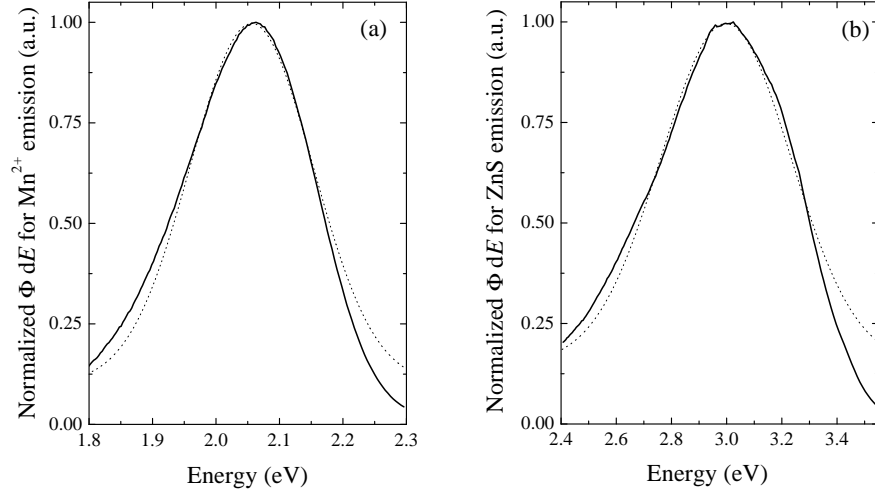
Figure 3.2: *(a) The Mn^{2+} related photoluminescence emission band for a sample of ZnS:Mn^{2+} nanocrystals measured at 290 K (solid line) together with a Gaussian fit of the data (dotted line). Excitation was at 300 nm. (b) The same, but now for the ZnS related emission.*

In figure 3.2(b) similar data are shown, but now for the ZnS defect related emission. The agreement between the Gaussian profiles and the experimentally observed emission bands is reasonably good, although on the high energy side the experimentally observed emission bands show a steeper increase than the Gaussian profiles while the tail on the low energy sides fall off more slowly than the Gaussian profiles. This indicates that the emission band resembles a Pekarian line shape, defined as the envelope of

$$I_{\mathrm{PL}}(E) \; \propto \; \sum_{m \geq 0} \frac{\exp(-S)S^m}{m!} \delta_{E_0 + m\hbar\omega - E} \; . \tag{3.2}$$

Here E_0 denotes the energy of the zero-phonon emission, S is the Huang-Rhys factor, $\hbar\omega$ is the energy of the lattice vibration that couples to the optical transition and δ_j represents the Kronecker delta function ($\delta_j = 1$ if $j = 0$ and $\delta_j = 0$ for all other values of j). For large values of S, the envelope of equation (3.2) will

resemble the Gaussian profile shown in equation (3.1) with high accuracy[2].

Gaussian band shapes are only expected for luminescent transitions with a very large Huang-Rhys factor (such as $S > 20$), while bands with a steeper slope on the high energy side are observed for luminescent transitions for which the Huang-Rhys parameter is typically between 2 and 10 [3]. For the analysis of the temperature dependence of the luminescence bands in this chapter, all emission bands have been fitted to the Gaussian profile given by equation (3.1). This is done because the two important parameters (the half-width at half maximum and the peak position) can be obtained with high accuracy from these Gaussian fits as can be seen from the dotted lines in figure 3.2.

From the data shown in figure 3.1 it can be concluded that the Mn^{2+} emission band shifts to higher energy as the temperature is increased. The bandwidth also increases with increasing temperature. At first sight it may seem that the increase of the Mn^{2+} related emission band (at $\sim$2 eV) occurs at the high-energy side of the spectrum. However, this is not the case as the peak also shifts to higher energy with increasing temperature. In figure 3.3(a) the position of the maximum of the Mn^{2+} emission band is plotted as a function of temperature, while in figure 3.3(b) the temperature dependence of the half-width at half maximum of the Mn^{2+} emission band is depicted. The half-width at half maximum and the energy of this emission band show a weak temperature dependence below $\sim$100 K and a strong increase with temperature above $\sim$100 K. For the strong-coupling regime the temperature dependence of the emission bandwidth can be written as [3]

$$\Gamma(T) \;=\; \Gamma_0 \sqrt{\coth\left(\frac{\hbar\omega}{2k_{\mathrm{B}}T}\right)} \, . \qquad (3.3)$$

Here Γ_0 is the bandwidth at 0 K and $\hbar\omega$ is the energy of the lattice vibration (i.e. the phonon) that couples with the electronic transition. Equation (3.3) has been derived for the strong coupling regime with the assumption that the luminescent transition only couples with a single type of lattice vibration. In reality, different types of phonons can couple to the same electronic transition. Nevertheless, a good agreement between the experimentally observed line broadening and equation (3.3) is obtained when coupling with a single (optical) phonon is assumed, as can be seen

---

[2]Note that some authors claim that equation (3.2) can be replaced by equation (3.1) for $S \gtrsim 10$. However, this is not correct but the difference between the two lineshapes becomes spectroscopically insignificant for such values of S. Only when $S \to \infty$ will equation (3.2) converge to equation (3.1) [20].
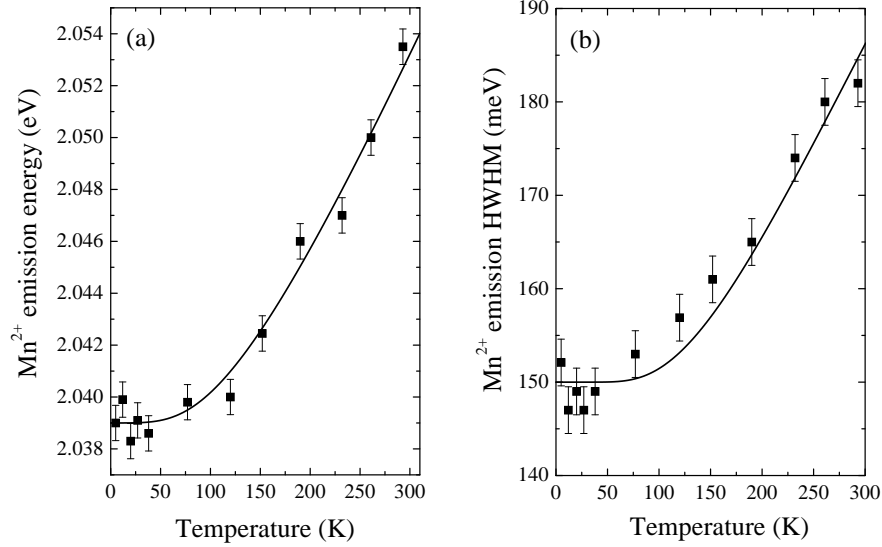
Figure 3.3: *(a) Temperature dependence of the emission energy of the Mn^{2+} related photo-luminescence for a sample of 3.7 nm ZnS:Mn^{2+} nanocrystals. (b) Half-width at half maximum of the Mn^{2+} related emission as a function of temperature. The lines through the data in figures (a) and (b) are fits using equations (3.4) and (3.3) respectively. In both cases $\hbar\omega = (40 \pm 2)$ meV was used.*

from the drawn line in figure 3.3(a), which represents a fit to the data for a phonon energy of $\hbar\omega = (40 \pm 2)$ meV.

The phonon energy of (40 ± 2) meV obtained from the fit is in good agreement with the value reported for the LO phonon energy in bulk ZnS:Mn^{2+} (41 meV [21]). Strong coupling with this high energy LO phonon is in line with what is typically observed for electronic transitions where coupling with the high energy local modes is dominant [22]. No significant difference is observed between the temperature-dependent broadening of the Mn^{2+} related emission in bulk and nanocrystalline ZnS:Mn^{2+}.

The broadening of the emission band does not influence the center of gravity of the band [6] and therefore the temperature-induced shift of the maximum of the emission band follows the shift of the zero-phonon line. Theoretical work on

the shift of zero-phonon lines has been done using approximations that are valid in the weak-coupling limit [4]. In the strong coupling limit the same theoretical description is often applied successfully, even though a non-perturbative theory is more correct [5, 6]. Assuming a Debye distribution of the phonon density of states (i.e. $\omega_{\mathbf{k}} = v|\mathbf{k}|$, where v is the speed of sound in the crystal and $\mathbf{k}$ is the wavevector, which results in a quadratic increase in the phonon density of states as a function of ω), the temperature dependence of the energy of the zero-phonon line is given by [4]

$$E(T) \;=\; E_0 \,+\, \mathcal{C}\, T^4 \int_0^{\frac{\hbar \omega_{\mathrm{D}}}{k_{\mathrm{B}} T}} \mathrm{d}x\; \frac{x^3}{e^x - 1}\;.\tag{3.4}$$

where E_0 is the energy of the transition at 0 K, ω_{D} is the Debye cut-off frequency and $\mathcal{C}$ is a (positive) constant.

The solid line in figure 3.3(b) is a fit of the experimental points to equation (3.4). Good agreement between the data and equation (3.4) is obtained for $\hbar\omega_{\mathrm{D}} = 40$ meV. This phonon energy of 40 meV corresponds to the phonon cut-off energy in bulk ZnS. Similarly to what was found for the broadening of the bandwidth, the temperature-induced shift of the emission band is the same for the Mn^{2+} emission in bulk and nanocrystalline $ZnS:Mn^{2+}$. The observation that the temperature dependence of the bandwidth and the spectral position of the Mn^{2+} related emission band is similar in bulk and nanocrystalline $ZnS:Mn^{2+}$ is not surprising because the optical transition of Mn^{2+} is a localized transition within the $3d^5$ configuration of the Mn^{2+} ion. This transition couples mainly with localized optical phonon modes that are not expected to be influenced by quantum confinement effects. Only for the long wavelength acoustic phonon modes will the size confinement significantly distort the phonon spectrum, as has been observed by the influence of size confinement on the relaxation rates between energy levels separated by very small energy gaps that can only be bridged by long wavelength (low energy) acoustic phonons [23, 24].

A more specific explanation for the blue shift of the Mn^{2+} related emission band with increasing temperature is the thermal expansion of the host lattice with increasing temperature. The Tanabe-Sugano diagram for the Mn^{2+} ion shows that the $^4T_1 \rightarrow \, ^6A_1$ transition in the Mn^{2+} ion strongly depends on the crystal field induced by the host lattice. Therefore, for increasing temperature, the thermal expansion of the ZnS host lattice results in a decrease of the crystal field and a concomitant increase in the Mn^{2+} related emission energy. Note that the thermal expansion of a lattice can be written in terms of a so-called Grüneisen parameter [25]. This predicts a Debye-integral for the change in volume of the crystal,

comparable to that shown in equation (3.4). As the expansion of the lattice is caused by interaction with phonons (due to anharmonic terms in the expansion of the potential energy of the crystal in the lattice displacements [25]), it is expected that the temperature dependence of the Mn^{2+} emission energy can be described by an equation similar to equation (3.4). In order to decide if this effect can explain the observed shift of roughly 15 meV (121 cm^{-1}), an estimate of the required increase in the crystal size will now be made.

The values for the crystal field energy and for the Racah parameter have been determined to be $B = 500$ cm^{-1} and $Dq = 510$ cm^{-1} for the zincblende modification (tetrahedral symmetry) of ZnS [26]. This means that $Dq/B \approx 1$ and that the crystal field dependence of the ${}^4T_1$ energy level is essentially linear [27]. The numerical value is

$$\partial_{Dq}E({}^4T_1) \approx -10 \; . \tag{3.5}$$

The minus sign is due to the fact that the energy of the ${}^4T_1$ energy level decreases for increasing crystal field strength. In crystal field theory, the value of Dq can be determined in terms of the material properties [3],

$$Dq = \frac{Ze^2 \langle r^4 \rangle_{3d}}{24\pi\varepsilon_0 a^5} \; . \tag{3.6}$$

Here $-Ze$ represents the charge of each of the (six) neighboring S^{2-} ligand ions; $\langle r^4 \rangle_{3d} = \int \psi_{3d}^\star r^4 \psi_{3d}\, d^3r$, where ψ_{3d} denotes the $3d$-wavefunctions and the integration is over all space; and a is the distance between the Mn^{2+} ion and the neighboring S^{2-} ligands.

As the temperature is increased two effects will occur: firstly the lattice will expand, resulting in an increase of a. Secondly, the $3d$-wavefunctions will change slightly, resulting in a small variation of $\langle r^4 \rangle_{3d}$. This second effect is ignored. The dependence of the crystal field splitting on the metal to ligand distance (i.e. the Mn^{2+} to S^{2-} distance) can then be determined as

$$\partial_a Dq = -\frac{5Ze^2\langle r^4\rangle_{3d}}{24\pi\varepsilon_0 a^6} = -\frac{5Dq}{a} \; . \tag{3.7}$$

This results in the dependence of the ${}^4T_1$ energy level on the lattice-size,

$$\partial_a E({}^4T_1) = \big(\partial_a Dq\big)\big(\partial_{Dq}E({}^4T_1)\big) = \frac{50Dq}{a} \; . \tag{3.8}$$
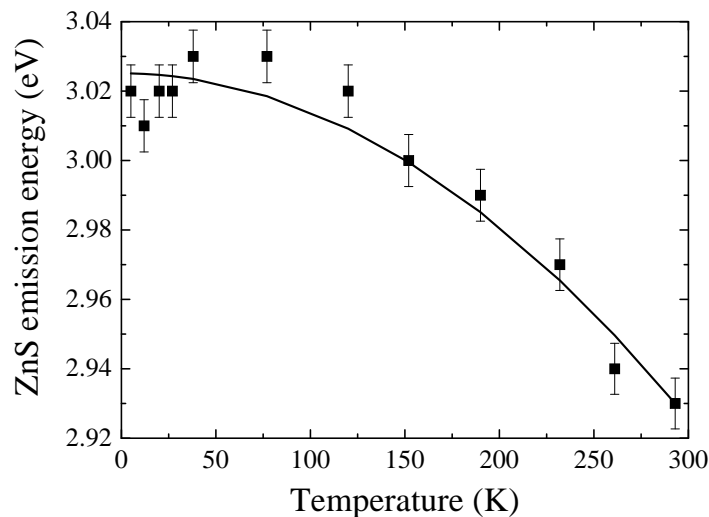
Figure 3.4: *Temperature dependence of the emission energy of the ZnS related emission for a sample of 3.7 nm ZnS:Mn²⁺ nanocrystals. The line through the data is a fit using equation (3.10).*

In other words, the change in energy of the $^4\text{T}_1$ energy level, $\delta E(^4\text{T}_1)$, in inverse centimeters is related to the relative change in crystal size, $\delta a/a$ through

$$\delta E(^4\text{T}_1) \;=\; \frac{50Dq}{a}\delta a \;\approx\; 25500 \cdot \left(\frac{\delta a}{a}\right) \;, \qquad (3.9)$$

when the value $Dq = 510$ cm^{-1} was used.

Equation (3.9) shows that to explain the observed shift in the Mn^{2+} related emission energy of 121 cm^{-1} ($\sim$15 meV) on going from 4 K to room temperature, the crystal must expand by roughly $\delta a/a = 0.5$ % over that temperature range. This seems to be a realistic value.

The bandwidth and the energy of the defect related emission of the ZnS host lattice show a temperature dependence that is opposite to that of the Mn^{2+} emission. Figure 3.4 shows that as the temperature increases the emission shifts to lower energies. Later, in figure 3.5, it will be shown that at the same time the emission bandwidth becomes smaller. The first observation can be easily understood and

is in agreement with the general observation that the bandgap of a semiconductor becomes smaller with increasing temperature. The narrowing of the band with increasing temperature is peculiar as the width of an emission band is expected to increase at higher temperatures. An explanation for the observed decrease of bandwidth for increasing temperature will be provided below.

First, the shift of the emission to lower energies for increasing temperatures is considered. The total shift between 4 K and 300 K is about 100 meV. The temperature-induced shift can be fitted using the the Varshni-equation that describes the temperature dependence of the bandgap of a semiconductor [28]

$$E_g(T) \; = \; E_0 \, - \, \frac{\alpha T^2}{T + \beta} \; . \tag{3.10}$$

Here E_0 is the bandgap at 0 K and α and β are fitting parameters. The model for the temperature dependence of the bandgap leading to equation (3.10) takes into account both the temperature dependence of the lattice parameter and of the electron-phonon interaction. It should be noted that equation (3.10) was originally derived in the infinite crystal approximation and has only been used to analyze bulk semiconductor systems. It is not immediately obvious that this equation will also apply to nanocrystalline semiconductors which have a different band-structure and a different phonon density of states.

The fit of the data using equation (3.10) is shown as a solid line in figure 3.4. The values obtained for the fitting parameters were $\alpha = (0.59 \pm 0.04)$ meV/K and $\beta = (2.9 \pm 0.5) \cdot 10^2$ K. These values agree with those found for the temperature dependence of the bandgap of bulk ZnS ($\alpha = 0.632$ meV/K and $\beta = 254$ K [29]) within the experimental uncertainty. A difference may be expected because the defect-related emission of the ZnS nanocrystals originates from recombination of an electron close to or in the conduction band with a hole trapped in a sulphur vacancy. The energy level associated with this trapped hole state is estimated to be 62 meV above the top of the valence band [14]. If the position of the trapped hole does not follow the shift of the top of the valence band edge as a function of temperature, then the temperature dependence of the energy of the defect related emission may deviate from that of the bandgap. However, in view of the significantly smaller effective mass of the conduction band electron in comparison to that of the valence band hole, it seems reasonable to expect that the temperature-induced change of the bandgap energy is mainly caused by the change in energy of the conduction band edge. The temperature dependence of the defect emission (involving the recombination of a conduction band electron) is therefore expected to be the same as that of the ZnS bandgap. This agrees with the similarity of the
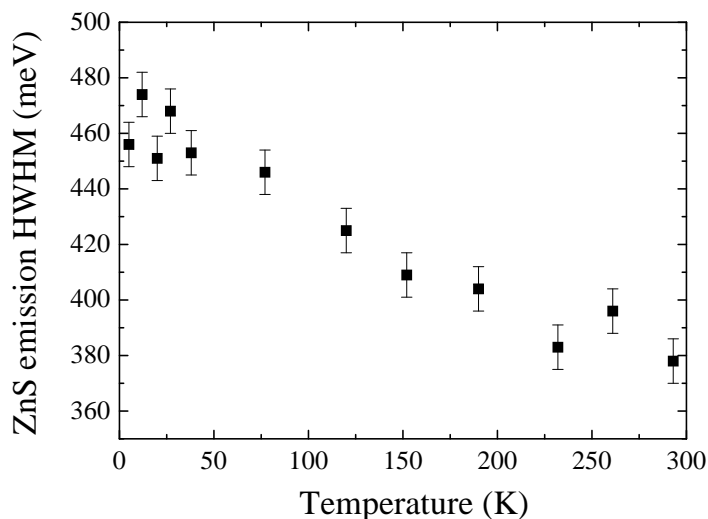
Figure 3.5: *The half-width at half maximum of the ZnS related emission peak as a function of temperature for a sample of 3.7 nm ZnS:Mn^{2+} nanocrystals.*

fitting parameters obtained for the bandgap of bulk ZnS and the defect emission in nanocrystalline ZnS. As a result, it is concluded that there is no large influence of quantum confinement on the temperature dependence of the bandgap for ZnS nanocrystals of about 4 nm. Note that since the uncertainty in the values obtained for the fitting parameters is large, a small influence of quantum confinement cannot be excluded.

The present findings are in agreement with results reported for 4 nm CdSe nanoparticles [30]. Theoretical considerations, supported by Raman scattering experiments, have shown that in such nanoparticles the electron-phonon coupling does not change as a function of the particle size. Finally, it is interesting to observe that in the lower temperature range (between 4 K and 50 K) the emission band shows a small but significant shift to higher energies. This initial shift is not expected from the model leading to equation (3.10). The origin of this anomalous shift will become clear after the narrowing of the defect related emission band for increasing temperature is discussed.

In figure 3.5 the half-width at half maximum of the ZnS related defect emis-

sion band is plotted as a function of the temperature. The data show that as the temperature is increased, the emission band becomes narrower. This unusual behavior is not explained by any of the theories for the temperature dependence of the line width (neither weak nor strong coupling) that were mentioned earlier in this chapter. To account for this observation it must be realized that the width of the emission band at low temperature has a large contribution from inhomogeneous broadening. There may be many shallow traps for electrons in a nanocrystalline sample of $ZnS:Mn^{2+}$ due to small perturbations related to surface states and defects in the crystal. Furthermore, the large surface to volume ratio in a nanocrystalline material gives rise to an increased inhomogeneous broadening for any emission band compared to that of a bulk single crystal due to the (relatively) large number of defect states present at the surface of a nanocrystal. After the excitation of the ZnS nanocrystals an electron can be trapped in a shallow trap state from which it cannot escape due to the low thermal energy at cryogenic temperatures. The luminescence must therefore occur through recombination of an electron in such a trap level with a hole trapped in a nearby sulphur vacancy. In a nanocrystalline material there will be many different trap levels, each with a slightly different trapping energy. As a result, the emission band in such a nanocrystalline material will have a large inhomogeneous width. The situation is illustrated in figure 3.6 where emission from two different trap levels (indicated by the dashed lines) as well as a conduction band edge electron is depicted, all giving rise to ZnS related defect emission at different energies.

At higher temperatures the trapped electrons can have sufficient thermal energy to escape from the trap level into the conduction band as indicated by the arrows in the dashed box in figure 3.6. The luminescence will now mainly originate from recombination of electrons at the bottom of the conduction band with holes trapped at the sulphur vacancies. In this situation more of the ZnS related emission originates from one energy level for the electron and therefore the inhomogeneous broadening will decrease. This explains the observation that the bandwidth of the emission becomes narrower at higher temperatures.

The exact temperature dependence of the narrowing of the emission band will depend on the distribution of electronic trap states and will also be strongly influenced by the synthesis conditions during the preparation of the sample. Therefore, the present explanation can only be qualitative because quantitative modelling through the introduction of a distribution of trap states is not feasible (too many parameters that can be changed). From the nearly continuous narrowing of the emission band between 4 K and about 200 K it can be concluded that the distribution
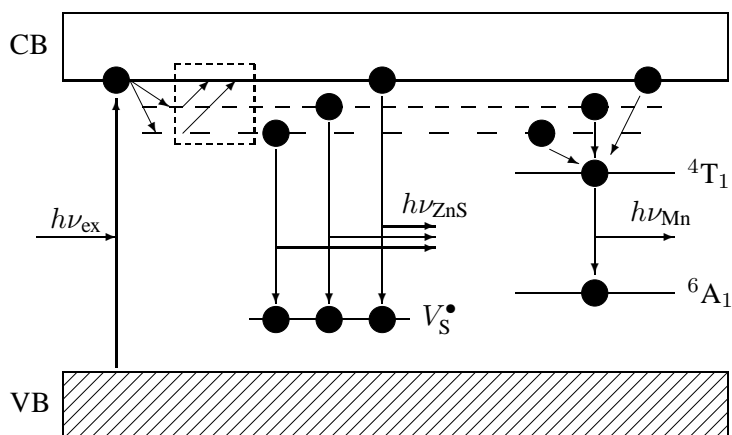
Figure 3.6: *Schematic representation of the electron-related energy transfer processes that lead to the ZnS and Mn^{2+} related photoluminescence emissions. The processes are discussed in detail in the text. The arrows in the dashed box indicate processes that can only occur at elevated temperature. Note that the energy transfer processes involving holes are omitted for clarity and the energy levels are not plotted to scale.*

of electron trap states includes deeper traps with trap depths corresponding to (at least) about 20 meV.

The model that is depicted schematically in figure 3.6 is supported further by the observation that the emission band shifts to higher energies between 4 and 50 K, as can be seen from the data in figure 3.4. The temperature dependence of the bandgap energy is very small and almost negligible in this temperature regime (as can be seen by equation (3.10), or the drawn line in figure 3.4). However, the thermal depopulation of the shallower traps will result in recombination of electrons from the (higher energy) conduction band and can therefore explain the anomalous blue shift between 4 K and 50 K in figure 3.4. The observed shift between 4 K and 50 K is about 0.02 eV. This indicates that in this temperature regime shallow traps with trap depths up to ∼5 meV are depopulated. Above 100 K the temperature dependence of the bandgap becomes strong and the shift of the emission band to lower energies (along with the decrease of the bandgap) can be described by equation (3.10) as discussed above. Again, the present model can only explain the results qualitatively. An alternative explanation, which cannot be

excluded, is that a different type of defect contributes to the 420 nm emission band at low temperatures. This band could give rise to larger inhomogeneous broadening at these temperatures and be quenched at higher temperature.

For comparison, the process leading to Mn^{2+} emission is depicted schematically on the right hand side of figure 3.6. Electron-hole recombination on the Mn^{2+} ion results in Mn^{2+} in the excited $^4T_1$ state. The energy of the $^4T_1$ excited state of the Mn^{2+} is not influenced by the energy of the conduction band electron involved in the recombination process and therefore the temperature dependence of the half-width at half maximum of the Mn^{2+} emission shows the normal broadening, which is described by equation (3.4) as shown above. For a detailed description and discussion of the Mn^{2+} related luminescence mechanism, see section 2.3.4.

3.4   Conclusions

The temperature dependence of the position and the width has been studied for the two emission bands of nanocrystalline $ZnS:Mn^{2+}$ particles (3.7 nm average diameter). The temperature-induced broadening and shift to longer wavelengths for the orange Mn^{2+} emission band is similar to that of the Mn^{2+} emission in bulk $ZnS:Mn^{2+}$, indicating that quantum confinement effects do not strongly affect the electron-phonon coupling for the $^4T_1 \rightarrow {}^6A_1$ transition. From fits of the observed temperature dependent results to theoretical models a strong coupling with the highest energy local modes of about (40 ± 2) meV can be deduced. A specific explanation is offered that can explain these results: the temperature dependence of the lattice parameter, which influences the crystal field. A change in the lattice parameter of 0.5 % explains the shift of the Mn^{2+} related energy.

The violet defect related emission band shifts to lower energies with increasing temperatures and the shift can be explained by a decrease in the ZnS bandgap energy for increasing temperature, similar to the change in the bandgap observed for bulk ZnS. The peculiar observation of a narrowing of the defect related emission band with increasing temperature is related to a larger inhomogeneous broadening of this band at low temperatures; this is due to shallow traps with trap depths up to ~5 meV, which are depopulated at higher temperature.

References

[1] L. E. Erickson, *Phys. Rev. B* **11**, 77 (1975).

[2] B. Di Bartolo, *Optical Interactions in Solids*, John Wiley & Sons: New York (1968).

[3] B. Henderson and G. F. Imbusch, *Optical Spectroscopy of Inorganic Solids*, Clarendon Press: Oxford, chapter 5 (1989).

[4] D. E. McCumber and M. D. Sturge, *J. Appl. Phys.* **34**, 1682 (1963).

[5] D. Hsu and J. L. Skinner, *J. Chem. Phys.* **81**, 1604 (1984).

[6] D. Hsu and J. L. Skinner, *J. Chem. Phys.* **81**, 5471 (1984).

[7] W. M. Yen, W. C. Scott and A. L. Schawlow, *Phys. Rev.* **136**, A271 (1964).

[8] H. F. Folkerts, J. Zuidema and G. Blasse, *Chem. Phys. Lett.* **249**, 59 (1996).

[9] F. A. Kröger, *The chemistry of imperfect crystals*, North-Holland Publishing Company: Amsterdam (1973).

[10] L. Brus, *J. Phys. Chem.* **90**, 2555 (1986).

[11] Y. Wang and N. Herron, *J. Phys. Chem.* **95**, 525 (1991).

[12] I. Yu, T. Isobe and M. Senna, *J. Phys. Chem. Solids* **57**, 373 (1996).

[13] B. D. Cullity, *Elements of X-ray Diffraction*, Addison-Wesley: Massachusetts, page 102 (1978).

[14] J. F. Suyver, S. F. Wuister, J. J. Kelly and A. Meijerink, *Nano Lett.* **1**, 429 (2001). See also chapter 2.

[15] A. A. Bol and A. Meijerink, *Phys. Chem. Chem. Phys.* **3**, 2105 (2001).

[16] W. G. Becker and A. J. Bard, *J. Phys. Chem.* **87**, 4888 (1983).

[17] S. Shionoya and W. M. Yen, *Phosphor Handbook*, CRC Press: Boca Raton, page 170 (1998).

[18] Y. Yang, J. Huang, S. Liu and J. Shen, *J. Mater. Chem.*, **7**, 131 (1997).

[19] G. Blasse and B. C. Grabmaier, *Luminescent Materials*, Springer-Verlag: Berlin (1994).

[20] Prof. Dr. R. Meester (Free University of Amsterdam), *Private communication.*

[21] T. C. Leslie and J. W. Allen, *Phys. Stat. Sol. (a)* **65**, 546 (1981).

[22] N. A. Vlasenko, *Opt. Spectr.* **8**, 445 (1960).

[23] R. S. Meltzer, S. P. Feofilov, B. Tissue and H. B. Yuan, *Phys. Rev. B* **60**, R14012 (1999).

[24] R. S. Meltzer and K. S. Hong, *Phys. Rev. B* **61**, 3396 (2000).

[25] J. M. Ziman, *Principles of the Theory of Solids*, Cambridge University Press: New York, page 66 (1972).

[26] G. Grebe and H. J. Schulz, *Phys. Stat. Sol. B* **54**, K69 (1972).

[27] Y. Tanabe and S. Sugano, *J. Phys. Soc. Japan*, **13**, 753 (1954).

[28] Y. P. Varshni, *Physica* **34**, 149 (1967).

[29] R. Pässler, E. Griebl, H. Riepl, G. Lautner, S. Bauer, H. Preis, W. Gebhardt, B. Buda, D. J. As, D. Schikora, K. Lischka, K. Papagelis and S. Ves, *J. Appl. Phys.* **86**, 4403 (1999).

[30] M. C. Klein, F. Hache, D. Richard and C. Flytzanis, *Phys. Rev. B* **42**, 11123 (1990).

Chapter 4

Photoelectrochemical characterization of layers of ZnS:Mn^{2+} nanocrystals

Measurements of the photoelectrochemical properties of electrodes of nanocrystalline ZnS:Mn^{2+} deposited on SnO$_2$:F coated glass are presented and discussed. The observation of both anodic and cathodic photocurrent is direct evidence for the nanocrystalline nature of the system. In-situ photoluminescence measurements show a nearly constant Mn^{2+} related photoluminescence intensity over a large potential range. Due to the unfavorable kinetics of electron and hole transfer across the interface between the nanocrystallites and the electrolyte solution, the photocurrent is small as most of the charge carriers generated by illumination recombine (radiatively or non-radiatively). Breakdown of the ZnS into elementary Zn and S^{2-} in solution was also observed at negative potential. This breakdown introduces new non-radiative decay paths and is responsible for the slow decrease of the luminescence intensity as a function of operating time. No electroluminescence was observed.

65

4.1   Introduction

Research on electroluminescent devices has started to focus on nanocrystalline composite materials [1–3]. The main reasons for the increasing interest in these materials are twofold. On the one hand, the fabrication of (doped) semiconductor nanocrystals has become straightforward via well-documented wet-chemical synthesis methods [4, 5]. On the other hand, in combination with a suitable semiconducting polymer and conducting substrate, electrons and holes can be injected directly into the conduction band and the valence band of the nanocrystals, at relatively low operating voltages [2, 6, 7]. This might allow the fabrication of an electroluminescent device using doped or undoped semiconductor nanocrystals as the optically active component.

Such a device is interesting for several reasons. For one, the electroluminescent nanocrystals can easily be assembled over a relatively large area using simple (and inexpensive) techniques. Furthermore, as the nanocrystals exhibit quantum confinement, the emission color of such a device can be tuned over a large spectral range by changing the particle size, without altering the rest of the device structure. This additional degree of flexibility can be very interesting for lighting applications. The exciton emission of a semiconductor nanocrystal has a tunable narrow-band emission spectrum, which is highly sought after (especially in the red part of the spectrum) for commercial applications. Another interesting point is that one can use a conducting polymer to inject one of the charge carriers. In this case the large surface to volume ratio of the nanocrystals is very useful, because the nanocrystals form a porous matrix, which may be permeable to the conducting polymer. Therefore, even though the charge carrier may not be mobile in the nanocrystalline layer, a high electroluminescence signal can still be obtained, because almost all the (nanocrystalline) material can contribute to the electroluminescence. In the long run, the most important reason to study nanocrystalline electroluminescent systems is likely to be the potentially very low operating voltage of such a device. This would in theory allow for an electroluminescent device with a total energy efficiency of more than 50 % [8]. Should such a device be realized, then it would be nothing less than a revolution in the lighting industry.

In this chapter the preparation of layers of Mn^{2+} doped ZnS nanocrystals is described. Photoelectrochemical methods are used to characterize the layers. In particular photocurrent-potential and in-situ photoluminescence measurements are used to show that the layers have properties that are typical of a nanoparticulate matrix. Electrochemical degradation of the nanocrystals is also measured and the mechanism is discussed. Finally, the (unfortunately unsuccessful) measurements

aiming at electroluminescence are discussed briefly.

4.2 Experimental

The inorganic wet-chemical synthesis that was used to prepare the ZnS:Mn^{2+} nanocrystals is similar to that described in the literature [9]. All steps of the synthesis were performed at room temperature and under conditions of ambient pressure and atmosphere. A capping polymer was used to prevent the agglomeration of the individual particles into a macroscopic (porous) crystal. For this purpose, 10.2 g of Na(PO$_3$)$_n$ was dissolved in 80 ml of ultrapure water ($\rho \sim 16$ MΩ cm). While the solution was stirred, 10 ml of a 1 M solution of Zn(CH$_3$COO)$_2 \cdot 2$H$_2$O was added and allowed to mix, followed by 10 ml of a 0.1 M solution of MnCl$_2 \cdot 4$H$_2$O and, after a few minutes stirring, 10 ml of a 1 M solution of Na$_2$S$\cdot 9$H$_2$O. A white opaque solution was formed directly after the addition of the sulfide solution. After centrifuging and washing the particles twice with ultrapure water a suspension of ZnS:Mn^{2+} nanocrystals in water was obtained.

As a substrate for the fabrication of the electrodes, a 600 nm layer of SnO$_2$:F (TFO) on glass was used. The TFO film had a surface resistivity of 7 $\Omega/\square$ and was transparent throughout the visible range. Substrates with a surface area of (1×3) cm^2 were dipcoated 15 times (dipcoated area: 2 cm^2) from the ZnS:Mn^{2+} suspension at a lift-rate of 0.13 mm/s while the suspension was slowly stirred. The dipcoated electrodes were given a mild temperature treatment for one hour at 200 °C to improve adhesion of the nanocrystals to the TFO layer and increase the surface uniformity. Several of the experiments discussed in this chapter were also performed on electrodes that were not submitted to this thermal treatment. Similar results were obtained, but the nanocrystal layer on the TFO was very fragile and easily destroyed. Therefore, all measurements discussed are performed on electrodes that did receive this thermal treatment. The thickness of the nanocrystalline layer was measured using a profilometer and found to be roughly 1 μm. However, a sizable variation from sample to sample was observed.

After the electrodes were dipcoated, the remaining suspension was centrifuged and washed once with ethanol. The particles were again centrifuged and left to dry in a vacuum desiccator for at least 15 hours. This resulted in a fine white powder. To determine the particle diameter, X-ray powder diffractograms of the powder were measured with a Philips PW 1729 X-ray diffractometer using Cu K$_\alpha$ radiation at a wavelength of 1.542 Å. The X-ray diffraction pattern showed broad peaks at positions that were in good agreement with the zincblende modification of

ZnS [10]. The particle size was calculated from the width of the diffraction peaks using the Debye-Scherrer equation, as shown in chapter 2 [11].

The (photo)electrochemical measurements were carried out in a conventional three-electrode cell using an EG&G model 366A potentiostat. The electrolyte was a 0.5 M solution of Na_2SO_3, the Hg/Hg_2Cl_2 redox couple was used for the reference electrode and the counter electrode was a platinum wire. Optical excitation of the electrodes was obtained using a 300 W Oriel Hg-Xe lamp in combination with a bandpass filter (250 nm to 390 nm, Schott model UG11-3). The in-situ photoluminescence emission spectra measured using with a Princeton Instruments liquid nitrogen cooled CCD camera (1024×256 pixels) in combination with an Acton Pro monochromator (150 lines/mm, blazed at 500 nm). A longpass filter (cutoff at 410 nm) was used to remove the excitation light. Scanning electron microscopy measurements were performed with a Philips XL30 FEG electron microscope.

4.3 Results and discussion

Several reference measurements on the nanocrystalline powder as well as on the electrodes were performed. The average particle diameter was calculated from the broadening of the X-ray diffraction lines [11], and found to be typically 3.6 nm. A similar value was obtained when the size was calculated from the onset of the absorption in reflection measurements performed on the powders using equation (2.2). This size is well within the quantum-size regime, where the physical properties of the nanocrystal are size-dependant [2]. The transmission of the electrodes was high up to the onset of the ZnS absorption, which indicates high quality electrodes with few impurities. The electrodes did not show strong signs of degradation, as similar results were obtained with a fresh electrode and a three-week-old electrode, stored in ambient air (in the dark).

Figure 4.1 clearly shows the influence of the $Na(PO_3)_n$ capping polymer on the quality of the electrodes. As can be seen from a comparison of figure 4.1(a) and figure 4.1(b), the addition of the polymer significantly improves the morphology and the surface smoothness of the electrode. At the same time, though not visible from this figure, the addition of the capping polymer increases the robustness of the layer. This has been determined by measuring the force required to scratch the surface of the electrode with a profilometer. The synthesis using $Na(PO_3)_n$ as a capping polymer resulted in robust electrodes with reproducible properties such as the photocurrent and in-situ photoluminescence characteristics. Because of this, the polymer was used in the synthesis of all the samples described in the remainder
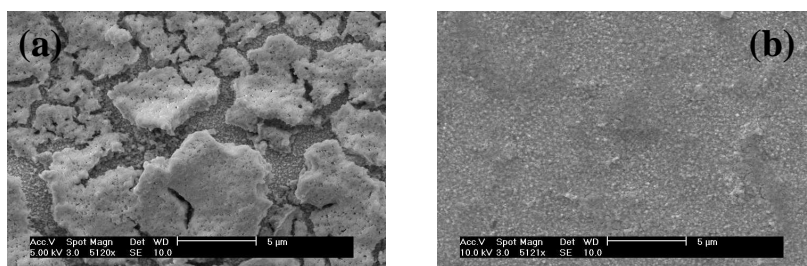
Figure 4.1: *Scanning electron microscopy measurements of a ZnS:Mn^{2+} electrode. (a) Results obtained for a synthesis performed without the addition of the capping polymer. (b) The same synthesis, but now with the addition of the Na(PO$_3$)$_n$ capping polymer during the synthesis.*

of this chapter.

Figure 4.2 shows a cyclic voltammogram[1] of an electrode consisting of ZnS nanocrystals doped with Mn^{2+}, deposited on TFO on glass. For this measurement, the potential was scanned from 0.3 V (vs. SCE) to -1.2 V (vs. SCE) and back to 0.3 V (vs. SCE) at a scan rate of 10 mV/s. During the potential scan the light source was turned on and off every 0.1 V in order to distinguish between the dark current, curve (a), and the photocurrent, curve (b).

The observed dark current at negative potential can be explained by the reduction of water and oxygen,

$$2\,H_2O + 2\,e^- \; \rightarrow \; H_2 + 2\,OH^- \;,\tag{4.1}$$

and

$$O_2 + 4\,H^+ + 4\,e^- \; \rightarrow \; 2\,H_2O \;.\tag{4.2}$$
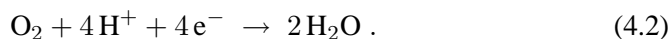
These reactions can occur both at the ZnS nanocrystals and at the TFO interface, because of the porosity of the nanocrystalline layer. However, it is likely that the reactions occur mainly at the conducting TFO layer, because the electron conductance of the nanocrystalline layer is poor, which will also be discussed below. There is also evidence for the reduction of ZnS at negative potentials, as will be shown below.

---

[1]In this technique the applied potential is varied while the resulting current is measured. This can be done either in the dark (to measure the dark-current), or under illumination. The difference between these two voltammograms is the photocurrent.
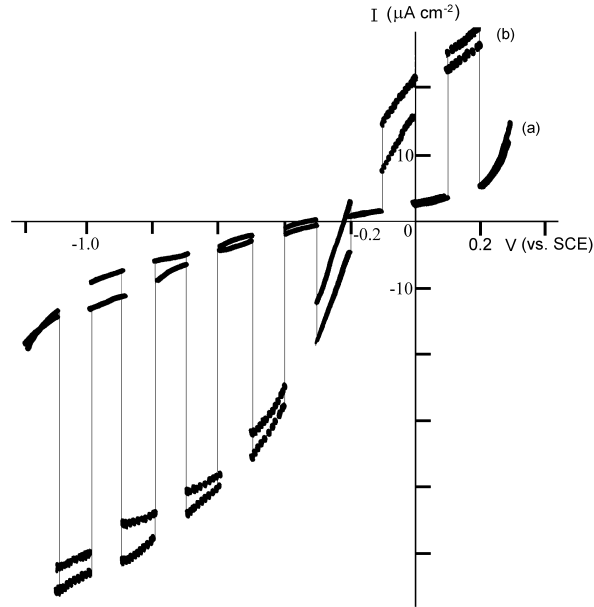
Figure 4.2: *Cyclic voltammogram of a 2 cm^2 electrode of ZnS:Mn^{2+} nanocrystals on TFO using a chopped light source (a) measured in the dark and (b) under illumination. A saturated calomel electrode (SCE) was used as the reference electrode and the illumination was a broad band (250 nm − 390 nm) Hg-Xe light-source. Measured at a scan rate of 10 mV/s.*

At positive potential, the dark current will be caused by the oxidation of SO$_3^{2-}$ and water,

$$\mathrm{SO_3^{2-} + H_2O \ \rightarrow \ SO_4^{2-} + 2\,H^+ + 2\,e^-} \ , \tag{4.3}$$

and

$$\mathrm{2\,H_2O \ \rightarrow \ O_2 + 4\,H^+ + 4\,e^-} \ . \tag{4.4}$$
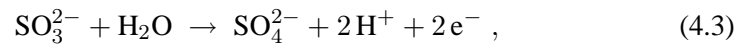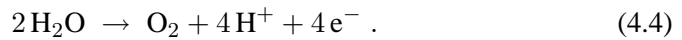
These reactions very likely occur almost exclusively at the TFO surface because the ZnS:Mn^{2+} layer is highly porous and the ZnS nanocrystals are very poor hole conductors. No oxidation of the ZnS host-lattice material is expected, because the hole density in the ZnS nanocrystals in the dark is negligible.

As can be seen from figure 4.2, both an anodic photocurrent of 22 μA/cm^2 and a cathodic photocurrent of 40 μA/cm^2 are observed. The contribution of the TFO layer to the photocurrent was also measured and found to be negligible. The cathodic photocurrent, at negative potential, can be explained by the reduction of oxygen by conduction band electrons,

$$O_2 + 4\,H^+ + 4\,e^- \;\rightarrow\; 2\,H_2O \; , \tag{4.5}$$

while the holes are transferred to the back contact and collected in the external circuit. Possibly the reduction of SO_3^{2-},

$$SO_3^{2-} + 6\,H^+ + 6\,e^- \;\rightarrow\; S^{2-} + 3\,H_2O \; , \tag{4.6}$$

might also contribute to the cathodic photocurrent [12]. However, this has not been proven and the effect is expected to be small.

At positive potential, the anodic photocurrent will be caused by the oxidation of SO_3^{2-} by valence band holes,

$$SO_3^{2-} + H_2O + 2\,h^+ \;\rightarrow\; SO_4^{2-} + 2\,H^+ \; . \tag{4.7}$$
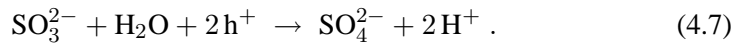
In this case the electrons are collected in the external circuit.

Figure 4.3 shows a photoluminescence spectrum measured at 0 V (vs. SCE) of the electrode before any electrochemical experime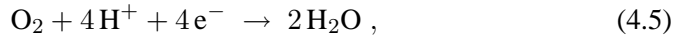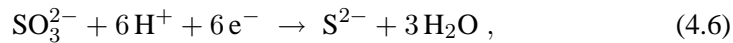nt has been performed. The spectrum shows a broad luminescence band at $\sim$600 nm which is attributed to the $^4T_1 \rightarrow {}^6A_1$ transition in the Mn^{2+} ion [13]. The much weaker band at $\sim$420 nm is attributed to a defect-related luminescence of the ZnS host lattice, as was discussed in chapter 2 [14]. The cut-off of this peak at 410 nm is due to a long-pass filter that was used during these measurements. When the applied potential of the electrode was scanned, this spectrum did not change in form and varied only slightly in intensity. This is consistent with experiments performed on bulk ZnS:Mn^{2+} [15].

Figure 4.4 shows the results of in-situ photoluminescence measurements. The data show that over the whole potential range only a slight (3 %) dependence of the Mn^{2+} related photoluminescence intensity (measured at 600 nm) on the applied potential is observed. The decrease of the photoluminescence intensity at negative potential is almost completely restored at positive potential and only a very small permanent decrease of the photoluminescence intensity is observed. However, long-term experiments have shown that this permanent decrease continues and repeated scanning of the potential for 8 hours resulted in a 50 % decrease of the photoluminescence intensity. In order to appreciate the data shown in figures 4.2 and 4.4, as well as to realize their deviation from what would be expected
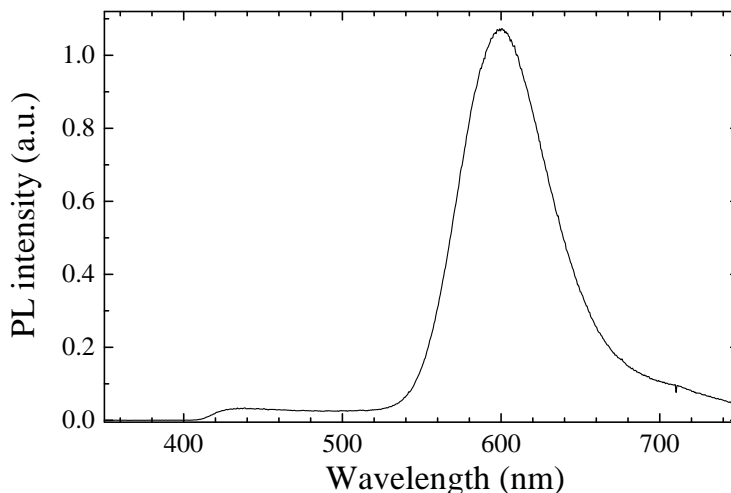
Figure 4.3: *Photoluminescence spectrum at 0 V (vs. SCE). An excitation wavelength-band from 250 nm to 390 nm was used. A long-pass filter for wavelengths longer than 410 nm was used to remove the excitation light.*

for bulk ZnS:Mn^{2+} electrodes, a brief review of some photoelectrochemistry theory and concepts is presented.

In a bulk *n*-type single crystal or polycrystalline electrode under depletion conditions the electric field of the space-charge layer results in band bending. This causes a depletion layer of typically ∼100 nm width which is schematically depicted in figure 4.5(a). As a result, photogenerated electrons and holes are separated. The holes migrate to the surface where they oxidize a species in solution or the semiconductor itself. The electrons are registered as an anodic photocurrent in the external circuit. Because the electrons and the holes are separated, no photoluminescence can be observed in this case.

Close to the flat band potential the situation changes. The concentration of majority carriers at the surface becomes high and one generally observes a reduction reaction and thus a cathodic dark current due to the electrons. The minority carriers that are generated by the illumination will now recombine effectively with the majority carriers. Therefore, the photocurrent becomes negligible and photolumi-
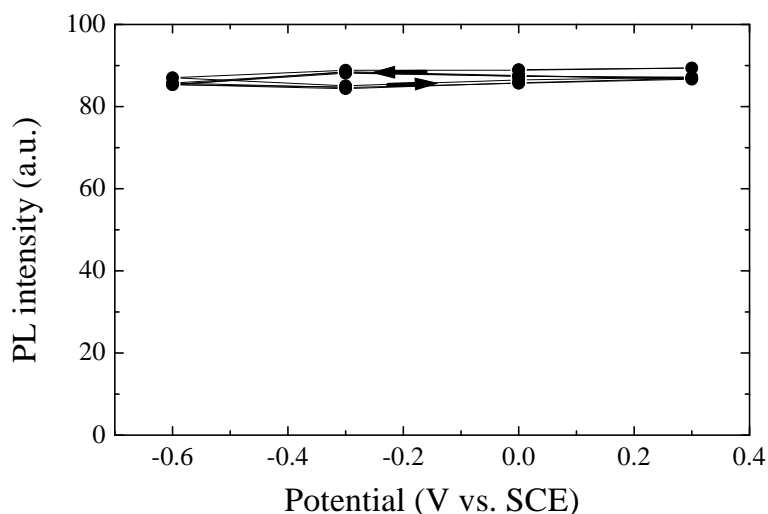
Figure 4.4: *In-situ photoluminescence measurement showing the dependance of the Mn^{2+} related photoluminescence intensity (measured at 600 nm) on the applied potential. The lines are drawn to guide the eye. An excitation wavelength-band from 250 nm to 390 nm was used. Measured at a scan rate of 10 mV/s.*

nescence is observed in this case.

The data presented in figures 4.2 and 4.4 show that the results obtained for electrodes composed of $ZnS:Mn^{2+}$ nanoparticulate layers on TFO are quite different from those described above for bulk electrodes. In a nanoparticulate electrode the electrons and holes are generated within a single nanocrystal. The dimensions of such crystallites are much too small (typically $\sim$5 nm) to allow for the formation of a depletion layer. As a result, there will be no band bending and the system will basically always be under flat-band conditions. This is schematically depicted in figure 4.5(b). The electron and hole are not spatially separated and therefore there is a high probability for recombination. If this process is radiative, then photoluminescence is observed. This can be the case even at positive potentials, which for a bulk electrode corresponds to (strong) depletion. This implies that the emission intensity in the case of a nanoparticulate electrode is, in contrast to that of a bulk electrode, essentially independent of the applied potential over a wide potential range. This is clearly the case for the presently studied nanoparticulate electrode
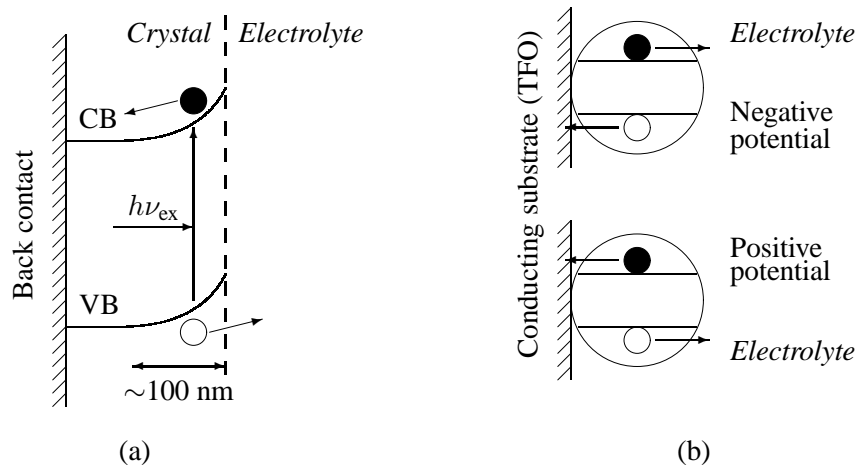
Figure 4.5: *Schematic depiction of the bands of (a) a bulk n-type semiconductor and of (b) a nanocrystalline semiconductor. Due to the fact that the nanocrystalline semiconductor is much smaller than the typical depletion layer width, no band bending occurs. Note the difference for positive and negative applied potential in the nanocrystalline case.*

as shown by experimental data in figure 4.4.

Because of the small dimensions of the nanocrystallites, both electrons and holes in a nanoparticulate electrode can easily diffuse to the interface with the solution [1]. If there is an effective hole scavenger present in the solution and the potential applied to the electrode is such that electrons can be removed via the conducting substrate, then an anodic photocurrent is observed. This is shown in figure 4.2 at positive potential and the charge transfer is shown schematically in the bottom part of figure 4.5(b). The surface hole reaction is very likely the oxidation of SO_3^{2-}, as is shown in reaction (4.7).

On the other hand, if the photogenerated electrons react at the interface with the electrolyte solution and the holes are removed via the back contact then a cathodic photocurrent results. This is seen at negative potentials in figure 4.2 as well as in the top part of figure 4.5(b). The reaction responsible for the cathodic photocurrent is probably the reduction of oxygen present in solution, as is shown in reaction (4.2).

While the anodic and cathodic photocurrent densities shown in figure 4.2 are
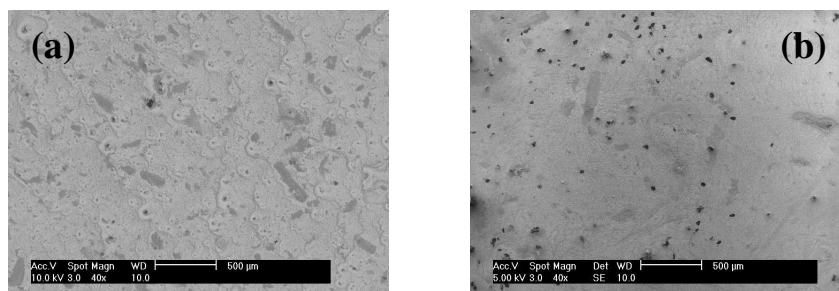
Figure 4.6: *Scanning electron micrographs of a ZnS:Mn^{2+} electrode before (a) and after (b) the electrochemical treatment as discussed in the text.*

significant, they are nevertheless small compared with what would be expected on the basis of the photon flux used. Clearly, the kinetics of electron and hole transfer across the interface between the nanocrystallites and solution are unfavorable compared to the kinetics of electron-hole recombination. This seems reasonable, as the semiconducting nanocrystals are isolated from each other by the insulating capping polymer.

Figure 4.6(a) shows the surface of the electrode directly after the dip-coating and before any electrochemical measurements were performed. The non-uniformity is attributed to agglomerated nanocrystals and the capping polymer. The uniformity changes from sample to sample, as can be seen from a comparison of figures 4.6(a) and 4.1(b). The surface structure is altered significantly when the electrode potential was continuously scanned for 8 hours between 0.3 V (vs. SCE) and -0.6 V (vs. SCE) at a scan rate of 10 mV/s, as can be seen from figure 4.6(b). The main features remain the same as before the treatment. However, a large number of small black dots are formed on the surface. Elemental scanning electron microscopy analysis indicated a high zinc to sulfur ratio in these dots. These results are consistent with the following reactions:

$$V < -0.2 \text{ V (vs. SCE)} : \quad ZnS + 2\,e^- \; \rightarrow \; Zn + S^{2-} \; , \qquad (4.8)$$

$$V > -0.2 \text{ V (vs. SCE)} : \quad Zn + H_2O + 2\,h^+ \; \rightarrow \; ZnO + 2\,H^+ \; , \quad (4.9)$$

$$\text{also} : \quad S^{2-} + 2\,h^+ \; \rightarrow \; S_{(ad)} \; . \qquad (4.10)$$
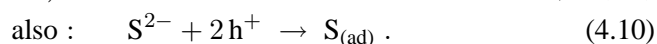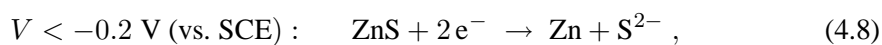
Reaction (4.8), the reduction of ZnS at negative potential, will result in the formation of elementary zinc on the surface and S^{2-} in solution. At positive potential,

most of the surface-bound zinc is oxidized, as indicated by reaction (4.9). Also at positive potential, some of the S^{2-} in solution will oxidize to sulfur, which is adsorbed on the surface of the electrode (reaction (4.10)). Very little sulfur is detected in the black dots with elemental scanning electron microscopy and no region with a high sulfur to zinc ratio is detected on the electrodes. Therefore, the rate for reaction (4.10) may be lower than that of reaction (4.9). The reaction indicated in (4.8) will limit the long-term stability of the electrode. This surface degradation gives rise to non-radiative (surface) recombination centers which leads to a permanent decrease of the luminescence intensity. However, figure 4.4 shows that this decrease takes place slowly, indicating that the reactions indicated in (4.8) − (4.10) will have low rates. As a result, it can be concluded that recombination (radiatively and non-radiatively) will account for most of the charge carriers generated by illumination. This agrees with the data shown in figure 4.2, where a low photocurrent efficiency was found, indicating that most charge carrier recombine. The gradual permanent decrease in the luminescence intensity, as is observed in figure 4.4, can therefore be attributed to the breakdown of the ZnS nanocrystals.

Several experiments have been performed to try to observe electroluminescence from these electrodes. Measurements using electrolytes that are very efficient hole-injectors, such as H$_2$O$_2$ and S$_2$O$_8^{2-}$, did not result in a visible electroluminescence signal. The effect of changing the pH of the electrolyte was also investigated. It was hoped that by changing the pH a plateau in the cyclic voltammogram would be observed. This would be an indication of hole injection and recombination of charge carriers and possibly electroluminescence. However, no such plateau could be observed in the pH range that was investigated (pH 1.8 − pH 12). Therefore, it is concluded that electroluminescence is not significant for these electrodes. This will probably be due to the poor carrier kinetics that were discussed earlier, in combination with an unfavorable position of the ZnS valence band with respect to the vacuum energy level.

4.4   Conclusions

This chapter is devoted to the potential dependent photoluminescence measurements on electrodes made from layers of ZnS nanocrystals doped with Mn^{2+} deposited on SnO$_2$:F on glass. Photocurrent-potential and in-situ photoluminescence measurements were used to show that the ZnS:Mn^{2+} layers have properties that are typical of a nanoparticulate matrix. The electrodes show both anodic and cathodic photocurrent, as is expected for a nanocrystalline electrode. The small pho-

tocurrent efficiency indicates that the kinetics of electron and hole transfer across the interface between the nanocrystallites and the electrolyte solution are unfavorable compared to the kinetics of electron-hole recombination (radiative or non-radiative). This is corroborated by the fact that the Mn^{2+} related luminescence is observed over a broad potential range and only small changes in the photoluminescence intensity are detected for each successive potential cycle. This implies that the photocurrent-generating reactions will have low rates. Therefore, it is concluded that electron-hole recombination accounts for most of the charge carriers generated by the illumination. Potential-induced breakdown of the nanocrystals is observed and explained. No electroluminescence of the nanocrystalline $ZnS:Mn^{2+}$ electrodes was observed.

References

[1] G. Hodes, I. D. J. Howell and L. M. Peter, *J. Electrochem. Soc.* **139**, 3136 (1992).

[2] N. C. Greenham, X. Peng and A. P. Alivisatos, *Phys. Rev. B* **54**, 17628 (1996).

[3] J. Leeb, V. Gebhardt, G. Müller, D. Haarer, D. Su, M. Giersig, G. McMahon and L. Spanhel, *J. Phys. Chem. B* **103**, 7839 (1999).

[4] K. Sooklal, B. S. Cullum, S. M. Angel and C. J. Murphy, *J. Phys. Chem.* **100**, 4551 (1996).

[5] A. van Dijken, A. H. Janssen, M. H. P. Smitsman, D. Vanmaekelbergh and A. Meijerink, *Chem. Mater.* **10**, 3513 (1998).

[6] J. Huang, Y. Yang, S. Xue, B. Yang, S. Liu and J. Shen, *Appl. Phys. Lett.* **70**, 2335 (1997).

[7] Y. Yang, S. Xue and S. Liu, *Appl. Phys. Lett.* **69**, 337 (1996).

[8] Prof. Dr. C. Ronda (Philips research, Aachen), *Private communication.*

[9] I. Yu, T. Isobe and M. Senna, *J. Phys. Chem. Solids* **57**, 373 (1996).

[10] R. Jerkins, W. F. McClune, T. M. Maguire, M. A. Holomany, M. E. Mrose, B. Post, S. Weissmann, H. F. McMurdie and L. Zwell, *Powder Diffraction File*, JCPDS International center for diffraction data (1985).

[11] B. D. Cullity, *Elements of X-ray diffraction*, Addison-Wesley: Massachusetts, page 102 (1978).

[12] B. R. Crane and E. D. Getzoff, *Curr. Opin. Struc. Biol.* **6**, 744 (1996).

[13] W. G. Becker and A. J. Bard, *J. Phys. Chem.* **87**, 4888 (1983).

[14] J. F. Suyver, S. F. Wuister, J. J. Kelly and A. Meijerink, *Nano Lett.* **1**, 429 (2001). See also chapter 2.

[15] J. Ouyang, F.-R. F. Fang and A. J. Bard, *J. Electrochem. Soc.* **136**, 1033 (1989).

Chapter 5

Luminescence of nanocrystalline ZnSe:Mn^{2+}

The synthesis and luminescent properties of nanocrystalline ZnSe:Mn^{2+} prepared via an inorganic chemical synthesis method are described. The photoluminescence spectra show distinct ZnSe and Mn^{2+} related emissions, both of which are excited via the ZnSe host lattice. The Mn^{2+} emission wavelength and the associated luminescence decay time depend on the concentration of Mn^{2+} incorporated into the ZnSe lattice, which is an indication of the (preferential) formation of Mn^{2+} pair-states. Temperature-dependent photoluminescence spectra and photoluminescence lifetime measurements are also presented and the results are compared to those of Mn^{2+} in bulk ZnSe. From the data it is concluded that the temperature dependence of the Mn^{2+} emission can be explained by electron-phonon coupling to an optical phonon of the ZnSe host lattice.

5.1   Introduction

Quantum-size effects in nanocrystalline semiconductors such as CdS, CdSe, ZnS
and ZnO have been studied extensively [1–6]. In some cases the method for the
synthesis of nanometer sized semiconductor particles is a simple room tempera-
ture reaction in water or alcohol (e.g. CdS, ZnS or ZnO) [4–6]. This was also the
case for the nanocrystals described in the first part of this thesis (chapters 2, 3 and
4). In other cases, more elaborate and challenging high temperature reactions with
air and moisture-sensitive reactants are required to obtain highly efficient lumi-
nescing nanocrystals (such as CdSe) [1, 2]. In addition to undoped semiconductor
nanocrystals, the luminescence of nanocrystalline semiconductors in which opti-
cally active ions are incorporated has received considerable attention, also in rela-
tion to possible applications [7, 8]. A simple wet chemical synthesis is attractive
for device applications since large amounts of well-defined nanocrystals can easily
be obtained in this way. As a result, many studies have focussed on ZnS and CdS
doped with Mn^{2+} or trivalent lanthanides [5].

Efficiently luminescing ZnS:Mn^{2+} nanocrystals (with a quantum efficiency of
more than 10 %) can easily be synthesized and are considered for application in
low-voltage electroluminescent devices [7, 9], as was also discussed in some detail
in chapter 4. However, the position of the ZnS valence band-edge is located too far
from the vacuum-level to allow direct injection of holes from presently available
p-type conducting polymers into the ZnS valence band. Better results are expected
for ZnSe, which has a valence band-edge at higher energy with respect to that of
ZnS [10], as will be shown in chapter 7.

Up to now, there have been no reports on the synthesis and luminescence prop-
erties of nanocrystalline ZnSe doped with a luminescent ion, such as manganese.
This is probably due to the fact the synthesis of nanocrystalline ZnSe particles
is not as simple as that of ZnS particles. Undoped ZnSe particles with quantum ef-
ficiencies of $1-5$ % have been obtained by a high temperature (300 °C) synthesis
in the organic soap hexadecylamine [11]. It seems reasonable that such a synthesis
can also be extended to include a luminescent dopant such as Mn^{2+} in the ZnSe
lattice.

In this chapter the preparation of nanocrystalline ZnSe particles doped with
Mn^{2+} is discussed. It will be shown that Mn^{2+} can be incorporated into nano-
crystalline ZnSe and made to luminesce by exciting in the ZnSe host lattice. To
this end, photoluminescence emission and excitation spectra are presented and
discussed. Furthermore, temperature-dependent luminescence and luminescence
lifetime measurements are also reported and compared to results obtained for the

luminescence of Mn^{2+} in bulk ZnSe.

5.2 Experimental

The synthesis route that was used to prepare the ZnSe:Mn^{2+} nanocrystals is a variation of the TOP/TOPO synthesis used for the preparation of nanocrystalline CdSe [12]. This synthesis route yields ZnSe nanocrystals with quantum efficiencies of $1-5$ % [11]. Both the preparation for, as well as the actual synthesis were performed in the protective dry-nitrogen atmosphere of a glovebox. In this glovebox, the water and oxygen concentrations were both below 10 ppm.

Hexadecylamine (HDA) was used as the solvent instead of tri-*n*-octylphosphine oxide (TOPO) because its bond to zinc is weaker and it is less alkaline than TOPO [11]. If the HDA is replaced with TOPO, then the reaction does not take place. Before the synthesis was started, a 45 ml sample of HDA was heated to 310 °C in a flask. A variable amount of the manganese precursor, manganese cyclohexanebuterate powder, was dissolved in 12 ml of tri-*n*-octylphosphine (TOP) in order to obtain samples with different Mn^{2+} concentrations. To this mixture 3 ml of a 1 M solution of TOPSe (previously prepared by dissolving elemental Se-powder in TOP) was added. After stirring, 0.32 g of diethylzinc was added. This solution was shaken and then added to the hot HDA using a syringe. The nanocrystals were grown at 275 °C for 4 hours. The influence of the synthesis time on the photoluminescence characteristics and the particle size is reported in chapter 6 for a comparable system. The mixture was then allowed to cool to 70 °C and the nanocrystals were precipitated by addition of 25 ml of anhydrous 1-butanol followed by 30 ml of anhydrous methanol. The residue was taken out of the glovebox, centrifuged and decanted. The samples were returned to the glovebox and washed with anhydrous methanol. Finally the samples were dried in a vacuum desiccator, and a fine white powder was obtained. This powder consists of the ZnSe:Mn^{2+} nanocrystals with a HDA capping.

The chemical composition of the samples was determined using a Perkin-Elmer Optima-3000 inductively coupled plasma spectrometer. To determine the average particle diameter, X-ray powder diffractograms were measured with a Philips PW 1729 X-ray diffractometer using Cu K_α radiation ($\lambda = 1.542$ Å). The photoluminescence emission and excitation spectra were recorded with a SPEX Fluorolog spectrofluorometer, model F2002, equipped with two monochromators (double-grating, 0.22 m, SPEX 1680) and a 450 W xenon lamp as the excitation source. All spectra were corrected for the spectral response of the emission mo-

nochromator and the photomultiplier tube. The excitation spectra were also corrected for the spectral distribution of the excitation source (xenon lamp) and the excitation monochromator. Photoluminescence lifetimes were measured using the third harmonic (355 nm) of a Quanta-ray DCR YAG:Nd laser as the excitation source. The emission light was transported through a fibre optics cable to the monochromator (Acton SP-300i, 0.3 m, 150 lines/mm grating, blazed at 500 nm). The time traces were recorded using a thermoelectrically cooled photomultiplier tube in combination with a Tektronix 2430 oscilloscope. Temperature-dependent photoluminescence emission and lifetime spectra were recorded using a liquid-helium flow-cryostat equipped with a sample heater to stabilize the temperature at temperatures between 4 K and room temperature.

5.3   Results and discussion

The amounts of Mn, Zn and Se present in the ZnSe:Mn^{2+} samples were measured using inductively coupled plasma analysis. Typically, about 10 % of the initial Mn^{2+} that was present during the synthesis was incorporated into the ZnSe lattice. The highest Mn^{2+} concentration in the ZnSe nanocrystals was found to be 3 %. When the Mn^{2+} precursor concentration was high enough for the incorporated Mn^{2+} concentration to be greater than 1 %, the yield became very low. This low yield may be due to the organic residue from the Mn^{2+} precursor which can hinder the formation of the ZnSe nanocrystals. Because of this low yield, only the samples that had a Mn^{2+} concentration less than 1 % were used in the measurements that are discussed below.

5.3.1   X-ray diffractograms

Figure 5.1 shows the X-ray diffraction pattern for a ZnSe:Mn^{2+} sample containing 0.4 % of Mn^{2+}. This pattern is much more complicated than that measured for nanocrystalline ZnS:Mn^{2+}, such as the pattern shown in figure 2.1. The two sharp peaks located at 38° and 44.5° are caused by the aluminum sample holder and can be ignored. However, at least eight more (small) sharp peaks can be identified in figure 5.1, as well as three broad bands. These sharp peaks cannot be related to the ZnSe nanocrystals. They may result from crystalline hexadecylamine in the capping layer surrounding the nanocrystals, or to residue from the chemical synthesis used to prepare the nanocrystals.

The three broad bands shown in figure 5.1 are likely to be due to the ZnSe
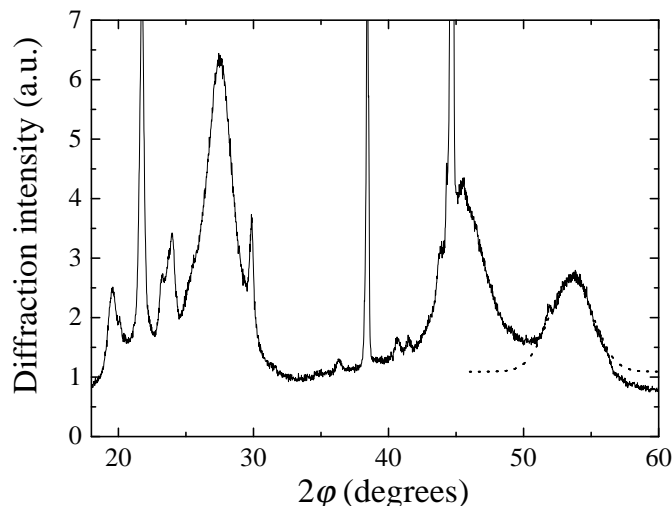
Figure 5.1: *X-ray diffractogram of a ZnSe:Mn^{2+} sample containing 0.4 % of Mn^{2+}. Similar patterns were obtained for other Mn^{2+} concentrations. The dashed line through the data is a Gaussian fi t of the broad band centered at $2\theta = 53.5°$.*

nanoparticles. These values were also expected, as according to the literature, the most intense lines correspond to d-values of 3.26_x, 2.00_7 and 1.71_4 [13]. As a result, the expected peak maxima are located at $2\theta = 27.4°$, $2\theta = 45.4°$ and $2\theta = 53.6°$, according to equation (2.5). A Gaussian fit of three broad bands shown in figure 5.1 results in peaks at $2\theta = 27.5°$, $2\theta = 45°$ and $2\theta = 53.5°$, which is in good agreement with the expected values.

Due to the many other peaks in the pattern shown in figure 5.1, an accurate fit of the principal X-ray diffraction band, at $2\theta = 27.5°$, is not possible. Fortunately, a fit of any one of the broad bands will suffice to calculate the diameter of the nanocrystals by means of the Debye-Scherrer equation, as shown in equation (2.3). Therefore, the peak at $2\theta = 53.5°$ could be used for the fitting. As can be seen from the dashed line through the data in the interval from $2\varphi = 51°$ to $2\varphi = 56°$, an accurate fit of this peak is possible. From this fit, and others like it for the different Mn^{2+} concentrations, it was calculated that the nanocrystals have a diameter d in the range $3-4$ nm. No relation between the size of the nanocrystals and the Mn^{2+}
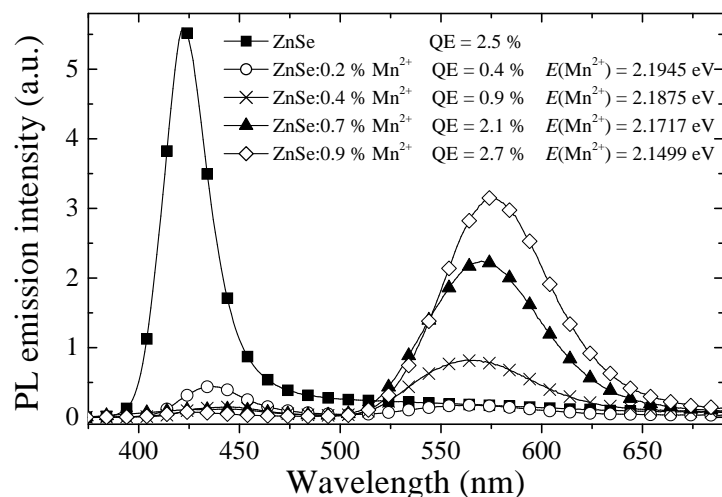
Figure 5.2: *Photoluminescence emission spectra for nanocrystalline ZnSe:Mn²⁺ samples with different Mn²⁺ concentrations, as indicated in the figure. All spectra were measured at room temperature and the excitation wavelength was 330 nm. The symbols (squares, circles, crosses, triangles and diamonds) are used to label the different spectra and the drawn lines are the measured curves. This is the case for all figures in this chapter. Relative intensities can be compared.*

concentration could be observed.

5.3.2 Photoluminescence excitation and emission

Figure 5.2 shows the photoluminescence emission spectra of several nanocrystalline ZnSe:Mn²⁺ samples with an incorporated Mn²⁺ concentration between 0 % and 0.9 %. The measurement conditions were identical in all cases and therefore relative intensities can be compared. The photoluminescence band centered at around 430 nm is attributed to the excitonic luminescence of the ZnSe host lattice. The band centered at ∼570 nm is attributed to the $^4T_1 \rightarrow {}^6A_1$ transition in the Mn²⁺ ion. The position of the Mn²⁺ emission is similar to that for Mn²⁺ in bulk ZnSe [14, 15]. On the lower energy side (600−640 nm) a third emission band is usually found for bulk ZnSe:Mn²⁺. This band is assigned to a self-activated lumi-

nescence, probably due to $Cl^{\bullet}_{Se}$-V''_{Zn} donor-acceptor pairs. (Here the Kröger-Vink notation is used for identifying defect states [16]). The observation that this self activated luminescence is absent (or very weak) indicates that the concentration of $Cl^{\bullet}_{Se}$-V''_{Zn} pairs in the ZnSe nanocrystals is low. This is likely to be due to either the small size of the nanocrystals (low probability for the presence of both types of defect in one nanocrystal); or to the purity of the chemicals used for the synthesis; or an effect of the confinement of the electron-hole pair: because of this there is no energy migration possible to the $Cl^{\bullet}_{Se}$-V''_{Zn} donor-acceptor pair.

The quantum efficiency of the various samples was calculated by comparing the integrated intensity of the emission spectrum with that of the commercial lamp phosphor $BaMgAl_{10}O_{17}$:Eu^{2+} (BAM), which was kindly provided by Philips. This phosphor has a known quantum efficiency of about 90 % when excited at 300 nm [17]. The emission spectra of BAM and of the ZnSe:Mn^{2+} sample were recorded under identical conditions. If the ratio of the integrals of the emission spectrum of the sample and that of BAM is denoted by x, the the quantum efficiency of the sample is simply $x \cdot 90$ %, when one assumes that the absorbance of the sample and that of BAM are identical.

The total luminescence quantum efficiency (indicated in figure 5.2) shows a large decrease when a small concentration of Mn^{2+} is incorporated into the ZnSe host lattice. This is a bit surprising, because it is known from the literature that efficient energy transfer from the ZnSe host lattice to the Mn^{2+} dopant is possible [18]. Apparently the decrease of the ZnSe related emission is not only due to energy transfer to Mn^{2+}, which does not affect the quantum efficiency. The drop in the quantum efficiency from 2.5 % to 0.4 % for the incorporation of 0.2 % Mn^{2+} therefore indicates that nonradiative quenching centers are also formed as a by-product of the synthesis including the Mn^{2+} precursor. This is probably due to the organic residue from the Mn^{2+} precursor, which may induce defects in the nanocrystal, or result in efficient quenching states on its surface.

At higher Mn^{2+} concentrations, the energy transfer to Mn^{2+} becomes more efficient and the intensity of the yellow Mn^{2+} emission increases. For 0.9 % Mn^{2+} the quantum efficiency has increased to 2.7 %, just above that of the ZnSe related emission in the undoped sample. The present results are typical for one concentration series of Mn^{2+} doped ZnSe nanocrystals. Since the quantum efficiencies of doped and undoped nanocrystalline semiconductors are strongly dependent on small variations in the synthesis procedure, higher quantum efficiencies can be expected on optimizing the synthesis procedure. Better results may also be obtained with another type of Mn^{2+} precursor.
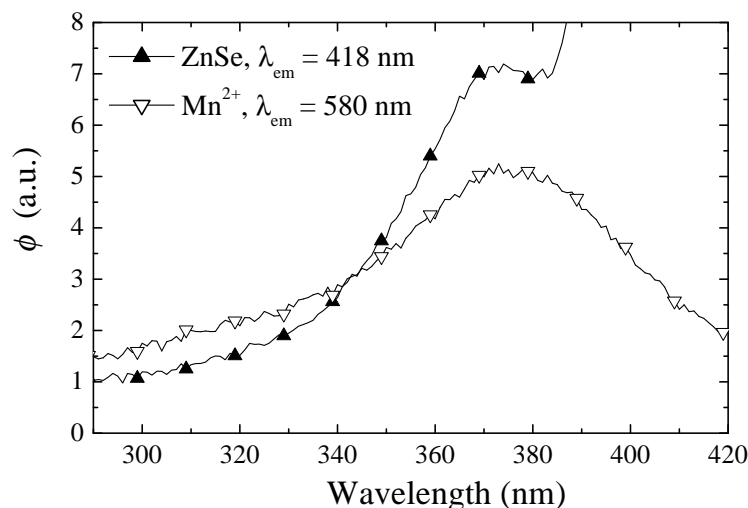
Figure 5.3: *Photoluminescence excitation spectra for the ZnSe: 0.2 % Mn^{2+} sample. The spectra were measured at room temperature and the emission wavelengths are indicated in the fi gure. The values of ϕ for the two curves cannot be compared.*

The observed photoluminescence emission energies for the Mn^{2+} related luminescence, obtained from a Gaussian fit of the Mn^{2+} related photoluminescence peak using the relative emitted photon flux per constant energy interval as a function of the energy, are indicated in figure 5.2. Due to the high quality Gaussian fits, the accuracy in the obtained emission energies was better than 1 meV. A shift in the maximum of the Mn^{2+} emission to lower energy is observed for increasing Mn^{2+} concentrations. This shift is possibly due to the formation of pairs of Mn^{2+} ions at higher concentrations. It is well known that the emission of Mn^{2+} pairs can be at lower energy than that of single ions [19]. Lifetime measurements presented below provide additional evidence for the formation of exchange-coupled Mn^{2+} pairs at higher Mn^{2+} concentrations.

Figure 5.3 shows the photoluminescence excitation spectra of both the ZnSe and the Mn^{2+} related emissions. In this figure, ϕ denotes the photon flux per constant wavelength interval. Both spectra show a clear maximum for excitation at ~370 nm. The steep increase beyond 390 nm in the excitation spectrum for the

ZnSe related emission is due to the detection of scattered excitation light which is not rejected by the monochromator, since the wavelength of the emission monochromator ($\lambda = 418$ nm) is close to the excitation wavelength. The position of the excitation maximum was found to vary slightly from sample to sample; a small variation in particle size (and thus in the bandgap) can explain such differences. This agrees with the results from X-ray diffraction measurements. Using the known values of the material parameters in ZnSe ($m_e^\star = 0.17m_0$ [20], $m_h^\star = 0.60m_0$ [21], $\epsilon_r = 8.1$ [22] and $E_g = 2.8$ eV [22]), the Brus equation (1.7) that relates the energy of the bandgap in electron volts to the radius of the nanocrystals in nanometers [3] becomes

$$E_g(r) \;=\; 2.8 - \frac{0.32}{r} + \frac{2.84}{r^2} \;.\qquad(5.1)$$

From equation (5.1) it is clear that the excitation maximum of 370 nm (3.35 eV), as found from figure 5.3, corresponds to a crystal radius of $r \approx 2$ nm, which is in good agreement with the value of $d \approx 3-4$ nm as was determined by X-ray powder diffraction.

The fact that both the ZnSe and the Mn^{2+} emissions have the same excitation maximum indicates that the excitation of the divalent manganese takes place through excitation of the ZnSe host lattice, followed by energy transfer to the Mn^{2+} ion. This agrees with the qualitative observation based on figure 5.2 that incorporation of Mn^{2+} in the ZnSe lattice results in a decrease of the ZnSe related photoluminescence and a concomitant increase in the Mn^{2+} photoluminescence. Efficient energy transfer to Mn^{2+} centers incorporated in ZnSe has been well studied in bulk $ZnSe:Mn^{2+}$ [23] and efficient transfer was expected to occur in nanocrystalline $ZnSe:Mn^{2+}$, as is indeed observed (although not with the same efficiency as can be seen from figure 5.2).

Figure 5.4 shows the excitation spectrum of the Mn^{2+} related photoluminescence at higher energy. The spectral range probed in this experiment, the UV to VUV range, is difficult to access because very few tunable radiation sources with a high photon flux are available for this range. Therefore, these measurements were performed at the HIGITI experimental station [24] of the Synchrotronstrahlungslabor HASYLAB at the Deutsche Elektronen-Synchrotron DESY in Hamburg (Germany). In the excitation spectra the ultimate spectral resolution is better than 0.5 nm [25] and all spectra were corrected for the spectral intensity distribution of the synchrotron radiation (using a spectrum provided by DESY). The relatively poor resolution in this spectrum is due to the short time that was available to perform this measurement.
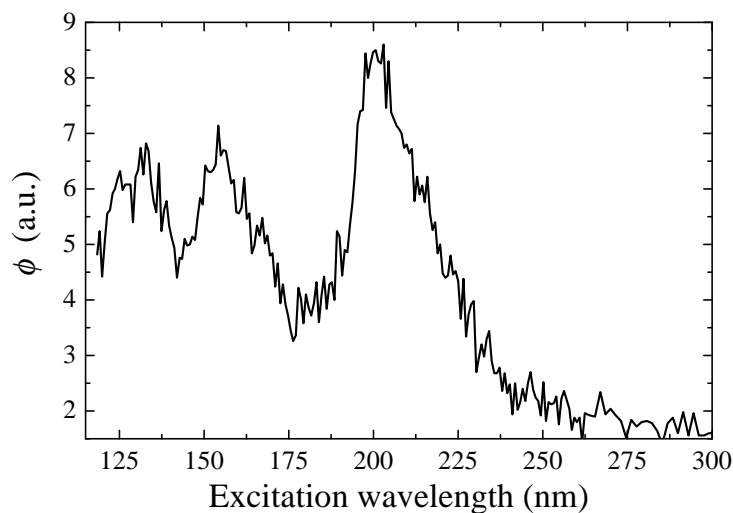
Figure 5.4: *Excitation spectrum of the Mn^{2+} related emission (measured at 580 nm) for high energy photons. The spectrum was measured using the HIGITI station (DESY, Hamburg, Germany) and recorded at 10 K.*

Figure 5.4 shows three additional excitation bands for the Mn^{2+} related emission, at the wavelengths ∼200 nm, ∼155 nm and ∼130 nm. The three excitation bands shown in figure 5.4, as well as the one observed in figure 5.3, can all be related to the ZnSe host lattice. This would imply that there are four excitation bands of the ZnSe below 10 eV: 3.35 eV (370 nm), 6.2 eV (200 nm), 8 eV (155 nm) and 9.5 eV (130 nm). It is interesting to note that the energy separation between these subsequent excitation bands decreases: 3.35 eV, 2.85 eV, 1.8 eV and 1.5 eV. This would also be expected as these values are a measure for the Fourier-components of the periodic potential (which must decrease to ensure convergence of the total Fourier sum). The third excitation band of the ZnSe, at roughly 8 eV, agrees rather well with a known excitation maximum of bulk ZnSe which involves a transition at the Γ point in **k**-space. However, a detailed assignment of each of these transitions was not performed because the band structure for a nanocrystal is likely to be different from that of a bulk crystal. Unfortunately, detailed band structure calculations for a ZnSe nanocrystal are not available. Note that in this discussion it
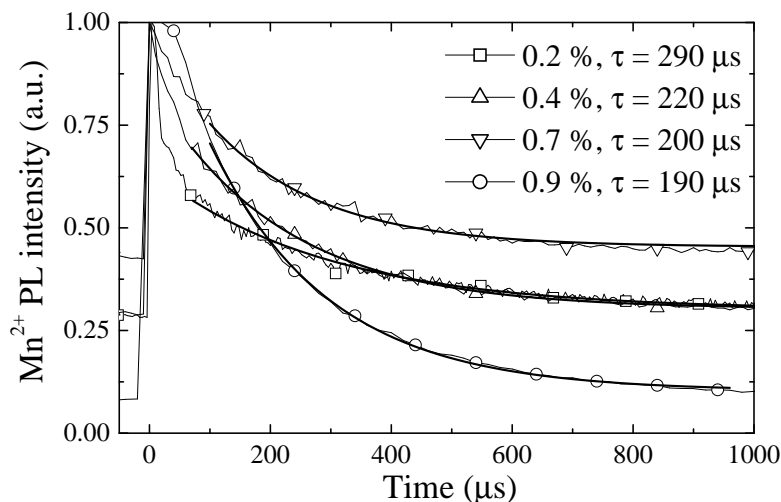
Figure 5.5: *Decay curves of the Mn^{2+} related emission at room temperature for different Mn^{2+} concentrations in ZnSe. The pulsed excitation wavelength was 355 nm and the pulse duration was about 10 ns.*

is assumed that the hexadecylamine layer surrounding the nanocrystals is transparent over this energy range. Another explanation of the structure seen in figure 5.4 could therefore be that these 'excitation bands' are in fact due to the absorption bands of hexadecylamine.

5.3.3 Luminescence lifetime

The time dependence of the ZnSe and Mn^{2+} related luminescence intensity after pulsed excitation was measured for the samples shown in figure 5.2. Figure 5.5 shows the Mn^{2+} luminescence decay curves (measured at 570 nm) for all the samples, measured at room temperature and scaled at $t = 0$. Note that because the spectra were scaled at $t = 0$, the baselines (i.e. the background intensities) are not the same due to the differences in quantum efficiency from sample to sample. Single-exponential fits of the decay curves up to 1 ms are shown as lines through the data. In all cases a good single-exponential fit was possible using a lifetime of the order of 200 μs. The exact values of the lifetimes are indicated in the figure. Even though

the fits shown in figure 5.5 describe the experimental data rather well, the decay is not purely single exponential. Therefore, the lifetime depends slightly on the time interval used in the fitting procedure. The samples containing a higher Mn^{2+} concentration have shorter lifetimes and a drop from $\sim$290 μs to $\sim$190 μs is observed between 0.2 % Mn^{2+} and 0.9 % Mn^{2+}. Finally, a fast ($\sim$100 ns) component of the lifetime is also found. This component is assigned to the ZnSe emission, rather than the Mn^{2+} emission. This is expected to be correct, because the ZnSe related emission overlaps slightly with the Mn^{2+} luminescence spectrum. A similar effect has been observed for nanocrystalline ZnS:Mn^{2+} [26, 27].

The interpretation of the measured lifetimes and the concentration dependence is not straightforward. In spite of extensive research on bulk ZnSe:Mn^{2+}, the radiative lifetime of the Mn^{2+} emission (from single ions) is not well established; values between 30 and 800 μs have been reported [14, 15, 28]. At room temperature the lifetime is reduced by thermal quenching, which has been found to be sample dependent. The concentration also influences the lifetime; even at Mn^{2+} concentrations as low as 1 % a reduction in the lifetime has been reported [15]. Due to the uncertainty in the single ion radiative lifetime and the non-exponential character of the luminescence decay curve, it is difficult to derive quantitative information from the luminescence decay results of figure 5.5. However, two qualitative conclusions can be made.

Firstly, the lifetime of the Mn^{2+} emission in ZnSe is of the order of hundreds of microseconds, which is much shorter than the lifetime of the Mn^{2+} emission in ZnS (where a lifetime of 1.8 ms was found). This has also been observed for the bulk materials and is explained by stronger spin-orbit coupling due to the heavier Se^{2-} ligands in comparison to S^{2-} [28].

Secondly, the lifetime of the emission is shorter at higher Mn^{2+} concentrations ($\sim$290 μs at 0.2 % Mn^{2+}, as compared to $\sim$190 μs at 0.9 % Mn^{2+}). It is known that due to exchange interaction the spin selection rule is partially lifted and the ^{4}T$_1 \rightarrow {}^6$A$_1$ transition in the Mn^{2+} becomes more allowed at higher Mn^{2+} concentrations [19]. This results in the fact that the lifetime of the Mn^{2+} emission will be reduced at higher Mn^{2+} concentrations when exchange-coupled Mn^{2+} pairs are formed.

It seems reasonable to attribute the shortening of the lifetime (shown in figure 5.5) and the shift in the luminescence emission energy (shown in figure 5.2) to the presence of Mn^{2+} pair-states. However, the concentration range in which this effect is observed is too low to be explained by random pair formation: for Mn^{2+} concentrations in the range of 0.2 % $-$ 0.9 %, it is calculated that the percentage

of Mn^{2+} pair-states will be between 1.9 % and 8.7 % based on random pair formation [29]. This implies that (assuming random pair-formation) roughly 90 % of the luminescence signal should be generated by isolated Mn^{2+} ions. The shift in the luminescence emission energy (shown in figure 5.2) as well as the shortening of the lifetime (shown in figure 5.5) both seem too large to be explained by less than 10 % of the total Mn^{2+} concentration. Therefore, this suggests that preferential pair-formation is responsible for the relatively large effect of the Mn^{2+} concentration on the emission energy and the luminescence lifetime.

Another explanation for the shortening of the Mn^{2+} luminescence lifetime and the shift in the luminescence emission energy, not requiring preferential pair for-mation, could be the more efficient trapping of electron-hole pairs after bandgap excitation by the Mn^{2+} pair-states compared to single ions. As a result of this ef-ficient trapping, the (low concentration of) Mn^{2+} pair-states could be responsible for the majority of the luminescence. This has been suggested previously for bulk ZnSe:Mn^{2+} [30].

The ZnSe luminescence decay curves (measured at 420 nm) were found to have $\sim$100 ns components as well as components that were too fast to be measured with the experimental setup used to determine the Mn^{2+} lifetime. The lifetime of the ZnSe related luminescence has therefore been measured using the much faster setup available at the HIGITI station at the DESY synchrotron in Hamburg. Figure 5.6 shows a decay spectrum of the ZnSe related emission (measured at 420 nm) recorded at 10 K under 370 nm excitation. The ZnSe luminescence has a single-exponential decay, as can be seen from the line through the data. The lifetime was found to be 3.6 ns at 10 K, which is reasonable for this (spin-allowed) transition. No measurements of the lifetime of the luminescence of bulk ZnSe have been published, and therefore no comparison can be made. However, it is expected that the lifetime for bulk ZnSe will be comparable to that found for the nanocrystalline material.

5.3.4 Temperature dependence

Figure 5.7 shows temperature-dependent measurements of the photoluminescence spectra for a ZnSe: 0.7 % Mn^{2+} sample under 330 nm excitation. It is clear that there is a strong quenching of the ZnSe and Mn^{2+} related photoluminescence in-tensities. This has also been reported for bulk ZnSe:Mn^{2+} [28, 31]. A detailed discussion of the quenching behavior, as well as an explanation of the mechanism (due to Auger quenching) have been reported in Ref. [32].

A clear shift of the ZnSe related photoluminescence emission energy to longer
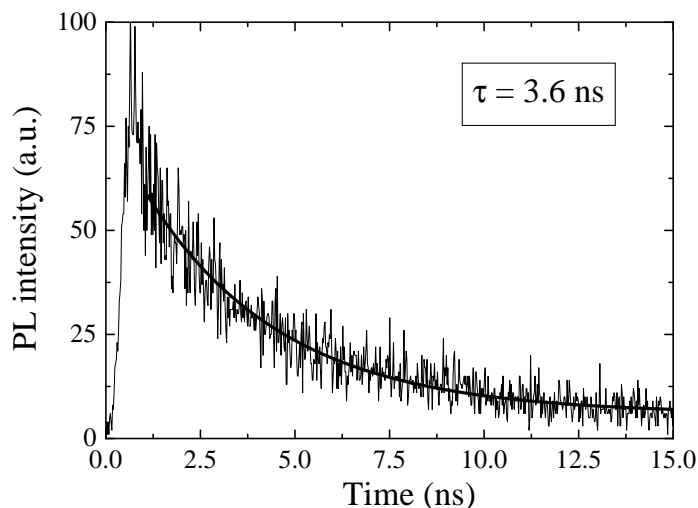
Figure 5.6: *Time dependence of the ZnSe related emission intensity. The thick line is a single exponential fit of the data resulting in the 3.6 ns lifetime indicated in the graph. The emission wavelength was 420 nm and the excitation wavelength was 370 nm. The measurement was performed at 10 K using the HIGITI setup at DESY (Hamburg). The pulse duration was 150 ps and the pulse separation was 192 ns. The final resolution that can be obtained is about 200 ps, mainly due to the response-time of the photomultiplier.*

wavelengths is also observed for increasing temperature in figure 5.7. The data is shown in figure 5.8(a), where the emission energy was obtained from a Gaussian fit of the emitted photon flux per constant energy interval as a function of energy. Note that for low temperatures (roughly below 50 K) a shift of the ZnSe related emission energy to higher energy is observed. This effect was also reported in chapter 3 for the luminescence of nanocrystalline ZnS:Mn^{2+} and is related to the detrapping of charge carriers from shallow defect states at elevated temperature. The shift of the ZnSe related emission energy (for temperatures higher than 50 K) could be fitted very well using the standard Varshni equation for the temperature dependence of the bandgap of a semiconductor [33]

$$E_g(T) \; = \; E_0 \; - \; \frac{\alpha T^2}{T + \beta} \, , \tag{5.2}$$
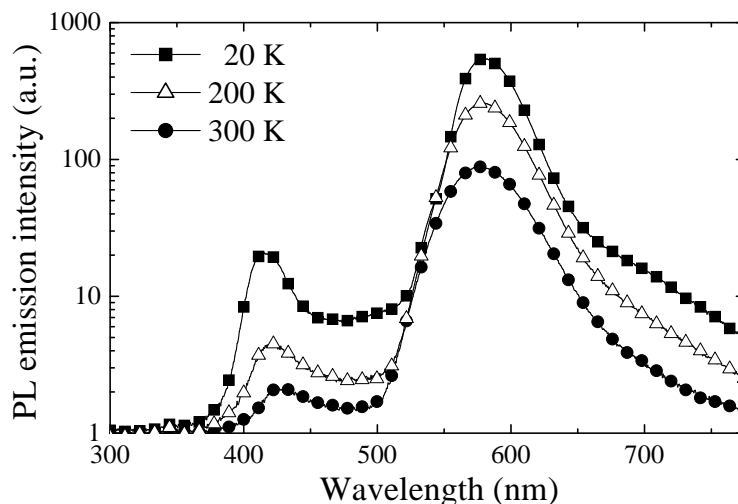
Figure 5.7: *Temperature-dependent photoluminescence spectra for the ZnSe:0.7 % Mn^{2+} sample. Note the logarithmic intensity axis. The excitation wavelength was 330 nm and the intensities can be compared.*

where E_0 represents the bandgap at 0 K and α and β are fitting parameters. It is known from the literature that β is of the order of the Debye temperature of the semiconductor. This equation takes into account both the change in lattice parameter and the temperature dependence of the electron-lattice interaction. As mentioned earlier (in chapter 3), equation (5.2) was originally derived in the infinite crystal approximation and is used to analyze bulk semiconductor systems. It is not immediately obvious that this equation also applies to nanocrystalline semiconductors which have a different band-structure and a different phonon density of states.

The temperature dependence of the ZnSe related photoluminescence could be fitted with equation (5.2), as is shown by the line through the data in figure 5.8(a). From these fits values of $\alpha = (9 \pm 3) \cdot 10^{-4}$ eV/K and $\beta = (3.8 \pm 1) \cdot 10^2$ K were found. These value compare well with those found for bulk ZnSe ($\alpha = 7.5 \cdot 10^{-4}$ eV/K and $\beta = 295$ K [34]).

Figure 5.8(b) shows the change in the Mn^{2+} related photoluminescence emis-
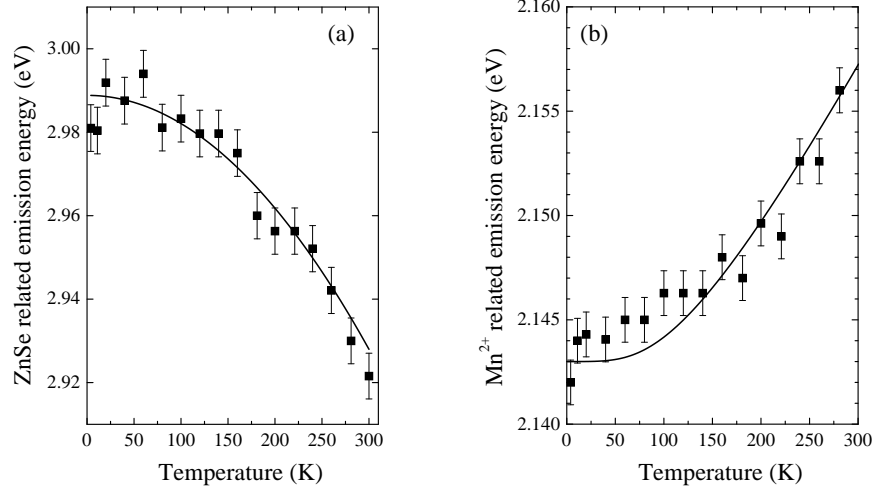
Figure 5.8: *Temperature dependence of the emission energy for a ZnSe: 0.7 % Mn^{2+} sample. (a) Maximum energy of the ZnSe related emission energy. The line through the data is a fi t of equation (5.2). (b) Temperature dependence of the Mn^{2+} related emission energy. The line through the data is a fi t of equation (5.3) with a phonon energy of $\hbar\omega = (27 \pm 2)$ meV.*

sion energy as a function of the temperature. Again, the emission energy was obtained from a Gaussian fit as discussed before. The shift of the Mn^{2+} emission energy to shorter wavelength for increasing temperature has also been observed for bulk ZnSe:Mn^{2+} [35]. The measured blue-shift can be fitted very well using the temperature dependence of the emission energy of the optical transition resulting from electron-phonon interaction as obtained by McCumber and Sturge, [36]

$$E(T) \;=\; E_0 \,+\, \mathcal{C}\,T^4 \int_0^{\frac{\hbar\omega}{k_{\mathrm{B}}T}} \mathrm{d}x\,\frac{x^3}{e^x-1}\;. \tag{5.3}$$

This is shown by the line through the data in figure 5.8(b). In equation (5.3) E_0 is the emission energy at 0 K, $\hbar\omega$ represents the energy of the lattice vibration that couples to the optical transition through the electron-phonon interaction and $\mathcal{C}$ is a (positive) fitting constant. The reason that this equation (strictly speaking
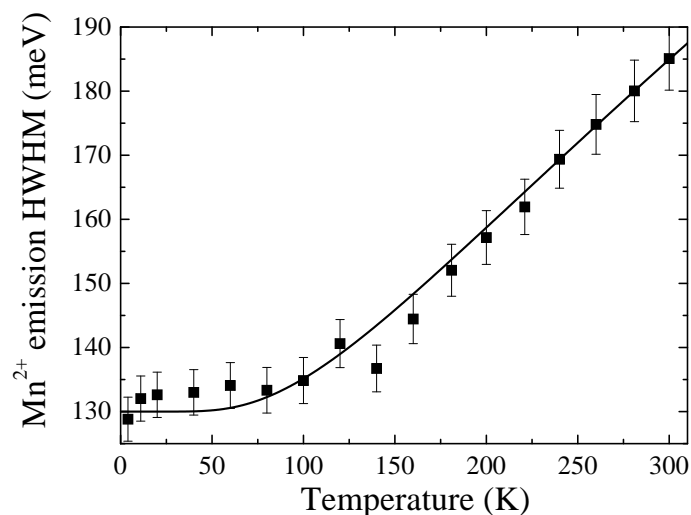
Figure 5.9: *Temperature dependence of the half-width at half maximum of the Mn²⁺ related emission for the ZnSe: 0.7 % Mn²⁺ sample. The line through the data is a fit using equation (5.4) with a phonon energy of ℏω = (27 ± 2) meV.*

only valid for the weak-coupling case) can be used in this case (involving strong coupling), has been discussed in detail in chapter 3. Figure 5.8(b) shows that a good fit of the data can be obtained using a phonon energy of $\hbar\omega = (27 \pm 2)$ meV in equation (5.3).

The data shown in figure 5.7 has also been used to determine the half-width at half maximum (HWHM) of the Mn²⁺ related emission band as a function of the sample temperature. This bandwidth was also determined from a Gaussian fit to the emission profile using the relative photon flux per constant energy interval as a function of energy. Due to the electron-phonon coupling this bandwidth changes with temperature, as can be seen from the data shown in figure 5.9. The emission bandwidth is an increasing function of the sample temperature and can in the strong coupling limit be written as [37]

$$\Gamma(T) \; = \; \Gamma_0 \, \sqrt{\coth\left(\frac{\hbar\omega}{2k_{\mathrm{B}}T}\right)} \; . \tag{5.4}$$

Here Γ_0 represents the bandwidth at zero temperature and $\hbar\omega$ is the energy of the lattice vibration that couples to the optical transition. The origin of this equation has also been discussed in detail in chapter 3. The fact that the data in figure 5.8(b) and the data in figure 5.9 could both be fitted using the same value for the phonon energy, $\hbar\omega = (27 \pm 2)$ meV, supports the validity of equations (5.3) and (5.4) in this case. This phonon energy agrees with the energy of a known optical phonon in bulk ZnSe [38]. Note that also here the thermal expansion of the lattice can explain the shift of the Mn^{2+} related emission, similar to what was discussed in chapter 3.

The temperature dependence of the ZnSe related bandwidth could not be obtained with an acceptable accuracy. This is due to the fact that the intensity of the ZnSe related emission is much lower than that of the Mn^{2+} related emission (remember that the intensity axis in figure 5.7 is logarithmic). As a result, a slightly different fitting interval gave equally good fits of this emission (similar χ^2 values), but with large differences in the bandwidth. This implies that the error was too large to allow for meaningful conclusions to be drawn from this data. Therefore this data is not presented here.

Finally, also the temperature dependence of the Mn^{2+} related photoluminescence lifetime was determined; figure 5.10 shows results for a ZnSe:0.4 % Mn^{2+} sample. In contrast to previous results for ZnS:Mn^{2+}, a temperature-induced decrease of the lifetime is observed. When this temperature-induced decrease of the Mn^{2+} lifetime is fitted on the basis of a simple thermally-activated non-radiative decay path competing with radiative recombination,

$$\frac{1}{\tau(T)} = \frac{1}{\tau_0} + \frac{1}{\tau_{\text{NR}}} \exp\left[-\frac{\Delta E}{k_{\text{B}}T}\right] , \qquad (5.5)$$

a good fit of the data can be obtained, as can be seen from the line through the data in figure 5.10.

The fit using equation (5.5) yields values for $\tau_0 = 303$ μs, $\tau_{\text{NR}} = 200$ μs and ΔE $= (26 \pm 2)$ meV. The value of ΔE is found to be independent of the Mn^{2+} concentration present in the ZnSe lattice. The decrease in lifetime can be explained by thermally-activated energy transfer to quenching centers since, in the same temperature regime in which the luminescence lifetime becomes shorter, the luminescence intensity decreases.
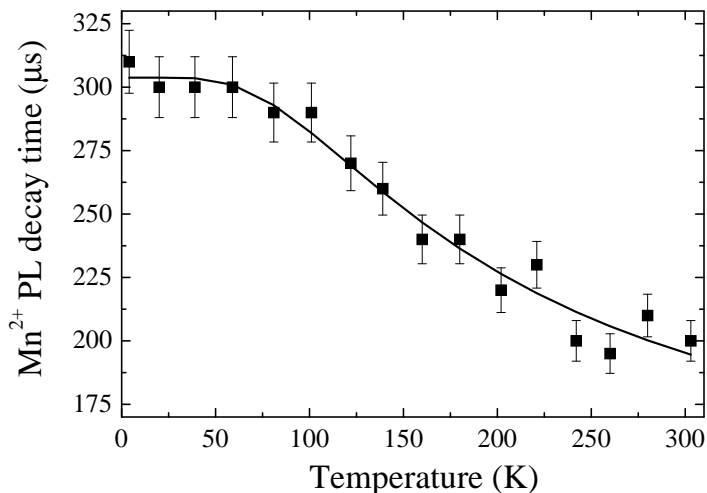
Figure 5.10: *Temperature-dependent lifetimes of the Mn^{2+} photoluminescence for a ZnSe:0.4 % Mn^{2+} sample. Pulsed excitation at 355 nm was used. The line is a fit to the data for the thermally-activated process described by equation (5.5) using an activation energy of $\Delta E = (26 \pm 2)$ meV.*

5.4 Conclusions

This chapter presents a chemical synthesis method for powders of ZnSe nanocrystals (average particle diameter in the range of $3-4$ nm) doped with Mn^{2+}. The photoluminescence emission spectra of these samples show a ZnSe related near band edge emission at ∼440 nm and a Mn^{2+} related band at ∼570 nm. The wavelength of the Mn^{2+} related emission shifts to lower energy for increasing amounts of Mn^{2+} incorporated into the ZnSe lattice. The photoluminescence excitation spectrum shows that the divalent manganese can be excited through the ZnSe host lattice. High-energy excitation spectra reveal that the ZnSe host lattice has four excitation bands below 10 eV. The Mn^{2+} luminescence decay curves yield a lifetime of ∼290 μs at room temperature, which decreases with increasing $[Mn^{2+}]$. The decrease in lifetime and emission energy of the Mn^{2+} related emission for increasing Mn^{2+} concentration may be due to the (preferential) formation of Mn^{2+} pairs in the nanocrystal. The temperature dependence of the Mn^{2+} lifetime can

be explained by a temperature-activated quenching with an activation energy of 26 meV. The ZnSe related luminescence wavelength has a temperature-induced shift similar to that of bulk ZnSe. The self-activated emission (expected at $\sim$640 nm), often observed in bulk ZnSe:Mn^{2+}, is not present in these nanocrystals.

References

[1] N. C. Greenham, X. Peng and A. P. Alivisatos, *Phys. Rev. B* **54**, 17628 (1996).

[2] B. O. Dabbousi, M. G. Bawendi, O. Onitsuka and M. F. Rubner, *Appl. Phys. Lett.* **66**, 1316 (1995).

[3] L. Brus, *J. Phys. Chem.* **90**, 2555 (1986).

[4] R. N. Bhargava, D. Gallagher, X. Hong and A. Nurmikko, *Phys. Rev. Lett.* **72**, 416 (1994).

[5] I. Yu, T. Isobe and M. Senna, *J. Phys. Chem. Solids* **57**, 373 (1996).

[6] A. van Dijken, E. A. Meulenkamp, D. Vanmaekelbergh and A. Meijerink, *J. Phys. Chem. B* **104**, 1715 (2000).

[7] J. Leeb, V. Gebhardt, G. Müller, D. Su, M. Giersig, G. McMahon and L. Spanhel, *J. Phys. Chem. B* **103**, 7839 (1999).

[8] J. Huang, Y. Yang, S. Xue, B. Yang, S. Liu and J. Shen, *Appl. Phys. Lett.* **70**, 2335 (1997).

[9] J. F. Suyver, R. Bakker, A. Meijerink and J. J. Kelly, *Phys. Stat. Sol. (b)* **224**, 307 (2001). See also chapter 4.

[10] G. H. Schoenmakers, E. P. A. M. Bakkers and J. J. Kelly, *J. Electrochem. Soc.* **144**, 2329 (1997).

[11] M. A. Hines and P. Guyot-Sionnest, *J. Phys. Chem. B* **108**, 3655 (1998).

[12] C. B. Murray, D. J. Norris and M. G. Bawendi, *J. Am. Chem. Soc.* **115**, 8706 (1993).

[13] R. Jerkins, W. F. McClune, T. M. Maguire, M. A. Holomany, M. E. Mrose, B. Post, S. Weissmann, H. F. McMurdie and L. Zwell, *Powder Diffraction File*, JCPDS International center for diffraction data (1985).

[14] H. Waldmann, C. Benecke, W. Busse, H.-E. Gumlich and A. Krost, *Semicond. Sci. Technol.* **4**, 71 (1989).

[15] D. F. Crabtree *Phys. Stat. Sol. (a)* **22**, 543 (1974).

[16] F. A. Kröger, *The chemistry of inperfect crystals*, North-Holland Publishing Company: Amsterdam (1973).

[17] G. Blasse and B. C. Grabmaier, *Luminescent Materials*, Springer-Verlag: Berlin, section 6.4 (1994).

[18] N. E. Rigby and J. W. Allen, *J. Lumin.* **42**, 143 (1988).

[19] C. R. Ronda and T. Amrein, *J. Lumin.* **69**, 245 (1996).

[20] D. T. F. Marple, *J. Appl. Phys.* **35**, 1879 (1964).

[21] M. Aven, D. T. F. Marple and B. Segall, *J. Appl. Phys.* **32**, 2261 (1961).

[22] S. Shionoya and W. M. Yen, *Phosphor Handbook*, CRC Press: Boca Raton, page 233 (1998).

[23] U. Stutenb¨aumer, H.-E. Gumlich and H. Zuber, *Phys. Stat. Sol. (b)* **156**, 561 (1989).

[24] U. Hahn, N. Schwenter and G. Zimmer, *Nucl. Instrum. Methods* **152**, 261 (1978).

[25] R. T. Wegh, H. Donker and A. Meijerink, *Phys. Rev. B* **56**, 13841 (1997).

[26] N. Murase, R. Jagannathan, Y. Kanematsu, M. Watanabe, A. Kurita, K. Hirata, T. Yazawa and T. Kushida, *J. Phys. Chem. B* **103**, 754 (1999).

[27] A. A. Bol and A. Meijerink, *Phys. Rev. B* **58**, 15997 (1998).

[28] T. C. Leslie and J. W. Allen, *Phys. Stat. Sol. A* **65**, 545 (1981).

[29] J. F. Suyver, R. Meester, J. J. Kelly and A. Meijerink. *Phys. Rev. B* **64**, 235408 (2001) and *Phys. Rev. B* **66**, 079901(E) (2002). See also chapter 8.

[30] S. J. Weston, M. O'Neill, J. E. Nicholls, J. Miao, W. E. Hagston and T. Stirner, *Phys. Rev. B* **58**, 7040 (1998).

[31] J. F. MacKay, W. M. Becker, J. Spałec and U. Debska, *Phys. Rev. B* **42**, 1743 (1990).

[32] S. G. Ayling and J. W. Allen, *J. Phys. C* **20**, 4251 (1987).

[33] Y. P. Varshni, *Physica* **34**, 149 (1967).

[34] L. Malikova, W. Krystek, F. H. Pollak, N. Dai, A. Cavus and M. C. Tamargo, *Phys. Rev. B* **54**, 1819 (1996).

[35] J. Xue, Y. Ye, F. Medina, L. Martinez, S. A. Lopez-Rivera and W. Giriat, *J. Lumin.* **78**, 173 (1998).

[36] D. E. McCumber and M. D. Sturge, *J. Appl. Phys.* **34**, 1682 (1963).

[37] B. Henderson and G. F. Imbusch, *Optical Spectroscopy of Inorganic Solids*, Clarendon Press: Oxford, chapter 5 (1989).

[38] P. J. Dean and J. L. Merz, *Phys. Rev.* **178**, 1310 (1969).

Chapter 6

Synthesis and luminescence of nanocrystalline ZnSe:Cu

A chemical synthesis is described in which ZnSe:Cu nanocrystals slowly grow to a final size that is dependent on the synthesis conditions. During particle growth, samples are extracted to study the luminescence as a function of particle size and temperature. The growth rate of the nanocrystals is strongly dependent on the synthesis temperature. For slowly growing crystals the transition from normal precursor-driven growth to Ostwald ripening could be identified. Quantum size effects are observed to influence both the ZnSe and the Cu related luminescence emissions. Temperature-dependent measurements of the luminescence intensity, lifetime and peak positions are reported and discussed.

6.1   Introduction

Nanocrystalline semiconductors showing quantum size effects are widely studied [1–6]. The change in electronic structure as a function of the particle size for the same chemical composition is of fundamental interest and may also become important for various applications (such as for low voltage electroluminescent devices [7, 8]).

Almost ten years ago research started on semiconductor nanocrystals in which luminescent dopant ions are incorporated. For dopant ions like Mn^{2+} and Pb^{2+} the characteristic emission of the luminescent ion is observed [4, 5, 9]. As the particle size decreases, the wavelength for excitation of the dopant emission (over the bandgap) shifts to higher energies while the emission color is unaffected. The insensitivity of the dopant emission energy to the particle size is due to the fact that an electronic transition occurring on Mn^{2+} or Pb^{2+} involves electronic wave functions localized on the dopant cation and the neighboring ligand anions. The localized wave functions are not influenced by quantum size effects. However, for other dopant ions emission of light may involve recombination of a delocalized charge carrier and the dopant. The emission from Cu^{2+} centers in ZnS and ZnSe is assigned to recombination of a delocalized electron (in the conduction band or shallow trap) with Cu^{2+} [10].

Measurements on bulk ZnSe crystals doped with copper have revealed the presence of green and red emission bands, which have been assigned to recombination of electrons in shallow traps with different Cu^{2+} centers [10–12]. The Cu^{2+} related emission wavelength in nanocrystalline ZnS or ZnSe semiconductor particles is expected to shift to higher energies in smaller particles. In some recent studies on ZnS:Cu this has indeed been observed [9, 13]. In this chapter the synthesis, growth and luminescence of nanocrystalline ZnSe:Cu is reported. In the synthesis procedure used, the ZnSe particles grow slowly and the luminescence properties of the ZnSe:Cu were studied as a function of particle size with samples taken at different times during the reaction. From the change in particle size as a function of time, different growth-regimes can be identified. In addition, temperature-dependent luminescence measurements are discussed. Based on the data, a model describing the luminescence mechanism is proposed.

6.2 Growth of the nanocrystals

The growth of ZnSe:Cu nanocrystals was investigated by studying the dependence of the luminescence of the nanocrystals on the synthesis time. In this way, different growth mechanisms responsible for the increasing crystal size were found in the course of the synthesis.

6.2.1 Experimental

The synthesis route that was used to prepare the ZnSe:Cu nanocrystals is similar to the well-known TOP/TOPO synthesis used for CdSe nanocrystals [14]. Hexadecylamine (HDA) was used instead of TOPO for reasons that were described in chapter 5 in some detail [15, 16]. The reactions were performed inside a glovebox in an inert dry-argon atmosphere. Chemical tests using diethylzinc and titanium tetrachloride indicated that the atmosphere contained less than 5 ppm of oxygen and less than 5 ppm of water.

A 35 g sample of hexadecylamine was heated to $\sim$150 °C under vacuum ($<10^{-4}$ bar) for several hours to remove residual water and other contaminants that were present in the sample as received from the supplier (Aldrich). The HDA was transferred to the glovebox and heated to 270 °C. In this synthesis, the HDA is used both as the solvent and as the surfactant. The copper precursor was a solution of $Cu(CH_3COO)_2$ in tri-*n*-octylphosphine (TOP). For the experiments presented in this section, $\sim$0.8 mg of $Cu(CH_3COO)_2$ was dissolved in 12 ml of TOP. To this solution, 3 ml of a previously prepared solution of 1 M TOPSe was added. After stirring, 0.32 g of diethylzinc was added. The resulting solution was shaken and then injected into the hot HDA. The nanocrystals were grown at a constant temperature of 260 °C. The synthesis was performed at this (rather low) temperature because the slower kinetics allow a more detailed investigation of the growth mechanism. At different times after the injection a $\sim$0.5 ml sample of the liquid was taken. This sample was quickly poured into 5 ml of anhydrous toluene, resulting in a stable colloidal suspension. The luminescence measurements presented in this section were performed on these suspensions, immediately after the samples were removed from the glovebox.

The particle radius was determined using the peak broadening in the X-ray powder diffractograms, as described in section 2.3.1. Photoluminescence emission and excitation spectra were recorded with a SPEX Fluorolog spectrofluorometer. All spectra were corrected for the spectral response of the emission monochromator and the photomultiplier tube. The excitation spectra were also corrected for
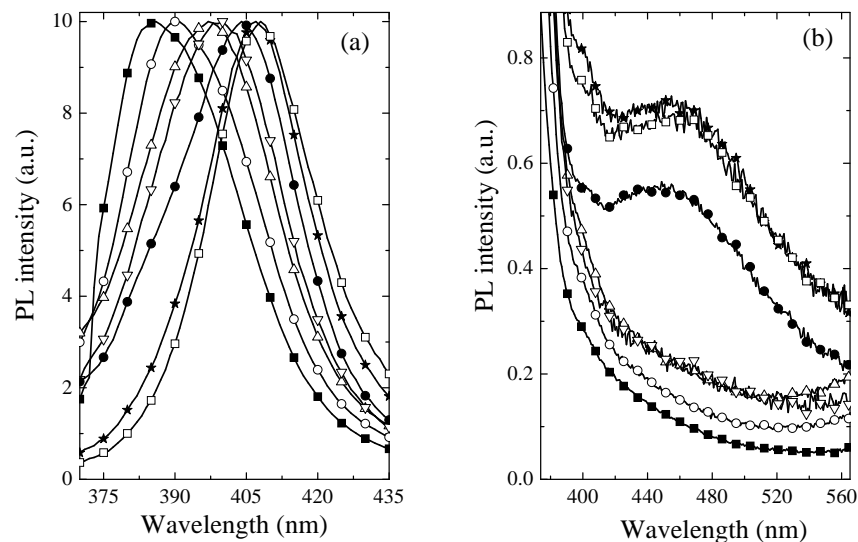
Figure 6.1: *Evolution of (a) the ZnSe related and (b) the Cu^{2+} related photoluminescence spectra of ZnSe:Cu nanocrystal suspensions in toluene for different synthesis times: 45 minutes (■), 1 hour and 40 minutes (○), 3 hours and 9 minutes (△), 5 hours and 13 minutes (▽), 22 hours (●), 73 hours (★) and 112 hours (□). The spectra were measured at 300 K for excitation at 330 nm. All spectra were normalized on the ZnSe emission maximum.*

the spectral distribution of the excitation source (xenon lamp) and the excitation monochromator. Photoluminescence lifetimes were measured using the YAG:Nd laser set-up, described in detail in the experimental section of chapter 5.

6.2.2   Results and discussion

Figure 6.1 shows the photoluminescence emission spectra for several samples of nanocrystalline ZnSe:Cu in toluene taken at different times during the synthesis. The emission spectra were all normalized on the ZnSe emission maximum. The photoluminescence spectrum shows two distinct emission bands. The first band is located at approximately 400 nm, as can be seen in figure 6.1(a); this band cor-

responds to the exciton emission of the ZnSe host lattice. The precise emission energy is found to be strongly dependent on the synthesis time. The second emission band is located at roughly 460 nm and is shown in figure 6.1(b). This peak is assigned to a copper-related dopant emission. The luminescence mechanism will be discussed in section 6.3.4.

Two important observations can be made on the basis of figure 6.1. Firstly, for increasing synthesis time, there is a clear shift of the ZnSe related emission maximum to longer wavelengths. This can be explained directly by the growth of the nanocrystals: an increase in the crystal size results in a decrease of the ZnSe bandgap, as shown in equation (1.7), and causes a red-shift of the ZnSe related exciton emission. This will be used to discuss the growth mechanism for these nanocrystals later in this section. Secondly, when a very low Cu precursor concentration is used, as was the case for the synthesis shown in figure 6.1(b), a long synthesis time is required to observe a significant Cu^{2+} related photoluminescence. The Cu ions are incorporated only very slowly into the ZnSe host-lattice. The copper precursor concentration used in this synthesis was 0.17 % with respect to the zinc precursor concentration. As a result, only 0.4 (smallest crystals) to 1 (largest crystals) Cu ion is expected per nanocrystal, assuming that all copper ions are incorporated and that there is a random distribution of the ions. In section 6.3.2 evidence will be presented to show that an increased Cu precursor concentration results in a faster incorporation of the Cu ions into the ZnSe lattice and an enhanced Cu^{2+} related emission intensity.

The position of the ZnSe related emission band, $E(t)$, and the half width at half maximum of this emission band, $\Delta E(t)$, have been determined from the data shown in figure 6.1(a) for different synthesis times t. The values were determined by fitting a Gaussian function through the emission spectrum plotted as relative emitted photon flux per constant energy interval [17]. In the remainder of this section, the synthesis time (t) is defined to be in minutes. Figure 6.2(a) shows the time evolution of the ZnSe related emission energy and figure 6.2(b) shows the time evolution of the half width at half maximum of this emission. It is clear from these figures that both the energy of the emission maximum and the width of the emission band for the ZnSe related emission shifts to lower values for increasing synthesis time.

Based on the known material parameters $m_e^{\star} = 0.17m_0$ [18], $m_h^{\star} = 0.60m_0$ [19], $\epsilon_r = 8.1$ [20] and $E_g = 2.8$ eV [20], together with the Brus equation [3], the particle diameter d in nanometers can be calculated from the bandgap energy E_g in electron
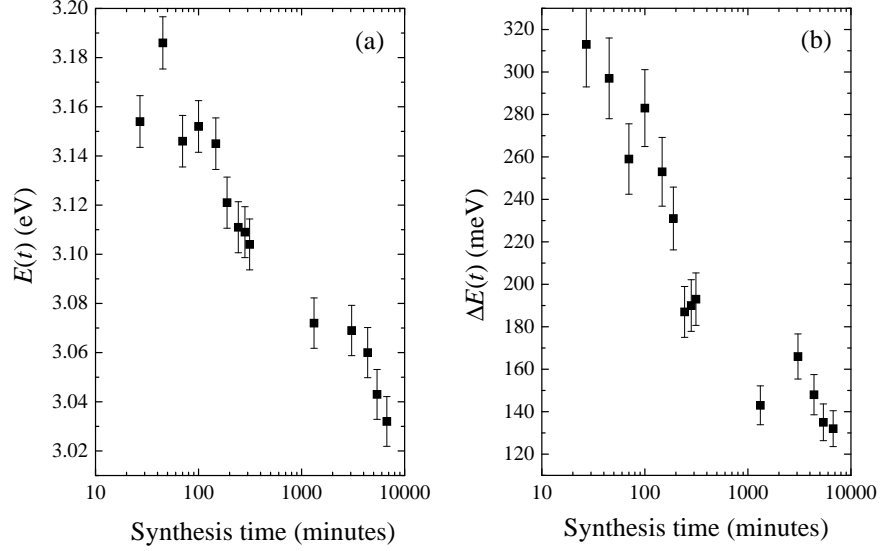
Figure 6.2: *Time evolution of (a) the ZnSe related emission energy and (b) the ZnSe related half width at half maximum for the ZnSe:Cu nanocrystalline suspensions in toluene. The spectra were measured at 300 K and the excitation wavelength was 330 nm. Note the logarithmic time-axis for both plots.*

volts as,

$$d(E_g) = \frac{0.32 - 3.37\sqrt{E_g - 2.79}}{2.8 - E_g} \ .$$
(6.1)

Using equation (6.1), the data in figure 6.2(a) was converted into the nanocrystal diameter as a function of the synthesis time. This data is shown in figure 6.3.

Figure 6.3(a) shows the (average) size of the nanocrystals as a function of the synthesis time. It is clear from this figure that even after 7500 minutes (more than 5 days) the nanocrystals continue to increase in size. However, the nanocrystals show only a moderate increase in size, especially after the initial growth at relatively short times. Furthermore, it is clear from this figure that two different growth-ranges exist: a (relatively) fast growth for synthesis times shorter than ∼1000 minutes, followed by a slower, but persistent, growth for longer synthesis
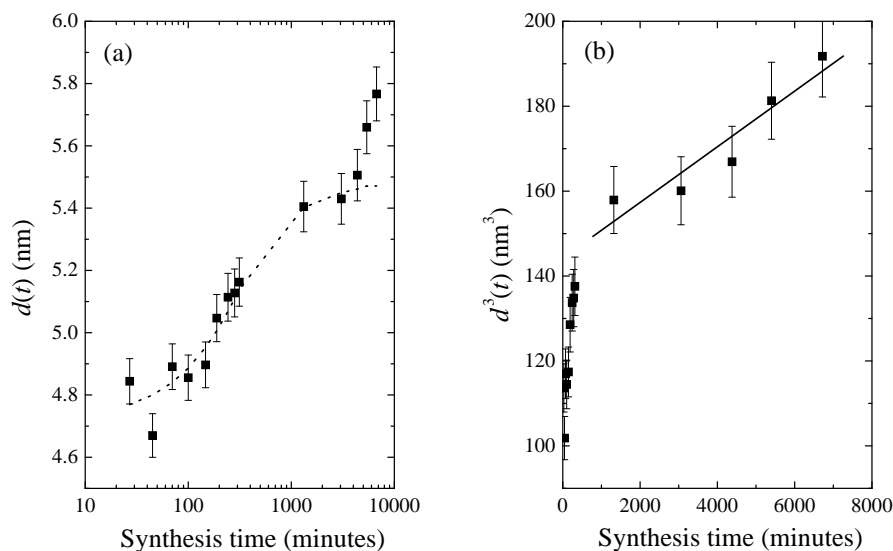
Figure 6.3: *(a) Time evolution of the size of the nanocrystals as calculated from the ZnSe emission energy using equation (6.1). Note the logarithmic time-axis. (b) The same data plotted as the cube of the crystal size on a linear time-axis. The lines through the data are discussed in the text.*

times. This trend can also be clearly seen in figure 6.3(b), which shows the cube of the crystal diameter on a linear time-scale.

During the synthesis, the concentration of reactants decreases. As a result, it is expected that the rate of the synthesis will also decrease. This means that the growth of the nanocrystals slows down as well, which agrees with the data presented in figure 6.3(a). It is difficult to accurately explain this data because of the relatively large error and the fact that the experiment was performed only once. Therefore, the explanation presented here does not exclude other possible growth-mechanisms and further experiments need to be done to establish the growth-mechanism more firmly.

After the injection of the precursors, the rapid nucleation of the nanocrystals will quickly result in nanocrystals of a diameter d_0. On a longer time-scale, the growth of the nanocrystals begins, which is shown in figure 6.3. Here it is assumed

that this growth is concentration-driven, rather than diffusion-limited [21], and proceeds by a first order reaction. As the initial concentration of the zinc precursor is similar to the initial concentration of the selenium precursor (2.6 mM and 3 mM, respectively), is it reasonable to assume a a simple, first-order reaction. In this case, the concentration $[C]$ of reactant decreases as a function of time as [22]

$$[C] = [C_0] e^{-kt} , \tag{6.2}$$

where $[C_0]$ represents the initial concentration of the reactant, k is the reaction constant and t is the reaction time. As the increase in the volume of the nanocrystals, $\mathrm{d}V/\mathrm{d}t$, is determined by the concentration of available reactants, it will be proportional to $\mathrm{d}[C]/\mathrm{d}t$. When the growth of the nanocrystals is reasonably limited, one can assume that the surface area of the nanocrystals does not increase significantly. In this case, the rate of growth of the radius of the nanocrystals, $\mathrm{d}r/\mathrm{d}t$, will be roughly proportional to $\mathrm{d}[C]/\mathrm{d}t$ and then the diameter d of the nanocrystals at time t can be found by integration of the growth-rate. The result is

$$d(t) = d_0 + \xi \left(1 - e^{-kt}\right) . \tag{6.3}$$

Here ξ is a constant determined by the material parameters and d_0 describes the 'initial' size of the nanocrystals (resulting from the rapid nucleation at the time of the injection of the precursors).

Equation (6.3) is strictly speaking only valid when one assumes that the surface area of the nanocrystals does not increase significantly because a change in the surface area also changes the concentration of reactants required to add one monolayer to the nanocrystal. As a result, for a bigger crystal the decrease in the precursor concentration required to add one layer to the nanocrystal must be larger than for a small crystal. This effect is ignored because the nanocrystals only grow by a moderate amount.

The dashed line through the data in figure 6.3(a) is a fit using equation (6.3). Shortly after the injection of the precursors, the average nanocrystal radius is already $\sim$2.3 nm. After this fast nucleation of the nanocrystals, the subsequent growth is rather slow. Clearly, the data can be described reasonably well by this fit for synthesis times less than roughly 2000 minutes. The fact that the fit seems to be quite good is in agreement with the assumption that the mechanism responsible for the growth of the nanocrystals for the first growth stage is concentration-driven, rather than diffusion-limited or some other process. However, further experiments will be required to confirm this growth mechanism and rule out other growth-mechanisms possible.

For longer synthesis times, equation (6.3) predicts a negligible growth of the nanocrystals, while a significant growth is still observed. In this long time range, Ostwald ripening is expected to be responsible for the growth of the nanocrystals, as the reagents have been depleted and there are no chemicals available for the synthesis. Figure 6.3(b) shows the cube of the average crystal diameter as a function of time on a linear time-axis. From the literature it is known that a plot of d^3 as a function of time should show a straight line for pure Ostwald ripening of the nanocrystals [23, 24]. Indeed, the data for a long synthesis time can be fitted quite well by the straight line in figure 6.3(b), suggesting that this growth is due to Ostwald ripening.

Finally, a reasonable estimate of the polydispersity of the nanocrystal ensemble can be made by computing

$$\Delta d(t) \;=\; \frac{d(E(t) - \Delta E(t)) - d(E(t) + \Delta E(t))}{2} \;,\qquad (6.4)$$

which can be regarded as an approximation of the half width at half maximum of the nanocrystal size distribution.

Figure 6.4 shows the estimate of the polydispersity of the nanocrystal ensemble determined from equation (6.4). As can be seen from the data, the polydispersity decreases for increasing synthesis times, which is especially clear for the synthesis times shorter than 1000 minutes. As diffusion-limited growth of the nanocrystals would result in a decrease of the polydispersity for increasing crystal size (i.e. synthesis time) [21], this result suggests that the reaction may be diffusion-limited to some extent.

6.3 Analysis of the luminescence

In this section the luminescence and the luminescence mechanism of nanocrystals of ZnSe doped with Cu is considered in detail. The temperature dependence of the photoluminescence and luminescence lifetimes are determined and an estimate of the temperature-induced shift of the conduction band edge is made. Furthermore, a model is presented that describes the luminescence processes.

6.3.1 Modified synthesis

The synthesis route that was used to prepare the ZnSe:Cu nanocrystals for this part is almost identical to that discussed in the first part of this chapter. The only dif-
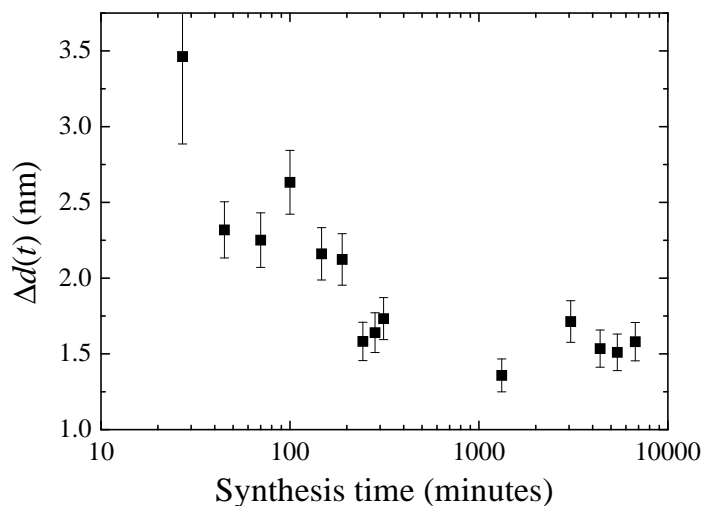
Figure 6.4: *Time dependence of the polydispersity of the nanocrystal ensemble as determined from equation (6.4). Note the logarithmic time-axis.*

ferences are the precursor concentrations, the synthesis temperature and the precipitation of the nanocrystals. As a result of the significantly higher synthesis temperature, the reaction is much quicker and the growth of the nanocrystals is faster. Furthermore, due to the higher Cu precursor concentration, more copper is expected to be incorporated into the nanocrystals.

The reactions were performed in the dry-argon atmosphere of a glove-box. A sample of 45 ml of HDA was heated to 290 °C. A solution of 4.8 mg $Cu(CH_3COO)_2$ in 12 ml TOP was prepared and to this solution 3 ml of a 1 M solution of TOPSe was added. After stirring, 0.32 g of diethylzinc was added. The resulting solution was shaken and then added to the hot HDA. The nanocrystals were grown at a constant temperature of 290 °C. A ∼1 ml (liquid) sample was taken at different times after the injection. The nanocrystals in each of the samples were precipitated by adding 5 ml of anhydrous 1-butanol. The precipitate was redissolved in 1-octanol for measurements on a suspension of nanocrystals, or washed with methanol and dried in a vacuum desiccator for powder measurements. The powders had a slightly grey color.
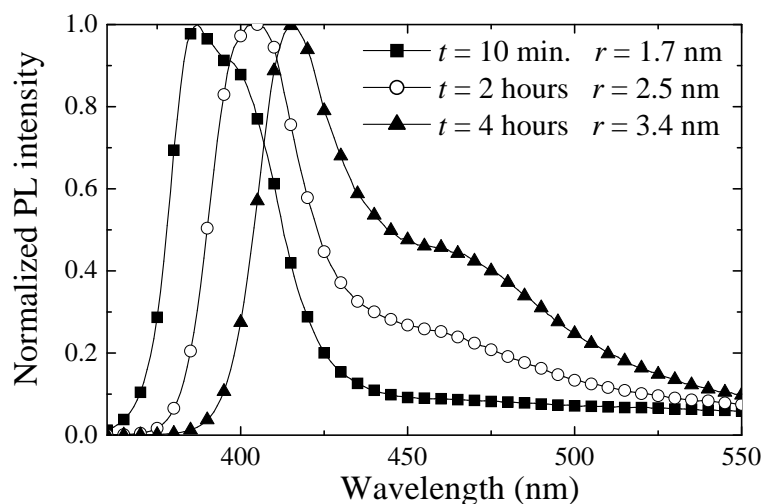
Figure 6.5: *Normalized luminescence spectra of ZnSe:Cu suspensions in octanol for different synthesis times. The spectra were measured at 300 K for an excitation wavelength of 330 nm.*

6.3.2   Results and discussion

Figure 6.5 shows photoluminescence spectra of ZnSe:Cu nanocrystals of different sizes. The near band edge emission shifts from 380 nm to 430 nm as the particles grow from a radius of about 1.7 nm to 3.4 nm. The sizes indicated in figure 6.5 were determined from the peak broadening in the powder X-ray diffractograms. A comparison with the data shown in figure 6.1 or figure 6.3(a) shows that the higher synthesis temperature results in a significantly enhanced growth rate of the nanocrystals, but that the initial size of the nanocrystals (due to the nucleation) is smaller. The higher growth-rate can be expected, because the rate of the chemical reaction increases exponentially with temperature (Arrhenius behavior) [22]. Furthermore, the final size of the nanocrystals in this experiment is larger than that found in the previous section. This is also expected due to the higher growth-rate at higher temperature.

For the larger particles, the longer wavelength emission band (assigned to the Cu^{2+} dopant as before) becomes visible between 400 and 500 nm. This emis-
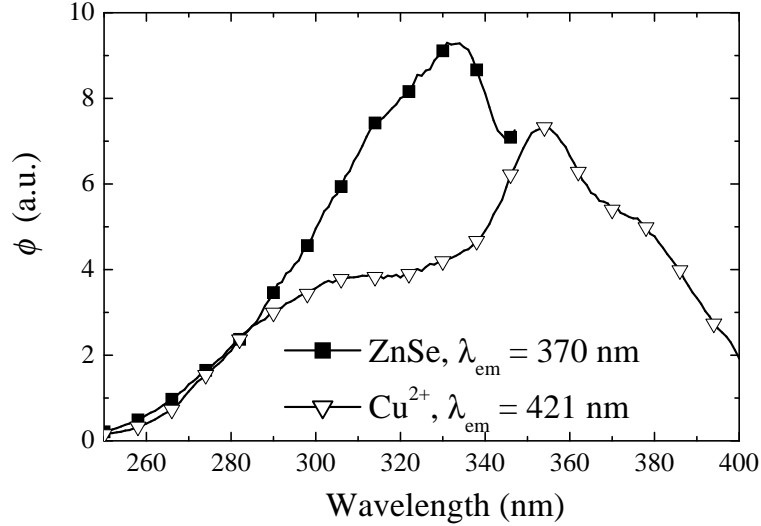
Figure 6.6: *Excitation spectra of a ZnSe:Cu sample with a radius of 1.7 nm in octanol. Measured at 4 K for the emission wavelengths indicated in the fi gure. Relative intensities of the two spectra can not be compared.*

sion band also shifts to longer wavelengths as the particle size increases. Because for this synthesis the crystal size is increasing quite rapidly, the shift of the Cu^{2+} related emission to longer wavelengths is much more pronounced than in figure 6.1(b). Due to the strong overlap of the ZnSe and Cu^{2+} related emission bands, it is difficult to determine accurately the position of the maximum of the Cu^{2+} emission band. The relative increase of the Cu^{2+} photoluminescence suggests that the Cu concentration in the ZnSe nanocrystals grows with synthesis time. This agrees with the data shown in figure 6.1(b). As a result of the much higher copper precursor concentration used in this synthesis (1.1 % compared to 0.17 % in section 6.2), the relative contribution of the Cu^{2+} related photoluminescence to the total luminescence is also much higher.

In figure 6.6 the excitation spectra of the low-temperature luminescence of ZnSe:Cu particles with a radius of 1.7 nm is shown. Here, ϕ denotes the photon flux per constant wavelength interval. The ZnSe related emission is at 370 nm, while the Cu^{2+} emission has a maximum at 421 nm at 4 K. The excitation spec-

trum shows that the 370 nm emission can be excited over the bandgap. For bulk ZnSe the maximum of the bandgap excitation band is at ∼440 nm at 4 K. Due to quantum confinement effects in the nanocrystals, the bandgap excitation maximum has shifted to 325 nm. Using the version of equation (6.1) that is valid at 4 K (because the bandgap of a semiconductor is dependent on the temperature it will be slightly different) the particle radius is calculated to be 1.75 nm. This agrees well with the ∼1.7 nm radius obtained from the X-ray diffraction measurements.

The excitation spectrum shows that the Cu^{2+} photoluminescence (measured at 421 nm) can also be excited via the bandgap of the ZnSe host lattice. Furthermore, an additional excitation band is observed at 355 nm. A similar sub-bandgap excitation band is also observed in the excitation spectra of the Cu^{2+} emission in bulk ZnSe:Cu crystals and this band has been assigned to the direct excitation of the Cu^{2+} dopant [10, 11]. The energy difference between the maxima of the bandgap and the Cu^{2+} excitation bands in the different excitation spectra is between 0.3 and 0.4 eV. The same energy difference is observed between the emission maxima of the near band edge and the Cu^{2+} emission bands. This energy difference indicates that the Cu^{2+} level is located in the bandgap about $0.3 - 0.4$ eV above the top of the valence band. This has also been reported previously for the green Cu^{2+} emission in bulk ZnSe [10]. This shows that the Cu^{2+} emission in the ZnSe:Cu nanocrystals is analogous to the well-known green emission from bulk ZnSe:Cu. Due to the quantum confinement the conduction band edge shifts to higher energies and therefore the green emission shifts to shorter wavelengths as the particle size decreases.

6.3.3   Temperature dependence and luminescence lifetime

In figure 6.7 the emission spectra of a powder consisting of ZnSe:Cu nanocrystals with a radius of 3.4 nm are shown as a function of temperature. At 4 K the Cu^{2+} related emission is the dominant spectral feature. The mechanism involved in the temperature dependence of the emission intensities will be discussed below. Both the Cu^{2+} and the ZnSe related emission bands shift to shorter wavelengths as the temperature is decreased. In figure 6.8 the position of the emission maximum is plotted as a function of temperature for both emission bands. In chapter 5, dealing with the luminescence of 3.5 nm diameter ZnSe:Mn^{2+} nanocrystals, it was shown that the shift of the ZnSe related emission can be described by the Varshni equation [25] which has been derived to describe the temperature dependence of the
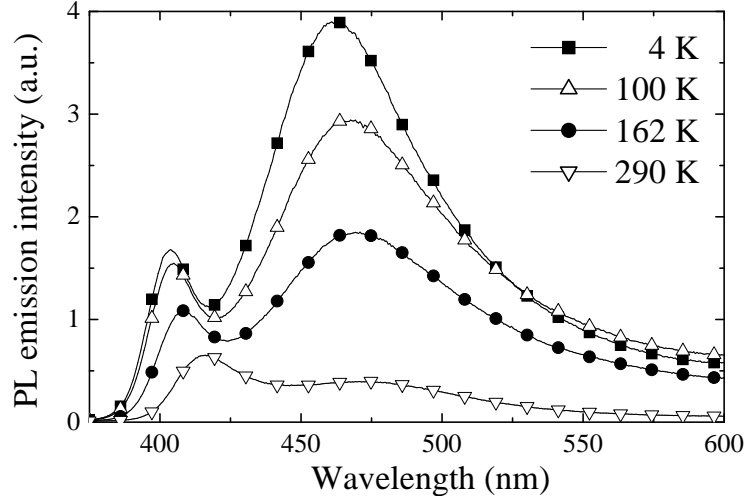
Figure 6.7: *Temperature-dependent photoluminescence spectra of a powder sample of ZnSe:Cu nanocrystals with a radius of 3.4 nm. Excitation was at 330 nm. The relative intensities can be compared.*

bandgap of bulk semiconductors. This expression states that

$$E_g(T) \;=\; E_0 \,-\, \frac{\alpha T^2}{T + \beta} \;, \tag{6.5}$$

where E_0 represents the bandgap at 0 K and α and β are fitting parameters. It is known from the literature that β is of the order of the Debye temperature of the semiconductor. This equation takes into account both the temperature-induced change in the lattice parameter and the temperature dependence of the electron-lattice interaction.

Figure 6.8 shows the temperature-dependence of the emission energy of the ZnSe and the Cu^{2+} related photoluminescence signals. The nanocrystals have a radius of 3.4 nm and the measurements were performed on a powder sample. The reported emission energies were found by fitting a Gaussian lineshape through the data using the relative emitted photon flux per constant energy interval as a function of energy. Similar results were also found for the smaller particles. For temperatures above 150 K (when the Cu^{2+} related photoluminescence is quenched), the
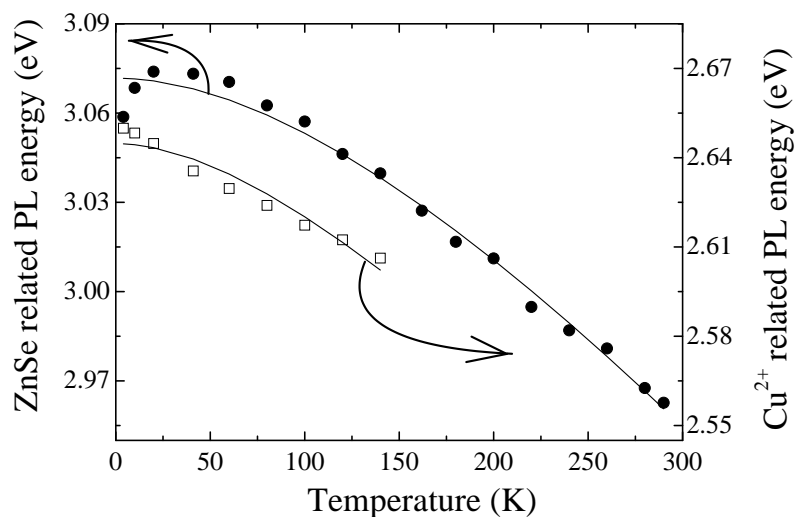
Figure 6.8: *Temperature dependence of the ZnSe (•) and Cu^{2+} (□) related photolumines-cence emission energies for a powder sample of ZnSe:Cu nanocrystals with a radius of 3.4 nm. The lines through the data are fits using the Varshni equa-tion (6.5).*

determination of the Cu^{2+} peak position becomes increasingly difficult. Because of the large uncertainties, these data are not shown in figure 6.8 and will be omitted in the further discussion. The lines through the data are fits using the Varshni equa-tion as shown in equation (6.5). The values of the parameters that were obtained from these fits are shown in table 6.1.

The change in the ZnSe related emission energy (i.e. the bandgap energy) be-tween 4 K and 300 K is about 0.12 eV, as is seen from the filled circles in figure 6.8. The small shift of the ZnSe emission to higher energy between 4 K and 50 K will be discussed in section 6.3.4. From an extrapolation of the Varshni fit the shift of the Cu^{2+} related emission (i.e. the conduction band) is calculated to be 0.09 eV between 4 K and 300 K. This means that the shift of the bandgap is dominated by the shift of the conduction band and that the shift of the valence band seems to be relatively small.

Due to the rather large error in the fit parameters (as shown in table 6.1), it is difficult to draw quantitative conclusions from these results. Furthermore, the

Table 6.1: *Values for α and β as were obtained by fitting equation (6.5) to the ZnSe and Cu^{2+} related luminescence data shown in figure 6.8. The literature values for bulk ZnSe are included for comparison.*

	ZnSe	Cu^{2+}	Literature [26]
α [10^{-4} eV K^{-1}]	8.8 ± 0.3	5.8 ± 0.7	7.5
β [10^2 K]	2.8 ± 0.5	2.6 ± 1.5	2.95

expected shift of the conduction band and valence band edges as a function of the temperature has been theoretically or numerically calculated for many cases and no consensus about the expected trends has been reached. Fan claims that the shift should be proportional to $(m^\star)^{-3/2}$ for nonpolar crystals and to $\sqrt{m^\star}$ for polar crystals, while the intermediate case (which would be expected for ZnSe) is not treated [27]. On the other hand, Gopalan *et al.* show calculations in which the shift is almost independent of the effective mass for the (somewhat polar) semiconductor GaAs [28]. Finally, Shen *et al.* have recently shown experimental data for PbSrSe indicating that the shift can be linear in the effective mass [29]. Seiwert proved that, for single crystal CdS, the temperature dependence of the lattice parameter must be responsible for less than 15 % of the experimentally observed shift in the bandgap energy [30]. This means that the majority of the shift must be due to the electron-phonon interaction. Now one interesting observation about the data shown in figure 6.8 can be made as the temperature-induced shift of the conduction band is (much) larger than that of the valence band. This indicates that the electron-phonon interaction in the conduction band is stronger than the electron-phonon interaction in the valence band for these ZnSe:Cu nanocrystals. A stronger electron-phonon coupling for the charge carrier with the smaller effective mass is expected (note that for ZnSe $m_e^\star = 0.17m_0$ and $m_h^\star = 0.60m_0$) since the wave function of that charge carrier will be more delocalized allowing for more wave function overlap with a phonon.

Figure 6.9 shows the time dependence of the Cu^{2+} related photoluminescence signal for a powder of 3.4 nm radius ZnSe:Cu nanocrystals after a $\sim$10 ns excitation pulse. The inset shows the same data on a logarithmic intensity axis. The thick line in the inset is a single-exponential fit to the data with a lifetime of $\tau = 0.97$ μs, which fits the data reasonably well. However, the decay is not single-exponential and a longer lifetime component can be identified in the tail of the plot. The thin line through the data in both plots is a double-exponential fit with a fast lifetime of
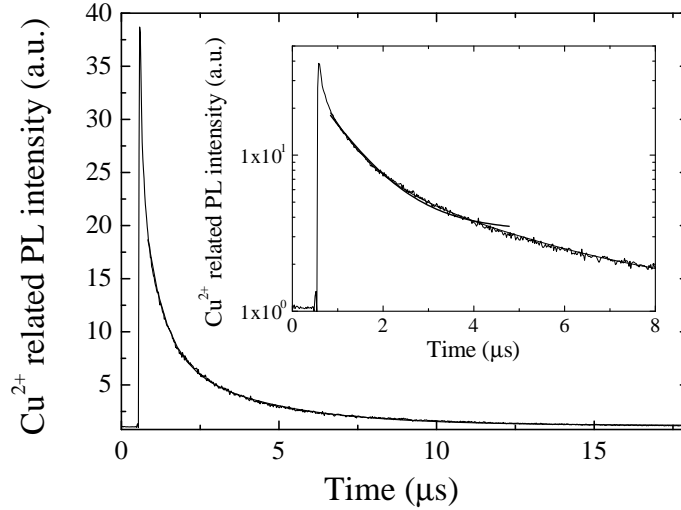
Figure 6.9: *Time dependence of the Cu^{2+} related photoluminescence signal for a powder sample of ZnSe:Cu nanocrystals with a radius of 3.4 nm. The line through the data is a double-exponential fit. Pulsed excitation was at 355 nm and the measurement was performed at 4 K. Inset: The same data using a logarithmic intensity axis. The thick line is a single-exponential fit and the thin line is the double-exponential fit.*

$\tau_f = 0.97$ μs and a slow lifetime of $\tau_s = 3.1$ μs. The contribution of the fast lifetime to the total luminescence signal was about 90 % at 4 K,

$$\int \mathrm{d}t\, I_{\mathrm{PL}}(\tau_f) \;\approx\; 9 \cdot \int \mathrm{d}t\, I_{\mathrm{PL}}(\tau_s) \;. \tag{6.6}$$

At higher temperatures the lifetime decreases, as will be shown below. Furthermore, the contribution of the fast lifetime to the total time-trace decreases as well, down to about 75 % at room temperature.

The temperature dependence of the lifetime of the Cu^{2+} related photoluminescence is shown in figure 6.10 together with the temperature dependence of the integrated photoluminescence for this emission. At low temperatures the Cu^{2+} emission is strong and from the single exponential decay curve of the emission intensity a luminescence lifetime of 0.97 μs is derived. There is no data available
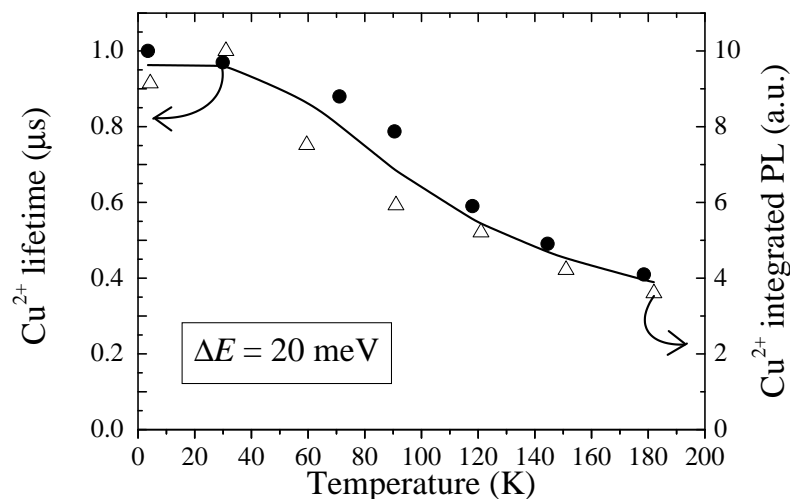
Figure 6.10: *Temperature dependence of the Cu^{2+} lifetime (●) and integrated photolumi-
nescence (△) for a powder sample of ZnSe:Cu nanocrystals with a radius of
3.4 nm. The line through the data is a fi t using equation (6.7). Excitation was
at 330 nm.*

on the lifetime of the green Cu^{2+} emission in bulk ZnSe:Cu for comparison. The
near band edge emission (at 400 nm) has a single exponential decay with a 3.6 ns
lifetime at 4 K, as was shown in the previous chapter.

As the temperature is increased above 50 K the Cu^{2+} emission intensity starts
to decrease. The quenching temperature, defined as that at which the integrated
emission intensity has dropped to 50 % of the value at 4K, is about 130 K. This
value is very similar to the quenching temperature of 140 K reported for the green
Cu^{2+} emission in bulk ZnSe:Cu [12], providing further support for the assign-
ment of the blue/green emission presented above. The luminescence lifetime of
the emission decreases at the same rate as the emission intensity. This behavior is
expected if the luminescence quenching is induced by a thermally activated non-
radiative decay channel, which depopulates the excited state from which emission
occurs. The quenching mechanism may be thermally activated depopulation of
trapped electrons from shallow electron traps close to the Cu^{2+} dopant, competing
with radiative recombination with Cu^{2+}. For such a thermally activated process,

an Arrhenius dependence of the emission intensity and the emission lifetime on the sample temperature is expected,

$$\mathcal{A}(T) \;=\; \frac{\mathcal{A}_0}{1 + \mathcal{C} \exp\left(-\frac{\Delta E}{k_{\mathrm{B}} T}\right)} \;,\qquad (6.7)$$

where $\mathcal{A}_0$ represents the value (of either the lifetime or the emission intensity) at 0 K and $\mathcal{C}$ is a fitting parameter.

Equation (6.7) fits the data rather well, as can be seen from the line through the data. Using both sets of data shown in figure 6.10, a value for the activation energy of $\Delta E = 20$ meV was found. This value does not agree with the position of the copper state in the ZnSe bandgap, as discussed before (about 0.3 eV above the top of the valence band). Therefore, it seems unlikely that this activation energy is due to hole detrapping from the copper ion. As a result, it is concluded that this activation energy is related to electron detrapping as will be shown in the next section.

From the data presented in figure 6.7 it is concluded that at 300 K the Cu^{2+} emission is quenched to 10 % of the intensity at 4 K. The quenching of the luminescence is a drawback for a potential application of ZnSe:Cu in (electroluminescent) devices. The quantum efficiency of the total emission was determined for a powder of ZnSe:Cu nanocrystals by comparing the light output with that of a commercial phosphor under identical measuring conditions. The details of this procedure were discussed in section 5.3.2. At room temperature a luminescence quantum efficiency between 2 and 4 % was found. The relatively low quantum efficiency is largely due to the thermal quenching of the Cu^{2+} emission, which is the dominant spectral feature at 4 K.

From the ratio of the integrals of the photoluminescence at room temperature and at 4 K the quantum efficiency at 4 K is estimated to be 30 %. Similar high quantum efficiencies for undoped nanocrystalline semiconductor particles have been obtained for CdSe synthesized with a similar method. If the quenching temperature for the Cu^{2+} emission can be increased, the material is promising for application in electroluminescent devices. This could possibly be achieved if one is successful in introducing a deeper electron trap in the ZnSe lattice, such as Cl^- on Se^{2-} sites. Further investigation of this, as well as the introduction of other electron traps might yield a material efficiently luminescing at room temperature.
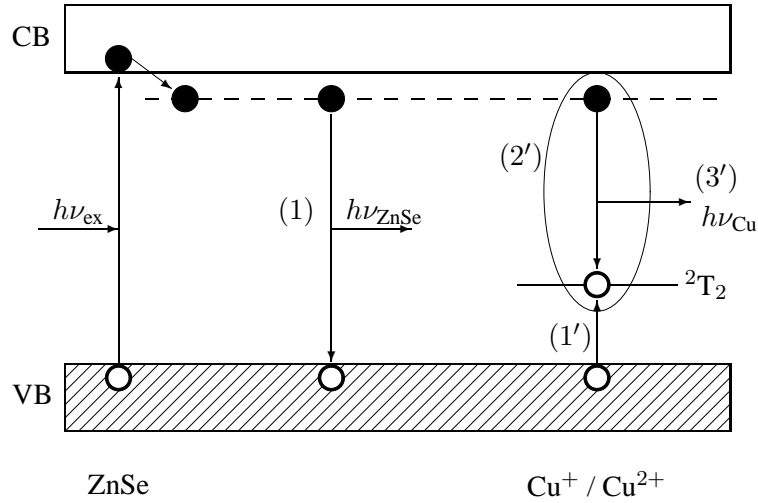
Figure 6.11: *Schematic representation of the energy transfer processes that lead to the ZnSe and Cu²⁺ related photoluminescence emissions. The processes are described in detail in the text. The energy levels are not plotted to scale.*

6.3.4 Description of the luminescence mechanism

After the excitation of the ZnSe host-lattice ($h\nu_{\mathrm{ex}} \geq E_g$), three possible processes can occur. First of all, non-radiative recombination of the electron and the hole may take place. This is a loss-process and obviously undesirable. As most defect-states will be on the surface of the nanocrystal, a good surface passivation (possibly also using another type of (wider bandgap) semiconductor, such as ZnS) will reduce the probability for non-radiative recombination. The second and third processes, both radiative, are schematically depicted in figure 6.11.

Immediately after the creation of the exciton, the electron can be trapped in a shallow trap-state which is delocalized over (nearly) the entire ZnSe nanocrystal. When the recombination of this electron with a hole in the ZnSe valence band occurs, indicated by process (1) in figure 6.11, the blue ZnSe related emission is observed,

$$(1) \quad \mathrm{e}^- + \mathrm{h}_{\mathrm{VB}}^+ \quad \longrightarrow \quad h\nu_{\mathrm{ZnSe}} \; .$$
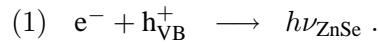
As the electronic trap-state is close in energy to the bottom of the conduction band,

the emission from this level can be regarded as the excitonic emission of the nano-crystal. At low temperature, most of the exciton emission will result from recombination of a shallowly trapped electron with a hole in the valence band. When the temperature is increased, some of the electrons will detrap to the conduction band. This results in a shift of the emission energy to higher energies, agreeing with the data shown in figure 6.8 between 0 K and 50 K. From the temperature range in which this effect occurs, a rough estimate of the energy separation between the delocalized electron-level (indicated by the dashed line in figure 6.11) and the bottom of the conduction band results in about 5 meV. A similar value has been reported in chapter 3 for the ZnS related luminescence in nanocrystalline ZnS.

In order to assign the Cu^{2+} related luminescence, the initial energy level of the electron must first be determined. This can be done using the low-temperature emission spectrum shown in figure 6.7. From this data an extrapolation of the emission bands to higher energy can be made, resulting in an estimate of the zero-phonon energy for the ZnSe and Cu^{2+} related emissions. The result is ∼370 nm for the ZnSe related emission and ∼400 nm for the Cu^{2+} related emission. In figure 6.6 the excitation spectra of the Cu^{2+} related emission was shown, indicating that the Cu^{2+} has an energy level located about 0.3 eV above the bottom of the valence band. This value agrees quite well with the difference in energy between the (extrapolation of) the zero-phonon energy for the ZnSe and Cu^{2+} related emissions. As a result, the initial energy level of the electron must be the delocalized electron-level (indicated by the dashed line in figure 6.11), about 5 meV below the bottom of the conduction band. However, as long as the electron is in this energy level, the close proximity of the conduction band will mean that the electron has mainly a conduction band character. Therefore, an intermediate step is required so that the electron will be bound to the copper resulting ultimately in the Cu^{2+} related emission.

The Cu^{2+} related luminescence mechanism begins when a hole from the valence band is trapped in a localized Cu^+ level, forming Cu^{2+} in an excited state or in the ground state. At sufficiently low temperature, a (delocalized) electron can be trapped in the potential well of the bound hole through the Coulomb interaction. This electron-hole pair can subsequently recombine via the Cu^{2+} ion, resulting in the characteristic green Cu^{2+} related emission. These processes can be

schematically written as

$$
\begin{array}{lll}
(1') & \mathrm{Cu^+ + h_{VB}^+} & \longrightarrow \quad \mathrm{Cu^{2+}} \;, \\[4pt]
(2') & \mathrm{Cu^{2+} + e^-} & \overset{\Delta E}{\longleftrightarrow} \quad \mathrm{Cu^{2+} + e_{trap}^-} \;, \\[4pt]
(3') & \mathrm{Cu^{2+} + e_{trap}^-} & \longrightarrow \quad \mathrm{Cu^+ + h\nu_{Cu}} \;.
\end{array}
$$
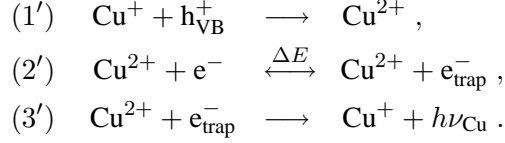
These processes, denoted by $(1')$, $(2')$ and $(3')$, are also schematically shown in figure 6.11. The transfer of the hole to the copper may result in $\mathrm{Cu^{2+}}$ in the $^2\mathrm{E}$ excited state or in the $^2\mathrm{T_2}$ ground state. If the $\mathrm{Cu^{2+}}$ is in the $^2\mathrm{E}$ excited state, it will most likely return quickly (either non-radiatively, or through infra-red emission) to the $^2\mathrm{T_2}$ ground state. The $\mathrm{Cu^{2+}}$ related luminescence observed in this chapter is exclusively due to the recombination with the $\mathrm{Cu^{2+}}$ in the ground state as only one emission band is observed. At elevated temperature, the bound electron-hole pair, created in step $(2')$, can dissociate, requiring an energy ΔE. When this happens, the electron-hole pair is lost and the $\mathrm{Cu^{2+}}$ related luminescence is quenched.

Note that the energy levels of the copper ion are fixed in the ZnSe bandgap. This implies that the energy of the $\mathrm{Cu^{2+}}$ related emission will change when the energy of the conduction band edge changes (e.g. through a change in the crystal size or a change of the sample temperature). This agrees with the data shown in figure 6.5.

The thermally-activated quenching of the copper emission intensity and life-time can now be understood: at elevated temperatures the electron-hole pairs dissociate (with activation energy $\Delta E = 20$ meV) and some of the electrons that are released may now recombine non-radiatively or generate ZnSe related luminescence. Because these processes compete with the radiative recombination from the copper ion, the lifetime of the $\mathrm{Cu^{2+}}$ related emission decreases, as shown in figure 6.10. This can therefore explain the decrease of the $\mathrm{Cu^{2+}}$ emission intensity in the temperature regime where the $\mathrm{Cu^{2+}}$ lifetime is reduced. When the electron-hole pair dissociates, the ZnSe related photoluminescence can still occur. As a result, the $\mathrm{Cu^{2+}}$ related photoluminescence is expected to quench at lower temperature than the ZnSe related luminescence, which is in agreement with the data shown in figure 6.7. The quenching temperature of the $\mathrm{Cu^{2+}}$ related emission can be increased by introducing a deeper electron trap into these ZnSe nanocrystals. As a result, efficiently luminescing ZnSe:Cu nanocrystals at room temperature may be achieved.

6.4 Conclusions

In conclusion, the dependence of the luminescence properties of suspensions and powders of nanocrystalline ZnSe:Cu on the particle size and the sample temperature is described. From measurements on the growth of the nanocrystals two distinct growth ranges are identified. In the first period a concentration driven chemical reaction may explain the observed trend. The data in the second period agree with Ostwald ripening behavior.

Size-dependent measurements show that the color of the Cu^{2+} emission is influenced by quantum confinement effects and can therefore be tuned by varying the size of the nanocrystals. Both the near band edge ZnSe emission and the Cu^{2+} emission shift to shorter wavelengths as the temperature decreases. This temperature dependence is well described by a theory derived for bulk semiconductors. The shift of the Cu^{2+} emission energy only reflects the temperature induced shift of the conduction band edge. The low quenching temperature of the Cu^{2+} emission ($\sim$130 K) is a serious drawback for potential application of ZnSe:Cu nanocrystals in (electroluminescent) devices. It is possible that the quenching temperature can be increased by incorporating a deeper electron-trap in the ZnSe lattice such as Cl^- on Se^{2-} sites.

References

[1] N. C. Greenham, X. Peng and A. P. Alivisatos, *Phys. Rev. B* **54**, 17628 (1996).

[2] B. O. Dabbousi, M. G. Bawendi, O. Onitsuka and M. F. Rubner, *Appl. Phys. Lett.* **66**, 1316 (1995).

[3] L. Brus, *J. Phys. Chem.* **90**, 2555 (1986).

[4] R. N. Bhargava, D. Gallagher, X. Hong and A. Nurmikko, *Phys. Rev. Lett.* **72**, 416 (1994).

[5] I. Yu, T. Isobe and M. Senna, *J. Phys. Chem. Solids*, **57**, 373 (1996).

[6] A. A. Bol and A. Meijerink, *Phys. Chem. Chem. Phys.* **3**, 2105 (2001).

[7] J. F. Suyver, R. Bakker, A. Meijerink and J. J. Kelly, *Phys. Stat. Sol. (b)* **224**, 307 (2001). See also chapter 4.

[8] J. Leeb, V. Gebhardt, G. Müller, D. Su, M. Giersig, G. McMahon and L. Spanhel, *J. Phys. Chem. B* **103**, 7839 (1999).

[9] A. A. Bol, J. Ferwerda, J. A. Bergwerff and A. Meijerink, *J. Lumin.* **99**, 325 (2002).

[10] G. Jones and J. Woods, *J. Lumin.* **9**, 389 (1974).

[11] M. Godlewski, W. E. Lamb and B. C. Cavenett, *J. Lumin.* **24/25**, 173 (1981).

[12] G. B. Stringfellow and R. H. Bube, *Phys. Rev.* **171**, 903 (1968).

[13] J. Huang, Y. Yang, S. Xue, B. Yang, S. Liu and J. Shen, *Appl. Phys. Lett.* **70**, 2335 (1997).

[14] C. B. Murray, D. J. Norris and M. G. Bawendi, *J. Am. Chem. Soc.* **115**, 8706 (1993).

[15] J. F. Suyver, S. F. Wuister, J. J. Kelly and A. Meijerink, *Phys. Chem. Chem. Phys.* **2**, 5445 (2000). See also chapter 5.

[16] D. J. Norris, N. Yao, F. T. Charnock and T. A. Kennedy, *Nano Lett.* **1**, 3 (2001).

[17] G. Blasse and B. C. Grabmaier, *Luminescent Materials*, Springer-Verlag: Berlin, Appendix 4 (1994).

[18] D. T. F. Marple, *J. Appl. Phys.* **35**, 1879 (1964).

[19] M. Aven, D. T. F. Marple and B. Segall, *J. Appl. Phys.* **32**, 2261 (1961).

[20] S. Shionoya and W. M. Yen, *Phosphor Handbook*, CRC Press: Boca Raton, page 233 (1998).

[21] A. van Blaaderen, J. van Geest and A. Vrij, *J. Colloid Interf. Science* **154**, 481 (1992).

[22] P. W. Atkins, *Physical Chemistry, 6th edition*, Oxford University Press: Oxford, Chapter 25 (1998).

[23] A. S. Kabalnov and E. D. Shchukin, *Adv. Colloid Interf. Science* **38**, 69 (1992).

[24] A. S. Kabalnov K. N. Makarov, A. V. Pertzov and E. D. Shchukin, *J. Colloid Interf. Science* **138**, 98 (1990).

[25] Y. P. Varshni, *Physica* **34**, 149 (1967).

[26] L. Malikova, W. Krystek, F. H. Pollak, N. Dai, A. Cavus and M. C. Tamargo, *Phys. Rev. B* **54**, 1819 (1996).

[27] H. Y. Fan, *Phys. Rev.* **82**, 900 (1951).

[28] S. Gopalan, P. Lautenschlager and M. Cardona, *Phys. Rev. B* **35**, 5577 (1987).

[29] W. Z. Shen, H. F. Yang, L. F. Jiang, K. Wang, G. Yu, H. Z. Wu and P. J. McCann, *J. Appl. Phys.* **91**, 192 (2002).

[30] R. Seiwert, *Ann. Physik* **6**, 241 (1949). Written in German.

Chapter 7

Electrochemistry of bulk ZnSe and the electroluminescence of ZnSe:Cu nanocrystals

The electrochemistry of n-type bulk ZnSe crystals was investigated in an indifferent aqueous electrolyte and in dry acetonitrile. From Mott-Schottky measurements on these electrodes, the flat band potential in the two electrolytes was determined to be -1.71 V (vs. NHE) and -1.19 V (vs. NHE), respectively. Electroluminescence measurements on bulk ZnSe in an aqueous electrolyte containing persulfate showed a broad orange defect-related emission band, whereas the ZnSe bandgap emission was not observed. Electrodes of ZnSe:Cu nanocrystals on a transparent conducting substrate were fabricated and the potential dependence of the photoluminescence of these electrodes in an aqueous electrolyte was studied. Electroluminescence of ZnSe:Cu nanocrystalline electrodes was observed and the efficiency is likely to be low.

7.1   Introduction

Many studies have been published on the quantum size effects that occur in nanocrystalline semiconductors [1–6]. The size dependence of the electronic structure for constant chemical composition is of fundamental interest and may also be important for applications such as low voltage electroluminescent devices using semiconductor nanocrystals as the optically active component [7, 8]. Research on semiconductor nanocrystals in which luminescent dopant ions are incorporated has mainly focussed on dopant ions like Mn^{2+} and Pb^{2+}, for which the characteristic emission of the luminescent ion is observed [4, 5, 9]. For these dopants the wavelength for excitation of the dopant emission (over the bandgap of the semiconductor host lattice) shifts to higher energies for smaller crystal sizes, whereas the emission color is unaffected.

The constant emission energy for Mn^{2+} and Pb^{2+} is due to the fact that the luminescent transition only involves wave functions localized on the dopant and the surrounding ligands. These wave functions are not influenced by the size dependence of the electronic structure of the host lattice. However, for other dopant ions the emission of light involves recombination of a delocalized charge carrier with the dopant. A well-known example is the emission of Cu^{2+} centers in ZnS or ZnSe. In this case, the luminescent transition is assigned to the recombination of a delocalized electron (in the conduction band or a shallow trap) with the Cu^{2+} ion. Bulk ZnSe crystals doped with Cu^{2+} show green and red emission bands, which are assigned to the recombination of electrons in shallow traps with different types of Cu^{2+} centers [10–12]. In a nanocrystal, the Cu^{2+} related emission is expected to shift as a function of crystal size [9, 13]. This effect has been shown in detail in chapter 6.

For the nanocrystalline electroluminescent device that was presented in section 1.3.1, two important requirements must be fulfilled. Firstly, there should be reasonably good electron conductivity in the nanocrystalline layer (i.e. from nanocrystal to nanocrystal). Secondly, there must be a surrounding medium in contact with the nanocrystals that will allow for hole-injection into the nanocrystal valence band. The ultimate aim for this surrounding medium will be a *p*-type conducting polymer in order to allow for industrial application. However, no such polymer is available yet and therefore it must be designed. For the choice and fabrication of a suitable polymer, the position of the valence band edge of the semiconductor with respect to the vacuum level must be known.

In this chapter, the electrochemistry and electroluminescence of bulk and nanocrystalline ZnSe is described. The first part of the chapter deals with bulk ZnSe

electrodes and focusses mainly on the determination of the ZnSe valence band edge in an aqueous and an organic electrolyte. As a possible route for the fabrication of a *p*-type conducting polymer involves organic solvents, acetonitrile (CH_3CN) was chosen for this study. Furthermore, the potential dependence of the electroluminescence of bulk ZnSe is studied in a persulfate (aqueous) electrolyte. The second part of this chapter describes electrochemical measurements on ZnSe:Cu nanocrystals deposited on a transparent conductor. In these measurements an aqueous electrolyte was used in order to measure the electroluminescence of the layers of nanocrystals.

7.2 Experimental

All electrochemical and electroluminescence measurements discussed in sections 7.3.1 to 7.3.3 were performed on a single crystalline (100) ZnSe wafer (*n*-type, doped with aluminum) of approximately (5×5) mm^2 obtained from Eagle-Picher Technologies (USA). The carrier concentration at room temperature was $4 \cdot 10^{17}$ cm^{-3}, the resistivity was less than 0.1 Ωcm and the mobility was 340 cm^{2}V^{-1}s^{-1} (data obtained from the supplier). The wafers were chemomechanically polished on the front side and an indium back contact was soldered on the wafer. The back contact of the wafer was glued on a copper holder using silver glue. To remove surface contaminants (such as carbon), the electrode was cleaned with ethanol and etched with a bromine in methanol solution before each experiment. The etchant was prepared by adding two drops of bromine to 10 ml of methanol. After etching the electrode was washed with ethanol.

The synthesis route used to prepare the ZnSe:Cu nanocrystals is similar to the TOP/TOPO synthesis used for CdSe nanocrystals [14]. The reactions were performed in a glovebox (dry-argon atmosphere). The main difference with the CdSe synthesis was the replacement of TOPO by hexadecylamine (HDA) [15, 16]. A 45 ml sample of HDA was heated to 310 °C. A solution of 4.8 mg $Cu(CH_3COO)_2$ in 12 ml tri-*n*-octylphosphine (TOP) was prepared and to this solution 3 ml of a 1 M solution of TOPSe (previously prepared by dissolving elemental selenium-powder in TOP) was added. After stirring 0.32 g of diethylzinc was added. The resulting solution was shaken and then added to the hot HDA. A 2 ml (liquid) sample was taken after a synthesis time of 4.5 hours. The nanocrystals were precipitated by adding them to 5 ml of anhydrous 1-butanol. The electrodes were prepared by allowing several drops of the nanocrystal/1-butanol suspension to evaporate on an ITO-covered glass plate. The electroluminescence measurements were performed

on these electrodes. The deposited layers had a slightly grey color.

 Electrochemical impedance measurements were performed using an EG&G potentiostat / galvanostat (model 273A) and an SI 1255 HF frequency response analyzer. The average size of the nanocrystals was determined from the broadening of the X-ray diffraction peaks using the Debye-Scherrer equation, as discussed in section 2.3.1. The luminescence signal was passed through a fibre optics cable to the monochromator (Acton SP-300i, 0.3 m, 150 lines/mm grating, blazed at 500 nm). The emission spectra were collected with a Princeton Instruments liquid nitrogen cooled CCD camera (1024×256 pixels).

7.3 Results and discussion

7.3.1 Aqueous electrochemistry of a bulk ZnSe electrode

In the beginning of this section the electrochemistry of bulk *n*-type ZnSe in an indifferent aqueous electrolyte is described. The electrochemical and electroluminescence measurements (which are described in section 7.3.3) were carried out using a standard three-electrode electrochemical cell. For these experiments, a platinum wire served as the counter electrode and a saturated calomel electrode (SCE) as the reference electrode. The indifferent electrolyte was a 0.1 M solution of Na_2SO_4 in water. The measurements were performed at room temperature and under ambient conditions.

 The determination of the ZnSe flat band potential was performed using so-called Mott-Schottky measurements [17]. In this technique, the current from the electrode is measured when a potential U is applied over the electrode while a small (sinusoidal) signal is superimposed on this applied potential. As a result, the current observed in the experiment will contain an alternating-current component besides the normal direct current contribution. Because the potential and the current will in general be out of phase, a complex impedance can be assigned to the electrode. When these measurements are repeated for (many) different frequencies of the superimposed signal, a Bode-plot of the real and complex parts of the impedance can be obtained which typically shows a semi-circle. From this Bode-plot, the system resistance and the capacitance of the semiconductor depletion layer, C, can be determined. Such a Bode-plot should be obtained for different values of the applied potential, as the capacitance of the semiconductor depletion layer is dependent on the applied potential according to the well-known
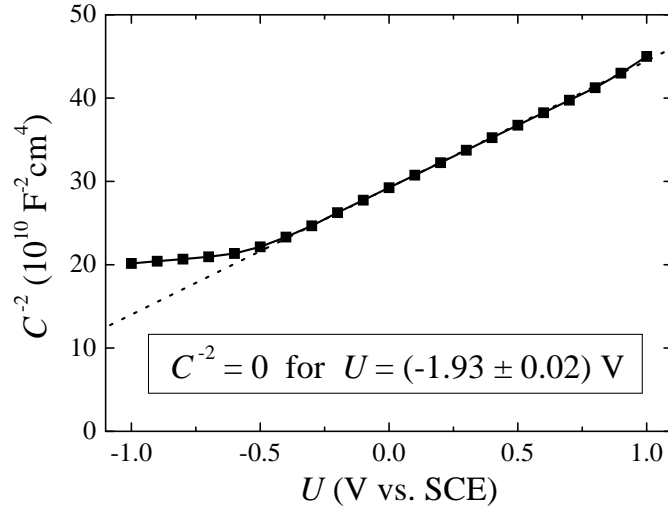
Figure 7.1: *Mott-Schottky measurement of a bulk n-type ZnSe sample recorded at a frequency of 10 kHz. The electrolyte was a 0.1 M solution of Na_2SO_4 in water. The dotted line is a linear fi t to the data in the potential range -0.5 V $\leq U \leq$ 1 V. The reference electrode was a saturated calomel electrode. The measurement was performed at room temperature and under ambient conditions.*

Mott-Schottky equation [18],

$$\frac{1}{C^2} = \frac{2}{e\epsilon_0\epsilon_r N_D}\left(U - U_{fb} - \frac{k_B T}{e}\right) \ .$$
(7.1)

Here ϵ_r denotes the dielectric constant, N_D is the donor density and U_{fb} represents the flat band potential. For the Mott-Schottky experiments that will be discussed in this section,

$$U - U_{fb} \gg \frac{k_B T}{e} \ ,$$
(7.2)

which means that the contribution of the thermal energy can be ignored in equation (7.1). As a result, in a plot of C^{-2} versus the applied potential, the flat band potential can be found at the intersection of the linear part of the data with the U axis.

Figure 7.1 shows a Mott-Schottky plot for an *n*-type ZnSe single crystal measured at a frequency of 10 kHz. Similar measurements showed no influence of the frequency on the data obtained in the frequency range from 100 Hz to 10 kHz. Because of the possibility of anodic dissolution of the ZnSe crystal, the applied potential was limited to $U \leq 1$ V (vs. SCE).

It is clear from the data presented in figure 7.1 that equation (7.1) is valid in a wide potential range. At negative potentials (roughly $U < $ -0.5 V (vs. SCE) for the n-type ZnSe wafer under investigation) a significant deviation from linearity is observed. This deviation is very likely related to the presence of surface states.

When the data in figure 7.1 is fitted using equation (7.1), a value for the flat band potential of U_{fb} = (-1.93 $\pm$ 0.02) V (vs. SCE) is found. This value is in good agreement with that found in the literature (-1.9 V vs. SCE) for a comparable electrode under similar conditions (electrolyte: 1 M solution of NaCl, pH = 6) [19]. The donor density was calculated using equation (7.1) and was estimated to be N_D = (1 $\pm$ 0.4) $\cdot$ 10^{18} cm^{-3}. This value agrees quite well with the reported carrier density of 4 $\cdot$ 10^{17} cm^{-3} considering that the dielectric constant of ZnSe is not known with high accuracy and the surface area of the irregularly shaped sample could only be estimated with a rather poor accuracy.

7.3.2   Anhydrous electrochemistry of a bulk ZnSe electrode

Similar measurements were performed in a dry acetonitrile electrolyte, using the same electrochemical cell. Before the measurements, the cell was sealed and flushed with dry nitrogen for at least several minutes to remove oxygen and water contamination. During the electrochemical experiments, a slight nitrogen over-pressure was maintained in the cell to prevent oxygen and water from diffusing into the cell.

The dry acetonitrile was obtained by refluxing for at least 2 hours under dry nitrogen in the presence of the drying agent CaH$_2$. All the equipment used, including the electrochemical cell, was kept in a dry-oven at $\sim$110 $^\circ$C until needed for the experiments. During the transport from the furnace to the experimental setup, the equipment was exposed to the ambient atmosphere (roughly 1 to 2 minutes). As a reference, a Ag/0.1 molar AgNO$_3$ electrode was made by filling a reference electrode setup with a 0.1 M solution of AgNO$_3$ in dry acetonitrile. The supporting electrolyte was a 0.1 M tetrabutylammonium hexafluorphosphate (TBAF$_6$) solution.

Figure 7.2 shows a Mott-Schottky measurement of the *n*-type ZnSe crystal in the TBAF$_6$/acetonitrile solution. This measurement was recorded at two different
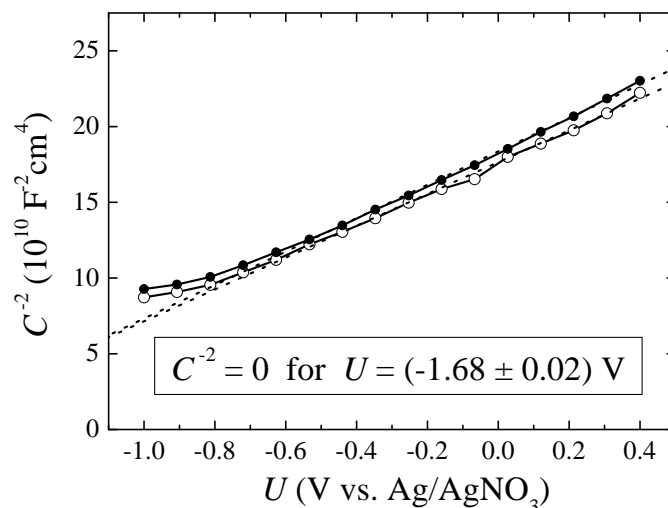
Figure 7.2: *Mott-Schottky measurement of an n-type bulk ZnSe sample recorded at a frequency of 10 kHz (○) or 4.5 kHz (●). The electrolyte was a 0.1 M solution of tetrabutylammonium hexafluorphosphate in acetonitrile. The dotted line is a linear fit to the data in the potential range -0.6 V $\leq U \leq$ 0.4 V. The reference electrode was a $Ag/AgNO_3$ reference electrode. The measurement was recorded at room temperature and in a dry nitrogen atmosphere.*

frequencies (4.5 kHz and 10 kHz), showing no significant influence of the frequency on the obtained result. Similar measurements recorded in the frequency range from 100 Hz to 10 kHz showed that there is no influence of the measurement frequency on the result over this entire frequency range.

From figure 7.2 a flat band potential of $U_{fb} = (-1.68 \pm 0.02)$ V (vs. $Ag/AgNO_3$) was obtained. Calculation of the donor concentration resulted in a value of $N_D = (1.4 \pm 0.3) \cdot 10^{18}$ cm^{-3}. To facilitate comparison of the data presented in figure 7.1 with that of figure 7.2, the flat band potentials were converted to that of a common reference electrode, the normal hydrogen electrode (NHE). The resulting values are

$$U_{fb}(\text{Water}) = -1.71 \text{ V (vs. NHE)},$$
$$U_{fb}(\text{Acetonitrile}) = -1.19 \text{ V (vs. NHE)}.$$
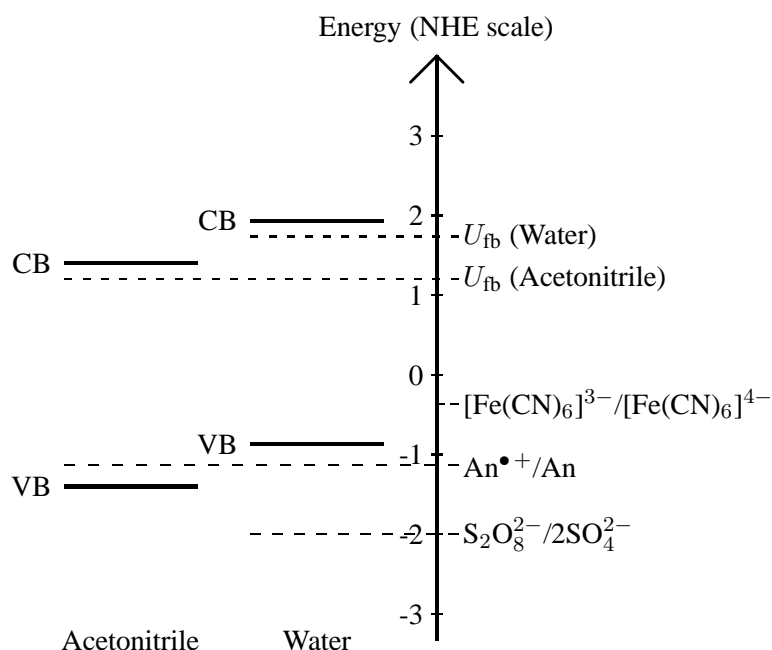
Figure 7.3: *Position of the ZnSe conduction band and valence band edges in acetonitrile and in water based on the flat band potential. In this picture, it is assumed that the conduction band edge lies ∼0.2 eV above the Fermi level and 'VB' and 'CB' denote the valence band edge and the conduction band edge of ZnSe, respectively. The redox potentials of the couples that are mentioned in this chapter are also included.*

As can be clearly seen from these values, there is a large difference in the flat band potentials of ZnSe in an indifferent aqueous electrolyte compared to that in dry acetonitrile. This difference is related to the electrical double-layer in solution.

Figure 7.3 shows the result from the Mott-Schottky measurements in a slightly different setting: this diagram shows the position of the ZnSe conduction band edge and valence band edge for the two different electrolytes that were used (denoted by 'Acetonitrile' and 'Water'). As the electrodes are *n*-type and have a significant carrier concentration, the Fermi energy (i.e. the flat band potential) will be close to the energy of the bottom of the conduction band. Here it is assumed that the conduction band edge lies ∼0.2 eV above the Fermi level. From the known

value of the ZnSe band gap (2.8 eV), the valence band edge can now be calculated. This is shown in figure 7.3. Also indicated in the figure are the redox potentials of the anthracene ($An^{\bullet+}/An$), persulfate ($S_2O_8^{2-}/2SO_4^{2-}$) and ferricyanide ($[Fe(CN)_6]^{3-}/[Fe(CN)_6]^{4-}$) redox couples. The persulfate and anthracene redox couples are used for the electrochemical and electroluminescence experiments described in this chapter. The ferricyanide couple is used by other workers and is shown for comparison.

7.3.3 Electroluminescence of bulk *n*-type ZnSe

In this section, the electroluminescence of the *n*-type ZnSe electrodes in an aqueous electrolyte is described. For the measurements, a 0.1 M K_2SO_4, 0.01 M $K_2S_2O_8$ electrolyte solution in water was used. The electroactive species in solution was $S_2O_8^{2-}$, which reacts in two steps,

$$(1) \quad S_2O_8^{2-} + e_{CB}^- \quad \rightarrow \quad SO_4^{2-} + SO_4^{\bullet-}\,, \qquad (7.3)$$

$$(2) \quad SO_4^{\bullet-} \quad \rightarrow \quad SO_4^{2-} + h_{VB}^+\,. \qquad (7.4)$$
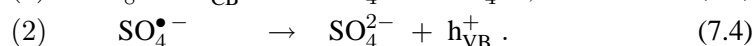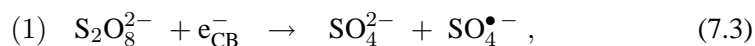
In the first step, an electron from the conduction band is used to generate a sulfate radical anion. In the second step, this radical anion subsequently removes an electron from the semiconductor valence band (i.e. it injects a hole into the valence band). If the electron and the hole recombine, electroluminescence can be observed.

Figure 7.4 shows a typical electroluminescence spectrum of the *n*-type ZnSe electrode recorded by time-integrating the electroluminescence signal while the applied potential was scanned ten times between -1 V (vs. SCE) and -3 V (vs. SCE) at a scan rate of 250 mV/s. A broad emission band is observed, centered at $\sim$630 nm ($\sim$1.97 eV). The ZnSe related bandgap electroluminescence, expected at $\sim$460 nm ($\sim$2.7 eV), was not observed. It is known from the literature that the intensity of this band is strongly dependent on the preparative conditions of the ZnSe crystal [20]. The fact that the surface of the electrode used in these experiments has been etched before each experiment (as discussed in section 7.2) may therefore explain the absence of the ZnSe bandgap emission in the experiments presented in this chapter. On the other hand, the ZnSe bandgap emission has never been observed for these samples, which indicates that this emission may be totally quenched due to the way the crystal has been made.

The broad, orange, electroluminescence band centered at $\sim$630 nm has been reported previously [21]. This band has been related to the self-activated luminescence of the ZnSe crystal [11]. The luminescence mechanism involves a zinc
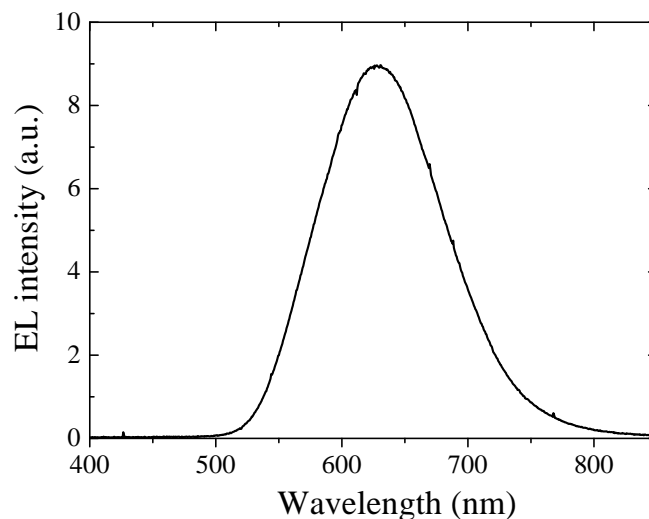
Figure 7.4: *Time integrated electroluminescence spectrum of n-type ZnSe in a 0.1 M so-lution of K_2SO_4 mixed with a 0.01 M solution of $K_2S_2O_8$ in water while the applied potential was scanned 10 times between -1 V (vs. SCE) and -3 V (vs. SCE). The measurement was recorded at room temperature and the scan rate was 250 mV/s.*

vacancy and a next nearest-neighbor donor impurity, such as aluminum on a zinc lattice position [22]. As there is a significant aluminum concentration present in the ZnSe crystal under investigation ($4 \cdot 10^{17}$ cm^{-3} according to the supplier), the absence of the bandgap emission could therefore be due to the much stronger self-activated luminescence of the ZnSe crystal.

Figure 7.5 shows the potential dependence of the integrated electrolumines-cence intensity of the *n*-type ZnSe electrode. The spectral distribution did not change as a function of the applied potential. The measurement was recorded at a scan rate of 100 mV/s. At a potential of about -2 V (vs. SCE) a sharp increase in the electroluminescence signal is observed, which agrees well with the value of the flat band potential reported in section 7.3.1. The increase of the electrolumi-nescence signal intensity continues until a maximum is found at roughly -3 V (vs. SCE). At this potential the cathodic current density was found to be ~20 mA/cm^2. To avoid damage to the electrode, the potential was not scanned to more negative
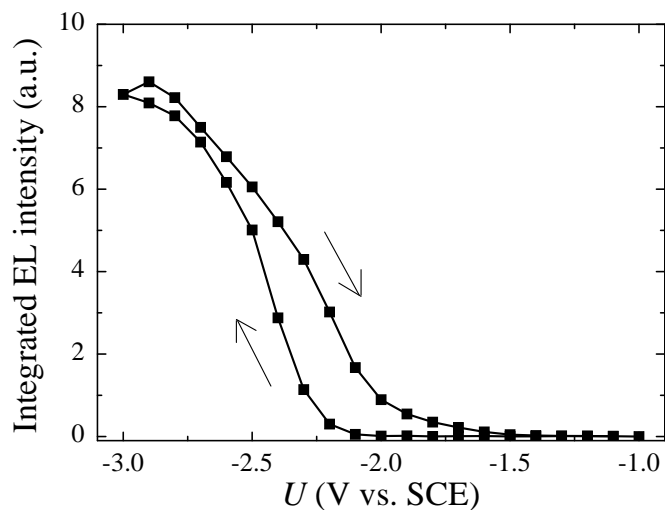
Figure 7.5: *Potential dependence of the integrated electroluminescence intensity of an n-type ZnSe electrode in a 0.1 M solution of K_2SO_4 mixed with a 0.01 M solution of $K_2S_2O_8$ in water. The measurement was recorded at room temperature and the scan rate was 100 mV/s. The line is drawn to guide the eye.*

values. However, it is known from the literature on the electroluminescence of *n*-type ZnSe in ferricyanide electrolytes that for more negative potentials the electroluminescence signal quickly decreases to about 30 % of the maximum intensity and then stays (roughly) constant [19].

In the scan to negative potential, a current plateau in the current density was found at about -2 V (vs. SCE). As the onset of the electroluminescence signal coincides with the plateau in the voltammogram, this current plateau must be related to the reduction of $S_2O_8^{2-}$ in solution, as shown in reactions (7.3) and (7.4). As a result, electroluminescence is observed at this potential.

In an aqueous electrolyte at negative potential, the ZnSe can be electrochemically reduced via

$$ZnSe + 2\,H^+ + 2\,e^- \; \rightarrow \; Zn^0 + H_2Se \; . \tag{7.5}$$
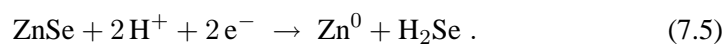
The metallic zinc will remain on the surface of the electrode, introducing additional non-radiative decay paths, resulting in a decrease of the electroluminescence and

photoluminescence efficiencies. The H_2Se will escape the electrolyte in the gas-phase or form H^+ and HSe^- depending on the pH of the electrolyte. The reaction shown in equation (7.5) will limit the long-term stability of the ZnSe electrode and is therefore undesirable.

7.3.4 Electroluminescence of ZnSe:Cu nanocrystals

The observation of electroluminescence from bulk ZnSe in aqueous solutions with persulfate suggests that it may be possible to generate electroluminescence from undoped or doped ZnSe nanocrystals in aqueous solutions. Specifically, the diagram depicted in figure 7.3, shows that even ZnSe nanocrystals, with their increased bandgap (due to the quantum confinement), should electroluminesce using a persulfate electrolyte as long as the confinement energy is less than roughly 1 eV. This corresponds to a nanocrystal radius of more than about 1.5 nm. Note that the average radius of the ZnSe:Cu nanocrystals described in the previous chapter is about 2.5 to 3.5 nm [23]. Therefore, it is expected that these nanocrystals can exhibit electroluminescence. As a result, the remainder of this chapter will present the electroluminescence of nanocrystalline ZnSe doped with Cu^{2+} in the persulfate electrolyte.

To measure the electroluminescence spectrum, electrodes of nanocrystalline ZnSe:Cu (the average particle radius was measured with X-ray diffraction to be 3.4 nm) on indium tin oxide (ITO) coated glass were made by allowing several drops of the nanocrystal suspension (in 1-butanol) to evaporate on an ITO substrate. The electrodes had a surface area of (1×2) cm^2. The adhesion of the nanocrystal layer to the ITO was poor, but may be improved by a suitably chosen temperature treatment, such as annealing in nitrogen at ~ 200 °C as was also done with the nanocrystalline ZnS:Mn^{2+} electrodes discussed in chapter 4.

Figure 7.6 shows the photoluminescence spectrum of an electrode of ZnSe:Cu nanocrystals deposited on ITO-coated glass. Two broad emission bands can be identified: a high energy band at ~ 415 nm (~ 3 eV), related to the ZnSe host lattice and a longer wavelength emission band between 440 and 520 nm, assigned to the Cu^{2+} dopant. A detailed discussion regarding the assignment of these emission bands and the luminescence mechanism can be found in chapter 6.

Potential-dependent photoluminescence measurements were performed under 350 nm excitation. The shape of the emission spectra was similar to that shown in figure 7.6 for each of the applied potentials used. To reduce degradation of the electrode, the applied potential was kept in the range of -2 V (vs. SCE) to +1 V (vs. SCE). The electrolyte used was a 0.5 M solution of Na_2SO_3 in water.
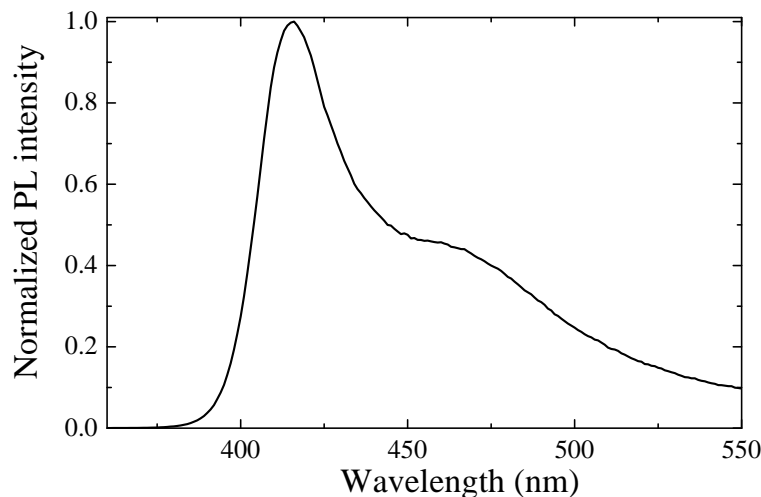
Figure 7.6: *Normalized photoluminescence spectrum of ZnSe:Cu nanocrystals deposited on an ITO-covered glass electrode. The spectrum was measured at room temperature and the excitation wavelength was 330 nm.*

The top part of figure 7.7 shows the integrated photoluminescence intensity of the ZnSe:Cu nanocrystals (integrated over the wavelength region 380 nm to 500 nm) as a function of the applied potential, which is depicted in the bottom part of the same figure. The integrated photoluminescence intensity has been normalized using the emission of an identical electrode with a constant applied potential of -0.5 V (vs. SCE) as a reference to correct for the increase in luminescence intensity due to UV curing [24]. When the applied potential was changed from -0.5 V (vs. SCE) to -1.7 V (vs. SCE), a clear and reversible change in the integrated photoluminescence is observed as can be seen from the upper part of figure 7.7. This effect may be attributed to the electroluminescence of the ZnSe:Cu nanocrystals at negative potentials.

The measured photoluminescence quantum efficiency of the ZnSe:Cu nanocrystals was 2 % to 4 % at room temperature. The top part of figure 7.7 suggests that the electroluminescence intensity is of the order of 1 % of the photoluminescence. However, since the current is not known, an estimate of the electroluminescence
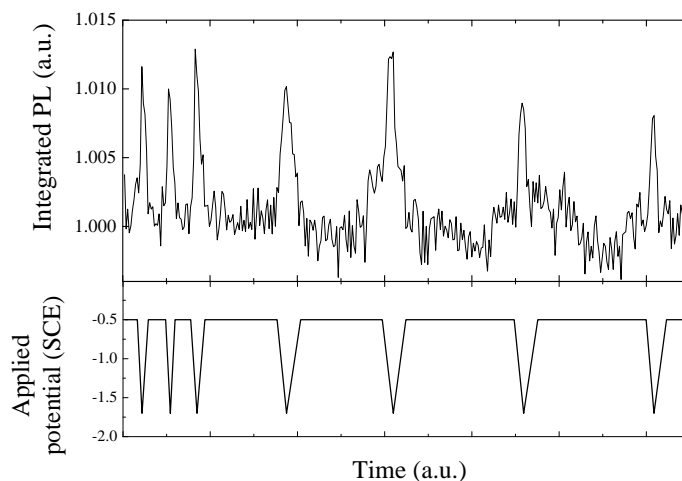
Figure 7.7: *Potential dependence of the integrated photoluminescence of ZnSe:Cu nanocrystals on ITO. The applied potential is depicted in the bottom part of the picture. The excitation wavelength was 350 nm.*

efficiency cannot be made, but the efficiency seems low. Early reports on the electroluminescence efficiency for bulk *n*-type ZnSe (efficiency of $\sim 10^{-4}$) in similar electrolytes [21] suggest room for improvement.

The efficiency could most likely be improved by using nanocrystals with a higher quantum efficiency, by changing the hexadecylamine capping layer, by introducing a temperature treatment or other processing steps. Furthermore, the electron conductivity from nanocrystal to nanocrystal and from nanocrystal to substrate is likely to be poor, due to the insulating capping layer of hexadecylamine surrounding the nanocrystals. These parameters have not been optimized for the data presented in the remainder of this chapter, and therefore a significant increase in the efficiency for electroluminescence might be expected.

Using a 0.5 M solution of Na_2SO_4 and 0.2 M solution of $Na_2S_2O_8$, it was also possible to obtain the electroluminescence and measure its spectrum. In this experiment, the potential was continuously scanned between -0.5 V (vs. SCE) and -2.0 V (vs. SCE) at a scan rate of 200 mV/s for five minutes. The time-integrated
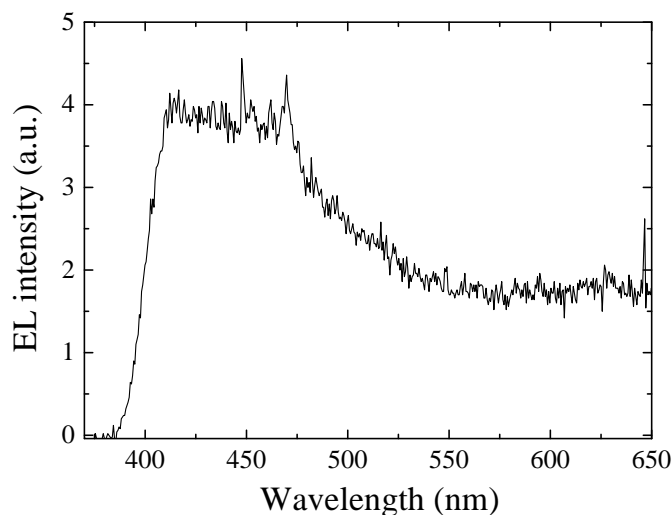
Figure 7.8: *Electroluminescence spectrum of an electrode consisting of ZnSe:Cu nanocrystals deposited on ITO. The electrolyte was a 0.2 M solution of Na$_2$S$_2$O$_8$ and the potential was cycled between -0.5 V (vs. SCE) and -2.0 V (vs. SCE) at a scan rate of 200 mV/s for five minutes. The spectrum was recorded at room temperature.*

emission spectrum is shown in figure 7.8. As can be seen from this figure, the electroluminescence spectrum resembles the emission spectrum shown in figure 7.6, although with a poor resolution. The rapid degradation of the electrode made it impossible to measure accurately an electroluminescence spectrum with a better signal-to-noise-ratio. The result shown in figure 7.8 may be improved by changing the capping of the nanocrystals to increase the carrier mobility of the system. Furthermore, improving the adhesion of the nanocrystals to the ITO substrate, by means of a temperature treatment, will probably increase the lifetime of the electrode.

7.4   Conclusions

This chapter describes electrochemical and luminescence measurements on bulk *n*-type ZnSe crystals and ZnSe:Cu nanocrystals. The investigation focusses on measurements in an aqueous electrolyte and in dry acetonitrile. From Mott-Schottky measurements on the bulk electrode, the flat band potential in the two electrolytes is determined to be -1.71 V (vs. NHE) and -1.19 V (vs. NHE) respectively. Electroluminescence measurements on bulk ZnSe in an aqueous electrolyte show an orange defect-related emission band, whereas the ZnSe exciton emission is not observed. Electroluminescence is observed for an electrode composed of ZnSe:Cu nanocrystals deposited on ITO-covered glass. The electroluminescence efficiency of ZnSe:Cu nanocrystals is estimated to be $\sim 10^{-4}$. The electrodes are not stable for a long time during the measurements in aqueous solutions.

References

[1] N. C. Greenham, X. Peng and A. P. Alivisatos, *Phys. Rev. B* **54**, 17628 (1996).

[2] B. O. Dabbousi, M. G. Bawendi, O. Onitsuka and M. F. Rubner, *Appl. Phys. Lett.* **66**, 1316 (1995).

[3] L. Brus, *J. Phys. Chem.* **90**, 2555 (1986).

[4] R. N. Bhargava, D. Gallagher, X. Hong and A. Nurmikko, *Phys. Rev. Lett.* **72**, 416 (1994).

[5] I. Yu, T. Isobe and M. Senna, *J. Phys. Chem. Solids*, **57**, 373 (1996).

[6] A. A. Bol and A. Meijerink, *Phys. Chem. Chem. Phys.* **3**, 2105 (2001).

[7] J. F. Suyver, R. Bakker, A. Meijerink and J. J. Kelly, *Phys. Stat. Sol. (b)* **224**, 307 (2001). See also chapter 4.

[8] J. Leeb, V. Gebhardt, G. Müller, D. Su, M. Giersig, G. McMahon and L. Spanhel, *J. Phys. Chem. B* **103**, 7839 (1999).

[9] A. A. Bol, J. A. Bergwerff, J. Ferweda and A. Meijerink, *J. Lumin.* **99**, 325 (2002).

[10] M. Godlewski, W. E. Lamb and B. C. Cavenett, *J. Lumin.* **24/25**, 173 (1981).

[11] G. Jones and J. Woods, *J. Lumin.* **9**, 389 (1974).

[12] G. B. Stringfellow and R. H. Bube, *Phys. Rev.* **171**, 903 (1968).

[13] J. Huang, Y. Yang, S. Xue, B. Yang, S. Liu and J. Shen, *Appl. Phys. Lett.* **70**, 2335 (1997).

[14] C. B. Murray, D. J. Norris and M. G. Bawendi, *J. Am. Chem. Soc.* **115**, 8706 (1993).

[15] J. F. Suyver, S. F. Wuister, J. J. Kelly and A. Meijerink, *Phys. Chem. Chem. Phys.* **2**, 5445 (2000). See also chapter 2.

[16] D. J. Norris, N. Yao, F. T. Charnock and T. A. Kennedy, *Nano Lett.* **1**, 3 (2001).

[17] S. R. Morrison, *Electrochemistry at Semiconductor and Oxidized Metal Electrodes*, Plenum Press: New York, chapter 4 (1980).

[18] A. J. Bard and L. R. Faulkner, *Electrochemical Methods: Fundamentals and Applications*, John Wiley & Sons: New York (1980).

[19] G. H. Schoenmakers, E. P. A. M. Bakkers and J. J. Kelly, *J. Electrochem. Soc.* **144**, 2329 (1997).

[20] J. C. Bouley, P. Blanconnier, A. Herman, P. Ged, P. Henoc and J. P. Noblanc, *J. Appl. Phys.* **46**, 3549 (1975).

[21] P. M. Smiley, R. N. Biagioni and A. B. Ellis, *J. Electrochem. Soc.* **131**, 1068 (1984).

[22] D. Curie and J. S. Prener, *Physics and Chemistry of II-VI Compounds*, North-Holland Publishing Co.: Amsterdam, chapter 9.4 (1967).

[23] J. F. Suyver, T. van der Beek, S. F. Wuister, J. J. Kelly and A. Meijerink, *Appl. Phys. Lett.* **79**, 4222 (2001). See also chapter 6.

[24] A. Henglein, *Top. Curr. Chem.* **143**, 151 (1988).

Chapter 8

Probabilities for dopant pair-state formation in a nanocrystal: simulations and theory

For certain dopants, luminescence measurements allow one to distinguish between single-ion and pair-state dopant emission in a (semiconductor) host. In a bulk crystal the concentration of each of these dopant-states can be calculated from the dopant fraction f present in the material, and is found to correlate with luminescence measurements. However, for a nanocrystalline host-lattice, these concentrations are different and have not been calculated. Here simulations of dopant pair-state distributions are presented for a zincblende nanocrystal of size ρ and dopant concentration f. The probability of finding at least one pair-state in the nanocrystal $\mathcal{P}(\rho, f)$ and the concentration of pair-states $\mathcal{Q}(\rho, f)$ were calculated on the basis of a statistical average of $1 \cdot 10^5$ simulations for the same crystal size and dopant concentration. Furthermore, the distribution of nanocrystal lattice positions over the surface and the bulk of the crystal are computed from the simulations and found to agree well with a first-order theory. A mathematical description of $\mathcal{P}(\rho, f)$ is derived that yields a closed-form approximation valid in any crystal lattice, and a rigorous upper bound for the error in the approximation is discussed. An exact analytical expression for $\mathcal{Q}(\rho, f)$ is also derived and the properties of the solution are discussed. Finally, the basis required to develop an algorithm based on preferential pair-formation is presented.

8.1   Introduction

There is a strong current interest in materials with nanometer dimensions [1–5]. New experimental facilities make it possible to study nanometer-sized structures. This research area is driven not just by scientific curiosity; as new applications based on nanosized building blocks are expected [6, 7]. One of the applications where a drive towards smaller sized structures is very evident, is in computer chips where with (V)UV lithography patterns of about 100 nm can be made. To realize a higher speed or larger information storage capacity, even smaller structures are needed. In the field of semiconductor research nanocrystalline particles of semiconductors (called quantum dots) show interesting changes in the electronic structure as the particles become smaller. Synthesis procedures to make very small $(1-10$ nm$)$ quantum dots are well established and fundamental research on the changing properties as a function of particle size has resulted in fascinating results [1–3, 7, 8]. Applications of quantum dots are suggested in electroluminescent devices, where electrical current can be converted into visible light by generating luminescence from the semiconductor quantum dots or from luminescent ions inside these dots [5, 6].

The most obvious difference between nanometer-sized materials and bulk materials is the much larger surface to volume ratio of the former. This is very beneficial in, for example, heterogeneous catalysis where reactions occur at the surface. For nanocrystalline semiconductors the electronic structure also changes due to quantum-size effects and the color of the semiconductor changes as the particle size is varied. An effect that has not been studied is the influence of the particle size on the formation of pairs of dopant (impurity) ions in nanometer-sized particles. The formation of pairs of dopant-ions can be important for the magnetic and optical properties [9, 10]. For example, the luminescence lifetime of the Mn^{2+} emission in ZnS doped with Mn^{2+} decreases and the emission shifts to longer wavelengths when Mn^{2+} pairs are formed in the ZnS crystal. These changes are due to magnetic interaction between the Mn^{2+} ions [11–14]. For studies on a single magnetic quantum dot (containing one magnetic dopant ion) [15, 16], it is also useful to determine the fraction of nanocrystals with one or more magnetic dopant ions. In oxide nanocrystals (e.g. YVO_4 and Y_2O_3) the luminescence properties of rare earth ions like Ce^{3+}, Sm^{3+}, Eu^{3+}, Tb^{3+} and Dy^{3+} have been studied in detail [17–19]. Also here, the luminescence properties are significantly influenced by dopant pair formation. For example, the emission from higher ^5D_J levels of Eu^{3+} or Tb^{3+} is quenched by cross-relaxation processes in pairs, whereas this is not observed for single ions [20].

For bulk crystals the probability for the formation of dopant pairs has been analyzed analytically as a function of the dopant concentration [21–25]. For nanocrystalline semiconductor quantum dots this is much more complicated and has not been done. The main problem is that the coordination number (i.e. the number of nearest neighbors with the same valence) of ions at the surface is lower than that of ions in the bulk. The contribution of ions in surface sites becomes increasingly important as the quantum dots decrease in size and this complicates the determination of the number of pairs. As a result, for the same concentration of dopant ions the fraction of pairs will be different for different particle sizes.

It is the aim of this chapter to provide a better understanding of the probability for pair formation as a function of particle size in nanocrystalline particles. To this end an algorithm has been developed which allows numerical simulations to be made to determine both the probability of finding at least one pair-state in the nanocrystal, and the percentage of dopants that are part of a pair-state in the quantum dot as a function of the particle size. In addition, the fraction of bulk and surface sites is also determined as a function of particle size. Furthermore, a mathematical probabilistic theory (Stein-Chen Poisson approximation) is presented which yields a closed-form approximation of the probability for the formation of at least one pair-state, which is valid in any crystal structure. Interestingly, the simulation-data show that the actual error introduced by this approximation is much smaller than the theoretically expected error based on the Stein-Chen Poisson approximation. An analytical expression is also derived for the fraction of dopants that are part of a pair-state. This expression is also valid for any crystal structure, dopant concentration and crystal size.

The simulations are performed assuming a random distribution of the dopant ions, i.e. it is assumed that there is no preferential pair formation or preference of dopant ions over host lattice ions for surface or bulk sites. In the case of the rare earth oxide nanocrystals this assumption is likely to be valid: the rare earth ions are chemically quite equivalent and a random distribution is expected. For $3d$ transition metal ions in an ionic semiconductor such as ZnS, a random distribution is not expected and the results of the model will give a lower limit for the fraction of pairs. The chapter ends with an outline for an algorithm to calculate these pair-state probabilities when preferential pair-formation is taken into account.

8.2   Simulations and numerical results

8.2.1   Definition of the algorithm

The lattice positions of a crystalline material with a cubic lattice are characterized by the crystal structure combined with the lattice parameter a [26]. Through the introduction of the dimensionless parameter $\rho \equiv (r/a)$, where r is the radius of the nanocrystal, a formalism can be described that does not depend on a and holds for any material with the same crystal structure. The method presented here is generally applicable to every nanocrystalline system. In order to calculate numerical values, a choice of the crystallographic structure is made. In the remainder of this section, the zincblende structure (space group $F\,\bar{4}\,3m - T_d^2$) is chosen, as an example. This crystal structure is found in a wide range of semiconductors such as in CuBr, ZnS, CdSe, InP and GaAs, and is chosen because nanocrystals of these materials have been fabricated and their properties are investigated. The adaptation of this algorithm to other crystal structures is possible. However, as in section 8.3 a mathematical theory is discussed which allows for the calculation of the probability of pair-state formation in any crystal structure, simulations for other crystal types are not necessary.

The number of available lattice positions n in a spherically chosen crystal of radius r will depend on the cube of the radius via

$$n(r) \;=\; 4 \cdot \frac{4}{3}\pi \left(\frac{r}{a}\right)^3 \;=\; \frac{16\pi}{3}\rho^3 \;\equiv\; n(\rho)\,, \qquad (8.1)$$

where the extra factor of 4 is determined by the number of lattice positions in the zincblende unit-cell. Note that equation (8.1) is exact only if $\rho \gg 1$. Since this is clearly not the case in the system under investigation, where ρ is typically between 2 and 10, equation (8.1) should only be viewed as an approximation. The exact value of n is determined by computer-analysis of the overlap of the zincblende crystal lattice with a sphere of radius ρ centered at a lattice position. The influence of this procedure, and some results regarding the number of lattice positions on the surface and in the bulk of the nanocrystal, are discussed in more detail in section 8.3.1.

To describe correctly the nanocrystal, the complete lattice of the crystal is defined via the set $K = \{\mathbf{p}_i;\ i \in [1, n]\}$ containing n vectors in $\mathbb{R}^3$. Each of these unique vectors in the set K points to a specific lattice position in the crystal. The separation matrix, defining the distance between any two vectors (i.e. lattice posi-

tions) in this set, is given by

$$\Omega_{ij} \equiv |\mathbf{p}_i - \mathbf{p}_j| = \sqrt{\sum_{\alpha=1}^{3} [(\mathbf{p}_i)_\alpha - (\mathbf{p}_j)_\alpha]^2} \, , \tag{8.2}$$

the Euclidian norm. The nearest-neighbor distance ζ in this lattice is now defined through

$$\zeta \equiv \min \{\Omega_{\mu\nu}; \; \mu, \nu \in [1, n], \; \mu \neq \nu\} \, . \tag{8.3}$$

For the zincblende crystal structure, $\zeta = a/\sqrt{2}$.

The complete crystal consists of n lattice positions. The situation in which a fraction f of these lattice positions is filled with dopant ions, can be simulated by choosing a random subset $L = \{\mathbf{q}_j; \; j \in [1, k]\}$ of $k = \lceil fn \rceil$ ($1 < k < n$) different vectors from the complete set K. Here k denotes the (expectation value of the) number of dopants present in the lattice. The set L consists of k different vectors, pointing to the lattice positions that contain a dopant ion. The separation matrix in this subset, Θ_{ij}, is defined in a manner similar to that of Ω_{ij}. In the terminology thus introduced, the assumption of a random dopant distribution requires that

$$\forall i \in [1, n] : \; \mathbb{P}(\mathbf{p}_i \in L) = f \, , \tag{8.4}$$

where $\mathbb{P}(x)$ denotes the probability for x. In this case the probabilities do not sum up to 1, but rather to k, as there are k dopants in the crystal.

Note that the matrices Ω and Θ are symmetric and the off-diagonal elements in both Ω and Θ are all non-zero, due to the fact that each of the sets K and L do not contain duplicate vectors. Therefore, only the above-diagonal elements in the separation matrix need to be evaluated. A pair-state in this crystal configuration is now defined to occur if and only if

$$\exists \lambda > \sigma \in [1, n] : \; \Theta_{\lambda\sigma} = \zeta \, . \tag{8.5}$$

By choosing the random subset $L \subset K$ a very large number of times, one can approximate the actual probabilities for pair-state formation. Let $\Phi(n, k)$ represent the probability of finding at least one pair-state in the nanocrystal. Furthermore, let $\Psi(n, k)$ denote the percentage of lattice positions that are part of a pair-state, relative to the number of dopants present in the nanocrystal. Note the difference in definition, which results in $\Phi(n, n) = 1$ and $\Psi(n, n) = 100 \, \%$.

To find the probability for the presence of at least one pair-state in the nanocrystal, a set of $1 \cdot 10^5$ nanocrystals of identical size and number of dopants is simulated. For each of these nanocrystals the validity of equation (8.5) is checked by

evaluating the above-diagonal part of the Θ matrix until a valid solution is found, after which the rest of the Θ matrix was ignored. After all the nanocrystals are checked $\Phi(n, k)$ is identified with the fraction of all the nanocrystals that contained a pair-state (i.e. a valid solution to equation (8.5)).

The algorithm replaces in each nanocrystal a fixed fraction f of the n lattice positions with dopant ions. However, a more realistic procedure would be to replace each lattice position with a dopant ion with a probability f since this resembles the way that doped nanocrystals are formed in nature. This will result in a binomial distribution of the number of dopant ions present in the nanocrystal with expectation value k. Using this fact, combined with the values of $\rho(n)$, the expression for finding at least one pair-state in the nanocrystal is given by

$$\mathcal{P}(\rho, f) = \sum_{i=2}^{n} \left(\begin{array}{c} n \\ i \end{array} \right) f^{i}(1 - f)^{n-i}\Phi(n, i) \; , \qquad (8.6)$$

where the summation begins with $i = 2$, because at least two dopant ions are required to form a pair-state. This definition of $\mathcal{P}(\rho, f)$ will be used throughout this chapter.

The percentage of pair-states relative to the total number of dopants present in the nanocrystal is found through a similar algorithm. Again $1 \cdot 10^{5}$ nanocrystals of identical size and number of dopants are simulated, but now the complete above-diagonal part of the Θ matrix is evaluated. The total number of valid solutions of equation (8.5) found in these $1 \cdot 10^{5}$ parts of the Θ matrices is defined as $\Psi(n, k)$. For small f, the percentage of dopants that are part of a pair-state is $2\Psi(n, k)/k \cdot 100\,\%$. The extra factor 2 is because equation (8.5) only checks the above-diagonal part of the Θ matrix. This finally results in

$$\mathcal{Q}(\rho, f) = 2\sum_{i=2}^{n} \left(\begin{array}{c} n \\ i \end{array} \right) f^{i}(1 - f)^{n-i}\frac{\Psi(n, i)}{nf} \cdot 100 \; [\%] \; , \qquad (8.7)$$

through a similar argument as was used for equation (8.6). Again, this definition will be used throughout this chapter.

Two typical simulations are shown in figure 8.1. These examples were calculated using $\rho = 4$ (i.e. $n = 1048$) and $f = 0.01$ (i.e. $k = 10$). In the simulation on the left, a pair-state has formed as can be seen in the top right part of the simulated crystal. The simulation on the right did not result in a pair-state. For this specific case, values were found of

$$\mathcal{P}(4, 0.01) \;=\; 0.4021 \; ,$$
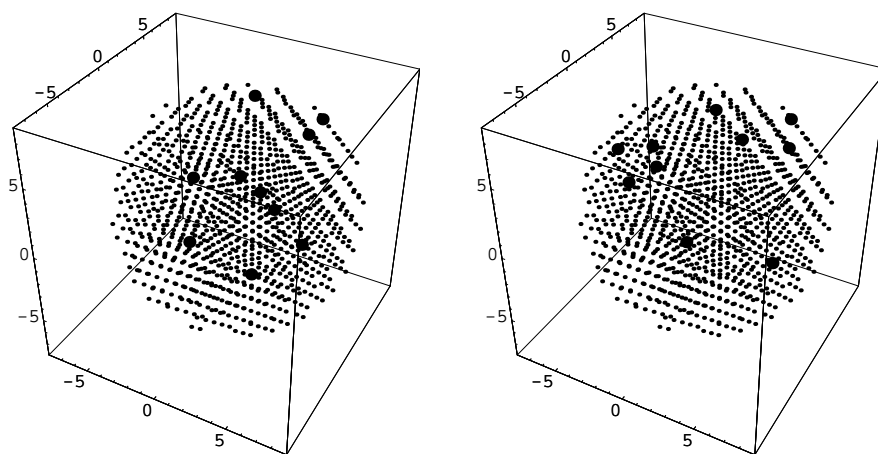
Figure 8.1: *Two typical simulations obtained for ρ = 4 and f = 0.01. The small dots (·) represent the zincblende lattice and the large dots (●) indicate the dopants present in this lattice. The fi gure is discussed further in the text.*

and

$$\mathcal{Q}(4, 0.01) = 8.80 \% .$$

The two algorithms presented in this section have been evaluated $1 \cdot 10^5$ times for every $\rho \geq 1$ and $k \geq 2$ using the bare 4.0.1 *Mathematica* kernel on a Compaq ES40 Alpha (Tru64 Unix 4.0d) system. The step size in the calculations was $\Delta k = 0.001n$ and $\Delta \rho = 0.5$. The listing for the *Mathematica* notebook used to calculate $\mathcal{Q}(\rho, f)$ is included in appendix A at the end of this chapter.

8.2.2 Probability of finding at least one pair-state

For the evaluation of the algorithm for the calculation of $\mathcal{P}(\rho, f)$ the increase of k was stopped when both $\Phi(n, k - 1)$ and $\Phi(n, k)$ were larger than 0.9999 and then ρ was increased by 0.5 up to a maximum value of $\rho = 8.5$. The results of these calculations are shown in figure 8.2. Note that for large ρ the probability distribution will converge monotonously to a step function, such that

$$\lim_{\rho \to \infty} \mathcal{P}(\rho, f) = \begin{cases} 0 & \text{if } f = 0 \\ 1 & \text{if } f > 0 \end{cases} . \tag{8.8}$$
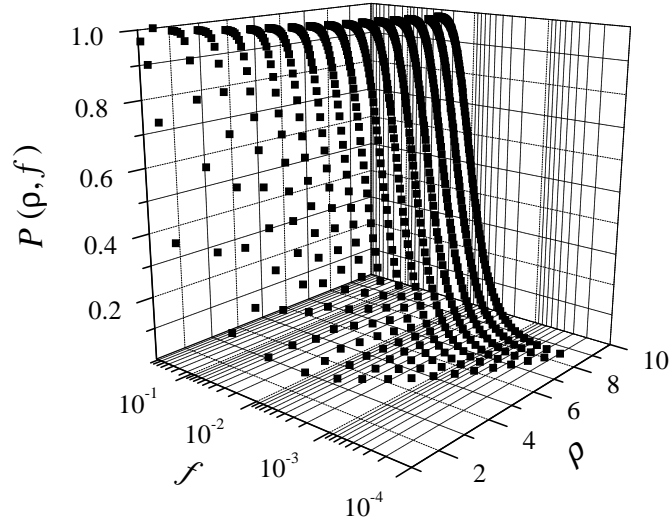
Figure 8.2: *The probability distribution* $\mathcal{P}(\rho, f)$*, which describes the probability of finding at least one pair-state in a zincblende nanocrystal with radius* ρ *and dopant fraction* f*. Note the logarithmic scale for the* f*-axis.*

This result is straightforward, since $\mathcal{P}(\rho, f)$ denotes the probability of finding at least one pair-state in the crystal.

Figure 8.3(a) shows the cation (or anion) sites in the zincblende crystal structure for a bulk lattice position. The collection of these sites form a face centered cubic sub-lattice. The hollow lattice positions are all one nearest-neighbor distance from the encircled lattice position. Figure 8.3(b) shows the same, but now for a surface lattice position. From this figure, it can immediately be seen that a surface lattice position has 8 nearest-neighbors, whereas a bulk lattice position has 12 nearest-neighbors.

Upon close inspection of figure 8.2, it can noted that for small particles (i.e. ρ < 5) the surface contribution to the probability distribution is very large. The fact that lattice positions on the surface have less nearest-neighbors than bulk lattice positions results in a drastic decrease of the probability for pair-state formation compared to larger crystals.

Figure 8.4(a) clearly shows the strong influence of the fraction of lattice posi-
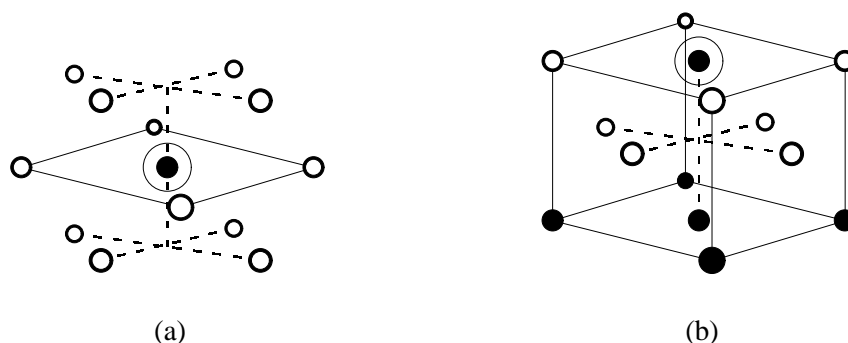
Figure 8.3: *Schematic representation of the relevant lattice positions for the zincblende crystal structure. The hollow circles are one nearest-neighbor distance from the circled lattice point. The circled lattice point in the two pictures represent (a) a bulk lattice position and (b) a surface lattice position, where the surface is at the top of the picture.*

tions at the surface of the nanocrystal on the total probability of finding at least one dopant pair-state. In this figure the dopant fraction in the nanocrystal is fixed at $f = 0.015$, while the crystal size is varied. It is important to stress that equation (8.8) shows that, even without worrying about the lattice positions on the surface, the probability of finding at least one pair-state in the nanocrystal will converge to 1 for large crystal sizes regardless of the surface to volume ratio. However, the trend shown in figure 8.4(a) actually goes much slower than would be expected. This can be clearly seen from the dotted line in this figure, showing the expected dependence of $\mathcal{P}$ on ρ when the surface contribution is ignored. The precise functional form of this dotted line was determined by means of the fomalism that will be discussed in section 8.3.2 (equation (8.19) with $C_s = C_b = 12$). At two specific crystal sizes, there are two simulation data points per crystal size. For these crystal sizes the concentration $f = 0.015$ was not simulated. The data points represent the simulations that were performed with dopant concentrations closest to $f = 0.015$ for these crystal sizes.

Figure 8.4(b) shows the influence of the dopant concentration on the probability of forming at least one pair-state (at constant crystal size $\rho = 4.5$). Also here, as in figure 8.4(a), the dotted line shows the expected dependence of $\mathcal{P}$ on f when the surface contribution is ignored. This shows once more the decreased probability for pair-state formation on the surface of the nanocrystal with respect to that of the bulk of the crystal. All the data presented in figure 8.2 could, just like the example
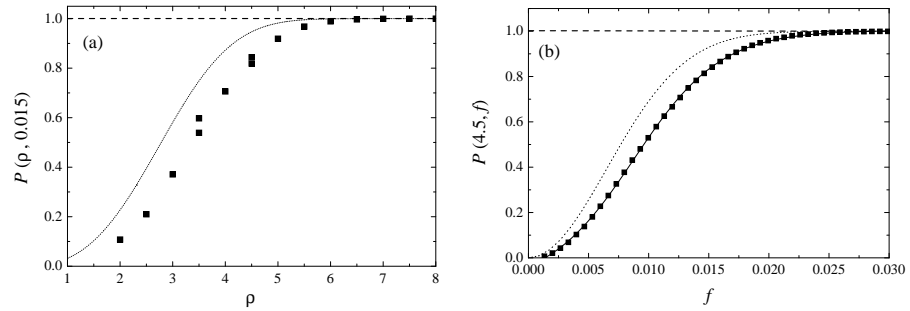
Figure 8.4: *(a) The probability of finding at least one pair-state in the nanocrystal as a function of crystal size for f = 0.015. The dotted line shows the expected trend if the surface contribution could be ignored. (b) The same, but now as a function of the dopant concentration for a constant crystal size ρ = 4.5. The drawn line is a fit of equation (8.9) and the squares represent the simulation data.*

in figure 8.4(b), be fitted very well using a stretched Boltzmann-type equation,

$$\mathcal{P}(\rho, f) = \left\{ \frac{1}{1 + \exp\left(\frac{F(\rho) - f}{G(\rho)}\right)} \right\}^{\beta(\rho)}, \qquad (8.9)$$

as can be seen from the drawn line through the data. The empirical variables $F(\rho)$, $G(\rho)$ and $\beta(\rho)$ have no physical meaning and their values can be obtained from a fit. The dependence of F, G and β on ρ is found to be quite complicated. In order to obtain high quality predictions, three-parameter fits of $F(\rho)$, $G(\rho)$ and $\beta(\rho)$ were needed. With the simplified Bleasdale-Nelder [27] functional form, good fits can be obtained. However, as the empirical variables have no physical meaning, this analysis will not be discussed further.

8.2.3   Pair-state concentration

In this section the results obtained from the simulations of $\mathcal{Q}(\rho, f)$, the percentage of dopant ions that are part of a pair-state, in the low-dopant concentration regime are described. It is important to stay roughly in the $0 < f < 0.1$ range, because for larger f the presence of triple-states needs to be taken into account. For these
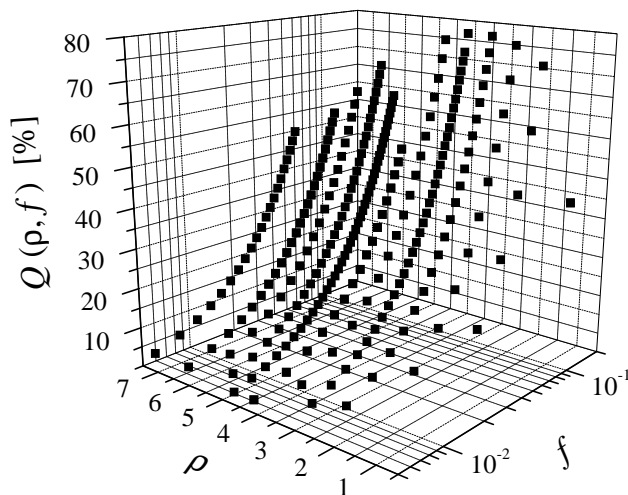
Figure 8.5: *The probability distribution $\mathcal{Q}(\rho, f)$, which describes the expected percentage of dopant ions in pair-states in a zincblende nanocrystal with respect to the total number of dopants present in this nanocrystal. Note the logarithmic scale for the f-axis.*

states, defined to occur if and only if

$$\exists \lambda \neq \sigma \neq \mu \neq \lambda \in [1, n] : \; \Theta_{\sigma\mu} = \zeta = \Theta_{\sigma\lambda} \; , \tag{8.10}$$

the symmetry properties of Ω_{ij} can no longer be exploited because a triple-state in the zincblende crystal structure can be three particles on a line (which would count as four dopant ions in pair-states in the algorithm presented in section 8.2.1), or three particles in a triangle shape (counting as six dopant ions in pair-states). The combinatorial problems associated with these "higher-order" corrections become increasingly more difficult to handle and require much more computer-time to be correctly evaluated. Therefore, the remainder of this analysis will only focus on the low dopant range ($0 < f < 0.1$), and the presence of triple-states will be ignored. With this assumption, equation (8.7) describes the percentage of dopant ions in pair-states in the nanocrystal.

Note that the evaluation of equation (8.7) already requires much more computer-time than that of equation (8.6), which was presented in the previous section, be-
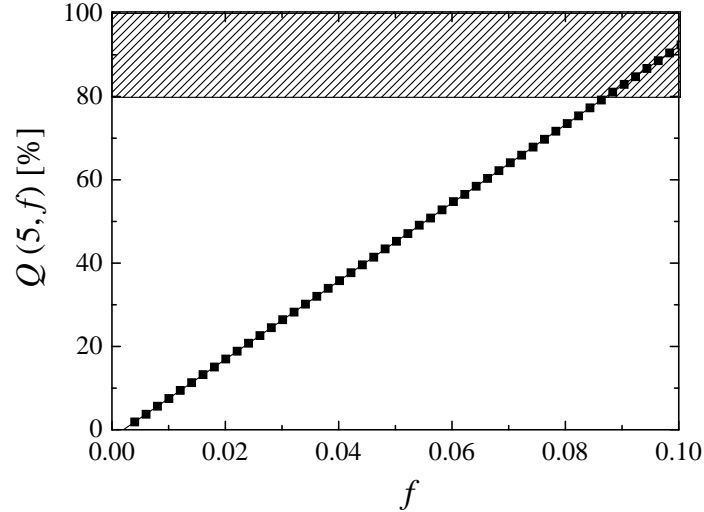
Figure 8.6: *The percentage of dopants that are part of a pair-state (for fixed $\rho = 5$) as a function of the dopant concentration. The line through the data is a fit using equation (8.11). The dashed box represents the results deemed 'unrealistic', which are discussed further in the text.*

cause in this case half of the Θ matrix has to be calculated for each simulation, instead of just evaluating the Θ matrix until the first valid solution of equation (8.5) is found. Naturally, this difference becomes increasingly more evident as the dopant concentration increases, or the crystal size becomes larger.

Figure 8.5 shows the resulting $\mathcal{Q}(\rho, f)$ determined by evaluating equation (8.7) for $1 \leq \rho \leq 7$. The influence of the surface can be seen clearly in the data, just as in the previous section. If the surface did not influence the results, then one would expect $\mathcal{Q}(2, f) = \mathcal{Q}(7, f)$ for all f. However, the data show that this is not the case as $\mathcal{Q}(3, 0.0108) = 8.5$ %, while $\mathcal{Q}(7, 0.0108) = 11.8$ %. Again, this difference is explained by the different probability for pair-state formation of a dopant at the surface of the nanocrystal with respect to a dopant in the bulk (due to the difference in coordination number). All data presented in this figure could be fitted exceptionally well using straight lines,

$$\mathcal{Q}(\rho, f) \;=\; \gamma(\rho) \,+\, \phi(\rho) \cdot f \;\; [\%] \,, \tag{8.11}$$

as can be seen from the example shown in figure 8.6. Again, no physical explanation is known for the (asymptotical exponential) forms of the empirical parameters $\gamma(\rho)$ and $\phi(\rho)$. As a result, no additional discussion of these parameters will be presented here.

Two observations can be made from figure 8.6. Firstly, the (extrapolation of the) data does not intersect with the origin, but crosses the horizontal axis for a non-zero value of f. This is caused by the fact that *two* dopant ions are required in the lattice before a pair-state can be formed. Secondly, the concentration range probed in this figure is quite large: for many materials 10 % of foreign ions in the lattice can no longer be thought of as 'dopants'. Such a large concentration of non-host lattice ions can seriously distort the band structure of the host lattice and either form a new phase or segregate to the surface of the crystal or a defect-site. However, there do exist materials that can incorporate $\sim$10 % of dopant ions and still retain the host lattice properties (e.g. Y_2O_3: 10 % Eu^{3+}).

The straight lines, such as the example shown in figure 8.6, do not seem to level off at $\mathcal{Q}(\rho, f) = 100$ %. Indeed for $f > 0.12$ in the example shown, it is found that $\mathcal{Q} > 100$ %. This is clearly the result of the presence of triple-states (valid solutions to equation (8.10) that allow for three dopants to count as up to six ions in pair-states), which can no longer be ignored. Therefore, all the simulations that had a dopant fraction such that $\mathcal{Q}(\rho, f) > 80$ % are considered unrealistic and are discarded. It is important to stress that the value of 80 % is chosen arbitrarily at this point. In section 8.4 it will become clear that this value is actually much too high (it will be closer to 40 %) and that the correct cut-off value will depend on the size of the nanocrystal.

Within the assumption that there are no triple-states in the nanocrystal, the reason that equation (8.11) is linear is straightforward. For low-dopant fractions, there are almost no triple-states, and this is the reason that the definition of $\mathcal{Q}(\rho, f)$ has the factor 2. Therefore, the number of dopants that are in a pair-state will scale with f^2 (two dopants need to be next to each other, each with probability f). As the number of dopants in the lattice scales with f, it is clear that the fraction of dopants that are in a pair-state scales with $f^2/f = f$. In other words, for small f, if no solution of equation (8.10) exists for the nanocrystal, then addition of one more dopant pair-state will most likely also not result in a solution of equation (8.10). This means that the increase in the fraction of pair-states goes linear with the number of dopants.

8.3   Mathematical formulation of the problem

This section is devoted to deriving a closed-form approximation of $\mathcal{P}(\rho, f)$ and a measure of the uncertainty in the approximation. An exact formulation for $\mathcal{Q}(\rho, f)$ will also be derived. The results have general applicability and therefore require a description of the crystal structure. This is done by making the results dependent on the material parameters: the number of neighbors of a bulk lattice position (the bulk connectivity, C_b), the number of neighbors of a surface lattice position (the surface connectivity, C_s) and a factor determining the number of lattice positions present in the unit-cell (ψ, defined in equation (8.12)). However, before $\mathcal{P}(\rho, f)$ and $\mathcal{Q}(\rho, f)$ can be discussed, another result is required. Therefore, in section 8.3.1 a simple first-order equation will be derived that allows the calculation of the fraction of lattice positions present on the surface of the nanocrystal without simulating the complete crystal.

8.3.1   Lattice position configuration

The algorithm presented in section 8.2.1 can be applied to derive the number of "bulk" and "surface" lattice positions, denoted as $n_b(\rho)$ and $n_s(\rho)$ respectively. Here, a lattice position is defined to be a surface position if it contributes to $n(\rho)$ but not to $n(\rho - \frac{1}{2})$. The bulk lattice positions are chosen to be those that belong to $n(\rho - \frac{1}{2})$ as the cation sub-lattice of the zincblende crystal structure is face-centered cubic. This lattice also has lattice-planes at half the height of the 'unit cell'. Therefore, the crystal size can be increased by $\frac{1}{2}$, rather than by 1. When one investigates the simple cubic sub-lattice this is not the case, and for this structure the bulk lattice positions will be those that belong to $n(\rho - 1)$.

The total number of lattice positions, given in equation (8.1) for the zincblende crystal structure, can be generally defined as

$$n(\rho) \equiv \sum_{\forall \mathbf{p}} 1 \approx \frac{4\pi\psi}{3}\rho^3 \, , \qquad (8.12)$$

where ψ represents the number of lattice positions in the unit cell. The evaluation of the summation was used in section 8.2.1 and gives an exact value for $n(\rho)$.

When the assumption indicated in the second part of equation (8.12) is made, then the number of surface lattice positions is given by

$$n_s(\rho) = n(\rho) - n(\rho - \frac{1}{2}) = \frac{\pi\psi}{6}\left[1 + 6\rho(2\rho - 1)\right] \, , \qquad (8.13)$$
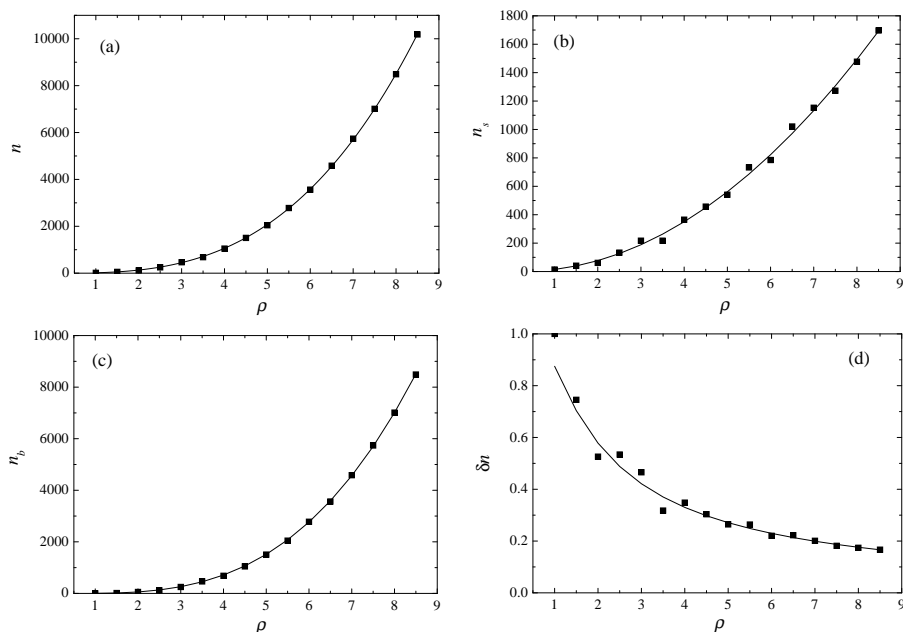
Figure 8.7: *Comparison of the exact summation and the approximation presented in equation (8.12). The squares in (a) through (d) represent the values found for $n(\rho)$, $n_s(\rho)$, $n_b(\rho)$ and $\delta n(\rho)$ from the simulations presented in section 8.2 (i.e. the evaluation of the sum in equation (8.12)), respectively. The lines through the data are predictions from equations (8.12) through (8.15), using $\psi = 4$.*

and the number of bulk lattice positions by

$$n_b(\rho) \;=\; n(\rho - \frac{1}{2}) \;=\; \frac{\pi\psi}{6}(2\rho - 1)^3 \; . \tag{8.14}$$

The fraction of lattice positions that is located on the surface of the nanocrystal, $\delta n(\rho)$, can be expressed in terms of $n_s(\rho)$ and $n(\rho)$ and yields

$$\delta n(\rho) \;\equiv\; \frac{n_s(\rho)}{n(\rho)} \;=\; [6\rho^{-1}(2 - \rho^{-1}) + \rho^{-3}]/8 \; . \tag{8.15}$$

Note that $\delta n(\rho)$ no longer depends on ψ.

The squares in figure 8.7(a)−(d) show the values that were found for $n(\rho)$, $n_s(\rho)$, $n_b(\rho)$ and $\delta n(\rho)$ respectively. For these values the assumption of equation (8.12) was not made, but the exact crystal configuration was used by means

of the simulation-data presented in section 8.2 (i.e. the complete sum in equation (8.12) was evaluated). However, as can be seen from this figure, the lines through the data, resulting from equations (8.12) through (8.15) indicate a good agreement between this first-order theory and the true nanocrystal structure. Note that the line through the data in figure 8.7(d) does not depend on ψ and is a direct prediction of the theory described above. This is significant, because it implies that $\delta n(\rho)$ as described in equation (8.15) is independent of the crystal structure (for cubic crystals). As is indeed expected, the limit $\rho \to \infty$ for the right-hand side of equation (8.15) is 0. This agrees very well with the data presented in the figure. From the data in figure 8.7 it may be concluded that equation (8.12) is a good approximation in the case of a zincblende crystal, even for a very small nanocrystal (such as $\rho = 2$).

8.3.2   Stein-Chen Poisson approximation

In this section, an approach is discussed which enables the computation of a very good approximation of $\mathcal{P}(\rho, f)$ for any given crystal, without performing any simulations. In addition, a rigorous upper bound of the error introduced by the approximation is also derived. The method that will be used is a special instance of the so-called Stein-Chen Poisson approximation method [28]. The main idea is that the number of pair-states is close in distribution to a Poisson random variable, in a sense to be made precise in a moment. This phenomenon is due to the fact that the pair-states are almost independent. If the pair states would be completely independent, then the total number of pair-states would have a binomial distribution. The binomial distribution is, under the circumstances that are relevant to this chapter, very close to a Poisson distribution. The proof that the binomial distribution will converge to the Poisson distribution can be found in appendix B, at the end of this chapter. The different pair-states in a nanocrystal turn out to be sufficiently independent as to make an approximation with a Poisson distribution extremely useful.

The number of (unordered) nearest-neighbor lattice positions in the crystal is denoted by N. In the notation introduced in section 8.3.1 this can be written as

$$
\begin{aligned}
N &= \frac{1}{2}(n_s C_s + n_b C_b) \\
&= \frac{\pi \psi (2\rho - 1)}{12} \left[(2\rho - 1)^2 C_b + (6\rho + (2\rho - 1)^{-1}) C_s \right] \; . \quad (8.16)
\end{aligned}
$$

To form a pair-state in the crystal, two lattice positions in the crystal must be

nearest-neighbors and on each of these lattice positions there must be a dopant. The probability that a lattice position contains a dopant is denoted by f and therefore the probability of two lattice positions being occupied by a dopant will be f^2. As there are N nearest neighbor pairs in the crystal, the expected number of dopant pair-states will simply be given by

$$\lambda = Nf^2 . \tag{8.17}$$

The number of pair-states in the nanocrystal will have approximately a Poisson distribution with expectation value λ. This implies that the probability $P(x)$ of finding x pair-states in the nanocrystal will be approximated by

$$P(x) = \frac{e^{-\lambda}\lambda^x}{x!} . \tag{8.18}$$

Therefore, the probability of finding at least one pair-state in the nanocrystal will be approximately

$$\begin{aligned}
\mathcal{P} &= 1 - P(0) \\
&= 1 - e^{-\lambda} \\
&= 1 - \exp\left[-\frac{\pi\psi f^2}{12}\left\{C_s(1 + 6\rho(2\rho - 1)) + C_b(2\rho - 1)^3\right\}\right] . \tag{8.19}
\end{aligned}$$

It is interesting to note that equation (8.19) indeed has a stretched-Boltzmann form, which agrees with the results from the simulations shown previously.

It is possible to determine an upper bound of the error that the Poisson approximation introduces in equation (8.19). In order to be able to calculate this upper bound, the general formulism is presented first. In this formalism, a measure for the 'difference' between two probability distributions can be calculated. Denote by T and W two random variables with corresponding probability distributions $\lambda(i)$ and $\mu(i)$. This implies that the probability of measuring $T = j$ is given by

$$\mathbb{P}(\{T = j\}) = \lambda(j) , \tag{8.20}$$

and the probability of finding $W = j$ by

$$\mathbb{P}(\{W = j\}) = \mu(j) . \tag{8.21}$$

The probability distributions are both normalized,

$$\sum_{i=0}^{\infty} \mathbb{P}(\{T = i\}) = \sum_{i=0}^{\infty} \mathbb{P}(\{W = i\}) = 1 . \tag{8.22}$$

For any $A \subset \mathbb{Z}^+$ the probability of measuring A (i.e. the probability of finding T to be an element of A) is defined by

$$\mathbb{P}(\{T \in A\}) = \lambda(A) = \sum_{i \in A} \lambda(i) = \sum_{i \in A} \mathbb{P}(\{T = i\}), \qquad (8.23)$$

which is a logical extension of equation (8.20).

Assume that the distributions $\lambda(i)$ and $\mu(i)$ are not completely identical (i.e. $\exists i \in \mathbb{Z}^+ : \lambda(i) \neq \mu(i)$). The 'difference' between λ and μ can now be measured using the so-called total variation norm d_{TV}, which is defined by [28]

$$\begin{aligned} d_{TV}(\lambda, \mu) &\equiv \sup\left\{ \left| \lambda(A) - \mu(A) \right|; \ A \subset \mathbb{Z}^+ \right\} \\ &= \frac{1}{2} \sum_{j=0}^{\infty} \left| \mathbb{P}(\{T = j\}) - \mathbb{P}(\{W = j\}) \right| . \end{aligned} \qquad (8.24)$$

The proof that the second line is indeed identical to the first line requires two steps. First, it will be shown that there indeed exists (at least) one $A \subset \mathbb{Z}^+$ for which the second line and the first line are identical. Secondly, it will then also become clear that this represents the maximum. Interestingly, this must mean that the supremum in the first line of equation (8.24) can therefore also be replaced by a maximum.

The proof goes as follows: construct the set $A \subset \mathbb{Z}^+$ such that

$$A = \left\{ i \in [0, \infty); \ \lambda(i) \geq \mu(i) \right\}. \qquad (8.25)$$

As the set A now contains all i for which $\lambda(i)$ is greater or equal than $\mu(i)$ it is immediately clear that for all elements of this set $|\lambda(i) - \mu(i)| = \lambda(i) - \mu(i)$. As a result, starting from the second line of equation (8.24), it can now be seen that

$$\begin{aligned} d_{TV}(\lambda, \mu) &= \frac{1}{2} \sum_{j=0}^{\infty} \left| \mathbb{P}(\{T = j\}) - \mathbb{P}(\{W = j\}) \right| \\ &= \frac{1}{2} \sum_{j \in A} \left(\mathbb{P}(\{T = j\}) - \mathbb{P}(\{W = j\}) \right) + \\ &\qquad \frac{1}{2} \sum_{j \notin A} \left(\mathbb{P}(\{W = j\}) - \mathbb{P}(\{T = j\}) \right) \\ &= \frac{1}{2} \left(\sum_{j \in A} \mathbb{P}(\{T = j\}) - \sum_{j \in A} \mathbb{P}(\{W = j\}) \right) + \\ &\qquad \frac{1}{2} \left(\sum_{j \notin A} \left(\mathbb{P}(\{W = j\}) - \sum_{j \notin A} \mathbb{P}(\{T = j\}) \right) \right. . \quad (8.26) \end{aligned}$$

The second and fourth parts of equation (8.23) are used to simplify this further to give the desired result,

$$
\begin{aligned}
d_{TV}(\lambda, \mu) &= \frac{1}{2}\big(\lambda(A) - \mu(A)\big) + \frac{1}{2}\big(\mu(\mathbb{Z}^+\backslash A) - \lambda(\mathbb{Z}^+\backslash A)\big) \\
&= \frac{1}{2}\big(\lambda(A) - \mu(A)\big) + \frac{1}{2}\big((1 - \mu(A)) - (1 - \lambda(A))\big) \\
&= \lambda(A) - \mu(A) \, .
\end{aligned}
\tag{8.27}
$$

This proves that for this particular A equation (8.24) is valid. Using the fact that $|a - b| \geq a - b$ it is directly clear that

$$
\sum_{j=0}^{\infty} |\mathbb{P}(\{T = j\}) - \mathbb{P}(\{W = j\})| \geq \sum_{j=0}^{\infty} \mathbb{P}(\{T = j\}) - \mathbb{P}(\{W = j\}) \, . \tag{8.28}
$$

As a result, for other choices of A (when the absolute-value operator may not be removed) the second line in equation (8.24) will be an upper bound. This completes the proof, because in the definition of $d_{TV}(\lambda, \mu)$ the supremum is taken for all $A \subset \mathbb{Z}^+$.

The second line of equation (8.24) will allow one to calculate the 'difference' between the simulation-data and the prediction of the Poisson approximation as shown in equation (8.19). However, actually calculating this difference is very hard. Fortunately, corollary 2.N.1 in Ref. [28] states (in the terminology introduced in this section) that an upper limit of the total variation norm shown in equation (8.24) will be given by

$$
d_{TV}(\mathcal{P}(\rho, f), \mathcal{P}) \leq \left(1 - e^{-\lambda}\right) \left\{ f^2 + (f + f^2)N^{-1} \sum_{i=1}^{n} z_i(z_i - 1) \right\} , \tag{8.29}
$$

where z_i represents the number of nearest-neighbors of lattice position i (identified through the vector $\mathbf{p}_i$). The proof that this upper bound is valid can also be found in Ref. [28] and is beyond the scope of this thesis. The sum in equation (8.29) can be evaluated directly by using the known values for n_s and n_b, introduced in equations (8.13) and (8.14), together with the surface and bulk connectivities C_s and C_b. This finally results in a closed-form expression of the total variation norm as

$$
\begin{aligned}
d_{TV}(\mathcal{P}(\rho, f), \mathcal{P}) \leq \; & \left(1 - e^{-Nf^2}\right) \left\{ \frac{\pi\psi(f + f^2)}{6N} \big[(2\rho - 1)^3 C_b(C_b - 1) + \right. \\
& \left. (1 + 6\rho(2\rho - 1))C_s(C_s - 1)\big] + f^2 \right\} .
\end{aligned}
\tag{8.30}
$$

From the first characterization of d_{TV} in equation (8.24) it can be seen that $|\mathcal{P}(\rho, f) - \mathcal{P}|$ is bounded by the right hand side of equation (8.30). The numbers resulting from equations (8.19) and (8.30) can be easily computed, and this means that simulations are no longer needed. As long as the upper bound for the error in $\mathcal{P}$, as found from the evaluation of equation (8.30) remains small, the Stein-Chen Poisson approximation of $\mathcal{P}$ and d_{TV} can be used directly.

As an example, consider the zincblende crystal structure of section 8.2.1, where $\psi = 4$, $C_b = 12$ and $C_s = 8$. A simple evaluation for $\rho = 4$ and $f = 0.01$ leads to $\mathcal{P} = 0.436$. This is in quite good agreement with the result from the simulations (0.402) presented in section 8.2.1. The upper bound on $|\mathcal{P}(\rho, f) - \mathcal{P}|$ can now also be computed, and results in $d_{TV} = 0.088$. The simulations of section 8.2 indicate that the actual error (0.034) is even much smaller than the theoretical upper bound that was obtained.

It is of interest to decide when the Stein-Chen Poisson approximation works satisfactorily. The upper bound at the right hand side of equation (8.30) can be estimated, and a small computation shows that the bound is small when f is at most of the order of $1/\sqrt{N}$. However, as will become clear from the example in section 8.4, a large bound does not necessarily imply a large discrepancy between the Poisson approximation and the simulated data. This is caused by the fact that the d_{TV} as defined in equation (8.30) is a 'worst-case' scenario. Apparently, the error introduced by the Poisson approximation is much smaller than this worst-case error.

8.3.3   Fraction of dopants that are part of a pair-state

Because λ represents the (expected) number of dopant pair-states and k represents the number of dopants present in the crystal, it might be expected that the percentage of dopants that are part of a pair-state can be approximated by

$$\mathcal{Q} \stackrel{?}{=} 2\lambda/k \cdot 100[\%] \, , \tag{8.31}$$

where λ is defined in equation (8.17) and $k = fn$. However, this is not correct. To understand the reason for the discrepancy, the expectation value operator is introduced: the expectation value of x, denoted by $\langle x \rangle$, is defined as [29]

$$\langle x \rangle \equiv \sum_{x:p(x)>0} x\, p(x) \, , \tag{8.32}$$

where $p(x)$ denotes the probability to measure x. It can be seen from equation (8.32) that $\langle x + y \rangle = \langle x \rangle + \langle y \rangle$, but that $\langle x/y \rangle \neq \langle x \rangle / \langle y \rangle$. This then also

explains where the error in equation (8.31) lies: It calculates $\langle 2\lambda \rangle / \langle k \rangle$, while the simulations calculate $\langle 2\lambda / k \rangle$, which is the relevant expectation value.

To calculate the correct expectation value, a general lattice will be studied in a rather abstract way. The formalism discussed here does not depend on the dimensionality of the problem but only on the connectivity structure. As a result, the final solution can be made to work in any dimension or with an arbitrary number of different connectivities. This point may be important for e.g. silicon nanocrystals, where the connectivity is different for the different crystal facets. Furthermore, the evaluation of the pair-state probabilities in a nanowire (no spherical symmetry) is also possible within this framework.

A crystal is studied that consists of n lattice positions, n_b of which are inside (i.e. the bulk) and n_s are on the outside (i.e. the surface). Naturally, $n = n_b + n_s$. The lattice positions on the surface all have C_s nearest neighbors and those in the inside have C_b nearest neighbors. Each of the lattice positions will be replaced by a dopant with probability f. Denote by γ_i the variable that indicates if a dopant is present at the ith lattice position. This results in $\gamma_i = 1$ for all lattice positions that contain a dopant and $\gamma_i = 0$ for all others. The total number of dopants in the lattice, denoted by X, can therefore be written as

$$ X = \sum_{i=1}^{n} \gamma_i \, . \tag{8.33} $$

Furthermore, the variable β_i is introduced which counts the number of nearest-neighbor dopants of a specific lattice position. This β_i can clearly be written as

$$ \beta_i = \sum_{j \in \{\text{NN of } i\}} \gamma_j \, , \tag{8.34} $$

where the summation extends over the nearest-neighbors of i.

Let Y be the number of dopants that are isolated, and let Z_i be its indicator. For all lattice positions that contain a dopant, $Z_i = 1$ if that dopant has no dopants as nearest-neighbors and $Z_i = 0$ if it does. If the ith positions does not contain a dopant then also $Z_i = 0$. This means that Z_i is defined as

$$ Z_i = \begin{cases} 1 & \text{if } (\gamma_i = 1 \wedge \beta_i = 0) \\ 0 & \text{otherwise} \end{cases} \, . \tag{8.35} $$

Now Y can be written, analogously to what was done in equation (8.33),

$$ Y = \sum_{i=1}^{n} Z_i \, . \tag{8.36} $$

In the terminology that was introduced so far, the expectation value of the fraction of dopants that are isolated is given by

$$\mathcal{R} \;=\; \langle \frac{Y}{X} \rangle \,, \tag{8.37}$$

and the expectation value of the fraction of dopants that are not isolated by

$$\mathcal{Q} \;=\; 1 - \mathcal{R} \;=\; 1 - \langle \frac{Y}{X} \rangle \,, \tag{8.38}$$

which is the relevant expectation value for this section. Note that this is not the same as calculating the fraction of dopant pair-states, as equation (8.38) also correctly evaluates triple-states and other (larger) clusters. Because of this, equation (8.38) is expected to be exact, irrespective of the dopant concentration or other material parameters.

To calculate $\mathcal{R}$ a very elegant trick is used,

$$\langle \frac{Y}{X} \rangle \;=\; \langle Y \int_{-\infty}^{0} \mathrm{d}t \, e^{t\,X} \rangle \,, \tag{8.39}$$

which is always valid as long as $X > 0$. To evaluate this integral, one must realize that this integral converges absolutely (the integrant is positive for all t and the total integral is finite) and therefore that the integration can be taken out of the expectation-value operator,

$$
\begin{aligned}
\langle Y \int_{-\infty}^{0} \mathrm{d}t \, e^{t\,X} \rangle &= \langle \int_{-\infty}^{0} \mathrm{d}t \, Y \, e^{t\,X} \rangle \\
&= \int_{-\infty}^{0} \mathrm{d}t \, \langle Y \, e^{t\,X} \rangle \\
&= \int_{-\infty}^{0} \mathrm{d}t \, g(t) \,,
\end{aligned}
\tag{8.40}
$$

where

$$
\begin{aligned}
g(t) &= \langle Y \, e^{t\,X} \rangle \\
&= \langle \sum_{i=1}^{n} Z_i e^{t\,X} \rangle \\
&= \sum_{i=1}^{n} \langle Z_i e^{t\,X} \rangle \,.
\end{aligned}
\tag{8.41}
$$

Because of the absolute convergence, the expectation-value operator and the sum could be interchanged. Now the sum is divided into two parts: one part corresponding to the surface-contribution and one corresponding to the bulk-contribution,

$$g(t) \;=\; \sum_{\text{surface}} \langle Z_i e^{tX} \rangle \;+ \sum_{\text{bulk}} \langle Z_i e^{tX} \rangle \;. \tag{8.42}$$

Each of these two contributions will have to be evaluated separately.

First, the point i is chosen to be on the surface. For this point the expectation value can be calculated directly by conditioning on the specific event that point i contains a dopant and that all of its neighbors do not,

$$\langle Z_i e^{tX} \rangle \;=\; \langle Z_i e^{tX} \mid \gamma_i = 1 \wedge \beta_i = 0 \rangle \cdot \mathbb{P}(\gamma_i = 1 \wedge \beta_i = 0) \;. \tag{8.43}$$

The probability that a specific lattice position contains a dopant is given by f. As this lattice position is on the surface, there will be C_s nearest-neighbors, each of which does not contain a dopant with probability $(1 - f)$. This results in the conditional probability for this event of

$$\mathbb{P}(\gamma_i = 1 \wedge \beta_i = 0) \;=\; f(1 - f)^{C_s} \;. \tag{8.44}$$

The condition $(\gamma_i = 1 \wedge \beta_i = 0)$ implies by definition that $Z_i = 1$, as shown in equation (8.35). The form of X given in equation (8.33) is used. Furthermore, it is known that in this case $\gamma_i = 1$ and that $\gamma_j = 0$ for all j that are nearest-neighbors of i. This means that these terms can be incorporated explicitly into the sum. As a result, equation (8.43) becomes

$$\langle Z_i e^{tX} \rangle \;=\; \big\langle e^{t(1 + \sum_{j \neq i, j \notin \{\text{NN of } i\}} \gamma_j)} \big\rangle \cdot f(1 - f)^{C_s} \;. \tag{8.45}$$

Using that $e^{a+b} = e^a e^b$ and that, because t is not a stochastic variable, $\langle e^t \rangle = e^t$, this equation can be evaluated further to read

$$\langle Z_i e^{tX} \rangle \;=\; f(1 - f)^{C_s} e^t \prod_{\substack{j \neq i \\ j \notin \{\text{NN of } i\}}} \langle e^{t\gamma_j} \rangle \;. \tag{8.46}$$

The product of the expectation values can be evaluated straightforwardly: with probability f there will be a dopant present at any lattice position, generating the exponent-term $e^{t\,1} = e^t$. Analogously, with probability $(1 - f)$ there will be no dopant present at any lattice position, generating the exponent-term $e^{t\,0} = 1$.

The product is evaluated for all n lattice positions, with the exception of the C_s nearest-neighbors and the position i itself. Putting all this together, equation (8.46) becomes

$$\langle Z_i e^{tX} \rangle = f(1-f)^{C_s} e^t \left(f e^t + (1-f) \right)^{n-C_s-1} . \tag{8.47}$$

The evaluation of a point located in the bulk is performed in a very similar way. Again choose a lattice position i and calculate the expectation value,

$$
\begin{aligned}
\langle Z_i e^{tX} \rangle &= \langle Z_i e^{tX} \mid \gamma_i = 1 \wedge \beta_i = 0 \rangle \cdot \mathbb{P}(\gamma_i = 1 \wedge \beta_i = 0) \\
&= f(1-f)^{C_b} \langle e^{t(1+\sum_{j \neq i, j \notin \{\text{NN of } i\}} \gamma_j)} \rangle \\
&= f(1-f)^{C_b} e^t \prod_{\substack{j \neq i \\ j \notin \{\text{NN of } i\}}} \langle e^{t\gamma_j} \rangle \\
&= f(1-f)^{C_b} e^t \left(f e^t + (1-f) \right)^{n-C_b-1} .
\end{aligned}
\tag{8.48}
$$

There are n_s lattice positions on the surface, each having a contribution to $g(t)$ given by equation (8.47), and n_b lattice positions in the bulk, each having a contribution given by equation (8.48) to $g(t)$. Now the fraction of dopants that do not have a dopant as nearest-neighbor can be calculated by evaluating the integral written in equation (8.40),

$$
\begin{aligned}
\langle \frac{Y}{X} \rangle = \int_{-\infty}^{0} \mathrm{d}t &\left\{ n_s f(1-f)^{C_s} e^t \left(f e^t + (1-f) \right)^{n-C_s-1} + \right. \\
&\left. n_b f(1-f)^{C_b} e^t \left(f e^t + (1-f) \right)^{n-C_b-1} \right\} .
\end{aligned}
\tag{8.49}
$$

The evaluation of this integral is left as an exercise for the interested reader. The final result is

$$
\mathcal{R} = \frac{(1-f)^{C_b} - (1-f)^n}{n - C_b} n_b + \frac{(1-f)^{C_s} - (1-f)^n}{n - C_s} n_s . \tag{8.50}
$$

This is probably the most important equation in this section. The result shown here is exact and generally applicable to any system. The extension of this result to include crystal-facets with different (i.e. more than two) connectivities should now also be straightforward. This might for example be interesting in the case of a cubic crystal with different crystal facets.

Using the known forms of n, n_s and n_b, as described in equations (8.12) − (8.14), an expression can be obtained that gives the fraction of dopants that are part of a pair-state in a perfectly spherical zincblende crystal,

$$\mathcal{Q} = 1 - \frac{\pi\psi(2\rho - 1)^3}{8\pi\psi\rho^3 - 6C_b}\left((1-f)^{C_b} - (1-f)^{\frac{4}{3}\pi\psi\rho^3}\right) - \frac{\pi\psi(1 + 6\rho(2\rho - 1))}{8\pi\psi\rho^3 - 6C_s}\left((1-f)^{C_s} - (1-f)^{\frac{4}{3}\pi\psi\rho^3}\right), \quad (8.51)$$

which follows from equation (8.50) and equation (8.38). For very small crystal sizes ($\rho \leq 2$) the approximation given in equation (8.12) begins to lose its validity. As a result, for very small crystal sizes, equation (8.50) will have to be used. However, this is not an important problem, as for these small crystals n, n_b and n_s can easily be computed exactly.

The two most important limits of equation (8.51) have been determined. First of all, the case of maximum dopant concentration yields

$$\lim_{f \to 1} \mathcal{Q} = 1, \quad (8.52)$$

as is of course expected. The infinite crystal limit of equation (8.51) is also interesting. A straightforward evaluation (with the trivial condition $0 < f < 1$) results in

$$\lim_{\rho \to \infty} \mathcal{Q} \propto (1-f)^{C_b}, \quad (8.53)$$

which agrees with the well-known result obtained by R. E. Behringer in 1958 for an infinite perfect crystal [21]. The fact that these two limits indeed agree with the expectation provides further evidence that equation (8.51) is indeed the correct expression for $\mathcal{Q}$.

8.4 Insightful and interesting examples

In this section several examples will be presented that show the usefulness of the mathematical theory developed in the previous part. As a set of typical examples, the probability of finding at least one pair-state and the percentage of dopant ions in pair-states in a ZnSe:Mn^{2+} sample are calculated. The ZnSe lattice has a zincblende structure ($\psi = 4$, $C_b = 12$ and $C_s = 8$) with a lattice parameter $a = 5.6676$ Å (i.e. $r = 3.4$ nm $\Leftrightarrow \rho = 6$) and the Mn^{2+} dopant ions are located on the Zn^{2+} lattice positions. The reader should be aware that this exercise is mainly

Table 8.1: *Results based on a ZnSe nanocrystal with a radius of 3.4 nm and a dopant fraction f. Both the results from the simulations (section 8.2) and from the mathematical formulation (section 8.3) are shown.*

f	k	Simulations		Mathematical formulation		
		$\mathcal{P}(6,\,f)$	$\mathcal{Q}(6,\,f)$	$\mathcal{P}$	d_{TV}	$\mathcal{Q}$
0.002	8	0.073	1.56 %	0.077	$3.19 \cdot 10^{-3}$	1.95 %
0.004	15	0.277	3.82 %	0.274	$2.27 \cdot 10^{-2}$	4.04 %
0.007	26	0.638	6.96 %	0.626	$9.12 \cdot 10^{-2}$	7.19 %
0.009	33	0.789	9.11 %	0.803	$1.51 \cdot 10^{-1}$	9.24 %
0.012	44	0.943	12.3 %	0.944	$2.37 \cdot 10^{-1}$	12.2 %
0.015	55	0.989	15.4 %	0.989	$3.12 \cdot 10^{-1}$	15.1 %
0.02	73	0.999	20.8 %	0.999	$4.22 \cdot 10^{-1}$	19.7 %
0.04	145	1.000	42.2 %	1.000	$8.62 \cdot 10^{-1}$	36.1 %
0.06	217	1.000	63.6 %	1.000	> 1	49.2 %
0.08	289	1.000	85.0 %	1.000	> 1	59.8 %

theoretical: as the size of Mn^{2+} is significantly larger than that of Zn^{2+}, it seems unlikely to assume a random dopant distribution, such as in equation (8.4), which is the basis for all simulations and theory presented so far.

First, an average nanocrystal radius of 3.4 nm is investigated. The results from the simulations presented in sections 8.2.2 and 8.2.3 can be used directly. These nanocrystals contain 3564 lattice positions, 785 (22 %) of which are on the surface of the crystal. Table 8.1 shows both the simulated result and the results obtained in the mathematical formulation. The expectation value for the total number of dopants present in the lattice, k, is also included.

The results from the Stein-Chen Poisson approximation are in very good agreement with the simulation data. Even for the larger dopant fractions, the differences between $\mathcal{P}$ and $\mathcal{P}(6,\,f)$ that are observed remain small. This result is important, because for this ZnSe nanocrystal $N = 20052$, so the total variation norm d_{TV} is expected to become large for $f \gtrsim 0.01$, as can be seen from the data in table 8.1.

The data in table 8.1 show that for $f > 0.02$ the difference between $\mathcal{Q}(6,\,f)$ and $\mathcal{Q}$ increases rapidly. As was expected, $\mathcal{Q}(6,\,f) > \mathcal{Q}$. This result can be understood in terms of the triple-states defined in equation (8.10). At high dopant concentrations, the presence of these triple-states becomes important. The algorithm

developed in the first part of this chapter ignores the possibility of these states and therefore overestimates the contribution of dopants that are part of a cluster (i. e. two or more dopants next to each other) to the fraction of dopants that are part of a pair-state, as was discussed in section 8.2.3.

To show clearly several trends, and provide more proof of the correctness of equations (8.19) and (8.51), figure 8.8(a)−(d) shows several simulation-examples together with their associated theoretical predictions.

Figure 8.8(a) shows the effect of the dopant concentration on the probability of finding at least one pair-state for a nanocrystal of a fixed size $\rho = 6$. Part of this data was also shown in table 8.1. It can be seen directly from figure 8.8(a) that for $f \gtrsim 0.01$ the total variation norm indeed becomes large (indicated by the dashed lines, which represents the confidence interval: the theoretical prediction plus or minus half of the total variation norm). However, it is also clear from this figure that the prediction for the probability of finding at least one pair-state in the nanocrystal based on the Stein-Chen Poisson approximation remains very accurate for all dopant concentrations simulated. This proves that the Poisson approximation will also yield reliable data for higher dopant fractions. Furthermore, it can be clearly seen that there is a significant influence of the surface lattice-positions (with their reduced probability for pair-state formation) on the total pair-formation probability from the dotted line. This line is a prediction of $\mathcal{P}(\rho, 0.015)$ without taking the reduced connectivity of a lattice position on the surface of the crystal into account (i.e. equation (8.19) is evaluated with the physically unrealistic condition that $C_s = C_b = 12$).

Figure 8.8(b) shows the strong influence of the ratio of surface to volume lattice positions in the crystal on the total probability of finding at least one dopant pair-state. In this figure the dopant fraction in the nanocrystal is fixed at $f = 0.015$, while the crystal size is varied. Also here a large influence of fraction of surface lattice-positions on the pair formation probability can be seen from the dotted line, which shows the expected result without taking the reduced connectivity of a lattice position on the surface of the crystal into account. The line through the data points is a prediction of the simulation data using the Stein-Chen Poisson theory described previously. The prediction from the theory gives the exact same trend as the simulation data. The part with $\rho < 2$ shows no data points from the simulations because in this range f is so small that the expectation value for the number of dopants present in the crystal becomes significantly smaller than 2. At two specific crystal sizes, there are two simulation data points per crystal size. They represent results for the dopant concentrations closest to $f = 0.015$.
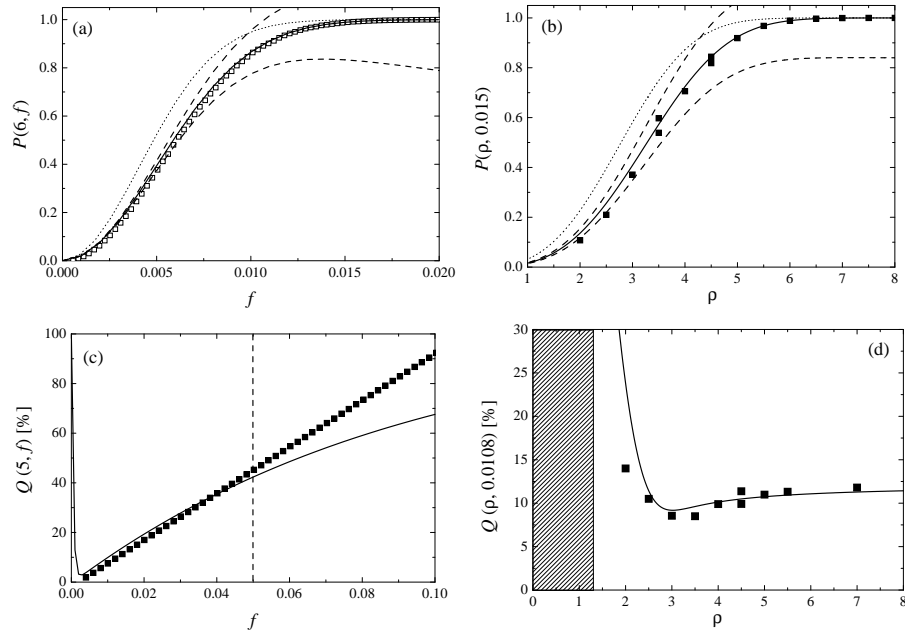
Figure 8.8: *(a) The probability of finding at least one pair-state in a nanocrystal of size $\rho = 6$ as a function of the dopant concentration. (b) The same, but now as a function of the crystal size for fixed dopant concentration $f = 0.015$. The lines through the data in (a) and (b) represent the prediction from equation (8.19) based on the Stein-Chen Poisson approximation and the dashed lines indicate the lines $\mathcal{P} + \frac{1}{2}d_{TV}$ and $\mathcal{P} - \frac{1}{2}d_{TV}$ and can be considered the confidence interval. The dotted lines indicate the expected result if the surface contribution is ignored. (c) The percentage of dopants that are part of a pair-state in a nanocrystal of size $\rho = 5$ as a function of the dopant concentration. (d) The same, but now the dopant concentration is fixed at $f = 0.0108$ and the crystal size is varied. The lines in figures (c) and (d) are the theoretical predictions from equation (8.51). The data-points in all figures are the results of the simulations presented in the first part of this chapter.*

The data shown in figure 8.8(c) provide evidence of the presence of triple-states at high dopant concentrations. In this figure the percentage of dopants that are part of a pair-state is shown as a function of the dopant concentration, for nanocrystals with a radius of $\rho = 5$. As was already shown in figure 8.6, the simulation data indicates that $\mathcal{Q}(5, f)$ is linear in f. The prediction from equation (8.51) indicates that this is indeed the case for dopant fractions below roughly 5 %. However, for large

dopant concentrations ($f > 0.05$, as indicated by the dashed line), a significant deviation of the linearity is observed. The calculation that led to equation (8.51) takes triple-states and higher order contributions into account correctly, whereas the simulations are known to overestimate their contribution to the fraction of dopants that are part of a pair-state. Therefore it is expected that $\mathcal{Q} < \mathcal{Q}(5, f)$, which is in agreement with the data shown in figure 8.8(c). As a result, the fact that for large f the prediction becomes sub-linear must be related to the formation of dopant triple-states.

Finally, a very counter-intuitive observation can be drawn from figure 8.8(d). The percentage of dopants that are part of a pair-state is shown as a function of the crystal size for a fixed dopant concentration $f = 0.0108$. It is clear from this figure that the concentration does *not* increase or decrease monotonously for increasing crystal size. The effect may be related to the fact that the expectation value for the number of dopants in the lattice (for constant f) increases with the cube of the crystal size, while the decrease of the fraction of lattice positions present on the surface of the nanocrystal is a more complicated function of the crystal size, as was shown in equation (8.15). The prediction of equation (8.51) agrees quite well with the data and is able to predict the observed trend: as the crystals become larger, the fraction of dopants that are part of a pair-state decreases, until a minimum is reached. From this minimum onward the fraction increases again and converges to the bulk value $(1 - f)^{C_b}$.

At very small crystal sizes ($\rho \approx 1.5$) a steep increase in $\mathcal{Q}$ is observed. This feature is merely an artifact of the the calculation that led to equation (8.51): for very small crystals, the expected number of dopants goes to zero. Therefore the number of pair-states also goes to zero. As a result, there are no dopants that are part of a pair-state and also no dopants that are isolated. This implies that $\mathcal{Q} = 0$ and $\mathcal{R} = 0$, which leads to a contradiction because of the fact that $\mathcal{Q} = 1 - \mathcal{R}$, as was defined in equation (8.38). At this point, equation (8.51) breaks down and can no longer be used (indicated by the dashed box). This is however only a mathematical problem, as the physical situation represents a lattice with no dopant ions. The observant reader can see the same problem emerging in figure 8.8(c) for $f \approx 0$.

It is important to stress that the lines through the simulation data shown in figure 8.8(a) $-$ (d) are not fits, they are theoretical predictions. The excellent agreement between the simulations and the theory suggests that the theory is valid in any crystal structure. Therefore, simulations of other types of nanocrystals are not required. All that remains now is a beautiful experiment to verify the correctness of equation (8.19) and equation (8.51). For such an experiment, one could think of

a rare-earth doped rare-earth oxide nanocrystal, such as Y_2O_3:Eu^{3+}. The reason to use rare-earths is the chemical equivalence of most of the rare-earth elements. As a result, preferential pair-formation is not expected and equations (8.19) and (8.51) should therefore be valid. As the actual number of dopants in a nanocrystal has a binomial distribution, many nanocrystals of identical size and (synthesized) dopant concentration will have to be investigated to obtain the high-quality statistics required to verify this theory.

8.5 Preferential pair-formation

A logical follow-up of the work discussed in this chapter, would be to include the concept of preferential pair-formation. This is interesting and important as many dopants actually tend to cluster in a material. For example, Mn^{2+} dopants in ZnSe nanocrystals will preferentially form dopant pair-states, as was demonstrated in chapter 5. Simulations of preferential pair-formation can be accomplished in many different ways. The method presented here is conceptually the simplest and works by introducing a normalized weight-distribution set $S = \{w_i; i \in [1, n]\}$, that specifies the probability of finding a dopant at any lattice position. The values of w_i are defined on the set of vectors that point to the lattice positions (the $\mathbf{p}_i$) and are elements of $[0, 1]$.

First, the lattice is defined via the construction of the set $F = \{\mathbf{p}_i; i \in [1, n]\}$, similar to the set K introduced at the beginning of this chapter. Next, the first of the k dopants is placed at random (i.e. $\forall i \in [1, n] : w_i = 1/n$) in the crystal. This results in one dopant present in the lattice: $k_{\text{in}} = 1$. The set $G = \{\mathbf{q}_i; i \in [1, k_{\text{in}}]\}$ points to all the dopants present in the crystal. Naturally, the set $G \subset F$ should not contain duplicate vectors. The asymmetric matrix Υ is now defined as

$$\Upsilon_{ij} \equiv |\mathbf{p}_i - \mathbf{q}_j| = \sqrt{\sum_{\alpha=1}^{3} [(\mathbf{p}_i)_\alpha - (\mathbf{q}_j)_\alpha]^2} \,, \qquad (8.54)$$

where it should be noted that Υ is not a square matrix, but a $(n \times k_{\text{in}})$ matrix. The nearest-neighbor distance is still denoted by ζ as defined in equation (8.3).

To evaluate correctly the preferential pair-formation process, the positive constant Γ is introduced, which represents the "additional" probability for a dopant to be located next to another dopant with respect to another lattice position. The process of finding the next dopant lattice position is schematically shown in figure 8.9 and consists of the following steps:
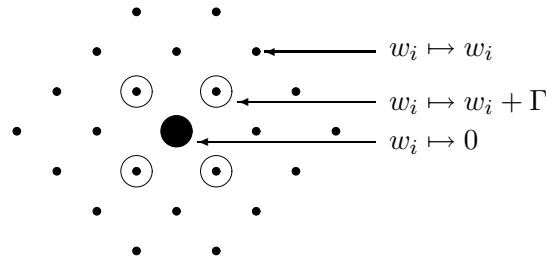
Figure 8.9: *Schematic representation of preferential pair-formation. The small dots represent the lattice positions and the large dot indicates the dopant present at this lattice position in the crystal. The encircled lattice positions have relative "additional probability" Γ to be occupied by a dopant ion, in accordance with equation (8.55).*

1. The elements of the set S are mapped onto themselves according to the transformation rules

$$w_i \mapsto \quad 0 \quad \text{if } \mathbf{p}_i \in G \tag{8.55}$$

$$w_i \mapsto \quad w_i + \Gamma \quad \text{if } (\Upsilon_{ij} = \zeta \ \wedge \ w_i \neq 0) \tag{8.56}$$

$$w_i \mapsto \quad w_i \quad \text{otherwise} \tag{8.57}$$

which are evaluated for every $j \in [1, k_{\text{in}}]$. Condition (8.55) results in

$$\forall \mathbf{p}_i \in G : \ w_i = 0 . \tag{8.58}$$

This is also expected, as only one dopant is allowed per lattice position. Finally, the set of weights is renormalized by means of

$$w_i \ \mapsto \ w_i \left(\sum_{i=1}^{n} w_i \right)^{-1} , \tag{8.59}$$

as this conserves probability.

2. The next dopant position is now determined by choosing a random number on the closed interval $[0, 1]$ constructed from the set of weights S and finding the accompanying lattice position $\mathbf{p}_i$. This procedure is shown in figure 8.10. Note the presence of one dopant in this lattice, signified by $w = 0$.

Figure 8.10: *Construction used to choose the next dopant. The total length of the line is 1 and the (available) lattice positions $\mathbf{p}_i$ have associated weights w_i.*

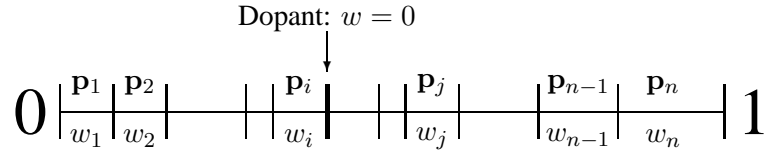3. Since now k_{in} has increased ($k_{\mathrm{in}} \mapsto k_{\mathrm{in}} + 1$), the Υ matrix needs to be re-calculated, by means of equation (8.54). Note that this matrix will increase in size. Next, the weight distribution is reconstructed by taking into account the new dopant in the lattice by evaluating equations (8.55) through (8.58) and renormalizing the set.

This procedure is repeated until $k_{\mathrm{in}} = k$.

Finally, it should be noted that when a lattice position $\mathbf{p}_i$ has m valid solutions for $\Upsilon_{ij} = \zeta$ it need not be the case[1] that $w_i \mapsto w_i + m\Gamma$, but this is ignored here. After the construction of the dopant distribution in the nanocrystal with given size, dopant concentration and preferential pair-state parameter Γ, equations (8.6) and (8.7) can be used to calculate $\mathcal{P}(\rho, f, \Gamma)$ and $\mathcal{Q}(\rho, f, \Gamma)$. Just as in the previous part of this chapter, triple-states and higher-order contributions are ignored. This will only give valid results in the low dopant regime. Correctly evaluating the triple-states and other clusters is very time consuming to simulate. It seems quite possible to extend the methods developed in section 8.3 to analytically include preferential pair-formation, but this was not investigated.

It is important to realize that this method relies on the fact that the sets F and S are stochastic sets. To understand what this means, the transformation operator T_{ij} is defined to work on a set $\{x_1, x_2, x_3, \ldots\}$ as

$$T_{ij}\left[\{\ldots, x_i, \ldots, x_j, \ldots\}\right] = \{\ldots, x_j, \ldots, x_i, \ldots\} \ . \tag{8.60}$$

The stochastic nature of the sets F and S implies that for any couple $i, j \in [1, n]$ the

---

[1] On the one hand, one can think of for instance Coulomb screening effects that decrease the additional probability obtained for a lattice position with m dopant neighbors. Or, on the other hand, one could think of a large size difference between the dopant and the lattice ion, which results in the segregation of all dopant ions to one position in the lattice, which increases the additional probability.

probabilistic results (i.e. the probability for the formation of a pair-state $\mathcal{P}(\rho, f, \Gamma)$ and the percentage of dopants in pair-states $\mathcal{Q}(\rho, f, \Gamma)$ respectively) computed from the sets F and S should be the same as the results from the sets $T_{ij}[F]$ and $T_{ij}[S]$. This is required for the construction presented in figure 8.10 to work properly and can be tested straightforwardly. This fact can also be used to speed up the simulations: the relevant vectors (i.e. the ones with additional probability) can be grouped to form a subset of F on which the transformations can be performed quicker. This is only efficient as long as $k \ll n$. No measurements on doped nanocrystalline materials are available that give reasonably precise fractions of dopant pair-states and dopant single-ions. Therefore, attempts to compute $\mathcal{P}(\rho, f, \Gamma)$ and $\mathcal{Q}(\rho, f, \Gamma)$ have not been pursued at this point.

8.6 Conclusions

This chapter discusses an algorithm, simulations and a mathematical approximation for determining the probabilities of finding dopant pair-states in a nanocrystal that have general applicability in nanocrystal science. The probability of finding at least one pair-state and the percentage of dopants that are part of a pair-state are calculated explicitly for a nanocrystal with the zincblende structure. The results are made independent of the lattice parameter and the adaptation of the algorithm to other crystal structures is possible.

The fraction of lattice positions present on the surface of the nanocrystal is simulated and compared with a first-order theory. Very good agreement is reached. Through Stein-Chen Poisson approximation, the probability of finding at least one pair-state is estimated and an upper bound for the error introduced by this approximation is provided. Furthermore, an analytical expression for the fraction of dopant ions that are part of a pair-state is derived. Both the approximation and the analytical expression are closed-form equations that are applicable to any nanocrystal, regardless of size and crystallographic structure. These results are valid for all dopant fractions. Finally, a general algorithm is sketched that will be able to include the concept of preferential pair-formation by means of an "additional-probability" parameter Γ.

References

[1] R. Rosetti, R. Hull, J. M. Gibson and L. E. Brus, *J. Chem. Phys.* **82**, 552 (1985).

[2]   L. Brus, *J. Phys. Chem.* **90**, 2555 (1986).

[3]   A. Henglein, *Chem. Rev.* **89**, 1861 (1989).

[4]   Y. Wang and N. Herron, *J. Phys. Chem.* **95**, 525 (1991).

[5]   B. O. Dabbousi, M. G. Bawendi, O. Onitsuka and M. F. Rubner, *Appl. Phys. Lett.* **66**, 1316 (1995).

[6]   N. C. Greenham, X. Peng and A. P. Alivisatos, *Phys. Rev. B* **54**, 17628 (1996).

[7]   R. Bhargava, *J. Lumin.* **70**, 85 (1996).

[8]   J. F. Suyver, S. F. Wuister, J. J. Kelly and A. Meijerink, *Phys. Chem. Chem. Phys.* **2**, 5445 (2000). See also chapter 5.

[9]   D. G. Thomas, J. J. Hopfield and C. J. Frosch, *Phys. Rev. Lett.* **15**, 857 (1965).

[10] J. I. Pankove, *Optical Processes in Semiconductors*, Dover Publications: New York, page 61 (1971).

[11] C. R. Ronda and T. Amrein, *J. Lumin.* **69**, 245 (1996).

[12] J. Ferguson, H. J. Guggenheim and Y. Tanabe, *J. Phys. Soc. Jpn.* **21**, 692 (1966).

[13] B. C. Barthou, J. Benoit, P. Bennalloul and A. Morell, *J. Electrochem. Soc.* **141**, 524 (1994).

[14] A. L. N. Stevels and A. T. Vink, *J. Lumin.* **8**, 443 (1974).

[15] A. A. Maksimov, G. Bacher, A. McDonald, V. D. Kulakovskii, A. Forchel, C. R. Becker, G. Landwehr and L. W. Molenkamp, *Phys. Rev. B* **62**, R7767 (2000).

[16] J. A. Gupta, D. D. Awschalom, X. Peng and A. P. Alivisatos, *Phys. Rev. B* **54**, R10421 (1999).

[17] K. Riwotzki and M. Haase, *J. Phys. Chem. B* **102**, 10129 (1998).

[18] H. Eilers and B. M. Tissue, *Chem. Phys. Lett.* **251**, 74 (1996).

[19] H. S. Yang, K. S. Hong, S. P. Feofilov, B. M. Tissue, R. S. Meltzer and W. M. Dennis, *J. Lumin.* **83-84**, 139 (1999).

[20] G. Blasse and B. C. Grabmaier, *Luminescent Materials*, Springer-Verlag: Berlin, section 5.3.1 (1994).

[21] R. E. Behringer, *J. Chem. Phys.* **29**, 537 (1958).

[22] M. M. Kreitman and D. L. Barnett, *J. Chem. Phys.* **43**, 364 (1965).

[23] N. B. Hannay, *Treatise on Solid State Chemistry: Defects in Solids*, Plenum Press: New York, page 373 (1975).

[24] W. Jones and N. H. March, *Theoretical Solid State Physics*, John Wiley & Sons: London, pages 128 and 1082 (1973).

[25] D. Adler, H. Fritzsche and S. R. Ovshinsky, *Physics of Disordered Materials*, Plenum Press: New York, page 144, 696 (1985).

[26] J. M. Ziman, *Principles of the Theory of Solids*, Cambridge University Press: New York, chapter 1 (1972).

[27] J. K. A. Bleasdale and J. A. Nelder, *Nature (London)* **188**, 342 (1960).

[28] A. D. Barbour, L. Holst and S. Janson, *Poisson Approximation*, Clarendon Press: Oxford, section 2.3 (1992).

[29] S. Ross, *A first course in probability, sixth edition*, Prentice-Hall: New Jersey, section 4.3 (2002). Note that equation (8.31) only applies to discrete random variables.

A   Mathematica notebook used for simulations

In this appendix, the listing is presented that was used for the calculation of $\mathcal{Q}(\rho, k)$. The output is written to four different files on disk, as the *Mathematica* kernel does not allow other (graphical) means of output. Only one value is written to each of these files for a given crystal size and dopant concentration. The file-names (shown at the end of the listing) clearly indicate the meaning of each of these values.

   A number of (temporary) variables are defined or introduced in the listing. The symbols n, ρ, k and f retain the physical meaning that they were given earlier in this chapter and the user must make a choice regarding the values of ρ and k. Throughout the listing a math-type symbol (x) is used to denote an integer. A set of numbers and a set of vectors is denoted as $\bar{x}$ in this listing. Italic text is used for comments in the listing.

Create a sphere of size $(\rho + 2) \times (\rho + 2) \times (\rho + 2)$ filled with a cubic lattice:
$\bar{b}$ = Table[If[$\sqrt{i^2 + j^2 + k^2} \leq \rho, 0, 9$], $\{i, -\rho - 1, \rho + 1\}$,
    $\{j, -\rho - 1, \rho + 1\}$, $\{k, -\rho - 1, \rho + 1\}$];
Change the cubic lattice to an fcc lattice within this sphere:
For[$i = 1$, $i < 2\rho + 2$, $i+ = 2$,
    For[$j = 1$, $j < 2\rho + 2$, $j+ = 2$,
        For[$k = 1$, $k < 2\rho + 2$, $k+ = 2$,
            If[$\bar{b}[[i]][[j]][[k]]== 0$,
                $\bar{b}$ = ReplacePart[$\bar{b}$, 1, $\{i, j, k\}$],],];
            If[$j + 1 < 2\rho + 2$ && $k + 1 < 2\rho + 2$, If[$\bar{b}[[i]][[j]][[k]]== 0$,
                $\bar{b}$ = ReplacePart[$\bar{b}$, 1, $\{i, j + 1, k + 1\}$],],],];
            If[$i + 1 < 2\rho + 2$ && $k + 1 < 2\rho + 2$, If[$\bar{b}[[i + 1]][[j]][[k + 1]]== 0$,
                $\bar{b}$ = ReplacePart[$\bar{b}$, 1, $\{i + 1, j, k + 1\}$],],],];
            If[$i + 1 < 2\rho + 2$ && $j + 1 < 2\rho + 2$, If[$\bar{b}[[i + 1]][[j + 1]][[k]]== 0$,
                $\bar{b}$ = ReplacePart[$\bar{b}$, 1, $\{i + 1, j + 1, k\}$],],];]]];
Define the cation and the anion sites in the lattice:
$\bar{c}$ = Table[0, $\{i, 1, (2\rho + 4)^3\}$, $\{j, 1, 3\}$];
$\bar{d}$ = Table[-1, $\{(2\rho + 4)^3\}$];
$s = 0$;
$n = 0$;
For[$i = 1$, $i < 2\rho + 2$, $i + +$,
    For[$j = 1$, $j < 2\rho + 2$, $j + +$,
        For[$k = 1$, $k < 2\rho + 2$, $k + +$,
            $s + +$;
            If[$\bar{b}[[i]][[j]][[k]]== 1$,
                $\bar{c}$ = ReplacePart[$\bar{c}$, $i - \rho - 1$, $\{s, 1\}$];
                $\bar{c}$ = ReplacePart[$\bar{c}$, $j - \rho - 1$, $\{s, 2\}$];
                $\bar{c}$ = ReplacePart[$\bar{c}$, $k - \rho - 1$, $\{s, 3\}$];
                $n + +$;

$\bar{\mathbf{d}}$ = ReplacePart[$\bar{\mathbf{d}}$, s, n],

$\bar{\mathbf{c}}$ = ReplacePart[$\bar{\mathbf{c}}$, 0, $\{s, 1\}$];

$\bar{\mathbf{c}}$ = ReplacePart[$\bar{\mathbf{c}}$, 0, $\{s, 2\}$];

$\bar{\mathbf{c}}$ = ReplacePart[$\bar{\mathbf{c}}$, 0, $\{s, 3\}$]]]]];

Now the cation fcc lattice positions will be chosen. They are defined as $\bar{\mathbf{K}}$*, identical to the set K which was defined above equation (8.2) at the beginning of this chapter.*

$i = 1$;

$\bar{\mathbf{K}}$ = Table[-1, $\{i, 1, n\}$, $\{j, 1, 3\}$];

While[$\bar{\mathbf{d}}[[i]] \neq -1$,

   $\bar{\mathbf{K}}$ = ReplacePart[$\bar{\mathbf{K}}$, $\bar{\mathbf{c}}[[\bar{\mathbf{d}}[[i]]]][[1]]$, $\{i, 1\}$];

   $\bar{\mathbf{K}}$ = ReplacePart[$\bar{\mathbf{K}}$, $\bar{\mathbf{c}}[[\bar{\mathbf{d}}[[i]]]][[2]]$, $\{i, 2\}$];

   $\bar{\mathbf{K}}$ = ReplacePart[$\bar{\mathbf{K}}$, $\bar{\mathbf{c}}[[\bar{\mathbf{d}}[[i]]]][[3]]$, $\{i, 3\}$];

   $i + +$;];

This is the actual calculation algorithm. Here $L \subset K$ is chosen 10^5 times and the number of nearest neighbor dopant pair-states is counted each time, the sum of which is denoted by t.

$t = 0$;

$\bar{\mathbf{L}}$ = Table[-1, $\{i, 1, k\}$, $\{j, 1, 3\}$];

For[$g = 1$, $g \leq 10^5$, $g + +$,

   $\bar{\mathbf{m}}$ = Table[-1, $\{i, 1, n + 1\}$];

   $j = 1$;

   Choose the set $\bar{\mathbf{L}}$, a random subset of $\bar{\mathbf{K}}$, with a total of k vectors.

   While[$j \neq k + 1$,

     i=Random[Integer, $\{1, n\}$];

     If[$\bar{\mathbf{m}}[[i]] == -1$,

       $\bar{\mathbf{m}}$ = ReplacePart[$\bar{\mathbf{m}}$, 0, i];

       $\bar{\mathbf{L}}$ = ReplacePart[$\bar{\mathbf{L}}$, $\bar{\mathbf{K}}[[i]][[1]]$, $\{j, 1\}$];

       $\bar{\mathbf{L}}$ = ReplacePart[$\bar{\mathbf{L}}$, $\bar{\mathbf{K}}[[i]][[2]]$, $\{j, 2\}$];

       $\bar{\mathbf{L}}$ = ReplacePart[$\bar{\mathbf{L}}$, $\bar{\mathbf{K}}[[i]][[3]]$, $\{j, 3\}$];

       $j + +$,]];

   Find the number of nearest-neighbor dopant pair-states:

   For[$i = 1$, $i \leq k$, $i + +$,

     For[$j = i + 1$, $j \leq k$, $j + +$,

       If[$(\bar{\mathbf{L}}[[i]][[1]] - \bar{\mathbf{L}}[[j]][[1]])^2 + (\bar{\mathbf{L}}[[i]][[2]] - \bar{\mathbf{L}}[[j]][[2]])^2 +$

       $(\bar{\mathbf{L}}[[i]][[3]] - \bar{\mathbf{L}}[[j]][[3]])^2 \leq 2$, $t + +$,];]]];

Output to disk:

$\rho >>>$ Particle_Radius.dat;

$n >>>$ Number_Of_Lattice_Positions.dat;

$k >>>$ Number_Of_Dopants_In_The_Lattice.dat;

$t/10^5 >>>$ Number_Of_Dopant_Pair_States_Per_Nanocrystal.dat;

B The binomial and Poisson distributions

The goal of this appendix is to prove that the binomial distribution $\mathcal{B}(n, k, p)$ converges to the Poisson distribution $P(n, k, p)$ in the limit $n \to \infty$. The binomial distribution is defined by

$$\mathcal{B}(n, k, p) \equiv \left(\begin{array}{c} n \\ k \end{array} \right) p^k (1 - p)^{n-k} = \frac{n!}{k!(n-k)!} p^k (1 - p)^{n-k} , \qquad (\text{B.1})$$

and the Poisson distribution is defined by

$$P(n, k, p) \equiv \frac{(np)^k}{k!} e^{-np} . \qquad (\text{B.2})$$

The limit $n \to \infty$ is now taken by keeping $\lambda \equiv np$ constant and leaving k fixed. As a result, $p \mapsto \lambda/n$ and equation (B.1) becomes

$$
\begin{aligned}
\lim_{n\to\infty} \mathcal{B}(n, k, p) &= \lim_{n\to\infty} \frac{n!}{k!(n-k)!} (\lambda/n)^k (1 - \lambda/n)^{n-k} \\
&= \lim_{n\to\infty} \frac{n!}{k!(n-k)!} \frac{(\lambda/n)^k}{(1 - \lambda/n)^k} (1 - \lambda/n)^n \\
&= \lim_{n\to\infty} \frac{\lambda^k}{k!} (1 - \lambda/n)^n \frac{n!}{n^k(n-k)!(1 - \lambda/n)^k} \\
&= \lim_{n\to\infty} \frac{\lambda^k}{k!} (1 - \lambda/n)^n \frac{\prod_{i=1}^{k}(n - k + i)}{(n - \lambda)^k} \\
&= \frac{\lambda^k}{k!} e^{-\lambda} \\
&= \frac{(np)^k}{k!} e^{-np} \\
&= P(n, k, p) . \qquad (\text{B.3})
\end{aligned}
$$

The step from the fourth to the fifth line in equation (B.3) uses the fact that

$$\lim_{n\to\infty} (1 - \lambda/n)^n = e^{-\lambda} , \qquad (\text{B.4})$$

and that

$$\lim_{n\to\infty} \frac{\prod_{i=1}^{k}(n - k + i)}{(n - \lambda)^k} = 1 . \qquad (\text{B.5})$$

This completes the proof.

Summary

This thesis deals with the properties of semiconductor nanocrystals (ZnS or ZnSe) in the size range (diameter) of 2 nm to 10 nm. The nanocrystals under investigation are doped with the transition metal ions manganese or copper. Besides the general introduction in chapter 1, dealing mainly with an overview of the field of doped semiconductor nanocrystals, this thesis consists of seven chapters, which can roughly be divided into three parts. The common goal of the first and second parts is to study photoluminescence and electroluminescence from doped ZnS and ZnSe nanocrystals, while the third part of this thesis describes simulations and theoretical work on the distribution of dopant ions in nanocrystals.

The first part starts with chapter 2, which describes the influence of the synthesis conditions on the properties of ZnS:Mn^{2+} nanocrystals. For the syntheses discussed, different Mn^{2+} precursors and different ratios of the precursor concentrations $[S^{2-}]$ / $[Zn^{2+}]$ were used. No influence of the Mn^{2+} precursor was observed, but on going from an excess of $[Zn^{2+}]$ precursor to an excess of $[S^{2-}]$ precursor, the particle diameter increases sharply by about 1 nm. Photoluminescence measurements showed the absence of the ZnS related emission when an excess $[S^{2-}]$ is used during the synthesis of the nanocrystals. The quenching of the ZnS luminescence at room temperature is attributed to the thermally activated detrapping of a bound hole from a sulfur vacancy. The detailed luminescence mechanism is described in detail for the Mn^{2+} and the ZnS emissions.

From the photoluminescence emission spectra recorded between 4 K and 300 K it is concluded that the bandwidth and the spectral position of the two emission bands observed in these ZnS:Mn^{2+} nanocrystals (related to ZnS and Mn^{2+}) change as a function of the temperature. In chapter 3, this effect is investigated in detail. The shift and the broadening of the Mn^{2+} related emission can be explained by theoretical models and parameters for electron-phonon coupling that are similar to those for bulk ZnS. For the ZnS related emission the shift to lower energies follows the decrease in bandgap of bulk ZnS with increasing temperature. The width of the

ZnS related emission band decreases as the temperature is raised. This anomalous behavior is explained by inhomogeneous broadening at low temperatures.

In chapter 4, the last chapter on nanocrystalline $ZnS:Mn^{2+}$ in this thesis, the photoelectrochemical properties of electrodes of nanocrystalline $ZnS:Mn^{2+}$ deposited on SnO_2:F coated glass are presented and discussed. Both anodic and cathodic photocurrent is observed. This is direct evidence for the nanocrystalline nature of the system. Due to the unfavorable kinetics of electron and hole transfer, the photocurrent is small and most of the charge carriers generated by illumination recombine. Decomposition of the ZnS into elementary Zn and S^{2-} in solution was also observed at negative potential which limits the stability of the electrode. No electroluminescence was observed.

The second part of this thesis starts with chapter 5, which describes the synthesis and luminescence properties of nanocrystalline $ZnSe:Mn^{2+}$ prepared via a high-temperature synthesis in a dry-nitrogen atmosphere. The ZnSe and Mn^{2+} related emissions can both be excited via the ZnSe host lattice. The Mn^{2+} emission wavelength and the associated luminescence decay time depend on the concentration of Mn^{2+}, which indicates the (preferential) formation of Mn^{2+} pair-states. Temperature-dependent photoluminescence spectra and photoluminescence lifetime measurements are also presented and the temperature dependence of the Mn^{2+} emission energy and bandwidth is explained by electron-phonon coupling to an optical phonon of the ZnSe host lattice.

Chapter 6 describes the synthesis, growth and luminescence of nanocrystalline ZnSe:Cu. During growth, samples are taken and the luminescence is studied as a function of the particle size. The transition between two growth-mechanisms is observed. In the first regime growth proceeds by the reaction of precursors, while Ostwald ripening is probably responsible for the growth in the long time range. The growth-rate of the nanocrystals is strongly dependent on the synthesis temperature. The size of the crystals influences both the ZnSe and the Cu^{2+} luminescence energies due to the quantum confinement. Temperature-dependent measurements of the luminescence intensity, lifetime and peak positions are described. The quenching of the Cu^{2+} related luminescence and concomitant decrease of the lifetime is related to detrapping of an electron from a Coulomb-bound electron-hole pair. The detailed luminescence mechanism is described in detail for the Cu^{2+} and the ZnSe related emissions.

The second part of this thesis ends with chapter 7. In this chapter, one of the goals of this thesis, electroluminescence of nanocrystalline electrodes, is achieved. First, the electrochemistry of *n*-type bulk ZnSe crystals is investigated in two dif-

ferent electrolytes. The flat band potential of ZnSe is found to be -1.71 V (vs. NHE) in an indifferent aqueous electrolyte and -1.19 V (vs. NHE) in dry acetonitrile. Electroluminescence measurements on bulk ZnSe in the aqueous electrolyte (containing persulphate) show a broad orange emission band from these electrodes. Electrodes of ZnSe:Cu nanocrystals on a transparent conducting substrate (indium tin oxide) were fabricated and the potential dependence of the photoluminescence of these electrodes in an aqueous electrolyte was studied. Electroluminescence of the ZnSe:Cu nanocrystalline electrodes was observed but the efficiency was likely to be low.

The third part of this thesis consists only of one chapter. Chapter 8 does not involve experiments, rather simulations and a mathematical theory are presented in order to calculate the probability for dopant pair-state formation in a nanocrystal. Knowing this probability is interesting because for certain dopants luminescence properties of single-ions and pair-states of dopant ions differ markedly. As it turns out, the probability for pair-state formation is size dependent due to the changing surface to volume ratio as a function of the crystal size. In the simulations, the probability of finding at least one pair-state in the nanocrystal and the concentration of ions in pair-states were calculated on the basis of a statistical average of $1 \cdot 10^5$ simulations for the same crystal size and dopant concentration. The chapter then continues with a technical part discussing how these results can be approximated (through Stein-Chen Poisson approximation for the probability of finding at least one pair-state) and predicted (by means of an exact analytical expression for the concentration of ions in pair-states) without simulations. These results are very powerful, as they were derived for a general crystal structure and are dependent on the connectivity structure, dopant concentration and crystal size. Therefore, these results are expected to be valid for any nanocrystal and no further simulations will be required. The chapter ends with the basis for an algorithm to simulate pair-state probabilities when preferential pair-formation is included.

After these eight chapters, the thesis ends with several obligatory sections: a summary in English and one in Dutch, a list of publications and conference visits, the acknowledgements in Dutch and a curriculum vitae in Dutch.

Samenvatting

Dit proefschrift behandelt de eigenschappen van een speciale klasse van halfgeleiders (halfgeleiders zijn materialen die veel slechter geleiden dan een metaal, maar nog altijd veel beter dan een isolator): de *nanokristallen*. Nanokristallen bezitten, net als een gewoon kristal, een strikte periodiciteit in het kristalrooster. Het bijzondere van nanokristallen is dat ze heel erg klein zijn: typisch slechts enkele nanometers. Een nanometer is ´e´en miljoenste van ´e´en millimeter. Dit betekent dat er zo'n 50.000 nanokristallen in een rij tegen elkaar aan zouden moeten liggen om de dikte van een mensenhaar te krijgen!

Er is iets speciaals aan de hand met nanokristallen. Normaliter is het zo dat de eigenschappen van een materiaal niet veranderen als de grootte van het materiaal veranderd wordt. Voor nanokristallen geldt dit niet. Als een nanokristal kleiner gemaakt wordt, veranderen de eigenschappen van het materiaal drastisch. Dit is duidelijk te zien aan de kleur van het materiaal, die sterk verandert doordat de absorptie van licht naar hogere energie verschuift als de deeltjes kleiner worden. Ook andere optische en elektrische eigenschappen kunnen sterk afhankelijk zijn van de grootte van de halfgeleider.

In dit proefschrift worden de eigenschappen van *gedoteerde* nanokristallen bestudeerd, zoals bijvoorbeeld een nanokristal van zinksulfide (ZnS) met een klein percentage mangaan (Mn) op de zink-posities van het kristalrooster. Dit kristal wordt mangaan-gedoteerd zinksulfide, ofwel $ZnS:Mn^{2+}$, genoemd. Het mangaan is tweevoudig geïoniseerd (Mn^{2+}) en zit op een zink-positie (welke ook tweevoudig geïoniseerd is) zodat het kristal ladingsneutraal blijft. Aan de ingebouwde doteringsionen kan luminescentie-*spectroscopie* gedaan worden, aangezien deze ionen licht uitzenden. Dit wil zeggen dat, als er licht van een goed gekozen kleur op het kristal geschenen wordt, er licht van een andere kleur door het doteringsion uitgezonden wordt. Natuurlijk zijn er vele toepassingen te verzinnen voor dit soort materialen, zoals bijvoorbeeld in de verlichtingsindustrie of voor een nieuwe generatie beeldschermen.

185

Het onderzoek dat in dit proefschrift beschreven wordt is vrij fundamenteel van aard, maar wel met een duidelijke toepassing in het achterhoofd: het maken van een nanokristallijn elektroluminescerend materiaal. Met dit materiaal kan vervolgens, in combinatie met een geleidend polymeer, een elektroluminescerend scherm gemaakt worden dat efficiënt licht uitzendt. Als er een efficiënt elektroluminescerend materiaal gevonden zou worden, dan is dit een grote doorbraak in de verlichtings- en beeldschermindustrie.

De nanokristallen die in dit proefschrift behandeld worden zijn gemaakt door middel van een chemische **synthese**. In zo'n chemische synthese rangschikken individuele ionen zich door chemische reacties in een oplossing, om zo een nanokristal te vormen. Door de synthese uit te voeren in de aanwezigheid van een speciaal polymeer, wordt ervoor gezorgd dat de kristallen slechts weinig kunnen groeien en dus nanokristallen blijven. Afhankelijk van het soort nanokristallen dat gemaakt moet worden, kan dit een eenvoudige synthese in water zijn (zoals bijvoorbeeld voor ZnS-nanokristallen) of een ingewikkelde synthese bij hoge temperatuur en in een speciale atmosfeer (zoals bijvoorbeeld voor ZnSe-nanokristallen). Natuurlijk zou men voor een industriële toepassing het liefst nanokristallen gebruiken die met een eenvoudige synthese gemaakt kunnen worden. Daarom begint dit proefschrift dan ook, na een algemene inleiding in hoofdstuk 1, met onderzoek aan ZnS:Mn^{2+}-nanokristallen. Dit staat beschreven in hoofdstukken 2, 3 en 4.

In hoofdstuk 2 wordt vooral veel aandacht besteed aan de synthese en de fotoluminescentie van de ZnS:Mn^{2+}-nanokristallen. Het blijkt dat een heel kleine verandering in de synthesecondities een heel groot effect kan hebben op de eigenschappen van de nanokristallen. Als de synthese uitgevoerd wordt met (iets) meer zwavel dan zink, dan worden de kristallen ongeveer 30 % groter en verdwijnt de luminescentie van het ZnS, zodat alleen de luminescentie van het mangaan overblijft. Door middel van temperatuurafhankelijke metingen van de fotoluminescentie kan dit effect verklaard worden. Op basis van de waarnemingen is er een model opgesteld voor het precieze luminescentiemechanisme.

Hoofdstuk 3 gaat verder met temperatuurafhankelijke metingen aan de fotoluminescentie van de ZnS:Mn^{2+}-nanokristallen. Dit onderzoek richt zich op de temperatuurafhankelijkheid van de emissie-golflengte en op de temperatuurafhankelijkheid van de breedte van de ZnS- en Mn^{2+}-gerelateerde luminescentiebanden. Het blijkt dat de theorieën, die ontwikkeld zijn voor grote kristallen, ook heel goed werken om de effecten te verklaren die de temperatuur op de luminescentie van deze kleine kristallen heeft. Er is echter één uitzondering: de bandbreedte van de ZnS-luminescentie blijkt kleiner te worden voor toenemende temperatuur. Dit ef-

fect is onverwacht en strijdig met de eerder genoemde theorieën, maar kan worden verklaard door een sterke verbreding van de luminescentieband bij lage temperatuur als gevolg van imperfecties in de nanokristallen.

Hoofdstuk 4 is de laatste van de hoofdstukken die zich met $ZnS:Mn^{2+}$-nanokristallen bezig houden. In dit hoofdstuk worden lagen van $ZnS:Mn^{2+}$-nanokristallen, gedeponeerd op een transparante geleider, bestudeerd. Het blijkt dat de nanokristallen foto-elektrisch actief zijn: als er licht op de nanokristallen geschenen wordt (terwijl er een potentiaalverschil over de laag is aangelegd) dan kan er lading gescheiden worden: er wordt een stroom gegenereerd. De daadwerkelijk gemeten stroom is vrij laag, maar de potentiaal-afhankelijkheid van de stroom is duidelijk anders dan wat verwacht zou worden voor grote kristallen van $ZnS:Mn^{2+}$. Dit effect wordt verklaard aan de hand van de speciale eigenschappen van een nanokristal. Helaas waren de experimenten om elektroluminescentie te meten van de $ZnS:Mn^{2+}$ nanokristallen niet succesvol.

Aangezien er geen elektroluminescentie kon worden gemeten van $ZnS:Mn^{2+}$-nanokristallen is er gezocht naar een ander materiaal. Vanwege speciale eigenschappen in de elektronische structuur is dit gedoteerd zinkselenide (ZnSe) geworden. Hoofdstuk 5 beschrijft de synthese en de eigenschappen van $ZnSe:Mn^{2+}$-nanokristallen. De synthese moest worden uitgevoerd in een speciale stikstof- of argonatmosfeer, omdat de chemicaliën die gebruikt worden zeer agressief reageren met zuurstof en water uit de lucht. De luminescentiespectra en de luminescentie-levensduur zijn bestudeerd als functie van de hoeveelheid Mn^{2+} in de nanokristallen. Uit deze metingen kon worden afgeleid dat het waarschijnlijk is dat de mangaanionen graag clusters vormen in het ZnSe-rooster en niet willekeurige posities in het kristal innemen. De temperatuurafhankelijkheid van de luminescentie-eigenschappen is ook bestudeerd en de gevonden resultaten zijn theoretisch verklaard.

De luminescentie van mangaan is speciaal: de overgang die voor de luminescentie zorgt is gelokaliseerd rond het mangaanion. Dit betekent dat verandering van de grootte van het nanokristal geen invloed zal hebben op de kleur die het Mn^{2+} uitzendt. Dit kan handig zijn, maar soms wil men deze kleur juist w´el kunnen variëren. In dat geval zal een ander doteringsion gebruikt moeten worden, zoals bijvoorbeeld koper (Cu). Daarom wordt in hoofdstuk 6 de luminescentie van ZnSe:Cu-nanokristallen bestudeerd.

Door middel van luminescentiemetingen wordt in het eerste deel van hoofdstuk 6 de synthese, en specifiek het groeien van de ZnSe:Cu-nanokristallen tijdens die synthese, bestudeerd. Er zijn twee verschillende groei-regimes te onderscheiden.

In het eerste regime groeien de nanokristallen als gevolg van de chemische reactie, maar in het tweede regime groeien de grote kristallen ten koste van de kleine. In het tweede deel van dit hoofdstuk wordt de temperatuurafhankelijkheid van de ZnSe- en Cu-gerelateerde fotoluminescentie bestudeerd. Met behulp van deze metingen blijkt het mogelijk te zijn om informatie te verkrijgen over de temperatuurafhankelijkheid van de energie van de valentieband en de geleidingsband afzonderlijk. Deze twee banden van de ZnSe-halfgeleider verschuiven allebei als functie van de temperatuur, maar de geleidingsband verschuift veel sterker dan de valentieband. Tot slot wordt een luminescentiemechanisme gepresenteerd dat de metingen kan verklaren.

Nu de synthese en de luminescentie van gedoteerde ZnSe-nanokristallen behandeld is, kan de (potentiële) toepassing van deze nanokristallen onderzocht worden. Dit gebeurt in hoofdstuk 7. Dit hoofdstuk bestaat uit twee losse delen, verbonden door een gezamenlijk doel: het verkrijgen van elektroluminescentie van de ZnSe-nanokristallen. In het eerste deel van het hoofdstuk worden de eigenschappen van een groot ZnSe-kristal bestudeerd. Het doel is om inzicht te krijgen in de waarden van enkele belangrijke materiaaleigenschappen van het ZnSe-kristal. Deze eigenschappen zijn belangrijk bij de ontwikkeling van een geleidend polymeer dat samen met de ZnSe-nanokristallen de basis kan vormen van een elektroluminescerend scherm. Aangezien dit polymeer op dit moment nog niet bestaat, zijn in het tweede deel van dit hoofdstuk andere experimenten gedaan om elektroluminescentie op te wekken. De luminescentie van lagen van ZnSe:Cu-nanokristallen is bestudeerd in een speciale vloeistof terwijl er een extern potentiaalverschil is aangelegd. Op deze manier is de elektroluminescentie van de nanokristallen waargenomen. De elektroluminescentie-efficiëntie was helaas nogal laag, maar het is heel goed mogelijk dat dit verbeterd kan worden. Na hoofdstuk 7 is het doel van dit proefschrift, het bestuderen van de luminescentie van de gedoteerde nanokristallen en het verkrijgen van elektroluminescentie van lagen van de nanokristallen, bereikt.

Hoofdstuk 8 bevat geen experimentele resultaten, maar beschrijft de *simulatie* van gedoteerde nanokristallen. Het behandelt de invloed van de grootte van het nanokristal op de waarschijnlijkheid dat twee doteringsionen toevallig naaste buren zijn. Het blijkt dat de grootte van het kristal een erg belangrijke rol speelt in het bepalen van deze waarschijnlijkheid, omdat het aantal naaste buren aan het oppervlak van het nanokristal anders is dan binnen in het nanokristal. Na de beschrijving van de simulaties en de behandeling van de resultaten, wordt in het tweede deel van het hoofdstuk de analytische theorie, die deze simulatieresultaten kan voorspellen,

in detail uitgewerkt. Het blijkt dat deze analytische theorie z´o goed werkt, dat deze uit te breiden is naar willekeurige kristallen waardoor nieuwe simulaties niet nodig zullen zijn. Het hoofdstuk eindigt met een korte beschrijving van een methode om ook de kans op paarvorming als functie van de grootte van het kristal te bestuderen voor kristallen waarin preferentiële paarvorming van doteringsionen optreedt.

Publications and conference visits

This thesis is based on the following publications:

- *Synthesis and photoluminescence of nanocrystalline ZnS:Mn^{2+}*, J. F. Suyver, S. F. Wuister, J. J. Kelly and A. Meijerink. Nano Letters **1**, 429 (2001). *Chapter 2.*

- *Temperature induced line broadening, line narrowing and line shift in the luminescence of nanocrystalline ZnS:Mn^{2+}*, J. F. Suyver, J. J. Kelly and A. Meijerink. Submitted to Journal of Luminescence (2002). *Chapter 3.*

- *Photoelectrochemical characterization of nanocrystalline ZnS:Mn^{2+} layers*, J. F. Suyver, R. Bakker, A. Meijerink and J. J. Kelly. Physica Status Solidi B **224**, 307 (2001). *Chapter 4.*

- *Luminescence of nanocrystalline ZnSe:Mn^{2+}*, J. F. Suyver, S. F. Wuister, J. J. Kelly and A. Meijerink. Physical Chemistry Chemical Physics **2** (23), 5445 (2000). *Chapter 5.*

- *Luminescence of nanocrystalline ZnSe:Cu*, J. F. Suyver, T. van der Beek, S. F. Wuister, J. J. Kelly and A. Meijerink. Applied Physics Letters **79**, 4222 (2001). *Chapter 6.*

- *Probabilities for dopant pair-state formation in a nanocrystal: simulations and theory*, J. F. Suyver, R. Meester, J. J. Kelly and A. Meijerink. Physical Review B **64**, 235408 (2001). *Erratum:* Physical Review B **66**, 079901(E) (2002). *Chapter 8.*

- *Synthesis, simulation & spectroscopy: physical chemistry of nanocrystals*, J. F. Suyver. To be published as a chapter in the book "Spectroscopy of systems with spatially confined structures", edited by B. Di Bartolo (2003). *Chapter 8.*

- *A theory waiting for an experiment: pair-state formation in a nanocrystal*, J. F. Suyver, R. Meester, A. Meijerink and J. J. Kelly. Accepted for publication by Journal of Luminescence (2002). *Chapter 8.*

Part of this work has also been published in the following proceedings volumes:

- *Applications of ZnS:Mn^{2+} nanocrystals*, J. F. Suyver, A. Meijerink and J. J. Kelly. Materials Research Society Symposium Proceedings **676**, Y3.8 (2001). *Chapters 2 and 4.*

- *Photoelectrochemistry of layers of ZnS:Mn^{2+} nanocrystals*, J. F. Suyver, A. Meijerink and J. J. Kelly. Proceedings of the 2nd International Symposium on Advanced Luminescent Materials and Quantum Confinement, 201st Meeting of the Electrochemical Society, 175 (2002). *Chapter 4.*

- *Luminescence of nanocrystalline ZnSe:Mn^{2+}*, J. F. Suyver, J. J. Kelly and A. Meijerink. Accepted for publication in the Proceedings of the 11th International Symposium on the Physics and Chemistry of Luminescent Materials, 201st Meeting of the Electrochemical Society. *Chapter 5.*

- *Synthesis and luminescence of doped nanocrystalline ZnSe nanocrystals*, J. F. Suyver, S. F. Wuister, T. van der Beek, J. J. Kelly and A. Meijerink. Materials Research Society Symposium Proceedings **667**, G4.8 (2001). *Chapters 5 and 6.*

- *(Electro)luminescence of solutions, powders and layers of ZnSe:Cu nanocrystals*, J. F. Suyver, J. J. Kelly and A. Meijerink. Proceedings of the 2nd International Symposium on Advanced Luminescent Materials and Quantum Confinement, 201st Meeting of the Electrochemical Society, 185 (2002). *Chapters 6 and 7.*

- *Pair-state formation in a nanocrystal: a theoretical perspective*, J. F. Suyver, R. Meester, A. Meijerink and J. J. Kelly. Materials Research Society Symposium Proceedings **676**, Y6.8 (2001). *Chapter 8.*

Other publications:

- *€uropium beveiligt de €uro*, Freek Suyver and Andries Meijerink. Chemisch 2 Weekblad **4**, 12 (February 2002).

- *Energy backtransfer and infrared photoresponse in erbium-doped silicon p-n junctions*, N. Hamelin, P. G. Kik, J. F. Suyver, K. Kikoin, A. Polman, A. Schonecker and F.W. Saris. Journal of Applied Physics **88**, 5381 (2000).

- *Oxidation and annealing of thin FeTi layers covered with Pd*, E. M. B. Heller, J. F. Suyver, A. M Vredenberg and D. O. Boerma. Applied Surface Science **150**, 227 (1999).

- *Optical and electrical doping of silicon with holmium*, J. F. Suyver, P. G. Kik, T. Kimura, A. Polman, G. Franzo and S. Coffa. Nuclear Instruments and Methods in Physics Research Section B: Beam Interactions **148**, 497 (1999).

The work discussed in this thesis was presented at the following international conferences:

- *International School of Atomic and Molecular Spectroscopy: 'Advances in Energy Transfer Processes'*, June 17 - July 1 (1999), Erice (Italy). Oral presentation.

- *European Science Foundation workshop: 'Nanoparticles - Electrical and optical properties'*, December 8 - 11 (1999), Duisburg (Germany). Poster presentation.

- *International Conference on Semiconductor Quantum Dots: 'Quantum Dot 2000'*, July 31 - August 3 (2000), München (Germany). Poster presentation.

- *Materials Research Society Spring Meeting*, April 16 - 20 (2001), San Francisco (United States). Two oral presentations and one poster presentation.

- *Materials Research 2001*, May 8 - 9 (2001), Veldhoven (The Netherlands). Poster presentation. Awarded with the prize for the best poster.

- *International School of Atomic and Molecular Spectroscopy: 'Spectroscopy of systems with spatially confined structures'*, June 15 - 30 (2001), Erice (Italy). Invited lecture.

- *CW Meeting*, April 22 - 23 (2002), Lunteren (The Netherlands). Oral presentation.

- *201st meeting of the Electrochemical Society*, May 12 - 17 (2002), Philadelphia (United States). Three oral presentations.

- *Materials Research 2002*, May 27 - 28 (2002), Veldhoven (The Netherlands). Oral presentation.

- *International Conference on Luminescence and Optical Spectroscopy of Condensed Matter*, August 24 - 29 (2002). Budapest (Hungary). Oral presentation.

Dankwoord

Hier is dan het meest gelezen stukje van elk proefschrift: het dankwoord. Vele mensen hebben, op allerlei manieren, bijgedragen aan het totstandkomen van dit proefschrift, zowel wetenschappelijk als privé. Ik hoop de belangrijksten hier kort de revue te laten passeren.

Als (gedeeld) eersten natuurlijk mijn promotoren, John Kelly en Andries Meije-rink. Het is wel zeker dat dit boekje er zonder jullie niet zou zijn. De vraag is nu natuurlijk of ik bij de "Kelly family"[1] of bij de "Meijerink family" hoor... Misschien een beetje bij allebei? Hoe dan ook, ik ben jullie zeer erkentelijk voor het enthousiasme en de vakkennis die jullie tentoongesteld hebben gedurende de afgelopen vier jaar. John, bedankt voor het spoedig nakijken van eindeloze lappen tekst met vage spectroscopie! Gelukkig is er uiteindelijk toch nog wat elektro-chemie in mijn proefschrift terecht gekomen. Andries, je schijnbaar encyclopedi-sche kennis van alle spectroscopische feitjes zal mij blijven verbazen! Ook de grote mate van vrijheid die jullie mij in mijn onderzoek hebben gegeven (zelfs toen het aantal formules begon te divergeren!) heb ik erg op prijs gesteld.

Over formules gesproken, meer dan 60 formules in één hoofdstuk is in onze groep een record. Zonder de geweldige hulp, inzet en motivatie van Ronald Mees-ter, inmiddels verbonden aan de Vrije Universiteit van Amsterdam, zou dat aan-tal nooit gehaald zijn en zou hoofdstuk 8 überhaupt nooit het daglicht hebben gezien. Ronald, ik ben je dan ook zeer dankbaar dat je zoveel tijd en energie in mijn *Meesterwerk* hebt willen investeren.

Er is nog een hoogleraar, verbonden aan onze groep, die een speciale vermeld-ing verdient: Cees Ronda. Van Cees heb ik geleerd waarom we al dit onderzoek doen: voor bijna alles bestaat er een toepassing. De prachtige verhalen die jij kunt vertellen over onderzoek binnen een bedrijf waren erg leerzaam en ook zeer ent-housiasmerend. Dat ik uiteindelijk besloten heb toch (nog) niet naar Philips te gaan

---

[1] Zie hiervoor het proefschrift van Petra de Jongh, pagina 195.

ligt dan ook zeker niet aan jou. Natuurlijk zal ik de gezellige tijd tijdens conferenties zoals in Erice ("We are all students, but some are more students than others") en in Philadelphia niet vergeten. Hopelijk is het niet de laatste keer geweest dat we samen op een conferentie zijn.

Toen ik net in de groep kwam voelde ik me een beetje een buitenstaander. Fysicus tussen chemici. Gelukkig heb ik van Ageeth Bol in feite een spoedcursusje anorganische chemie (lees: stink-syntheses) gehad. Daarvoor ben ik je erg dankbaar, alhoewel ik er nog steeds van overtuigd ben dat jouw idee om mijn zilveren (trouw)ring in koningswater te wassen niet zo'n goed idee was! Natuurlijk waren al onze gezamenlijke (snoep)reisjes ook altijd erg gezellig. We hebben samen maar liefst 4 buitenlandse conferenties bezocht! Maak je geen zorgen, Marieke was nooit echt jaloers.

Tijdens mijn promotieperiode heb ik vier studenten bij hun experimenteel onderzoek mogen begeleiden: Sander Wuister, Ruud Bakker, Timmo van der Beek en Patrick Steegstra. Een indrukwekkend aantal resultaten was het resultaat van deze samenwerking. Zonder jullie had dit proefschrift er vast heel anders (dunner?) uit gezien. Ik heb met jullie allemaal met veel plezier samengewerkt en wil jullie hartelijk bedanken voor jullie inzet!

Een aparte alinea voor de 'technisch ondersteuning' lijkt me zeker terecht. Als eerste en toch ook wel als belangrijkste, wil ik hier Hans noemen. Hans, ik ben je zeer dankbaar voor de snelheid waarmee je allerlei (meestal vieze) chemicaliën voor me bestelde, de expertise waarmee je kapotte apparatuur repareerde, de nuttige tips die je had toen ik mijn thuisbioscoop maakte en de gezelligheid van een praatje. Ook Stephan heeft, vooral op het computer- en electrochemievlak, nuttige bijdragen aan het totstandkomen van dit proefschrift geleverd. Natuurlijk had ik alle lage-temperatuur-metingen nooit kunnen uitvoeren zonder de vele liters vloeibaar helium en nog meer liters vloeibaar stikstof van Nico, Jan en Johan, waarvoor mijn dank.

Ik heb veel goede herinneringen aan alle conferenties die ik heb mogen bezoeken. Eén van de voornaamste redenen daarvoor is het feit dat dit altijd samen met één of meerdere groepsgenoten gebeurde. Naast de twee generaties Ericegangers (Ageeth, Koert, Liesbeth, Paul en Sander) wil ik zeker ook Peter, Celso en Andries niet vergeten. Jullie hebben er mede voor gezorgd dat ik tijdens deze gelegenheden altijd minder heb geleerd dan ik had gekund. ;-)

Natuurlijk wil ik ook mijn kamergenoten, Marcel en Bert, bedanken voor de goede werkomgeving. Jullie desinteresse voor planten snap ik nog steeds niet. Volgens een voorzichtige berekening hebben Marcel en ik samen zo'n 4 m^3 thee

gezet en opgedronken. Hoezo drankprobleem?

Verder wil ik alle andere (voormalige) groepsgenoten Aarnoud, Addy, Alexander, Arjan, Celso, Daniël, Erik, Floris, François, Gijs, Harold, Koert, Liesbeth, Paul, Peter, Petra, Ren´e, Stephen, Vladimir, Xinghua en Zeger bedanken voor de gezelligheid en de getoonde interesse in mijn werk. Natuurlijk hebben ook alle studenten bijgedragen aan de goede sfeer!

Ik hoor vaak mensen beweren dat er ook leven is naast het werk. Dat is ook zo, zelfs voor mij. Daarom wil ik ook een paar mensen noemen die mijn ontspanning mogelijk maken. Als eerste dan maar mijn 'vriendin': Martina. Gezellig samen naar Egypte, duiken, Rammstein, film kijken, wijn, etc. is natuurlijk altijd goed. Hopelijk is Michel niet al te jaloers. Verder mag Vera natuurlijk niet ontbreken, we moeten maar weer eens gaan klaverjassen. Over spelletjes gesproken: Petra en Detlef, wanneer spreken we weer af om eens koeien te gaan verbouwen? Een bijzondere vermelding voor Evert en Miriam, zonder jullie was de kaft vast niet zo mooi geworden.

Ook wil ik hier mijn ouders, schoonouders, oma, familie en schoonfamilie bedanken voor de getoonde belangstelling in mijn werk. Ik heb de samenvatting geschreven met het idee dat jullie het in ieder geval ongeveer moeten kunnen begrijpen. Hopelijk is dat gelukt! Anders ben ik natuurlijk, zoals jullie wel weten, altijd bereid om uitgebreid te vertellen over alle details van het onderzoek dat in dit proefschrift staat...

Als laatste, en verreweg als belangrijkste, wil ik Marieke bedanken. Zonder jouw liefde en onvoorwaardelijke steun gedurende de laatste acht jaar ben ik niet compleet. Zonder jou was dit proefschrift ook vast lang niet zo mooi geworden. Op naar het avontuur in Zwitserland, samen natuurlijk!

Curriculum Vitae

De auteur van dit proefschrift werd geboren op 14 juli 1975 te Den Haag. In 1994 behaalde hij zijn diploma in het voortgezet wetenschappelijk onderwijs aan het Luzac-college te Den Haag. In september van datzelfde jaar begon hij met zijn studie Natuurkunde aan de Universiteit Utrecht. Tijdens de studie volgde hij keuzepakketten in de subatomaire fysica, materiaalfysica, fysische informatica en vaste-stoffysica en deed hij een klein experimenteel onderzoek bij de groep grenslaagfysica. Het afstudeeronderzoek werd uitgevoerd bij het FOM-instituut voor Atoom- en Molecuulfysica te Amsterdam en werd gedurende de zomer van 1998 onderbroken voor een stage bij het CERN instituut voor hoge-energie fysica te Genève (Zwitserland). Het doctoraaldiploma werd in januari 1999 ontvangen (met genoegen).

Op 16 februari 1999 trad hij als onderzoeker in opleiding in dienst van de Nederlandse Organisatie voor Wetenschappelijk Onderzoek in de groep Chemie van de Gecondenseerde Materie van het Debye Instituut van de Universiteit Utrecht onder leiding van Prof. Kelly en Prof. Meijerink. Hij verrichtte daar onderzoek naar de eigenschappen van gedoteerde nanokristallijne halfgeleiders in het kader van het Prioriteitsprogramma Materialen. De resultaten van dat onderzoek staan beschreven in dit proefschrift en zijn ook gepubliceerd in een aantal wetenschappelijke artikelen en gepresenteerd op diverse internationale conferenties. De details hiervan zijn te vinden in dit proefschrift.

Naast het verrichten van onderzoek, vervulde hij diverse onderwijstaken, waaronder het begeleiden van de onderdelen luminescentie en elektrochemie van de practica 'fysisch chemisch meten' en de einddeelproef van het tweedejaars practicum maken II. Verder begeleidde hij een aantal bijvak- en hoofdvakstudenten.

201

© 1993 by Bill Watterson.